UNIVERSITÀ DEGLI STUDI DI PADOVA

Dipartimento di Tecnica e Gestione dei Sistemi Industriali

Corso di laurea magistrale in Ingegneria Gestionale

Tesi di Laurea

OPTIMIZATION OF A DIE INSERT PRODUCED THROUGH METAL POWDER BED FUSION

Relatore
Ch.mo Prof. Franco Bonollo

Correlatore
Ing. Nicola Gramegna

Laureanda
Nicole Nardo

Anno Accademico 2018-2019

To my mum,
who wanted me in the medicine field.
But loved me despite and above everything.

Summary

1 INTRODUCTION

High-pressure die casting process (HPDC) is one of the most exploited casting processes. Nowadays the process is used more and more to cast bigger and far more complex castings. The principle of the HPDC process is that molten metal (mostly aluminium or zinc) is pressed into the cavity under high pressure. The cavity is filled in a few hundredths of a second. After the melt has solidified, the casting is removed from the open die and afterward the cavity surface is sprayed with a die lubricant and blown with air to avoid water stagnation. The die is then closed and ready to receive a new portion of molten metal. The permanent die undergoes severe thermal cycles, since the range of temperatures involved and the little cycle time. Thermoregulation during the heat removal is crucial not only to obtain a good quality part, but it also affects the die life and the production time cycle, cost-effectiveness of the process results strongly dependent onto these factors.

HPDC dies are made of hot working steel, such as H11 and H13. The complex cavity shape is conventionally obtained with machining processes (CNC, drilling, …), thermoregulation circuits are so restricted to straight line shapes. Thus, meaning that conventional thermoregulation circuits don't impart optimal thermal (and thermomechanical) behaviour, especially in case of great complexity of the cavity (such as curved-in shapes, thin thickness inserts, …).

The advent of Additive Manufacturing (AM) for metals, and its consolidation declined in the Powder Bed (and Direct) methods, has paved the way for fast prototyping and an innovative production. The design is actually freed from conventional tooling (machining) constraints, the material usage is lowered abandoning the substractive conventional processes, design and different processes and scenarios can be easily evaluated through increasingly reliable simulation means.

Conformal Cooling technique takes advantage of AM characteristics listed above, die inserts can so be equipped with free form and small diameter (down to 2 mm) cooling channels, enabling the redesign of the conventional die inserts, making feasible a much more fine control of the thermomechanical behaviour of the die.

While the literature already explored and proved the value of applications of AM tooling for injection moulding, it appears to be still pretty unexplored for HPDC. The aim of this thesis is to establish through a Design of Experiments (DOE) method the possibilities to exploit AM for the design and application of conformal cooling to HPDC tooling, and to evaluate the advantages and disadvantages through a techno/economical comparison between a conventionally tooled die insert and the redesigned version produced through AM.

A brief overview of the mathematical and physical models underlying the HPDC and AM processes may be helpful to have a better understanding of this study, its aims and applications. The math models presented will not only deal with the physical characterisation of the reality of the processes, but also with simulations tools involved, to get a deeper insight of what are the simulations results representing. In addition, basic heat exchangers theory will be presented too, this because the design of any cooling or thermoregulation circuits, despite the complexity of the shape that can be reached with modern techniques derives from directly from the thermophysical models established for studying and designing heat exchangers.

2 STATE OF ART

2.1 HPDC

High pressure die casting is a high rate manufacturing process for producing accurately dimensioned, near net shaped and sharply defined metal parts. A shot of molten metal is injected at high velocity, under high pressure into a reusable steel die. The high pressure and velocity create a turbulent flow condition.

Modern HPDC machines divide in two configurations: cold chambered and hot chambered. The main difference is in the way the molten metal is delivered to the feed system. Hot chambered machines, used mainly for low melting point metals and not iron aggressive metals, have part of the feeding system immersed in the melt, which is hydraulically forced to shot chamber, minimizing heat loss and oxides formation. Cold chambered machines have the melt ladled to the shot chamber, it is necessary for high temperature melting and iron aggressive metal. Since an aluminium part is going to be analysed through this work, it is assumed to be used a cold chambered machine. The die is designed in two halves to permit removal of the castings, it is conventionally manufactured through machining processes (such as drilling, CNC, …). The most complex shapes are obtained applying customized inserts, cores, slides, … There are then, other important mechanical features, a feeding system for the melt front to reach every part of the cavity is composed by runners, gates and vents, and the thermal system, which is necessary since the die also works as a heat exchanger. In die casting, the dies are usually separated into parts which can be retracted individually in a way that it is easy for the part to be removed without damage. The die surfaces and one or many cores (loose or fixed) forms the outer profile of the casting produced. The individual parts of the die are arranged on the machine so that one is stationary (cover die) while the other is movable (ejector die).The process begins with the die opened, the first phase, known as die preparation, comprises five steps: spraying, blowing, placing of movable inserts, die closing and shot preparation. During the spraying step a die lubricant is sprayed on the cavity surfaces, this helps the castings ejections and enhance the heat exchange, while the blowing step uses air to prevent liquid stagnation in the cavity. The die halves, after being equipped with the right inserts, are clamped tightly together by the machine closing mechanism. Then the liquid alloy is ladled to the shot sleeve. Usually some seconds of delay are placed right before the second phase: the filling. During the filling the liquid casting alloy is forced into the cavity by the plunger, it is divided in three stages. During the first phase, the plunger moves slowly (0.02/0.34 m/s) to avoid turbulence, which causes air to be trapped with many disadvantages linked to it, the transition from first to second stage is called switch point or change over position (COP), during second to avoid premature metal solidification and incomplete casting, the plunger moves at a higher speed (0.4/5.4 m/s). The third stage starts when the cavity is filled, high pressure is applied to the plunger till the solidification is complete, to avoid shrinkage and to pack the air that couldn’t be vented. When the casting is solidified, some time is devoted to let it cool down to a temperature by which ejection won’t cause additional strain. The die halves are then opened, movable side plates are removed, and the casting is ejected. At this point the cycle can start again as shown in figure 1 below[1].

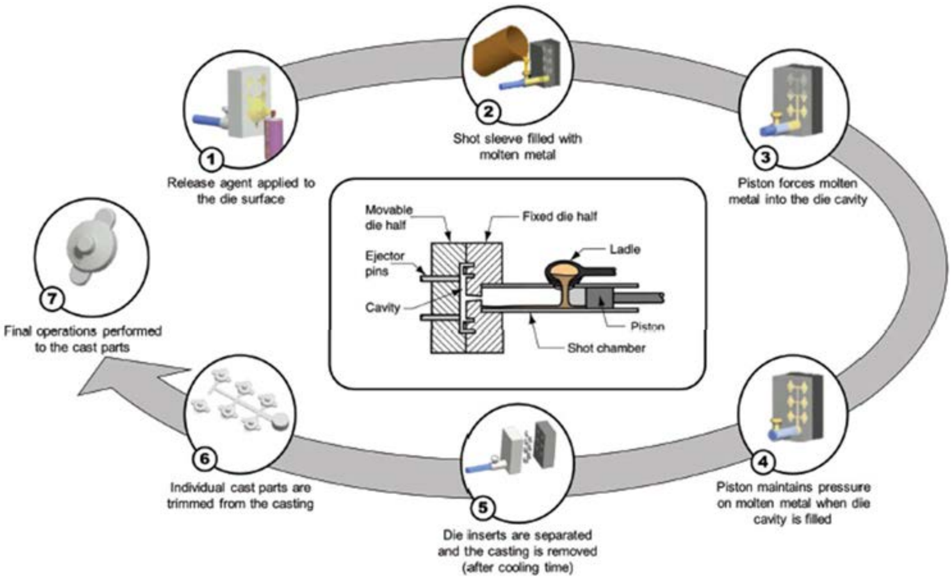

Figure 1- HPDC process overview

2.2 AM of metals

Additive manufacturing (AM) processes build three-dimensional (3D) parts by progressively adding thin layers of materials guided by a digital model. Intricate parts, true to their design can be made in one-step without the limitations of conventional processing methods (such as straight cuts, round holes) or commercial shapes (like sheet, tubes). In addition, a significant reduction in the part count can be realized by eliminating or reducing the need to assemble multiple components integrating more functionalities in the design, even with the possibility relative motion. Production can take place on demand, with no need of spare parts and decreasing the lead time for critical components. The layers can be created in different ways, AM appears declined in seven different process categories: binder jetting, directed energy deposition, material extrusion, material jetting, powder bed fusion, sheet lamination, vat photopolymerization [2]. For the usage of metals of particular relevance are Powder Bed Fusion (PBF) and Directed Energy Deposition (DED) categories. While direct energy deposition AM process uses a focused thermal energy, such as a laser or an electron beam, powder bed fusion AM process create the layers by selectively fusing region of a powder bed applying thermal energy, which is layer after layer, lowered and the powder is restored through a levelling system with a recoating blade or roller. In this thesis the focus is on PBD category, more specifically laser PBD (L-PBD) process. Both DED and PBF processes can use as heat source a laser or an electron beam, they have different characteristics though, from the power involved to the geometrical accuracy, which is far better in PBF process. Among the many additive manufacturing (AM) processes for metallic materials, laser powder bed fusion (L-PBF) process is arguably the most versatile in terms of its potential to realize complex geometries along with tailored microstructure[3]. However, the complexity of the L-PBF process, and the need for predictive relation of powder and process parameters to the part properties, demands further development of computational and experimental methods. In order to understand the complex relationship between basic processing science, defects, and the product of an AM process, it is useful to consider a general process flow chart (figure 2). The process inputs are AM hardware and software, part geometry, scan strategy, build chamber atmosphere and feedstock quality. The process outputs are mechanical properties (static and dynamic), minimization of failed builds and geometric conformity (feature size, geometry scaling). In the flow chart, a box encloses thermal interactions due to applied energy, beam inter- actions, heat transfer and process temperature. These interactions, if properly modelled, should be able to describe dynamic process temperature, which is one of the most (if not the most) defining quantity of metal AM processing[4].

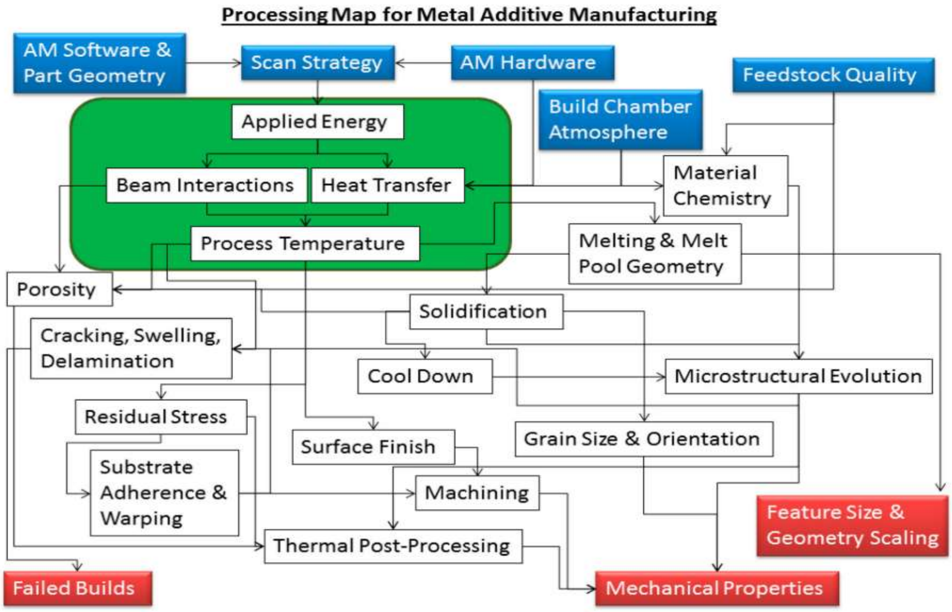

Figure 2

Three main steps can be recognized in L-PBF process:

- I step → Powder deposition: The metal powder is either fed by a hopper or provided by a reservoir next to the work area, for uniform distribution of the powder a levelling system, like a roller or a recoater blade is used.
- II step → Laser exposure: According to the cross section of the part, the metal powder is selectively exposed to the laser beam in the x-y-plane. By exceeding the melting temperature of the material the powder is completely melted along the parts contour and filling. Usually, the sequence of the individual melt tracks follows a pattern, the so-called scan strategy, whereby the melt tracks overlap with a certain hatch distance h; During solidification of the melt the individual melt tracks and the already solidified layer below are fused;
- III step → Lower Base Plate: After the laser have passed along all the cross-section of the layer, the base plate is lowered to be recoated with a new layer of deposited powder;

The L-PBF process main characteristics are represented in figure 3.

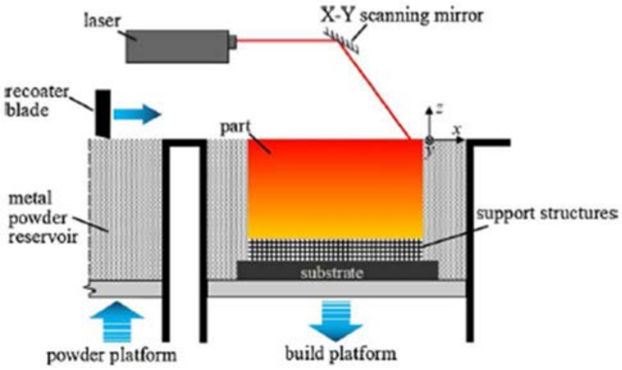

Figure 3

Metal powders for AM can be produced through different methods, and their production results critical, due to big ratio surface/volume, rising the sensitivity to oxidation of these materials. There are mainly four ways to produce metal powders: gas atomization (GA), water atomization (WA), rotary atomization (RA) and plasma rotating electrode processes (PREP). Powders derived from different processes have different characteristics in shape, size distribution, surface morphology, composition and flowability. Typical particle sizes for L-PBF are in the range of 10/60 µm and 60/105 µm for EB-PBF. The PREP powders are perfectly spherical in shape with smooth surfaces. The powder particles from the RA process also exhibit smooth surface but are not spherical in shape. The GA process forms powders with spherical morphology and dimpled surface texture although the presence of the satellite particles increases the surface roughness. The powders from the WA process are usually irregular in shape with coarse surface texture resulting in lower flowability. As a result, these powders lead to deposition of thinner layers in comparison to that with the powders from GA process under the same AM processing conditions. Because of the coarse surface texture and irregular shape of the powders from WA process, the components made by these powders exhibit high surface roughness. The PREP and WA processed powders exhibit the most and the least uniform size distributions, respectively. The powders with uniform size distribution promote homogenous melting, and good interlayer bonding, structure, mechanical properties and surface finish. In contrast, the GA processed powders often contain entrapped gas bubbles leading to porosity in the component. Experimental results have shown that a component fabricated using PREP powders exhibits lower porosity than that made by GA powders under the same processing conditions. However, high quality powders are expensive because of the high cost of the fabrication process such as PREP and low yield of the atomization process. In PBF process, the solid powders can be reused to reduce cost although such reuse of powder particles result in irregular shape and poor surface finish of the final part. Therefore, the powders as feedstock materials must be selected by considering both their quality and cost in association with the corresponding AM process For PBF AM, the powder packing structure is a critical parameter. Experimental characterization of powder is typically limited to measuring bulk properties (like mean diameter, particle size distribution, and packing density) and is inadequate to resolve the local configuration of individual particles on the powder bed. Alternatively, numerical simulation has been used to obtain the packing structure. Many of the numerical algorithms used stem largely from geometrical considerations (e.g., filling of open space by spheres) and did not consider the particle-to-particle mechanical interactions. On the other hand, a group of dynamic simulation algorithms has been applied to simulate the transient packing process where individual particles, roller and their mechanical contact interactions are directly considered based on numerical solution of equations of motion using methods such as Discrete Element Method (DEM). Although it may appear to be large, the number of particles simulated (of the order of 10,000) is still fairly small when compared to that used in the actual build. Moreover, the particles’ shape in the simulation is assumed to be perfectly spherical. Hence, validation of the numerical prediction using the experimental data remains a crucial effort in the future [5]. Typically, powder particle diameter varies in the range of 10-50 μm, layer thicknesses in the range of 20-100 μm and laser beam spot sizes in the range of 20-200 μm are employed. Also, in standard linear scan patterns the distance between two successive laser tracks, denoted as hatch space or spacing h, is an important process parameter. This is typically chosen in the range of half the layer thickness such that a sufficient overlap and remelting between two subsequent tracks is guaranteed.

2.3 Conformal Cooling

Conformal Cooling is a solution for achieving a more uniform cooling (and a better thermoregulation) of the dies. Its principle is to deliver the coolant flow along circuits which path contours the part shape in a more accurate way than conventional circuits would do, due to conventional machining techniques limitations. In the early 2000's some studies presented conformal cooling solutions, but still limited to conventional machining such as milled grooves. In the last ten years the advent and consolidation of AM for metals techniques, along with the development of simulation software, rose the feasibility for conformal cooling circuits, and different methods of their design and optimization have started to be explored especially in the field of injection moulding. In 2008 Meckley and Edwards investigated through Moldflow the differences between a conventionally cooled mould insert and three examples of conformal cooling circuits designed through their experience[6]. In the same year Park and Pham proposed a method of design and optimization of conformal cooling circuits for injection moulding consisting in splitting the mould surface in temperature even zones, each cooled by a subconformal circuit and optimized by minimizing cooling time[7]. In 2011 Wang Et Al established an automatic method to generate conformal cooling circuits following a path determined using an algorithm based on Centroidal Voronoi Diagram(CVD)[8]. During the same year Yu et al developed a methodology based on the visibility technique[9]. In 2014 Choi et al combined the CVD with a binary branching law that generates more channels in case the temperature deviation does not satisfy a given limit[10]. Other studies explored the application of design of experiment technique(DOE) through variation of parameters such as diameter, pitch distance, depth of the cooling channels[11][12][13]. Agazzi et al in 2013 presented a conformal cooling method, they called morpho-cooling, based on channels built on certain isothermal surfaces[14]. In 2016 Mazur et al published an article to evaluate the possibilities of selective laser melting process using H13 steel to build a not only conformally cooled mould but also using lattice structure, opening possibilities to be the lattice structure itself a cooling circuit[15]. In 2017 Mazur et Al went deeper on the analysis of H13 steel processed with AM, analysing process parameters and microstructure and proposing a method for designing conformal cooling circuit based on cooling variation[16]. All these researches were carried out in the field of injection moulding and are valid starting points to start to explore what is feasible and improvable in HPDC process thanks to AM process. Some already are on this route. Pereira in his master thesis in 2013, assessed the manufacturability of AM produced components for in-die use, suitable to withstand the HPDC process condition[17]. Baradaran and Pradeep in a paper of late 2018 explored a case study of a conformally cooled with lattice structure insert, the thermal analysis was satisfying, while the structural was not a total success[18]. Anyway, the actual results depict an interesting new path for conformal cooling circuits for HPDC.

3 THEORETICAL AND ANALYTICAL BACKGROUND of HPDC PROCESS

3.1 Boundary conditions and governing equations

HPDC process can be described as a blend of a hydraulic, thermal and mechanical process. Since its complexity HPDC process has to be modelled on different levels. The three fundamental factors characterizing the process are:

- The thermal behaviour of the casting alloy that can be quantified by the thermal constants.
- The shot end of the casting machine and the shot sleeve or goose neck that provide the liquid metal required to fill the die cavity.
- The shape of the part that defines the flow path of the liquid metal as it travels through the cavity. The introduction xi surface area to volume ratios and the distance that the metal must travel are important mathematical characteristics of each net shape.

[19]

The high pressures involved, the turbulence of the melt flow, the severe thermal cycles due to high temperatures and the change of phase, solidification) of the metal casted yield the necessity to model a process with many variables to take in account. As for the analytical representation of the process, also for the more complex mathematical models behind software tools, everything starts from the knowledge of the process and of the physical phenomena that influence it the most. The first step in solving the given problem comprises describing this problem by the proper physical terms. For instance, the mould filling can be taken as a fluid flow problem, solidification is recognized as a heat transfer problem and the distortions as a solid mechanical problem. The second step would be to describe these physical problems by a proper mathematical model applied in 3-D[20]. It's not that different if we take in account the analytical physical models or the more complex mathematical models that are managed in a software tool. Is important to remember that any model, as far as complex and detailed it can be, it is still an approximation of the reality, nevertheless simulation tools make possible to retrieve quite accurate results in a pretty short time, still appealing to the manufacturing industries short times.

The physical 3-D models that describe the HPDC process are in fact complex and time consuming for an analytical solution. The molten metal cavity filling, involves high

turbulence, since low cavity fill time is desirable to maintain the casting alloy above the latent heat of fusion during fill[19], preventing an undesired freezing phenomenon, this is strongly linked to the behaviour of the superheated alloy involved, and by its thermal characteristics, but this will be furtherly deepen in the thermal part of modelling the HPDC process.
In the following image a comprehensive outlook of the multitude of the physical phenomena involved in the casting processes (figure 4, a cast iron part is shown):

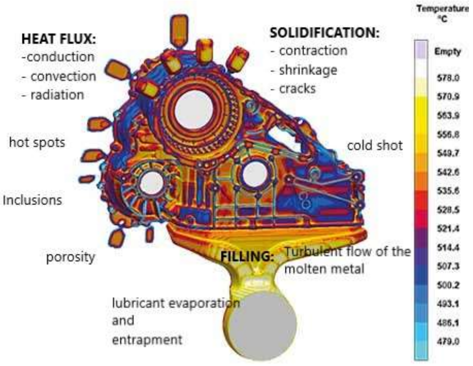

Figure 4

3.1.1 Hydraulic and mechanical model

In this case as mentioned beforehand, the cavity filling can be described as a fluid-dynamics problem, and like in many other technological problems/processes fluids can be treated as a continuum, on the macroscopic scales, even though matter is not continuous but discrete, made of molecules, but its properties are averages over a large number of molecules. The fluid considered is the molten metal, the melt has a viscosity value really near to the water viscosity, however due to multiple times higher density, liquid metals has a much larger energy content, which leads to high turbulence, even in processes with much lower speeds and pressures involved than in HPDC process. The turbulent fluid flow during the filling can be modelled through the 3-D Navier-Stokes equations (N-S equations).

To derive the N-S equations the approach considered involves:

- Defining a small control volume within the flow;
- Applying the mass conservation and force-momentum principle to the control volume;
- Considering what happens in the limit as the control volume becomes infinitesimally small;

All the laws of mechanics are written for a *system,* which is defined as an arbitrary quantity of mass of fixed identity. Everything external to this system is denoted by the term *surroundings,* and the system is separated from its surroundings by its *boundaries*[21]. But it is in the author opinion handier, the derivation of the N-S equations considering a control volume and not a whole system, this is the most common approach also in fluid mechanics textbooks.

Important basis on which the N-S equations are built on mass, momentum and energy conservation. In order to derive the equations of fluid motion, we must first derive some equations to adjust system laws to a specific region, which will host a system only for an instant, since other systems come along with the fluid flowing. The basic laws are reformulated to apply to this local region called a control volume[21]. To achieve the reformulated laws Reynold's Transport theorem and Divergence Theorem must be derived and applied. However, this derivation will not be carried out due to lack of space and due to the scope of this work. For a complete derivation of the up cited and following theorems and equations, please refer to [21].

However, the next paragraphs give a basic overview of the N-S equations.

To generalize the conservation principle applied to mass, momentum and energy it is important to understand how intensive properties are conserved in the fluid field.

The derivation of the conserved property ϕ follows a general rule: *the rate of change of the conserved quantity inside the control volume is equal to the net influx plus appropriate contribution from the sources of ϕ inside of this control volume*. A simple sketch illustrated in figure 5 explains the essence of the conservation principle[20].

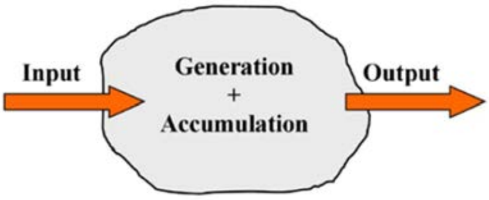

Figure 5

This coupled with the continuity hypothesis, the Newton's Second Law of motion and the First Law Thermodynamics give the N-S equations, that must be considered in a differential form to get point by point results for the flow field.

3.1.1a Mass conservation

The conservation of mass equation can be acquired by writing a mass balance over the stationary volume through which the fluid is flowing. The mass conservation principle denotes that the change of mass within the control volume is equal to the mass entering, minus the mass leaving the control volume, it can be written as:

Rate of accumulation of mass = net rate of inflow of mass by convection

This is regarded as the starting point of deriving the mass conservation equation. This statement can be written in the following equation form:

$$\frac{\Delta m}{\Delta t} = \sum_{i} m_i$$

With some substitutions and derivation that equation can be rewritten in the following differential form:

$$\frac{\partial \rho}{\partial t} + \frac{\partial (\rho u_1)}{\partial x_1} + \frac{\partial (\rho u_2)}{\partial x_2} + \frac{\partial (\rho u_3)}{\partial x_3} = 0$$

This equation represents the mass conservation valid for both compressible and incompressible fluids. Concerning the incompressible fluids (ρ = const.) this equation can be furtherly simplified.

3.1.1b Momentum conservation

Newton`s second law of motion applied to a control volume gives the momentum equations. This means that in a 3-D space, there will be three equations for the linear momentum along the three axes. The derivation of those bring the following equation:

$$\frac{\partial}{\partial t}(m u_i) = \left[\sum_{in} (\dot{m} u_i) - \sum_{out} (\dot{m} u_i)\right] + \left[\sum_{j} f_{i,j} + \sum_{k} b_{i,k}\right]$$

The first term in the brackets on the right side of the equation is the convection term. It brings the x-direction momentum into (or out of) the control volume. The second term on the right side of the equation comprises the sum of the x_i-direction components of the forces acting on the control volume. Two kinds of forces act on the control volume. First, surface forces (for instance pressure forces, viscous forces, surface tension forces) and, second, body forces (for instance gravity force, centrifugal force, Coriolis force, electromagnetic force).

That can be declined into the differential equation of motion, deriving the N-S equation upon direction x_1 in the three dimensions, as follows:

$$\frac{\partial}{\partial t}(\rho u_1) = -\left[\frac{\partial}{\partial x_1}(\rho u_1 u_1) + \frac{\partial}{\partial x_2}(\rho u_2 u_1) + \frac{\partial}{\partial x_3}(\rho u_3 u_1)\right] - \left(\frac{\partial \tau_{11}}{\partial x_1} + \frac{\partial \tau_{21}}{\partial x_2} + \frac{\partial \tau_{31}}{\partial x_3}\right) - \frac{\partial p}{\partial x_1} + \rho g_1 + X_1$$

The first term on the right side in the square brackets represents the x_1 component of the convective transport. It originates from the bulk motion of the fluid. The second term is the diffusive transport term (again the x_1 component) arising from the viscous stresses. The third term originates from the gradient of the static pressure. The remaining two terms are the body force term and any additional terms denoted by X_1 equation is valid for any fluid satisfying the continuum assumption. Before this equation can be used to solve problems, expressions for stresses must be acquired in terms of the velocity and pressure fields:

$$\tau_{21} = \mu\left(\frac{\partial u_2}{\partial x_1} + \frac{\partial u_1}{\partial x_2}\right)$$

$$\tau_{31} = \mu\left(\frac{\partial u_1}{\partial x_3} + \frac{\partial u_3}{\partial x_1}\right)$$

$$\tau_{11} = -p - \frac{2}{3}\mu \nabla \cdot \vec{V} + 2\mu \frac{\partial u_1}{\partial x_1}$$

If these expressions are introduced into the differential equation of motion, it is then obtained Navier-Stokes equation in the x_1-direction in 3-D; equations for the other two directions could be obtained accordingly. Since the nature of molten alloys, can be associated to incompressible fluids with constant viscosity, the N-S equation takes the following form:

$$\rho\left(\frac{\partial u_1}{\partial t} + u_1\frac{\partial u_1}{\partial x_1} + u_2\frac{\partial u_1}{\partial x_2} + u_3\frac{\partial u_1}{\partial x_3}\right) = \rho g_1 - \frac{\partial p}{\partial x_1} + \mu\left(\frac{\partial^2 u_1}{\partial^2 x_1} + \frac{\partial^2 u_1}{\partial^2 x_2} + \frac{\partial^2 u_1}{\partial^2 x_3}\right)$$

Navier-Stokes equations of fluid motion combined with the mass conservation equation provide a sufficient description of the velocity field and an overall picture of the behaviour (of both compressible and) incompressible moving fluids. Since the multiple nature of the HPDC process and it's strong thermal process component, and to fully describe the basis of fluid flow problem and the temperature distribution within the calculation domain, one more governing equation must be introduced, conservation of energy.

3.1.1c Energy conservation

The energy equation for a control volume element can be in words formulated as:

Rate of accumulation of internal and kinetic energy =
Net rate of inflow of internal and kinetic energy by convection +
Net rate of heat addition by conduction +
Net rate of heat addition by radiation –
Net rate of work done by system on surroundings +
The strength of the internal heat sources/sinks

This statement is the first law of thermodynamics written for the open unsteady system. For weakly compressible and incompressible fluids, e.g. melt alloys, the kinetic energy contribution to the total energy can be left out; hence the total energy equation will be replaced by the thermal energy equation. In addition, two terms small for casting processes can be excluded and neglected. The first one is the work against gravity forces and the second one is the rate of work done against the static pressure. It would be necessary to retain this term if it is assumed that the melt is compressible. As we assume the melt as incompressible these terms can be easily omitted. The final non-conservative form of the energy equation is the following:

$$\rho\frac{\partial}{\partial t}(cT) = -\left[(\rho u_1)\frac{\partial}{\partial x_1}(cT) + (\rho u_1)\frac{\partial}{\partial x_2}(cT) + (\rho u_1)\frac{\partial}{\partial x_3}(cT)\right] + \frac{\partial}{\partial x_1}\left(k\frac{\partial T}{\partial x_1}\right) + \frac{\partial}{\partial x_2}\left(k\frac{\partial T}{\partial x_2}\right)$$
$$+\frac{\partial}{\partial x_3}\left(k\frac{\partial T}{\partial x_3}\right) + \mu\Phi_v + \rho\Delta H_L\frac{\partial f_s}{\partial t} + S_T$$

The specific heat c = cp = cv and the term Φ_v stands for the viscous dissipation function. For casting phenomena, this viscous dissipation function in the thermal energy equation results of significance if one wants to model the semi-solid process, otherwise it is negligibly small. Based on this equation it is possible to grasp and completely describe the behaviour of the moving fluid in terms of the temperature. For the remaining variables all of them are already known from the prior conservation laws (mass conservation and momentum conservation).

3.1.2 Thermal model

Die casting is basically a thermal process[19] even though the preceding paragraphs exposed a fluid mechanical model. As reported by Bill Andresen's experience, reported in his book published in 2005, in fact, an attentive thermoregulation of the process makes a big difference in the process cost, especially in terms of casting quality, but still it is something many manufacturers barely pay attention too.

The dynamic nature of temperature=heat energy of typical aluminium alloy die casting cycles is demonstrated in following diagram (figure 6).

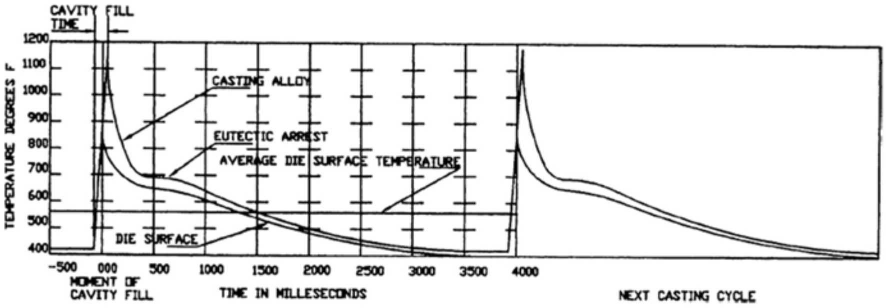

Figure 6

It is evident where high temperatures are necessary to maintain the liquid state of the casting alloy and where rapidly decreasing temperatures convert the casting alloy back to the solid state prior to ejection.

Notice how the large gradient between metal temperature and die surface temperature during cavity fill closes dramatically during solidification that occurs during the dwell time of the casting cycle. The casting alloy is superheated in the melting and holding furnaces prior to delivering it to the injection chamber. At this extremely elevated temperature, the viscosity reduces to about that of water at room temperature so that the alloy will behave like a hydraulic fluid while the near net shape is formed during the filling of the cavity.

Superheat varies for different base metals, and alloys behave differently from the pure base metal. The base metal is the preponderantly present metal in an alloy, and it is customary practice to express its name first in defining the system.

In figure number 7 some cooling patterns are diagrammed for different pure metals. It appears evident the difference with figure 8 where the cooling patterns reported refer to three aluminium alloys, the flat part of the curve results not completely flat. Only the eutectic alloy follows a cooling pattern similar to the pure metals, thus because eutectic alloys behave like pure metals, having one temperature of solidus, while other alloys have a range of temperature in between liquidus and solidus lines, which means they solidify at a changing temperature. These and other differences are due to the alloying metals, that have different influences on the microstructure of metals depending on the percentage of alloying metal present and its own microstructure.

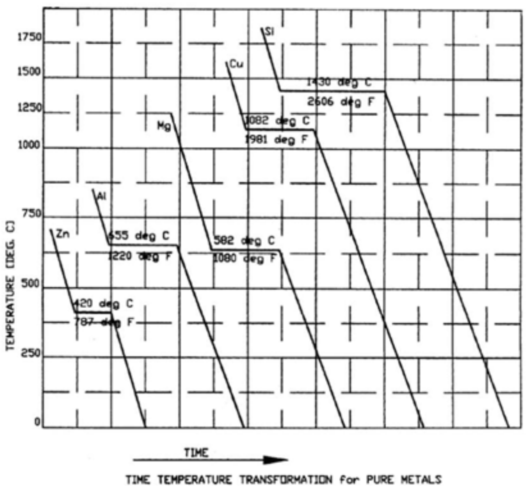

Figure 7

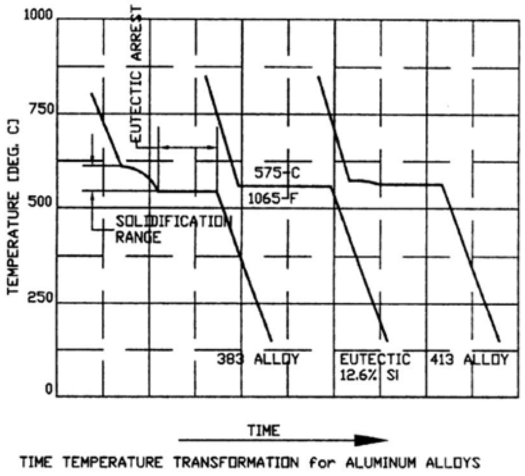

Figure 8

It is beyond the scope of this thesis to unravel more specific information on the difference among pure metals and their alloys, for further knowledge about metallurgy refer to [22].

The role of the casting die as a heat exchanger is obvious from the discussion thus far because raising the casting alloy to the injection temperature is not a part of the die casting process. It is the pattern and speed at which the superheat energy is removed between cavity fill and ejection that are critical. It is all about heat removal[19].

The rate of heat removal is very important as it determines the solidification time of the casting and the temperature distribution in the material. These phenomena affect both directly and indirectly the structure of the material, precipitation of pores and slag inclusions, distribution and shape of shrinkage pores and thus ultimate qualities and properties of castings. Heat transport and solidification processes in casting are very complex and often difficult to fully comprehend[20]; nevertheless, the knowledge of the basic laws of heat transport and their applications in the field of casting is of relevant importance to establish a model behind the heat removal phenomena and to assert design rules for a more efficient process.

Heat transmission happens through three different means: conduction, convection and radiation; and it is described through the Fourier equation.

3.1.2a Conduction

Conduction is the transfer of heat from one part of a body at a higher temperature to another part of the same body at a lower temperature, or from one body at a higher temperature to another body in physical contact with it at a lower temperature[23]. It works on a molecular level, where molecules with higher kinetic energy transfer it to molecules at a lower energetic level. It is easier to picture conduction among gas molecules, where the molecules are in constant random motion, but if it is thought about solids the conduction happens through lattice waves caused by atomic motion, but in case of solids which are good electronic conductors it is handed over by the motion of free electrons.

Besides what happens at a molecular level, the heat flux taking place during conduction can be described, with macroscopic point of view, with the following equation:

$$q = -k\frac{\partial T}{\partial x}$$

where the proportionality constant k is a *transport* property known as the *thermal conductivity* and is a characteristic of the material. The minus sign is a consequence of the fact that heat is transferred in the direction of decreasing temperature. The up cited equation is a one-dimensional formulation, to get a more complete formulation it is necessary to introduce the following vectorial equation:

$$q = -k\nabla T$$

From this equation it is seen that the heat flux vector q actually represents a current of heat (thermal energy) that flows in the direction of the steepest temperature gradient. It is furtherly possible to write a partial differential equation, which provides the basic tool for heat conduction analysis. From its solution, it is possible to obtain the temperature distribution in a medium, for instance a casting or a mould, resulting from conditions imposed on its boundaries as a function of time. The conduction equation is structured right below:

$$\frac{\partial}{\partial x}\left(k\frac{\partial T}{\partial x}\right) + \frac{\partial}{\partial y}\left(k\frac{\partial T}{\partial y}\right) + \frac{\partial}{\partial z}\left(k\frac{\partial T}{\partial z}\right) + q_{vol} = \rho c_p\frac{\partial T}{\partial t}$$

where ρ denotes the material density [kg/m^3], c_p the specific heat capacity [J/kgK], T is the temperature field [K], and q_{vol} the volumetric heat source term [W/m^3].

If the conductivity is constant the equation can be rewritten as follows:

$$\frac{\partial^2 T}{\partial x^2}+\frac{\partial^2 T}{\partial y^2}+\frac{\partial^2 T}{\partial z^2}+\frac{q_{vol}}{k}=\frac{1}{\alpha}\frac{\partial T}{\partial t}$$

Where α is the thermal diffusivity of material which is a measure of how fast temperature is conducted in a solid. In words, the heat conduction equation states that *at any point in the medium the rate of energy transfer by conduction into a unit volume plus the volumetric rate of thermal energy generation must equal the rate of change of thermal energy stored within the volume.* Once the distribution of the temperature is known, the conductive heat flux at any point in the medium or on its surface may be computed from Fourier's law. Other important quantities of interest may also be determined. For a solid, knowledge of the temperature distribution could be used to determine structural integrity through determination of thermal stresses, expansions and deflections.

In addition to the heat conduction equation it is necessary to specify appropriate initial and boundary conditions in order to describe fully the physical problem under consideration. The initial boundary conditions specify the initial temperature distribution throughout the body. In many technological problems, also in casting processes and HPDC process, the initial temperature is generally assumed constant. With regard to the boundary conditions, there are five principal boundary conditions which are used in mathematical theory of heat conduction as idealizations of the actual physical processes. Basically, these boundary conditions are based on the three modes of heat transfer. For more detailed analysis, refer to[23].

3.1.2b Convection

Convection, sometimes identified as a separate mode of heat transfer, relates to the transfer of heat from a bounding surface to a fluid in motion, or to the heat transfer across a flow plane within the interior of the flowing fluid[23]. Linked to the motion mode of the fluid, turbulent or laminar, convection mechanism has two different names, respectively *forced* and *natural* convection. Detailed inspection of the heat transfer process in these cases reveals that, although the bulk motion of the fluid gives rise to heat transfer, the basic heat transfer mechanism is *conduction.* More specifically, it is not *heat* that is being convected but *internal energy.* This rise of the heat transfer if there is forced convection is of great interest in the design and process control of thermo regulation circuits, which give a great contribution to the die heat balance in HPDC process.

However, there are convection processes for which there is, in addition, *latent heat exchange.* This latent heat exchange is generally associated with the evaporation or the solidification of the fluid. For instance, evaporation is too avoid in cooling channels, because it can cause violent phenomena which endanger the integrity of the die and the safety of the operators, while the solidification of the melt at the right moment, with minimized time, is one of the aims of an efficient HPDC process. The following equation represents Newton's law of cooling which is applied in order to express the overall effect of convection can be used commonly as a boundary condition or to describe the convection during the solidification or solid state cooling:

$$q = -hA(T_s - T_f)$$

Where h is the convection heat transfer coefficient, and it's value is strongly dependent on the fluid velocity and the shape of the casting or thermoregulation channels, T_s and T_f are respectively the temperature of the mould surface and the fluid overall temperature, A is the surface between fluid and solid exchanging heat. Convection topic will be deeper addressed in the chapter regarding the theory behind conformal cooling circuits, where forced convection it's of major interest, but considering the convection of the melt this overview may be enough.

3.1.2c Radiation

Radiation, or more correctly *thermal radiation,* is electromagnetic radiation emitted by a body by virtue of its temperature and at the expense of its internal energy. Thus thermal radiation is of the same nature as visible light, x rays, and radio waves, the difference between them being in their wavelengths and the source of generation[23]. Therefore, radiation is the only one of the three mode of heat transfer which can take place even in absence of matter.

The starting point is Stefan-Boltzmann Law, which describes the energy flux emitted by an ideal radiator, also known as blackbody:

$$q = \sigma T^4$$

Where σ is the Stefan-Boltzmann constant which value is 5.669 × 10 -8 W/(m^2K^4), but real surfaces do not perform as ideal surfaces, so the law up cited is modified as follows, inserting the emissivity of the surface, ε, it is a unidimensional value which varies from 0 to 1:

$$q = \sigma \varepsilon T^4$$

For our purposes, the analysis of the casting processes, however, we only consider two simple cases with radiant heat exchange between two surfaces A_1 and A_2. In both cases the net heat exchange can be found from the following expression:

$$q = -A_1\varepsilon_{mean}\sigma(T_2^4 - T_1^4)$$

Where ε_{mean} refers to the specific geometric configuration the equation is applied to, there are two base cases that appear to be enough for the discussing of the casting behaviour during HPDC process.

- **CASE 1:** $A_1 << A_2$ when the mean emissivity can be considered equal to the small surface one $\varepsilon_{mean}=\varepsilon_1$ (it could be well represented by a small surface A_1 completely enclose by a much bigger surface A_2)
- **CASE 2:** The two surfaces are equal, and immediately adjacent in this case the mean emissivity is given by the following formula:

$$\varepsilon_{mean} = \frac{1}{\frac{1}{\varepsilon_1} + \frac{1}{\varepsilon_2} + 1}$$

So, the heat flux intercepted by surface A_2 will be represented as:

$$q = -A_1\varepsilon_{mean}\sigma(T_2^4 - T_{12}^4)$$

To have an equal formulation to the Newton's Law of cooling the up cited relation can be easily rewritten as:

$$q = -A_1 h_{rad}(T_2 - T_1)$$

Where h_{rad} is represented as follows: $h_{rad} = \sigma\varepsilon_{mean}(T_1^3 + T_1^2T_2 + T_1T_2^2 + T_2^3)$.

Considering the heat transfer from the melt/casting to the die surface there is still something important to point out. The melt and the die cannot be considered in ideal contact and this can lead to a significant temperature drop across the interface due to the thermal resistance to heat transfer. This temperature change is attributed to what is known as the thermal contact resistance. The existence of a finite contact resistance is due principally to surface roughness effects. Contact spots are interspersed with gaps that are, in most cases air filled. The mechanism of heat transfer can take place by conduction and/or convection, due to possible gaps between melt and the die surface, where gas is entrapped, also radiation can take place when the temperature differential is high. Since it is difficult to model all of these effects on the microscopic level, the overall resistance to heat transfer across the gap is usually accounted for by using an equivalent interface heat transfer coefficient (HTC) between the materials.

3.1.3 Other physical phenomena to consider in casting processes

From the principles of metallurgy many models must be included in the modelling of casting processes. Depending on the alloy poured, different feeding behaviours and self-feeding capabilities need to be considered to provide a defect free casting. Therefore, it is not enough to base the prediction of shrinkage defects solely on hot spots derived from temperature fields but also to be able to quantitatively predict them. Solidification simulation had to be combined with density and mass transport calculations in order to evaluate the impact of the solidification morphology onto the feeding behaviour, as well as to consider alloy dependent feeding ranges. This is accomplished through the description of temperature dependent thermophysical properties.

It is intended to give a brief overview of the most significant additional models needed, but it remains a marginal scope of this thesis deepen into metallurgy, therefore for a more detailed handling of physical mechanism and mathematical models behind microstructure formation and possible casting defects please refer to [22].

3.1.3a Solidification and shrinkage

During the solidification process the casting besides the changing phase phenomenon undergoes many other phenomena, linked mostly to the cooling down of the melt and the microstructure formation and evolution. For instance four different volumetric changes take place during the HPDC process: liquid contraction, solidification, solid contraction and solid state transformations[20].

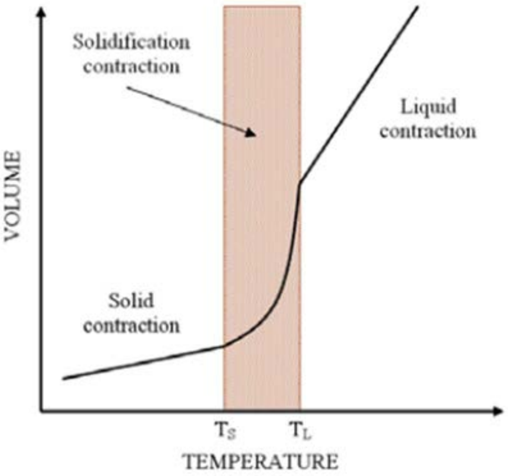

Figure 9- change in volume for casted parts along the cooling/phase change

In Figure 9 the first three types of volumetric change can be easily pointed out, and as it is clear the biggest volume differential is to be found during solidification, as the change of phase radically changes matter structure and molecules disposition.

3.1.3b Feeding

Campbell[24] distinguishes between five different feeding mechanisms, some of them involving solid material and acting during different stages of the solidification process. The feeding mechanisms are summarized in figure 9, for metals with a freezing range. The image refers to three phases solid, liquid and the Mushy zone, which is more a compresence of liquid and solid phase while the melt is between the range of solidus-liquidus This taking into account in general foundry processes, In figure 10 the three feeding mechanisms are represented for a gravity die casting feeder to give a visual idea of the phenomenon, if the reference is HPDC process, despite the lack of feeders, and the very rapid filling, the melt can start to solidify before the completion of the filling, thus falling back in one of the modes of feeding aforementioned, with risk of defects on the casting. Furtherly, the compresence of solid and liquid phase is one of the reasons why the pression after metal injection in HPDC process has a pressure intensification phase, to force the melt to fill interdendritic spaces. It is more correct then, to refer in case with of HPDC to filling issues and related defects.

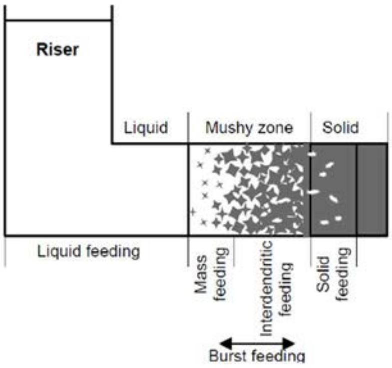

Figure 10- three feeding mechanism represented in gravity casting

3.1.3c Deformation during solidification and hot tearing

In this paragraph, the origin of deformation and stress during solidification and solid state cooling will be discussed. Dimensional changes are required to accommodate the volume change upon solidification, and more importantly, the thermal contraction of the solid upon cooling to room temperature. These dimensional changes produce stresses if one or more of the following conditions are met: non-uniform temperature, non-uniform mechanical properties, constraints induced by the mould or the casting geometry[20].

The starting point of this discussion, like any discussion dealing with classical Mechanics, must be Newton's second law of motion, from which is derived the equilibrium principle, stating that the summation of the external forces on a body equals the mass times the acceleration. Since the static nature of the casting during HPDC process the summation of external forces must be equal to zero. This will simplify the Newton's 2nd law as follows:

$$\sum_{i=1}^{3} F_i = 0 \ \rightarrow \sigma_{ij,i} + p_j = 0$$

Where p_j is the body force at any point within the plate and σ_{ij} is the stress tensor.

3.1.3d Thermal strain

Any body subjected to heating will expand and subjected to cooling will contract, if it is allowed to deform freely. This a behaviour induced by thermal stress, or strain. If the heating of a body takes place uniformly, and the body is not restrained, it will expand uniformly, this is represented by the following equation, where α represents the coefficient of volumetric expansion:

$$\varepsilon^{th} = \int_{T_1}^{T_2} \alpha dT$$

The coefficient α represents how a body reacts to the change of one degree in temperature.

It is, to go on with this discussion, practical to recall Hooke's law, which relates stresses to strain in the elastic field:

$$\sigma = E\varepsilon^{el}$$

3.1.3e Thermal stresses and constraints

It is commonly known that internal stresses may occur in a heated or a cooled body either due to a highly local heating/cooling or external constraint, or a combination of both causes. These internal stresses are referred to as thermal stresses.

There are internal and external constraints on castings. The casting constraint which is a result of uneven cooling is an example of the internal constraint; furthermore, constraining from the mould/die on the casting could be regarded as the external constraint. This type of constraining is readily understood and quite easy to visualize. The rate of constraining is determined via the shape complexity of the casting, which plays an important role for the mould/die constraint. It is important to note that expansion and contraction can lead to different cases: deformation only (when the part is completely free to contract/expand), stress only (when the body is completely constrained, thus it cannot deform) and a combination of the aforementioned cases.

Total strain is a composition of elastic and plastic coupled in the term called mechanical strain (ε^{mech}) and thermal strain:

$$\varepsilon^{tot} = \varepsilon^{mech} + \varepsilon^{th}$$

3.1.3f 3-D thermo elasticity and generalization of Hooke's law

Considering now a more general configuration, a multidimensional stress state, the stress equation can be reformulated for the 3-D domain, as follows in the tensor notation:

$$\sigma_{ij} = \frac{E}{1+\nu}\left\{\varepsilon_{ij} + \frac{\nu}{1-2\nu}\delta_{ij}\varepsilon_{kk}\right\} - \delta_{ij}\frac{E\alpha\Delta T}{1-2\nu}$$

The version of Hooke's generalized law expressing stresses in terms of strains is normally the version that is used in a numerical formulation of a thermo-mechanical problem. This is because the governing equations are the equilibrium equations and these are expressed in terms of stresses, which can also be rewritten in tensor notation:

$$\varepsilon_{ij}^{tot} = \varepsilon_{ij}^{mech} + \delta_{ij}\varepsilon^{th}$$

3.1.3g 3-D thermo-elastoplasticity

The elastic domain is limited by the yield stress, via the yield function which describes when the material starts to behave plastically. It is important to include in the modelling also the plastic domain. There are different models describing plastic deformation, the one that it is going to be discussed in this work is the, so called, J_2 flow theory of plasticity. Which is derived from the Von Mises hypothesis "plastic flow in a general stress state is initiated when the second invariant J_2 reaches the critical value of the second invariant J_2 that initiates plastic flow in the uni-axial stress state" and it's applied under the hypothesis of isotropic material.

The formulation of Von Mises effective stress based on the invariant J_2 is reported below:

$$\sigma_e = \sqrt{3J_2} = \sqrt{\tfrac{3}{2}s_{ij}s_{ji}} \quad \text{where} \quad s_{ij} = \sigma_{ij} - \tfrac{1}{3}\delta_{ij}\sigma_{kk}$$

The component s_{ij} represents the deviatoric part of the stress tensor, while the term on the right, $-(1/3)\delta_{ij}\sigma_{kk}$ is the hydrostatic pressure which does not contribute to plastic deformation.

The yield function can then be formulated as follows:

$$f(\sigma_e, \varepsilon_e^{pl}, T) = \sigma_e(s_{ij}) - \sigma_y(\varepsilon_e^{pl}, T)$$

Where ε_e^{pl} is the equivalent plastic strain, σ_e is the effective Von Mises stress and σ_y is the stress dependent on temperature and plastic strain. It is now possible to write elastic and plastic states formulations based on the yield function, if f<0 the material is behaving elastically, when f=0 the material starts to yield, behaving plastically (f>0 is not admissible because it's not physically possible to have deformation outside the yield surface). The consistency condition enforces the solution to stay on the yield surface evolving.

The derive flow rule that determines plastic strain evolution is then written as below:

$$d\varepsilon_{ij}^{pl} = d\lambda \frac{\partial f}{\partial \sigma_{ij}} \qquad \text{where} \quad \frac{\partial f}{\partial \sigma_{ij}} = s_{ij}$$

where λ is a load parameter which stands for the size of the plastic strain increment, while the direction of this increment is given by the second term which is the outwards pointing normal to the yield surface. The yield function is derived from the consistency criterion as follows:

$$f = f\left(s_{ij}, \varepsilon_{ij}^{pl}, T\right) = \frac{\partial f}{\partial s_{ij}} s_{ij} + \frac{\partial f}{\partial \varepsilon_{ij}^{pl}} \varepsilon_{ij}^{pl} + \frac{\partial f}{\partial T} T$$

This condition relates the development of stress in the domain to the change in yield stress of the material governed by the isotropic hardening and the softening of the material as function of the temperature increment during the applied load increment.

This can be easily visualized in 2-D, in figure 11, where on the left it is shown how the yield function decreases by increasing the temperature (softening) and on the right it is shown how the yield function increases by increasing the plastic strain:

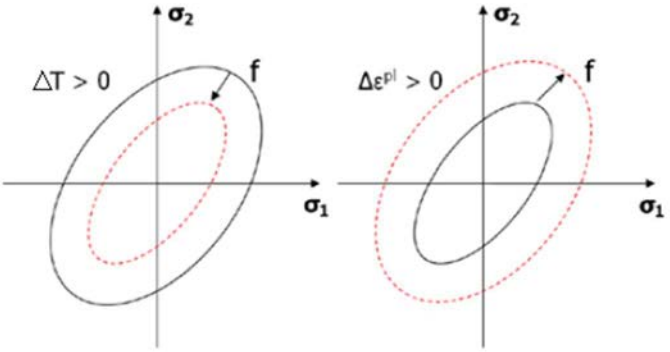

Figure 11

3.1.3h Heat balance

The die, in HPDC process, has among its many function, the important duty to discard the thermal input coming from every shot sleeve injected during the process. Positive ang negative thermal contribution must have the same value, to cancel each other, preventing the die from over and underheating:

$$q_{in} = q_{out}$$

The input heat is given by the amount of melt injected, and the characteristics of the specific alloy exploited and the overheating the melt is subjected to. The production start-up is affected by thermal pulses to each cycle with temperature values that tend, in the same points, to rise up to the reaching of a stable and repetitive situation, which it is generally referred to as thermal regime or steady state. The thermal regime can be then defined as that state in which the temperature, in a generic point at the end of the cycle, coincides with the one at the beginning of the cycle The balance is reached at a certain temperature as the steady state is reached in relation to the discharging capacity of the die[25]. Heat dissipation of each thermal intake occur through five modes:

- Convection towards the environment, linked to external die surface area and temperature differential among the die’s outer surface and the room temperature;
- Radiation, depending on the die temperature and the material emissivity;
- Conduction towards the process machine’s coldest zones in contact with the die;
- Heat dissipation linked to the thermoregulation circuit (convection);
- Heat dissipation due to the spraying phase of the process (convection and phase change of the water part of the die lubricants);

During the solidification the temperature reaches its highest value, this due to the phase change, which includes both sensible and latent heat. The minimum is reached during the spraying phase. More precisely, in case of die-casting, the maximum value of the mould surface heat is obtained when the injected alloy has reached a 70-80% solidification, while the minimum one after the lubrication phase[26]. Temperature variation along the cycle is presented in figure 12, the diagram in figure 13 shows the variation of temperature during the cycle detected by thermocouples located in the nearby of the cavity surface:

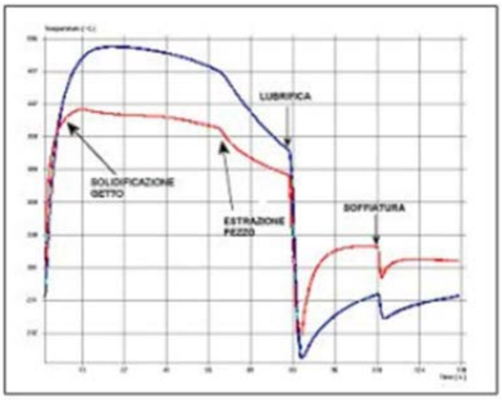

Figure 12

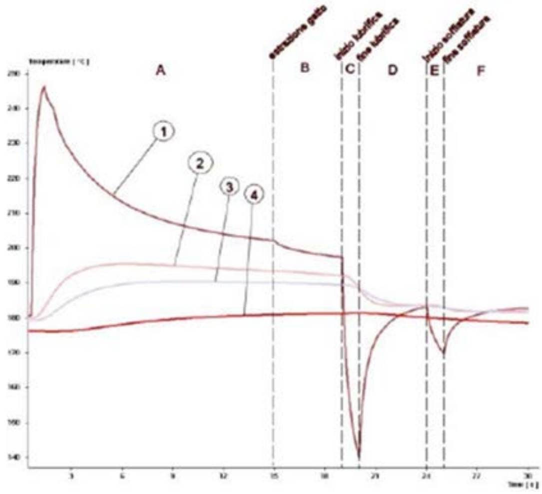

Figure 13

The model behind the heat balance is based on the mechanisms aforementioned, which enable the heat loss, and the heat transfer equation. Heat balance is utterly important to achieve good quality castings and to prolong the die life, while the natural heat loss towards the machine and the environment cannot be controlled (but it's on the other hand nearly marginal), a fine design of thermoregulation circuits, and their control and maintenance coupled with a studied use of lubricants in the spraying phase are necessary to carry out HPDC process efficiently and effectively. In figure 14 thirteen thermal cycles of HPDC process are reported to show the reaching of a stable regime:

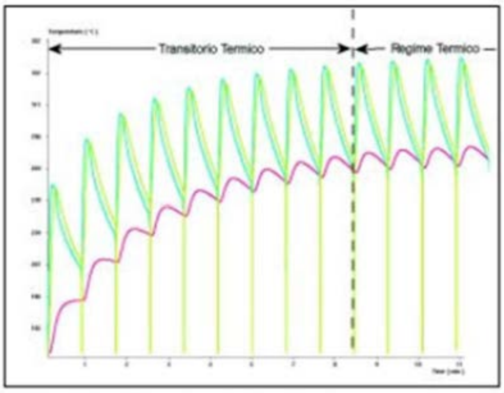

Figure 14

Production interruption strongly affects the heat flux when the process is started again as the temperature drop shows in figure 15:

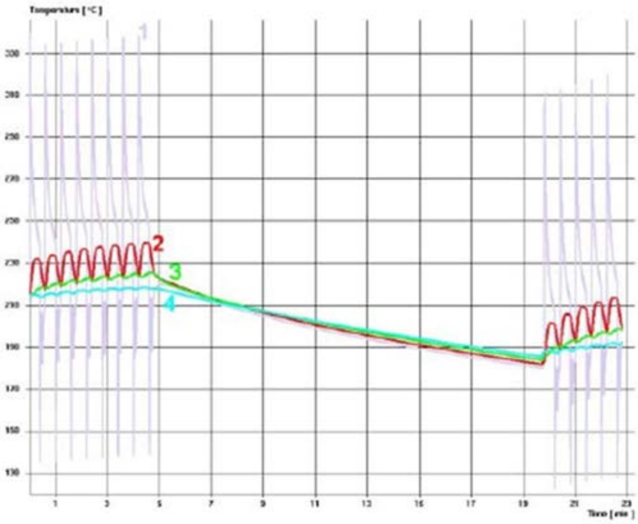

Figure 15

The heat input is released by the alloy releases in three different phases:

- liquid cooling (from the casting temperature to the liquid temperature, as the melt results superheated to be delivered to the cavity in the best conditions);
- the transformation phase from liquid into solid (latent heat);
- solid cooling (the final cooling from the solid temperature to ambient or ejection temperature);

A numerical analysis, taking into account 1 Kg of aluminium alloy, makes clear that the main contribution is provided by the latent heat ranging at 430 kJ/kg, being about the 50% of the total heat flux[26].

The dies working temperature is usually in a range between 200° and 300° C, in this range it's obtainable a good cavity filling and a uniform cooling of the casting. The first cycles carried out when the production starts in absence of pre-heating of the dies may lead to part rejection and considerable thermal shocks, leading also to die surface cracks, which then grow due to the thermal fatigue in the following production phases.

The die heat balance is not so easy to be predicted and therefore the theoretical design is initially based on the search for the best compromise, taking into account the effects of a too high or too low mould temperature. Both case present difficult ejection, despite for different reasons, in fact, for a high die temperature soldering can occur, while for a low temperature the part manifests shrinking around core, pins and lug bolts. In the first case the surface layer of the lubricant-separator tends to a quick lowering, and the die tear and wear increases; the cycle time goes over the prediction and the size instability of the component may show considerable shrinkage porosities. In the second case the risk for cold shuts is much more present and cavity lacking fillings may take place.

The application of the lubricant implies a considerable thermal loss due to the difference in temperature between the die surface and the lubricant working fluid.

From the thermal point of view, several are the factors determining the flux of lost heat during spraying with the lubricant: vector temperature, mould temperature, air pressure, medium pressure, distance from the surface, angle of impact with the surface, application time, concentration and chemical composition of the lubricant[26]. The ΔT between die surface and lubricant must be wide enough to allow instant evaporation of the watery component, so the heat flux is maximized, otherwise the heat extraction is reduced. Also, the lubricant application time has strong influence on the die, more time enables a higher heat extraction, but also means higher temperature drop, which leads to the shortening of thermal fatigue life of the die.

The thermal effect of the following blow phase is similar: the air that flows in pressure towards the die surfaces generates a softer heat loss than the lubrication. These two phases deal with the die surface temperature, the inner zones of the die are thermoregulated through cooling channels, in which can flow water (pressurized or not) or oil. Cooling channels, conventionally are circular conducts, which heat discharge is identifiable through surface of heat exchange (length and diameter), cooling medium characteristics (water, oil, pressure, temperature, laminar or turbulent mode,…). A complete discussion about heat transfer models can be found in heat transfer hanbooks, as [23]. The heat transfer coefficient (HTC) that was conventionally determined on diagrams, is nowadays integrated in many simulation tools to assist the design of the best alternative for thermoregulation. It’s actually better having more control on the temperature of the die through cooling channels, than from lubricant spraying, which cools very effectively the surface but draws out severe thermal gradients promoting localized high thermal stresses on the die.

3.1.3.i Relevant heat exchanger fundamentals theory

Some discussion of tube heat exchanger theory can give a deeper insight on the application of cooling circuits in HPDC process. Being these straight line circuits or of a conformal cooling type, the heat flux exchange may be written as follows:

$$Q = \frac{\Delta T}{R} \qquad where\ R = \frac{1}{UA}$$

R is the thermal resistance and its function of the global thermal conductivity, U, and the surface through which the heat exchange takes place, A, in this case hence it refers to the channels surface. The thermal global conductivity is function of the material which the channel is build in and to the convective coefficient associate to the fluid flowing inside the circuits. [27]

3.2 Defects

It’s the casting process with the highest productivity, process parameters must undergo a fine calibration to obtain castings of acceptable quality. There are different types of defects a HPDC part can manifest, and there are different classifications of them in literature. In the author’s opinion a goodly detailed classification is proposed by Gariboldi, Bonollo and Rosso[28], in fact it’s a three level categorization, accepted as a normative from the 2015(CEN TR 16749:2014 [29]):

- I level: surface, internal and geometry defects
- II level: gas presence, material/volume contraction during solidification and during cooldown, incorrect filling, metal/mold interaction, defects cause by the co-presence of different phases
- III level: specification of the metallurgical origin of the defects of level second.

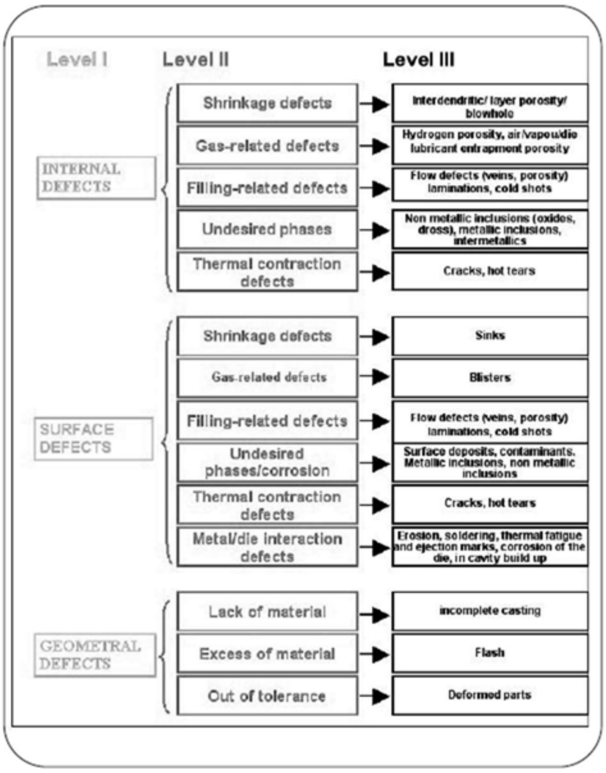

Figure 16

In figure 16[28] the classification is fully represented.

Among the whole classification of defects, some are of higher relevance for this thesis because they are linked to thermoregulation of the die. The most obvious examples die soldering defects, but also porosity, hot spots, cold shots, lamination and others are influenced by how heat extraction is managed by the die, spraying phase and cooling circuits. Both others and the just mentioned defects are also affected by the way the metal is provided to the shot chamber, the filling, undesired phases or inclusions, gas entrapment and lack of material. Quality of the castings and die life are strongly connected, since a cracked or damaged die gives unacceptable castings creating therefore waste.

3.2.1 Shrinkage and porosity

The soundness of the casting depends on uninterrupted flow of liquid metal to the region that solidifies to feed the mass deficit resulting from solidification contraction. Failure to feed the mass deficit will produce shrinkage defects[30]. Some of these defects will be referred as porosity. During liquid cooling and solidification, a significant amount of the dissolved gas is rejected by the liquid and, if a critical pressure is overcome, a gas bubble forms thereby initiating porosity. If the gas bubble fails to find an open liquid surface it interacts with the solid/liquid (S/L) interface eventually forming gas porosity. This is not a shrinkage defect, which is determined by the volume contraction during solidification and cooling and lack of melt to compensate it. If the gas forms in the mushy zone in the later stages of solidification, after dendrite coherency, it will be entrapped in the dendritic network and nucleate small local shrinkage cavities termed microporosity or microshrinkage.

Both types, shrinkage defects and porosity, involve the nucleation and growth of pores, in one case due mainly to the evolution of dissolved gases, and in the other as a result of failure to feed solidification shrinkage. Although the two types each have different morphology, both can be described using the same set of governing equations to determine the pressure drop in the mushy zone associated with liquid feeding and the segregation of dissolved gases. These governing equations are based on the extended mass conservation equation seen before in the derivation of the N-S equations, comprising now a compressible term:

$$\frac{\partial \rho}{\partial t} + \nabla \rho u = 0$$

Where ρ is averaged upon the densities of the various phases:

$$\rho = \rho_l g_l + \rho_s g_s + \rho_p g_p$$

Where the subscripts respectively mean liquid, solid and porosity, thus the third term relates to the gas density, which is actually negligible, so we can rewrite the up initial equation as:

$$\frac{\partial \rho_0}{\partial t} - \rho_l \frac{\partial g_p}{\partial t} + \nabla(\rho_l g_l u_l) + \nabla(\rho_s g_s u_s) = 0$$

The first term on the left represents the change in density due to the combined effects of solidification shrinkage and thermal contraction of the solid and liquid phases. This change in density must be compensated by three phenomena: void growth in the liquid (second term), inward flow of interdendritic liquid (third term) or compression of the solid phase (fourth term). If the solid phase is under a tensile load, arising for instance from external constraints, void growth and interdendritic flow must produce additional compensating volumes, which can lead to hot tears, as discussed in the dedicated section. If the strains in solid form are not considered the conservation equation simplifies as follows:

$$\frac{\partial \rho_0}{\partial t} - \rho_l \frac{\partial g_p}{\partial t} + \nabla(\rho_l g_l u_l) = 0$$

There are two unknown fields in this equation, the pore fraction $g_p(x, t)$ and the velocity field $u_l(x, t)$. For the discussion of the cases where this formulation is furtherly on this topic, refer to Smallman and Ngan[22].

In the following figures 17, 18 and 19 the main shrinkage and porosity types of defects are exposed in a gravity die casting scheme.

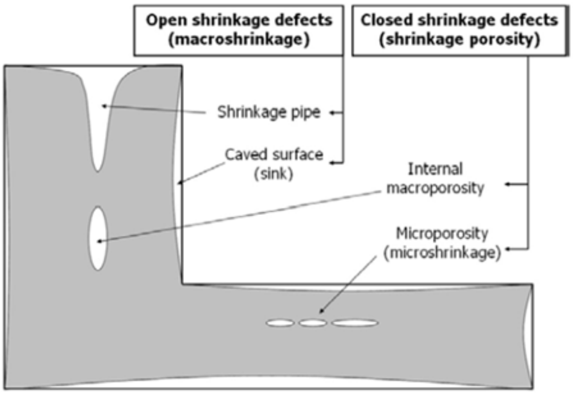

Figure 17- macroshrinkage and shrinkage porosity in gravity die casting example

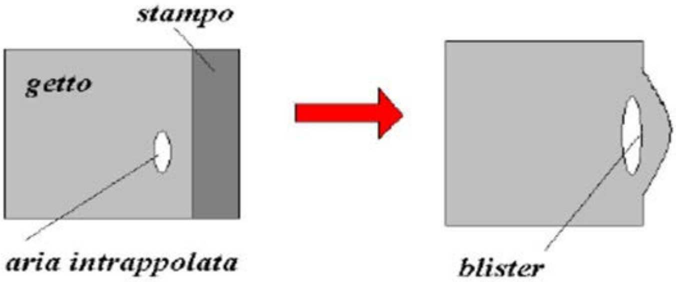

Figure 18- trapped air during HPDC process causing the phenomenon of blistering

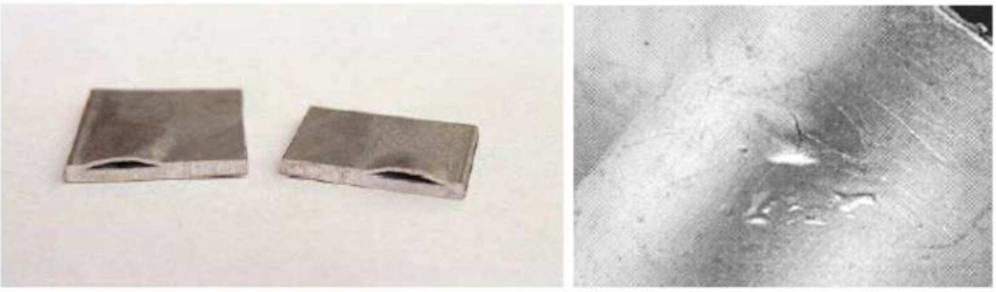

Figure 19- blisters visible on high pressure die casted part

3.2.2 Hot tearing

Thermally induced stresses and strains during casting develop mainly in the fully solid part. These are then transmitted to the mushy zone and tend to localize at the weakest regions, liquid films are present even at relatively low temperature, and when the mushy zone is cut off from feeding, this lead to hot tearing. Hot tears appear usually as strongly oxidized ragged cracks. If liquid is not available under tensile loading, due to the feeding flow being cut off, additional porosity may form. This porosity forms late in solidification, along grain boundaries and it is the initiation site for a hot tear.

There are many causes to hot tearing: alloy composition, design of the feeding system, casting design, the mould, melt composition and handling,… but the hot tearing problem will not be deepen more in this thesis, to a further understanding of the issue please refer to Campbell [24] and Kotas-Hattel [20] studies.

3.2.3 Macrosegregation and microsegregation

Macrosegregation refers to spatial variations in composition that occur in metal alloy castings and range in scale from several millimetres to centimetres or even meters. These compositional variations have a impact on the subsequent processing behaviour and properties of cast materials and can lead to rejection of cast components or processed products. The prediction of segregation requires information derived from phase diagrams, as well as distribution and diffusion coefficients. Macrosegregation is present in virtually all casting processes, including HPDC process despite its cooling rate, where dendrite arm spacings in the range of 5 to 50 microns are obtained. Casting structure is usually fine-grained equiaxed, and segregate spacings are sufficiently fine that a high degree of homogeneity can be obtained through subsequent thermal treatments[31]. There are different models carried out on this phenomenon, the first where established in the ‘60s by Flemings and co-workers. Fleming et al. elaborated the so-called Locale Solute Redistribution Equation (LSRE), which considering the flow of interdendritic liquid through a fixed dendritic solid network, as illustrated in figure 11, while accounting for the different densities of the solid and liquid. This equation is based on a solute balance on a small-volume element inside the mushy zone. Flemings and co-workers assumed that: (1) local solute diffusion in the solid phase is neglected, and (2) the liquid flowing through the volume element is assumed to be well mixed and in local equilibrium with the solid, i.e. the liquid is not undercooled. These are the same assumptions as made in the derivation of the Scheil equation, which will be present in this discussion too. However, in this thesis, will be given a brief overview of the LSRE, for further investigation on classical models and modern derivations please refer to [31], [32],[33] and [34].

In addition to the aforementioned hypothesis, the solute concentration in the liquid, C_l, is given as a function of temperature by the liquidus line of an equilibrium phase diagram (Figure 20) according to $C_l = (T - T_m)/m$ (where T is the temperature, T_m is the melting point of the pure solvent, and m is the slope of the liquidus line).

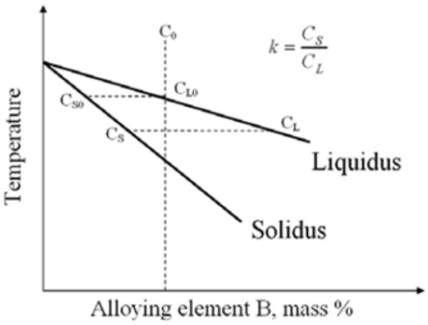

Figure 20

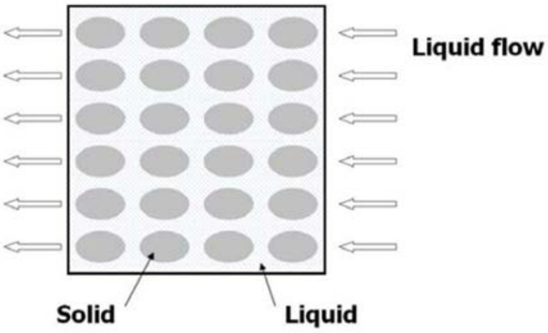

Figure 21

In figure number 21 a representation of the fluid flow through the mushy zone is given, the grey ovals stand for the dendrite's arms. Accounting for advection of solute by the liquid flow in or out of the volume element, and for the different densities of the solid and liquid phases, the following LSRE results:

$$\frac{df_s}{dC_l} = \frac{(1 - f_s)}{C_l}\frac{(1 - \beta)}{(1 - k)}\left(1 - \frac{u_n}{R}\right)$$

where f_s is the solid volume fraction, k is the partition coefficient, u_n is the liquid flow velocity in the direction normal to the isotherms and R is the isotherm velocity and β is the solidification shrinkage. In one dimension, mass conservation yields that the liquid velocity needed to feed the solidification shrinkage is given by:

$$u_{n-shr} = R\left(1 - \frac{\rho_s}{\rho_l}\right) = -R\frac{\beta}{1 - \beta}$$

Note that shrinkage-driven flow is in the direction opposite to the isotherm velocity, that is, in the direction of decreasing temperature toward regions of higher solid fraction, only in case of expansion during solidification the case is the opposite. The flow factor, ξ, is so defined:

$$\xi = (1 - \beta)\left(1 - \frac{u_n}{R}\right)$$

LSRE equation can be integrated to achieve a modified form of Scheil's equation:

$$\frac{C_l}{C_0} = (1 - f_s)^{(k-1)/\xi}$$

The physical meaning of these equations can be understood (with k<1) as follows:

- When ξ=1 Scheil's equation is obtained, impying the absence of the macrosegregation phenomenon, there are only two limit cases possible: absence of shrinkage and absence of liquid flow or a liquid velocity perfect to compensate the shrinkage;
- When ξ≠1 macrosegregation occurs, due to liquid concentration difference from what Scheil's equation predict, there are three cases linked to different mechanism and outcome of the phenomenon: negative segregation (when ξ>1),Positive or inverse segregation (when 0<ξ<1) and local remelting (when ξ<0);

3.2.4 Thermomechanical fatigue and die life

Since the main focus of the thesis is the integration of conformal cooling circuits in HPDC die inserts the, last but not least, phenomena that will be discussed here are the thermo-mechanical fatigue which the die undergoes during the HPDC process, and the heat balance(see next paragraph) that is to be achieved in order to carry out a cost efficient productive HPDC process.

Thermo-mechanical fatigue (TMF) is the damage process caused by the coupling of cyclic thermal and mechanical loading, and the theory of TMF addresses the creep-fatigue interactions that occur[35]. When TMF conditions occur, the result is microstructural damage that can evolve on a macrostructural level eventually. The lifetime of components which undergo TMF results smaller than the same component life in an isothermal ambient, even if the component is exposed constantly at the maximum temperature of operation. TMF is the most influential failure mode in die-casting, it mainly reveals itself in two ways: heat checks and stress cracks. Thermal fatigue cracks occur as the die cavity surfaces are placed under tension when the cold (~25°C) water-based release agent impinges on the hot surfaces previously exposed to the melt. The cooling effect of the die lubricant spray on the underlying hot material causes a tensile stress in the hot die surface, causing surface cracks. This cycle is repeated each time a casting is made. The characteristic feature of heat checks is the appearance of fine cracking lines on surfaces that look like a spider's web. Stress cracks appear mainly in corners, and appear as individual and clearly defined cracks, sometimes filled with casting alloys. Thermal fatigue can occur due to the alone action of cyclic variation in temperature without the influence of other external loads, meanwhile thermo-mechanical fatigue can be identified with fatigue due to cyclic loads at high (or low) temperatures. Usually both phenomena produce a joint action:

a. Acting like a load whose mechanical effects are of more complexity that those that are achieved under mechanical loads.

b. Producing an alteration in the properties of the material, driving to an activation or attenuation of the fatigue effects[36]. The model presented in this thesis, works at a macroscopic level, is a constitutive model, which as all constitutive models are based on the infinitesimal strain theory. The strain is portioned in three components:

$$\varepsilon_{ij} = \varepsilon_{ij}^{e} + \varepsilon_{ij}^{in} + \varepsilon_{ij}^{T}$$

Where the three terms on the right are respectively, starting from the left the elastic strain tensor, the inelastic strain tensor and the thermal strain tensor. For non-unified viscoplasticity theories the inelastic strain tensor can be furtherly divided into the rate-independent plastic strain tensor and the creep strain tensor:

$$\varepsilon_{ij}^{in} = \varepsilon_{ij}^{pl} + \varepsilon_{ij}^{cr}$$

For unified viscoplasticity theories, there is no distinction between plastic and creep strains – only ε_{ij}^{in} exists, representing the combined effect of rate-independent deformation (plastic deformation) and rate-dependent deformation (creep and relaxation).

For all models, inelastic flow is governed by the inelastic flow equation *f* in the stress space, expressed as:

$$f = f\left(J\left(\sigma'_{ij} - X_{ij}\right), K, R\right)$$

Where σ_{ij}' is the stress deviator; X_{ij} is the back stress tensor, *K* is the drag stress and *R* defines the evolution of the elastic limit. *J* defines an invariant function in stress space; the von Mises invariant is typically used for isotropic material, while the term R is considered equal to zero in case of models without elastic domain. In the associated plasticity framework (the flow potential is identical within the yield surface), the normality assumption states that the inelastic strain is given by:

$$\varepsilon_{ij}^{in} = \lambda \frac{\partial f}{\partial \sigma_{ij}} = \lambda n_{ij}$$

Where λ is the inelastic multiplier. In case of rate-independent plasticity, λ is determined by the consistency condition of plastic flow f=f'=0. In the rate-dependent (viscoplasticity) case, f is the viscous part of the stress (or overstress) and λ is defined as a given function of f.

$$\lambda = F_1(f)$$

F_1 is modelled differently according to different modelling, it can appear for example as a step function differentiating plastic dominated and creep dominated deformation, or hyperbolic sine function, or others [37]. While λ is equal to norm of inelastic rate, in the plasticity framework:

$$\overline{\varepsilon_{ij}^{in}} = \left(\frac{2}{3}\varepsilon_{ij}^{in}\varepsilon_{ij}^{in}\right)^{\frac{1}{2}}$$

In the following equations respectively it is to be found the back stress (which is linked to cyclic loading and unloading the hysteresis loop) decomposed as a sum of independent variables, each of which obeys the same rule with different material parameters and it usually contains and its decomposition in a linear hardening term, a dynamic recovery term, a static recovery term, and temperature rate term:

$$X_{ij} = \sum_{k} X_{ij}^{(k)}$$

$$X_{ij}^{(k)} = F_2\left(\dot{\varepsilon}_{ij}^{in},\, X_{ij}^{(k)}, \dot{T}\right)$$

Similarly, to the back stress equations, the isotropic hardening equation may also include three terms to represent linear hardening, dynamic recovery, static recover, or temperature rate change, as show in equation below:

$$\dot{R} = F_3\left(\varepsilon_{ij}^{in}, R, \dot{T}\right)$$

In figure 22 and 23 a representation of the fatigue effects propagation is shown both on a schematic level and on a real case example:

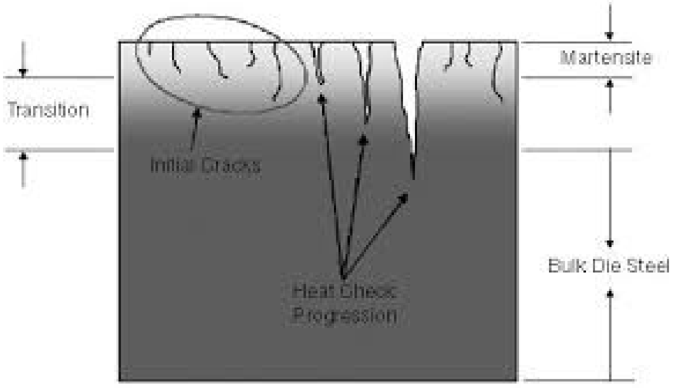

Figure 22- heat cracks initiation and propagation along the die

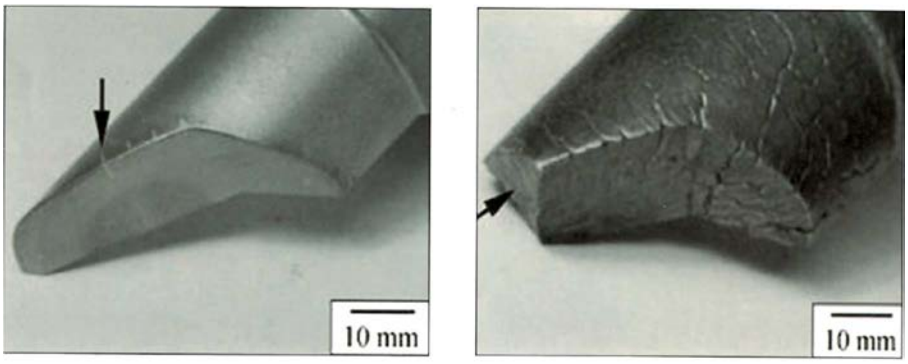

Figure 23-HPDC die insert at crack initiation on the left to insert fail on the right

3.3 HPDC models and simulation

Numerical simulation is the process of solving a physical model through mathematical (differential) equations and the display of the calculated domain (the casting and the mould) through discrete single elements. In order to calculate the differential equations, several methods were developed (FEM, FDM, FVM, BM, MM, etc.), which will not be discussed in detail here. simulation results display casting quality as the combination of a multitude of parameters, which can be manipulated individually[38].

Each method has specific benefits and drawbacks and can yield good qualitative results depending on its area of application. The finite element methods have their roots in load simulations. The finite difference and finite volume methods come from the fluid flow simulation and show benefits in the description of heat and material transport phenomena.

The method to be selected has to be seen as independent from the subdivision of the calculation domain, meshing method. Different meshing methods, as for the computational methods, have different advantages and drawbacks, for example, while linear tetrahedrons experience numerical problems, they approximate the geometry very accurately. Hexahedrons, however, have superior calculation quality, but the transition between the casting and the mold has to be fitted using specific algorithms. Therefore mixed approaches, depending on application and physics, are currently used[38]. The choice eventually, of numerical and mesh methods depend on the specific case, or the choice of a specific software tools with its specific models and methods implemented, is mainly drawn by the compromise between computational quality/accuracy and computational time.

The fluid-dynamics simulation implies to solve the Navier-Stokes equations, which is always a very complex calculation. The Fourier equation that governs the heat transfer, must be also solved. The solution to both phenomena, fluid-dynamics and heat transfer, must be then coupled. In addition, many physical effects related with the physical metallurgy are included, typically the determination of the shrinkage defects and in more advanced calculations, aspects as the microstructure types or the grain sizes. The numerical complexity is increased by the fact that the solution must be calculated for transient regime and usually complex geometries. This is especially true for the case of the High Pressure Die Casting (HPDC) simulation, where part geometries are usually considerably complex, and the alloy is injected at really high velocities[39].

All of that usually imply long calculation times. In complex cases can lead to several days or indeed several weeks. Despite these difficulties, at present the numerical simulation is widely used by the metal casting industry. Sometimes the industry needs to predict the metal casting process as reliable as possible. So, it is needed to go to detailed models able to reproduce accurately the situation at the industrial plant and wait for long time until the solution is reached. But sometimes a fast solution is required although it implies a loss of accuracy. Typical situations are related with the industrial necessities, for example during the offer phase or for the quick evaluation of several alternatives. The up cited hydraulic and thermal models are then just the fundamentals of the many models implemented in the software tools.

To support the analysis carried out in this thesis, the simulation and optimization tool adopted is MAGMASOFT®. A modular software design covers the complete process chain of cast components. The software can be applied for optimized process robustness and part quality from conceptual to final component design, during the tooling layout and prototyping, all the way through to the production and heat treatment processes[40]. The simulation of die casting needs to replicate the following typical problems: Patterns and temperatures in the melt flow: last filled areas, venting of the die, aggregation of die agents, ‘dead areas’ in the runner, turbulences in the melt, disintegration of the melt and merging of melt fronts, cold shuts, or weld lines. Temperatures of the die: the complete die filling (especially during thin-wall casting), cycle times, core wear, adhesive tendency, or heat loss when spraying.

Solidification of the casting: the creation of shrinkage cavities and pores, hot tears, microstructure formation, possible feeding in the final pressure phase or during local squeezing, as well as the formation of residual stress and consequently arising distortion[41].

In fact, the first assessment in casting simulation is, after the acquirement of the 3-D model of the part to produce, an only solidification simulation, which within minutes give the first idea of critical zones. Fluid flow, thermal and mechanical models are the basis of the simulation tool, but many other metallurgical and microstructural phenomena, as some formerly mentioned (for instance porosity), have to be taken in account for an integrated and more holistic analysis of the case study, be it the casting quality, process productivity, …or them all together for a complete look at the HPDC process and production.

The aforementioned theory of stresses and strains occurring in a solidifying casting has been presented for one reason. All this and much more needs to be calculated by the numerical stress solver implemented in MAGMASOFT®, in order to model and predict phenomena such as deformation, residual stresses, for instance von Mises stress, hot tears or cold cracks within a given casting. Considering just hot tearing, if it was not for these stress-strain calculations, it would not be possible to evaluate strains, strain rates, transient stresses, etc., which all contribute substantially to this very common defect in steel castings. Obviously, one should never forget that thermal calculations need to be carried out as well to get an idea on how the casting cools down, if uniformly or not, since nonuniform solidification and thermal contraction drive the formation of thermal stresses and strains[20].

In the early period of casting process simulation, foundries very often asked the question, "Is there any data for my alloys?" This question was important and correct, as approximately 50% of the accuracy of a simulation is determined by the algorithms used and the remaining 50% can be attributed to the thermophysical data[38]. Nowadays materials database are available in software tools either in literature, including thermophysical, rheological and thermo-mechanical properties are generally stored in a temperature dependant format, since the huge temperature ranges involved in casting processes, for the most alloys existent on the market. After the main physical phenomena all casting processes have in common, simulation differs through different characteristic of each casting process, even small process steps, such as the die opening sequence and spraying processes, are considered in detail by simulation tools. Heating and cooling channels cannot only be considered, but can be controlled by virtual thermocouples, and can be evaluated on a fluid dynamic level, which routes the way to an optimal thermoregulation of the process.

MAGMASOFT® employs the Volume-Of-Fluid (VOF) method for tracking interfaces to solve the heat and mass transfer on a rectangular grid. It is useful for simulating molten metal flow in a permanent mold since it can provide useful information about the filling pattern. It also produces reasonably accurate data on casting-related features such as premature solidification, air entrapment, velocity distribution, runner and gate effectiveness. However, the rectangular grid artificially introduces stairstep artefacts along curved and sloping boundaries, that can be reduced through a grid/mesh refinement, with the disadvantage to dilatate computational time and a bigger memory needed to store the results. Plus, the VOF formulation for modelling the free surfaces leads to artificial diffusion and mass conservation problems in these regions. Despite these issues, MAGMASOFT® return results very close to experimentally collected data and/or other modelling methods as reported in some papers, for instance refer to Ha et al [42] study which a comparison between MAGMASOFT®, Smoothed Particles Hydrodynamics (SPH) and water modelling is carried out. To have a deeper understanding of the VOF method, and its alternatives, please refer to [43].

A module which evaluates the stress loads which the die undergoes, and linked to them a calculation of the die life, is also available in MAGMASOFT®, which will be exploited in this thesis.

For a holistic discussion about numerical simulation of foundry processes, therefore HPDC process included the advised reference is the work of Bonollo and Odorizzi [44].

4 THEORETICAL and ANALYTICAL BACKGROUND of L-PBF PROCESS

4.1 L-PBF boundary conditions and governing equation

4.1.1 Physical phenomena occurring during L-PBF process

The physical phenomena involved in PBF processes are multiple, and they worth a discussion on three different levels: macroscopic approaches aim to consider for example the determination of residual stresses or dimensional distortion defects at the component level, mesoscopic approaches focus on the detection of defects such as excessive surface roughness, residual porosity or inclusions that occur at the mesoscopic length scale of individual powder particles, microscopic approaches investigate the metallurgical microstructure evolution resulting from the high temperature gradients and extreme heating and cooling rates induced by the process. Consideration of physical phenomena on all of these three length scales is mandatory to establish the understanding needed to realize high part quality in many applications, and to fully exploit the potential metal AM processes[3]. Figure 24 [3] represents the three levels of scales above mentioned and the physical phenomena that are considered in the models of each scale:

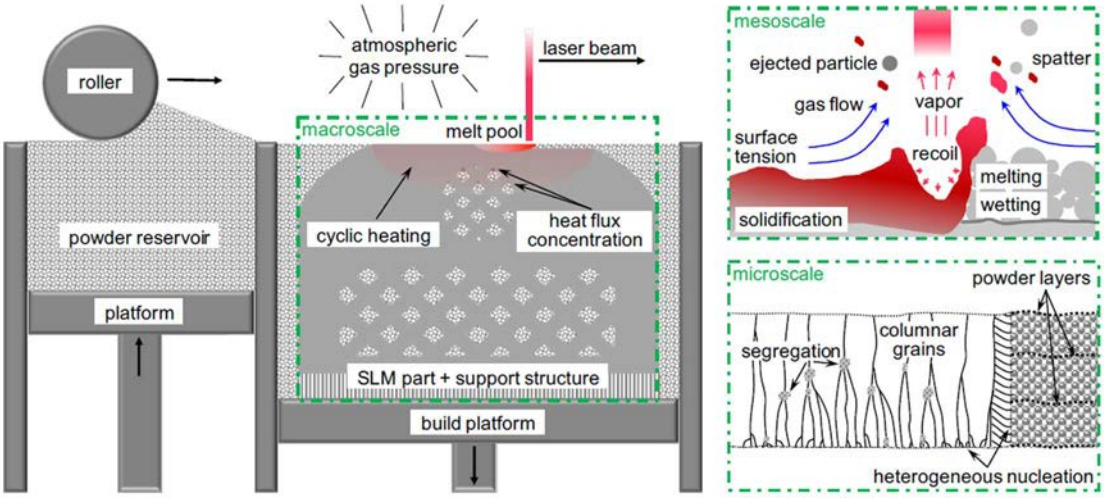

Figure 24

Sames et al[4] in fact, define the L-PBF process modelling as a multi-scale problem, identifying an additional level compared to the three levels above mentioned proposed by Meier et al, resulting as follows:

- Micro-scale (10^{-9} m 10^{-6} m)

- Particle scale (10^{-6} m 10^{-3} m)
- Meso-scale (10^{-3} m)
- Macro-scale (10^{-3} m ÷ 1m)

Where basically the first two scales refer to the microstructure, as it is in the microscopic approach for Meier et al.; Cattenone et al[45] identify only two levels: particle level and part level, which can be associated respectively to microscopic/mesoscopic approaches and macroscopic approaches. Independently on the partition of the modeling scales, what appears clear is the need to model not only at a macroscopic/part level but also on a microscopic/microstructural level(be it grains level, or even finer) for taking in account the multiple physical mechanism characterizing AM processes and AM produced parts. In this thesis the three scales macro, meso and micro are discussed, giving the idea of the possibilities nowadays, but the simulation of the process for the case study will stay on the macroscale.

Because of the rapid heating, melting and solidification of an alloy by a moving heat source such as a laser or an electron beam, different regions of the build experience repeated heating and cooling which affect its local structure and properties. The spatially variable thermal cycles result in location dependent, inhomogeneous microstructure and properties. Transient, three dimensional (3D), temperature fields are prerequisites for understanding the most important parameters that affect the metallurgical quality of the components such as the spatially variable cooling rates, solidification parameters, microstructures and residual stresses and distortion of the components. AM has more similarities with welding than casting. Moving heat source, formation of a fusion zone with recirculating liquid metal that travels along with the heat source are important physical processes that are shared by both welding and most AM processes. There are also differences between welding and L-PBF because the heat source interacts very differently with a powder; furthermore, the scanning speeds and heat source powers are very different. In addition, solid metal surrounds the fusion zone on both sides of the weld but not so for the AM processes. Interaction of the feedstock material with the heat source, progressive build-up of the layers, multiple thermal cycles at any specific location as new layers are added on the previously deposited layers, transient changes in the geometry are some of the features that are necessary for the understanding of AM. As a result, the overall L-PBF process is highly complex and governed by a variety of (competing) physical mechanisms, therefore it can be referred to as a Multiphysics and multiscale problem, the following of this paragraph will deal at a finer detail with what happens in the powder bed, in the melt pool and in the solidified phase of the material.

4.1.1a Powder bed

The effective laser beam absorption within the powder bed is governed by multiple reflections of incident laser rays within the open-pore system of the powder bed, each with partial absorption of the incident radiation. The laser beam can penetrate to considerable depths, which can even reach and overcome the range of the powder layer thickness. The laser beam energy source can be thought of as a volumetric heat source distributed over the powder bed thickness, a further approximation is considering it a surface heat source. The factors influencing overall absorption and local energy distribution are numerous, including the laser beam power, wavelength, polarization, angle of incidence, powder temperature, surface roughness, surface chemistry (for instance oxidation) and contamination. The last factors starting from the surface roughness are strongly dependent on the manufacturing process of the metallic processes, the different processes to obtain powder alloys have been briefly reviewed in the introduction paragraph about AM process. For a more complete insight in powder production processes and characteristics please refer to the study presented by Joly et al [46].

When considering the intra-particle heat transfer, it can be observed that the time scales governing this process are typically larger than the time scales governing particle melting. In other words, under typical L-PBF process conditions, there is not enough time for conductive homogenization of non-uniform energy and temperature distributions across the powder bed but also across individual particles. As consequence, partially molten particles may cause defects such as pores or inclusions[47]. The large size of individual powder grains as compared to powder layer thickness and laser beam spot size typically leads to non-uniform energy distributions, across the entire powder bed but also across individual particles, which may have considerable influence on the resulting melting behaviour and melt pool hydrodynamics. These comparatively large heterogeneities cause differences in the resulting temperature fields and melt track shapes when considering different samples of stochastically equivalent powder layers. Also, heat losses are to be found towards the built platform passing through the solidified layers. While on a macroscopic level powder is modelled as a continuum, on a mesoscopic and microscopic level powder characteristic imply powder structure modelling, which can be carried out, despite the simplification of considering all the powder grains spherical, with different distribution of the sizes and the packing enables the numerical evaluation of the energy absorptions mechanisms taking place during the AM process considered. To summarize the discussion just faced, at the powder level the main issues are:

- Powder modelling (non-uniformity of the powder nature)

- Energy absorption (heat transfer mechanisms, radiation model and scattering phenomenon)

Further information about powder energy absorption will be presented along this study.

4.1.1b Melt pool

When a laser is focused to a small spot size, there is a region above and below the focal plane where the laser energy density is high enough to form a melt pool[48]. As soon as the melting temperature is reached at local positions on the powder grain surface, the phase transition from solid to liquid as well as the formation of a melt pool and, ideally, a continuous melt track is induced[3]. Due to surface tension and capillary forces tending to minimize the surface energy, coalescence of single melt drops occurs. Also, these two physical phenomena coupled with the wetting behaviour of the low viscosity melt on the underlying substrate and the surrounding powder grains, affect the melt pool shape, continuity and adhesion to the previous layer. Oxidation on the powder grain or substrate surfaces, either due to contaminated primary powder material or due to thermally induced oxidation during the process, is known to considerably decrease the wetting behaviour of the melt which might result in instable, balled melt pools and rough surfaces, pores or delamination due to insufficient layer-to-layer adhesion. The aforementioned phenomena plus inertia effects are responsible of the pool shape and dynamics, as well as the surrounding powder morphology by attracting or rejecting individual grains. The melt track is divided into three sections: a topological depression, a transition and a tail region, each being the location of specific physical effects. Heat transfer is mainly driven by convection, rather than conduction, the so called, Marangoni effect, which will be deepen in the section regarding the physical models governing the melt pool.

Depending on the amount of absorbed energy density and the surrounding atmospheric pressure, the peak temperature within the melt pool might exceed the boiling temperature and considerable material evaporation may take place[49]. The evaporation itself as well as the gas flow induced by evaporation may influence the melt pool thermo-hydrodynamics and the overall process as consequence of an evaporative mass loss and additional cooling, of a recoil pressure considerably distorting the melt pool surface and representing a means of transport for potential pollutants, of melt drops spattered out of the pool and even of powder particles ejected away from the direct vicinity of the laser beam[50]. A cavitation phenomenon driven by metal evaporation, the so called, keyhole mechanism or mode, can contribute to porosity and burst the solidified phase due to expansion of trapped gas.

Malekipour and El-Mounayri[51] propose a defect classification (diagrammed in figure 25), 4 main families are identified: geometry and dimension defects, surface quality defects, microstructure defects and mechanical properties. Each of these four groups is furtherly divided in different type of defects. A further discussion on defects can be found at paragraph 5.2 .

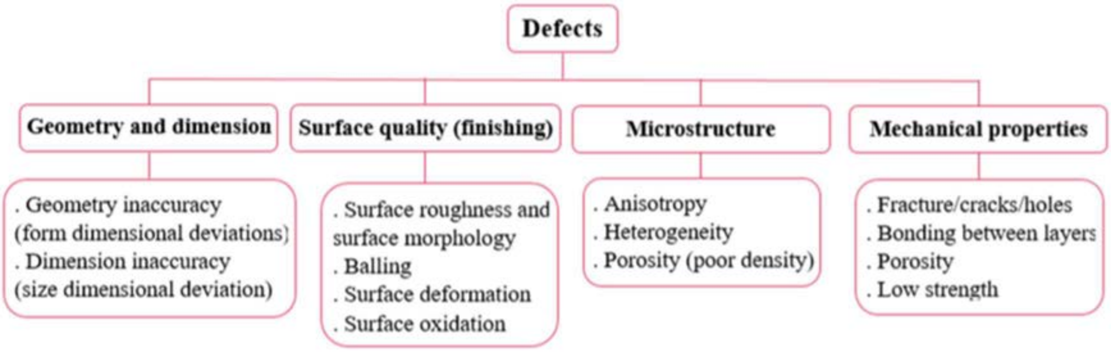

Figure 25

4.1.1c Solidified phase

In L-PBF processes, two regimes can be distinguished in the solidified phase: The first regime is given by the temperature field in the direct vicinity of the laser beam, in the so-called heat affected zone (HAZ), which is governed by the mechanism which is controlled by highly complex mechanisms such as radiation absorption and heat conduction in the powder bed as well as convective heat transfer within the melt pool with all the individual physical phenomena and process parameters of influence and presents metastable microstructure in the early solidification, the second regime is to be identified in the solidified phase is subjected to repeated thermal cycles, which intensity decreases hand-in-hand with the lasers processing adjacent scan tracks, and consecutive new layers. The heat transfer in this regime is rather determined by global part properties, like the global laser beam scanning strategy, the build direction, the fixation of the part on the built platform, the temperature of the built platform but also by the part porosity and the metallurgic microstructure distribution itself, which both influence the (effective) thermal conductivity[3]. Temperature gradients, cooling rates, solidification front, part geometry characteristics like building direction, scan patterns, but also the thermal cycles which the solidified phase is subjected to strongly affect metallurgical microstructure characterized by (grain size, shape and orientation), for instance higher material strength is to be found in the build direction. With increasing distance from the top powder layer, the maximal temperature values and gradients experienced by a material layer during the repeated thermal cycles decrease and, similar to a heat treatment, these cycles might lead to a coarsening of the microstructure, a reduction of brittle non-equilibrium phases and, consequently, to more ductile material characteristics. Thermal cycles taking place during the process affect so the built part on a microstructural level, which consequences are certain mechanical characteristic of the part, but also subject the part to thermal expansion and shrinkage of the material which induce thermal strains. And since the part is kinematically constrained to the build plate, thermal strains lead to thermal stresses, that are also affected by the material properties and its microstructure, which in its turn affect the stress prevalence of residual stresses. These phenomena require a complex thermo-mechanical coupling.

In order to reduce residual stresses on large surface areas, these surfaces are typically subdivided in smaller islands that are completed successively. During the L-PBF process, a relaxation of residual stresses might also occur since the stress amplitude is likely to decrease during the repeated heating and cooling cycles at lower temperature levels. Furthermore, annealing is typically applied to the final part before removing support structures in order to relief residual stresses. The absence of support structures might end in reduced residual stresses, this advantage has to be paid for by dimensional warping, or in the worst case scenario a part fail if during the process the part geometry is not able to be self-supporting towards the upcoming layers. The entire thermal history between solidification and cooling down to the ambient temperature, governed by many heating and cooling cycles at different temperature levels and time scales, considerably determines the resulting metallurgic microstructure as well as the macroscopically observable material properties such as ductility, micro hardness, yield strength or tensile strength as well as their spatial distribution in a possibly inhomogeneous and anisotropic manner.

It is possible the to summarize the main process characteristics as follows. The basic process phases can be distinguished in: powder deposition, selective laser melting of the layer and platform movement, solidification of the melt tracks. Among these the following physical phenomena take place and they can be distinguished in main effects and secondary effects. The main effects comprise:

- Heat conduction
- Absorption
- Convection
- Melting/Solidification
- Wetting
- Gravity
- Capillary Forces

While among the secondary effects the list includes:

- Radiation
- Vaporization
- Marangoni convection
- Solidification shrinkage

In the next paragraphs the mathematical models representing the main physical mechanism occurring during L-PBF are discussed briefly, to move then to how they are exploited and developed on the different scales and in simulation tools that are currently available.

In the following figure (26[3]) a scheme of the multiscale modeling of AM process:

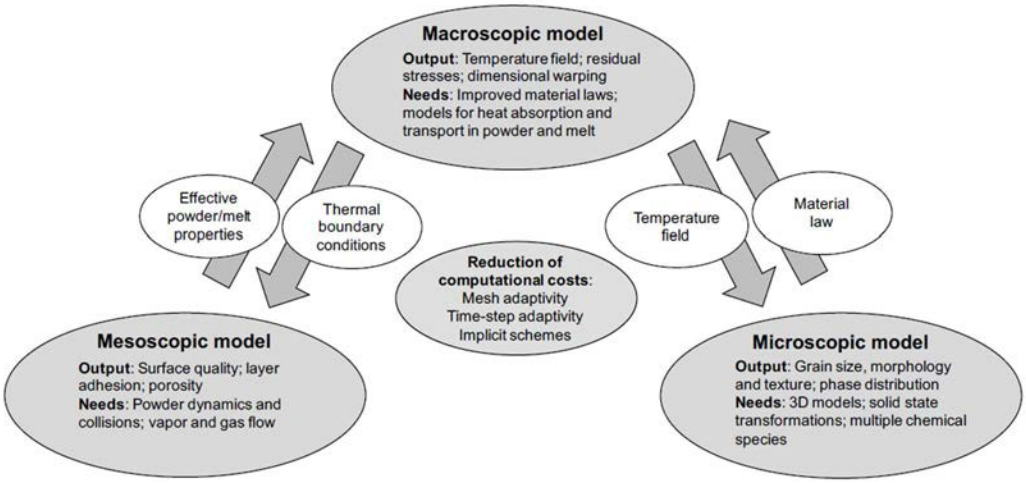

Figure 26

4.1.2 Microstructure

With the solidification of the melt pool, the development of the metallurgical microstructure begins. The evolution of the solid-phase microstructure characterized by grain size, grain shape (morphology) and grain orientation (texture) are governed by the prevalent spatial temperature gradients, the cooling rates, as well as the velocity of the solidification front[50].

Characterizing microstructure and mechanical properties is fundamental for AM simulation. Grain morphology, grain texture and phase identification are typically accomplished via light optical microscope (LOM), SEM, electron backscatter diffraction (EBSD), X-ray diffraction (XRD) or some combination of these methods. Microstructure in AM metal properties has peculiar characteristics, columnar microstructure is dominantly present, with a strong grain orientation. Along axis-z variation of grains and phases takes place due to the material being subjected to subsequent thermal cycles.

The scan strategy can be used to control the microstructure, recent results show significant progress towards demonstrating control. In the image below (figure 27 [5]) the microstructure of three different alloys, respectively high silicon steel(6,8%), IN718, Ti6Al4Va, detection along axis-z are reported. While in Figure 28 ([5]) on the left a photo of a top (transverse to z-axis) surface shows the melt pool marks, on the right its microstructural detection.

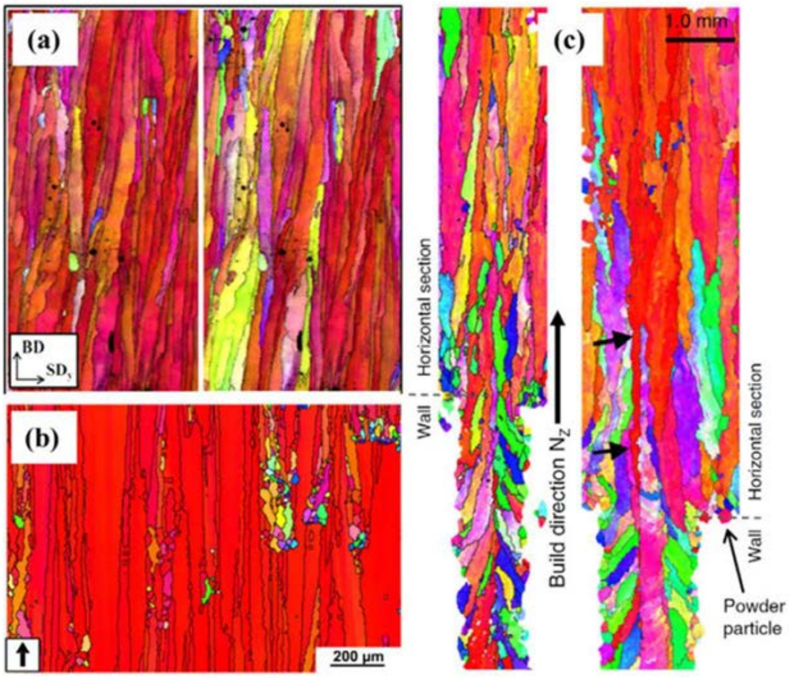

Figure 27

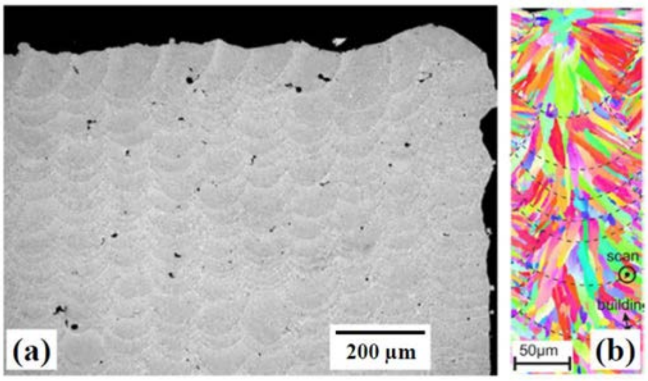

Figure 28

4.1.3 Defects

The AM of metal part shows several defects in the final part. These defects are related to different causes and some of them can be limited by controlling specific process parameters or rather mitigated or eliminated in the post-processing phase (for instance heat treatment, etc.). Follows an overview of the principal defects and a grouping of the main root causes. The categorization is in accordance to that proposed by Malekipour in [51]. The defects of the metal laser AM process are divided into four categories:

1. Geometric and dimensional
2. Surface quality
3. Microstructure
4. Mechanical properties

Below a deeper description of the 4 presented categories and their contributed parameters are described. For a more detailed description the reader is referred to [51].

1. Defects related to geometry and dimensions can be distinguished in:
   i. Geometry inaccuracy (form dimensional deviations) linked to:
      - Staircase effect: in figure 29 the problematics of the building of a part through layers is represented, the smaller is the layer thickness, the closer is the part geometry to its CAD model

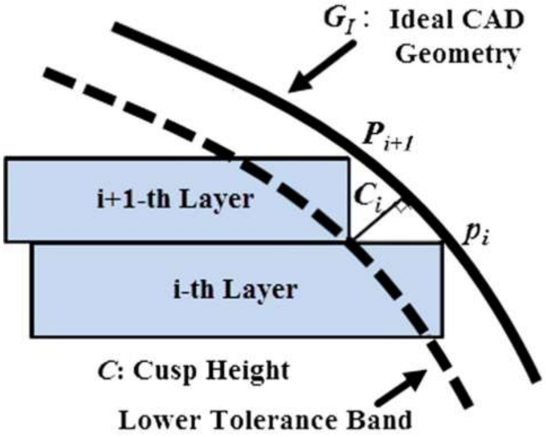

Figure 29

      - Machine error parameters;

ii. Dimensions inaccuracy (size dimensional deviations) are mainly due to:

- Tap density: after deposition powder can be pressed to achieve a higher density of the part but this may lead to vertical displacement, therefore inaccuracy;
- Shrinkage: there two types of shrinkage, sintering shrinkage is linked to the densification of the part during cooling, while thermal shrinkage is caused by thermal cycles characteristic of the process;
- Laser spot diameter: due to light diffusion the laser spot is usually bigger then the machine exerted laser;
- microstructural waviness: phenomena as balling and hatching space cause a "microstructural waviness"
- Building direction: how the part is oriented in respect to z-axis may strongly impact the part quality;

2. Defects related to surface quality (finishing), mainly caused by:

i. Surface roughness and surface morphology

- Scan strategy and laser specifications: the overlapping of layers enables complete fusion and welding of the zone of interest of the layer, a higher overlapping ratio (which parameters are represented in figure 29) in addition to a high energy density (which can be correlated to scan speed and laser power, as shown in figure 30) can decrease surface roughness of the surface of the built part;

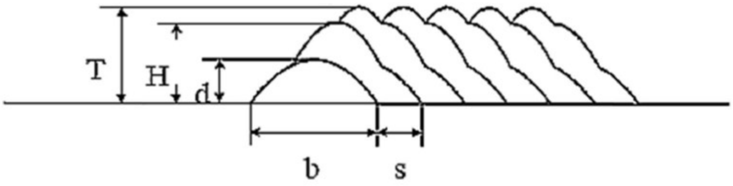

Figure 30

- Powder deposition: the issues linked to powder depositions are due to non-uniformal distribution of particles during the recoating phase;
- Pits on the surface: it occurs that spherical particles with a bigger dimension than the building layer are formatted due to rapid solidification,

the recoating blade or roller can detach these formations leading to pits, as shown in figure 31;

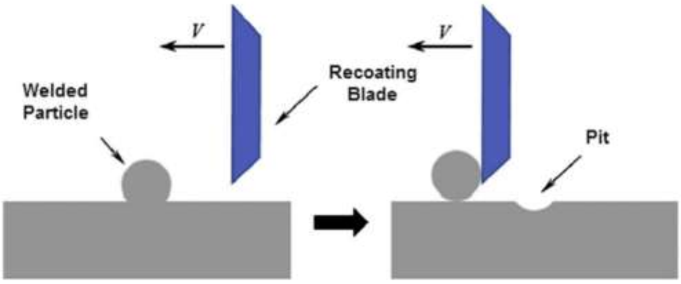

Figure 31

- Fractures, cracks, and holes: fractures can be caused by altered scanning specifications, a general representation is given in figure 32;

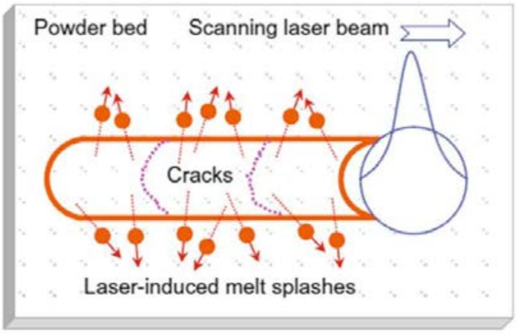

Figure 32

- Quality of the substrate: the roughness of a deposited layer affects the quality of the surfaces of the subsequent levels;
- Staircase effect: as already mentioned, the smaller the layer thickness is the surfaces are better represented;
- Surface orientation: side surfaces result having better quality then top surfaces;

ii. Balling defect manifests in discontinuous tracks, figure 33 gives a schematic representation of some of the causes-effects of this phenomena, the main contributors to this defect are listed below:

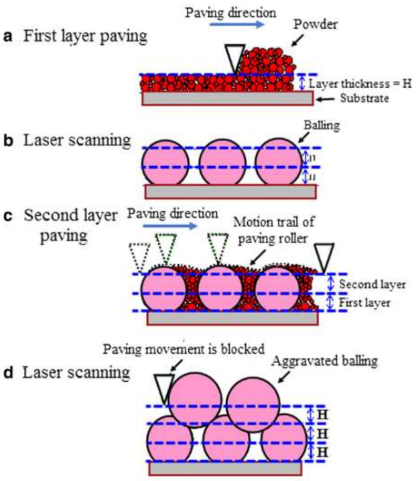

Figure 33

- Energy density (energy input): corelates laser specifications to layer thickness → $E\,[J] = \frac{P\,[W]}{v\left[\frac{mm}{s}\right]\cdot h[mm]\cdot d\,[mm]}$ where P is laser power, v scan speed, h hatch space and d layer thickness; in literature the correlation of laser power and speed is often presented, in diagrams such the two below, in figure 34 and 35 ([4]) where on the y- axis the values represent beam power, while on the x-axis the scan speed is to be found, different areas are highlighted according to the good results obtainable (or weldability) or the possible defects:

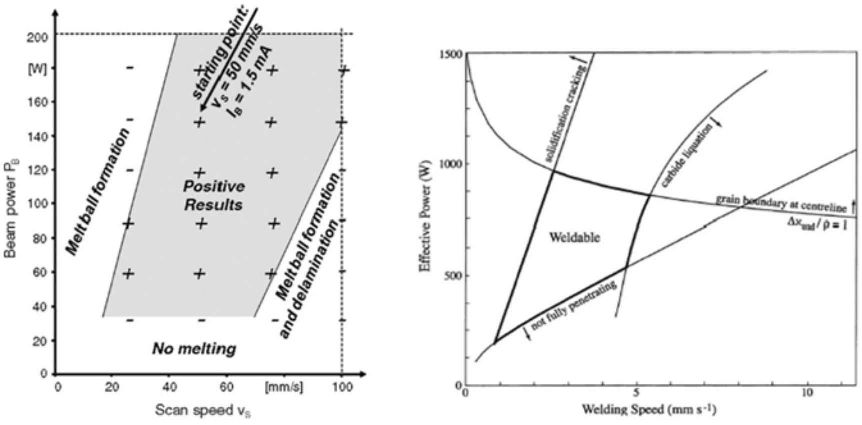

Figure 34 *Figure 35*

- Contained gas of chamber: any change in the composition of the air/gas in the enclosed AM machine, like an increment of oxygen can take part the balling formation;
- Rate of cooling: melt in contact with a cooler substrate tends to reshape into balls;
- Powder effect: preheating of the powder till the mushy zone rises the viscosity, but on the other hand smaller particles are more subjected to the Marangoni effect;
- Plateau's coefficient (Rayleigh-Plateau limit): the pinch effect is at $\lambda/2r=\pi$, under this condition, the structure of a liquid cylinder, in this case assimilable to a laser track, collapses into a series of droplets (balls) when the length (λ) of cylinder exceeds its circumference;
- Poor wetting: high scan speed and low scan power lead to poor heating, hence to poor wetting which causes balling, but oxide reduction, removal, or prevention leads to significant improvement in the wetting conditions;

iii. Surface deformation: there are two types of surface deformation that are mainly created by thermal specifications of the process→ warping means a surface bent out of its natural shape while distortion means any type of changes, not necessarily bending, in the appearance of the surface.

  - Warping: Thermal stress as a result of the thermal gradient, high laser power also causing melt pool instabilities, long scan tracks lead to distortion and warpage;
  - Layer distortion: is dependent on laser specifications such as scan speed, beam power, scan tracks, etc. it also increases with increasing number of layers and due to rotation of deposition starting point;
  - Surface oxidation: oxidation during the process it's usually controlled in vaccum or inert gas (argon) chambers, but contaminants are also present in the powder from its composition, but also due to handling and storage methods carelessness;

3. Defects related to microstructure
    - i. Anisotropy
        - Scan direction: affects many mechanical properties, a multi-scanning direction strategy is required;
        - Layer orientation: maximum compressive strength is present on layers at 90° in relation to z- axis, the minimum is to find at 0° and 45°;
    - ii. Heterogeneity
        - Powder conditioning: both powder and melt density can be improved after a vacuum conditioning for instance fo 12 hours at 450°;
        - Scan strategy: raster scanning and short hatch space can improve part heterogeneity, in figures 36 and 37 some examples of scan patterns and linked parameters;

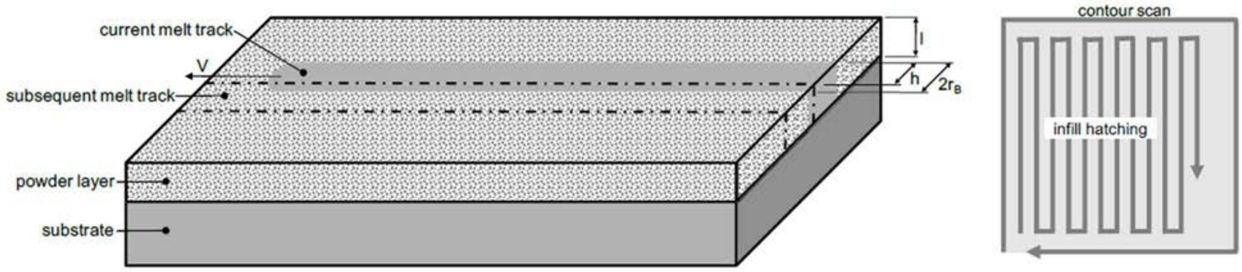

Figure 36

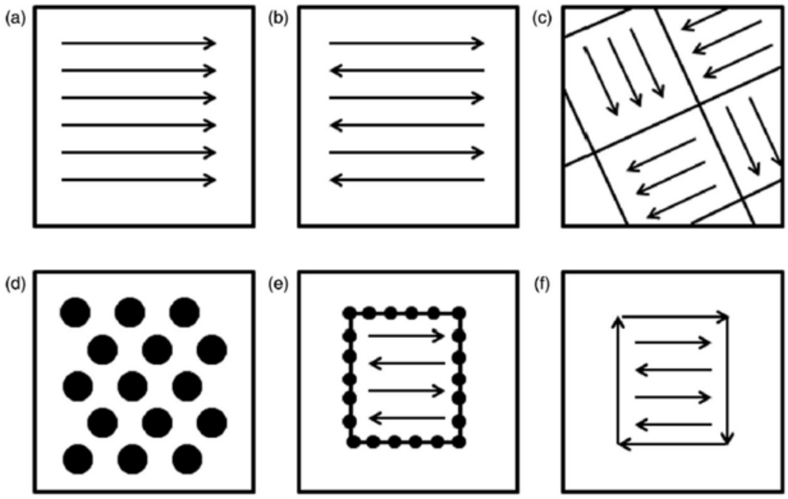

Figure 37

- Energy density: higher energy density leads to more homogenous parts;
- Temperature;
- Solidification condition: different solidification conditions lead to different microstructures;

iii. Porosity (poor density): is one of the most common defects in AM process, it’s caused by many different parameters, and leads to (localized) poor density of the part, many fit in this category the defects linked to keyhole mode, which is represented in figure 38 [52], the main parameters involved in porosity are linked below:

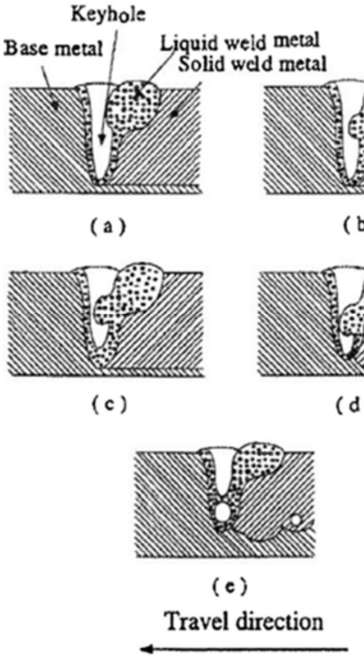

Figure 38

- Laser specification: there are many benchmarks in literature correlating scan speed and beam, for instance the diagram below, figure 39 [51], where laser power and porosity are evaluate at three different speeds:

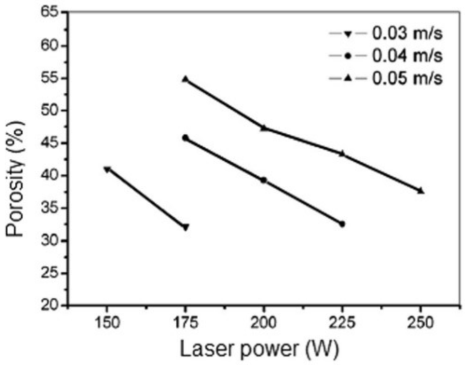

Figure 39

In figure 40 different types of porosity are associated with scan speed and beam power:

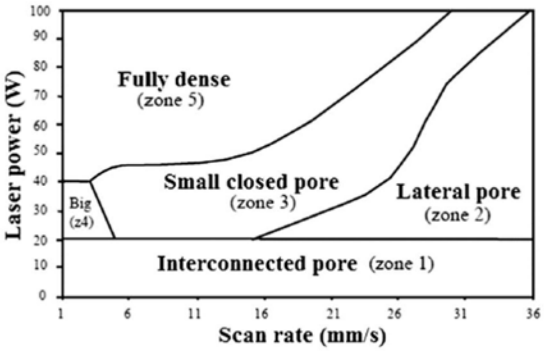

Figure 40

- Scan Strategy:
- Balling;
- Powder size: the smaller the powder size the littler porosity values are detected;
- Powder morphology;
- Drying treatment: humid powder lead to worse porosity;
- Layer thickness: smaller layer thickness enables a deeper laser penetration, therefore a better bonding between layers;
- Melt poll size and morphology: Marangon effect can create more narrow melt pools enabling intra-tracks porosity and keyhole defects;
- Poor wetting;
- Powder packing density (powder apparent density)
- Overlapping ratio
- Entrapped gas: gas present among powder grains may remain entrapped in the melt creating porosity;
- Layer orientation: layer orientation relative to vertical Z-axis at 90° show the littlest porosity value;
- Densification,
- Gas flow condition: uniform inert gas flow prevents porosity formation;

4. Defects related to weak mechanical properties
    i. Fractures, cracks, and holes
    ii. Bonding between layers (fusion bond)
    iii. Porosity
    iv. Low strength

In table 1, the classification and the main contributing parameters are summarized;

Table 1

Defects categories	Subcategories		Contributing parameters
Geometric and dimensional	*Geometry inaccuracy (form dimensional deviations)*	staircase effect	*layer thickness*
		machine error parameters	*laser positioning error* *platform-movement error*
	Dimensions inaccuracy (size dimensional deviations)	Tap density	*powder packing distribution after deposition*
		Sintering shrinkage	*densification*
		Thermal shrinkage	*along x: laser power and scan length* *along y: laser power and scan speed* *along z: laser power, scan speed, hatsch space, bed temperature*
		Laser spot diameter	*diffusivity of the laser beam*
		microstructural waviness	*hatching space*
		building direction	*building orientation*
		gas flow rate	…
Surface quality	*Surface roughness and surface morphology*	Scan strategy	*laser patterns*
		laser specifications	*scan speed* *hatch spacing* *laser spot size*
		Powder deposition	*powder fluidity* *powder grain shape*
		Pits on the surface	*rapid solification* *building layer height*
		Fractures, cracks, and holes	*altered scan specification*
		The quality of substrate	*roughness of deposited layer*
		Staircase effect	*layer thickness*
		Surface orientation	*part orientation*
	Balling		*energy density* *gas in the chamber* *cooling rate* *pre-heating of the powder* *(poor) wetting*
	Surface deformation	Warping	*laser power* *thermal stress* *scan length*
		Layer distortion	*scan specifications* *deposition starting point* *length of plate* *number of layers*
	Surface oxidation		*protective ambient* *powder production, handling, storage*
Microstructure	*Anisotropy*		*scan direction* *layer orientation*
	Heterogeneity		*powder conditioning* *scan strategy* *energy density* *temperature variations* *solidification condition*
			laser specifications (power, scan speed, spot size) *balling* *powder specificationss (size, morphology, …)*

	Porosity		*process parameters (layer thickness, overlapping ratio, layer orientation, laser mode, scan strategy, …)* *densification* *melt pool size and morphology* *(poor) wetting*
Mechanical properties	*Fracture, cracks and holes*		*laser specification* *melt pool size and dynamics*
	bonding of layers		*layer thickness* *heat penetration* *Marangoni convection* *overlapping ratio* *powder deposition* *inert gas flow direction*
	Porosity		*(same parameters as aforementioned)*
	Low strentgh		*scan strategy* *powder specifications* *inert gas flow rate*

4.1.3a Grain structure

Grain structure in L-PBF is dominated by highly oriented, columnar grains. These characteristics develop because of the melt pool geometry and its heat flow. High power per area capabilities has a direct impact on the amount of remelting and epitaxial growth. In L-PBF, the typical scan strategy used (island scanning) has evolved to reduce residual stress and cracking, but it has recently been noted to cause repeating patterns in grain orientations. This
differs significantly from the oriented columnar structure seen using a rectilinear raster (no islands). Depending on the desired grain structure, this may be a limitation. In general, residual stress impacts grain structure from the standpoint of the scan strategies used to avoid it or as a driving force for heterogeneous recrystallisation. Furtherly the start point of scanning can lead to grain nucleation at edges from powder particles in PBF, which can result in increased misorientation near edges or in thin walled structures.

4.1.3b Phase formation

Phase formation and solid-phase transformation has been object of many studies in literature. L-PBF process presents rapid solidification of the scanned tracks, hence phases may go through coarsening and/or dissolving during subsequent passes of the heat source. Depending on the powder alloy obviously, additionally non-equilibrium Laves eutectic heterogeneities are reported to be found, for instance considering Iconel 718, these phases transform into δ-needles during reported to be found in L-PBF produced parts, similarly to needles formations observed in over-aging[4].

4.1.3c Microstructure control

Recent works have demonstrated that beam modulation, with a rapid variance, can give good results in the control of the microstructure[53]. This method rises the dynamic phenomena inside the melt pool due to rapid changing of the heat flux, it aims to create finer grains.

Phase control is more complex, as formation can be influenced by solidification and solid-state phase transformation, with the thermal cycles due to heat source subsequent passes. Phenomena as aging, may occur the process duration itself. As reported by Sames et al. [4]ore research is needed to establish efficient method of phase control.

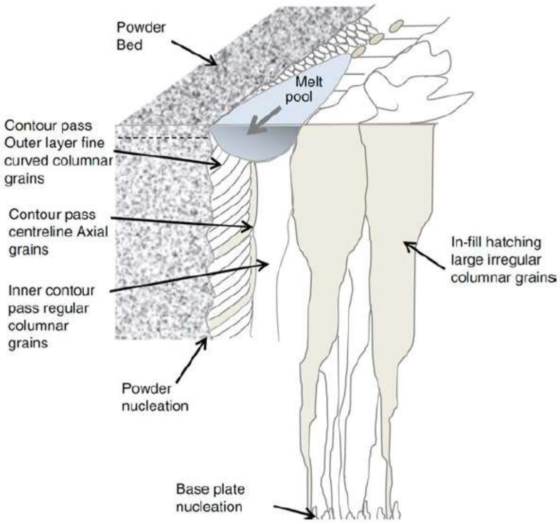

Figure 41

Figure 41[5] represents a summary of the different oriented and columnar grain formation during the process.

4.1.4 Governing Equations

Thermal and mechanical model are presented in the following paragraphs with the formulation adopted by Meier et al. [3]

4.1.4a Thermal Model

The basis for all the approaches that will be mentioned along this chapter are grounded on the mathematical formulation of the physical phenomena taking place along the melt track.

Therefore, the starting point is the thermal problem characterization, which is the base of the heat transfer in the melt pool as well in the solidified phase, it can be formulated as follows:

$$\frac{\partial(\rho c_p T)}{\partial t} + \nabla(\rho c_p T v) = \nabla(k\nabla T) + u_s \qquad \forall(x,t) \in \Omega \times]0, t_{end}[\; where\; (k\nabla T) := -q_k$$

The equation above represents a formulation of the energy equation generally employed for AM process models, where Ω it's the domain, (0,t_{end}) is the time step considered, ρ the density, c_p the specific heat at constant pressure, T the temperature, v stands for the velocity field, k is the tensor representing thermal conductivity and u_s it's the heat source term. On the left side of the equation the two terms represent the material time derivative of the thermal energy density constituted of the local and convective time derivative. A more accurate thermodynamical model would consider the material *compressible*, demanding for additional terms, but most of the models are built on the approximation of considering the material *incompressible*, and in this case the equation above is accountable as complete. The conductivity is usually considered isotropic and will be deeper discussed as effective conductivity in paragraph 5.1.4e. The heat source term is often obtained using the irradiance of the heat source with the Ray Tracing Equation (RTE) model, the irradiance can by the way be derivated also with other means as the RT model, and the other approaches presented in 5.1.4a.

$$T = \bar{T} \qquad \forall(x,t) \in \Gamma_T \times]0, t_{end}[$$

$$q = \bar{q} \qquad \forall(x,t) \in \Gamma_q \times]0, t_{end}[$$

The right above two equations are boundaries formulations of the Dirichlet boundary condition respectively of the temperature and heat flux differentials each of the along its own boundary of the domain.

Relatively to the natural boundary condition of heat flux $\bar{q}$, which usually takes in account radiation emission $\bar{q}_r$ and thermal convection $\bar{q}_{conv}$ along powder surface normal (n_p), with T_{ref} as the temperature of the gas atmosphere, h_{conv} the convection coefficient and ε the emissivity:

$$\bar{q}_{conv} = c(T - T_{ref})n_p \qquad \bar{q}_r = \varepsilon k_{SB}(T^4 - T_{ref}^4)n_p$$

The Stefan-Neumann equation, presented right below, describes the phase change at the interface powder-melt, where the indices $_s$ and $_l$ refers to temperature gradients and thermal conductivites gradients respectively in the solid and liquid phase; T_m is the melting temperature, H_m is the latent heat of melting and n_{sl} is the normal vector of the solid-liquid interface.

$$T = T_m \ \ and \ \ n_{sl}\left(k_s \frac{\partial T_s}{\partial x} - k_l \frac{\partial T_l}{\partial x}\right) = H_m \rho n_{sl} \dot{x} \qquad \forall(x,t) \in \Gamma_m \times \left]0, t_q\right[$$

Least the above equation prescribes the initial temperature T_0:

$$T = T_0 \qquad \forall(x,t) \in \Omega \times 0$$

4.1.4b Mechanical model

A set of equations for the characterization of the mechanical problem is going to be presented in the following of this paragraph.

$$\rho \dot{v} = \nabla \sigma + \rho b \quad \forall(x,t) \in \Omega \times \left]0, t_{end}\right[$$

The equation above represents the mechanical equilibrium of linear momentum.

In this equation, the Cauchy stress tensor σ(u,T) = σ(ε_e(u); ε_p(u); ε_T (T)) is related to the primary displacement field u and temperature field T by constitutive parameters with contributions from elastic ε_e, plastic ε_p and thermal ε_T strains. The mechanical equilibrium of angular momentum is satisfied through the symmetry imposed to Cauchy stress tensor, the total time derivative $\dot{v}$ represents the material acceleration vector and b is the vector of volume forces acting on the physical domain Ω. Similarly, to the thermal problem, boundary conditions have to be defined, therefore the next two equations are written respectively to represent displacement ($\bar{u}$) and traction ($\bar{t}$) differentials:

$$u(x_u, t) = \bar{u} \qquad \forall(x,t) \in \Gamma_u \times \left]0, t_{end}\right[$$
$$\sigma \cdot n|_{(x,t)} = \bar{t} \qquad \forall(x,t) \in \Gamma_u \times \left]0, t_{end}\right[$$

The following equation, on the other hand, represents the requirement of displacement continuity and mechanical equilibrium at the relevant interfaces(therefore the index $_I$) , for instance the interface powder-melt or the interface melt-solid, characterized by a normal vector field n_I. The superscripts + and - denote quantities on the two different sides of the interface. However, most of the considered macroscopic models do typically not resolve these interfaces in the sense of a sharp 2D interface with discontinuous material parameters, but are rather based on a smooth, homogenized transition between the different phases, with the latter variant being easier to realize numerically.

$$(u_I^+ - u_I^-)|_{x_I} = 0 \;\text{ and }\; (\sigma^+ - \sigma^-) \cdot n_I|_{(x,t)} = 0 \qquad \forall (x,t) \in \Gamma_I \times]0, t_{end}[$$

Finally, the initial position and velocity field are respectively given by the below equations:

$$u(x,0) = u_0 \qquad \forall (x,t) \in \Omega \times 0$$
$$v(x,0) = v_0 \qquad \forall (x,t) \in \Omega \times 0$$

4.1.5 Micro scale models

The microscopic models are mainly built to evaluate the microstructural evolution in the solidified phase, since the melt pool physical phenomena (change of phase, heat transfer mechanisms linked to the melt-solid-gas interaction) are deeper considered on the meso scale level. In general, the microstructure evolution during solidification processes is governed by the spatial temperature gradients (G), cooling rates $\dot{T}$ and solidification front velocities v; as it represented in figure 42 below a qualitative solidification map can approximately be divided into areas of high and low cooling rates and into regimes of columnar and equiaxed structures.

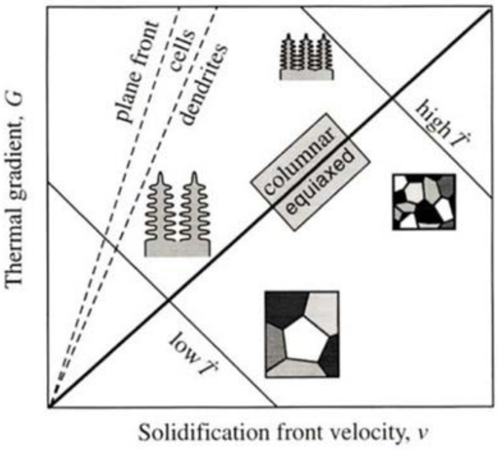

Figure 42

High solidification velocities lead generally to a fine grain microstructure, on the other hand high thermal gradients lead to dendrites formation, with a preferred solidification direction. Relating to AM process, highly localized energy supply yielding extremely high heating rates. The magnitude of heating and cooling rates typically lies in the range of 10^3-10^8 K/s[3].

The succession of extreme heating and cooling rates eventually also results in high spatial temperature gradients (103-108K/m) and solidification front velocities (1-30m/s). Such a large range of cooling rates and thermal gradients induces a large variety of microstructures of as-deposited materials differing by grain size, morphology, and orientation. All these characteristics lead also often to the formation of meta-stable phases and relatively small grain size, leading to a higher strength in comparison to cast materials. Along the build direction higher temperature gradients are to be found, which result in elongated, dendritic grain morphologies accompanied by a higher material strength in build direction. But as mentioned in the paragraph about physical phenomena, throughout the process the solidified phase is subjected to thermal cycles, which can be associate to heat treatments, with decaying intensity as the process adds more and more layers, this phenomenon enables phases transformation and grains coarsening.

The knowledge of the resulting microstructure characteristics might provide important details for the formulation of process-specific continuum constitutive laws, which are crucial for accurate residual stress predictions as intended by macroscopic simulation models. On the other hand, global temperature distributions provided by macroscopic continuum models represent essential input variables for studying the solidification process by means of microstructure models [3].

i. Phase field method

Since the compresence of different phases, on a liquid-solid level, but also on the presence of different solid phases, a phase field model based on the free energy functional can be used to model the micro scale level. The free-energy functional is generally represented as follows:

$$\Pi(\phi, c, T, \Psi) = \int_{\Omega} \widetilde{\Pi}(\phi, c, T, \Psi) d\Omega$$

with $$\widetilde{\Pi}(\phi, c, T, \Psi) = f(\phi, c, T) + \frac{c_{\Phi}^2}{2} \|\nabla\phi\|^2 + \widetilde{\Pi_o}(\phi, T, \|\nabla\Psi\|)$$

Where, ϕ represents the phase field variable or order parameter taking on the value ϕ= 1 in the solid phase, ϕ= 0 in the liquid phase, and a value among 0 and

1 thick interface region of smooth phase transition. Furthermore, c represents the volume-mass ratio of a certain chemical species prevalent in the problem of interest. For general systems consisting of n species, n-1 variables ci are required. As before, T is the absolute temperature. Also grain orientation is considered in the phase field model, with the variable Ψ, which represents a vector-valued parametrization of grain orientation, for instance given by rotation vectors, quaternions or Euler parameters. The first term of the equation representing $\widetilde{\Pi}()$ presents the temperature-dependent Gibbs free energy either associated with the liquid or solid phase at a certain location in the liquid or solid domain, or a proper interpolation of these values for locations on the phase boundary region. The second term represents energy contributions stemming from liquid-solid phase boundaries characterized by an existing gradient $\nabla\phi$ of the phase field. The choice of the parameter c_ϕ determines the resulting phase boundary thickness and requires a compromise between an accurate resolution of the small boundary layer thickness typically prevalent in physical systems (high value of c_ϕ) and a certain degree of artificially increased thickness for reasons of computational efficiency and robustness (low value of c_ϕ). Eventually, the last term $\widetilde{\Pi_o}(\,)$ yields energy contributions due to crystallographic orientation gradients ∇Ψ. This contribution fosters uniform growth within individual grains and penalizes the misorientations at grain boundaries, making larger grain sizes with reduced overall grain boundary surface favourable in configurations of Thermodynamic equilibrium. Variation of the free-energy functional yields the Euler-Lagrange equations of the variational problem, determining the equilibrium solution ϕ*, c*, Ψ* of the variables ϕ, c and Ψ:

$$\Pi(\phi^*, c^*, T, \Psi^*) = extremum \xrightarrow{yields} \frac{\partial\Pi}{\partial\phi}(\phi^*, c^*, T, \Psi^*) = 0, \qquad \frac{\partial\Pi}{\partial c}(\phi^*, c^*, T, \Psi^*) = 0,$$

$$\frac{\partial\Pi}{\partial\Psi}(\phi^*, c^*, T, \Psi^*) = 0$$

Starting with a non-equilibrium system, e.g. an undercooled melt, the equilibrium solution defined by the free-energy functional is found in practical simulations by transforming the latter formulation above into a transient problem and searching for the associated steady state solution. If time is entered in formulation above, Thereto, the so-called time-evolution phase-field approach applies additional rate terms proportional to $\dot{\phi}, \dot{c}$ and $\dot{\Psi}$ on the right-hand sides of equations right above. In L-PBF, the temperature field is required as input variable for the phase field model and might be provided from the macroscopic model resolution. For a deeper insight on phase field model please refer to [54]. The phase-field models include formulations for pure substances, for multicomponent systems, and for polycrystalline structure and solidification in eutectic, peritectic, and monotectic systems. Phase field models are probed in literature to have the ability to make predictions of growth velocity also at the nanoscopic length scale, which can be represented with a molecular dynamics model. Molecular dynamics models, while a phase field model describes the evolution of a system on the basis of motion equations of particles, grounds on the evolution of continuous local order parameter field. A study dealing with the comparisons of these two types of modelling can be found in Berghoff et al work[55], in which a study of Ni is carried out with the Embedded Atom Method(EAM).

i. Other modelling possibilities: Monte Carlo technique and Cellular Automata

The current computational models for simulating dendritic growth at the microscopic scale are based on different methods such as the above described phase field (diffusive or sharp interface), Level Set, Cellular Automaton (CA) and Monte Carlo (MC diffusive or kinetic) methods. Each of these methods has its advantages and disadvantages: some can simulate the finest details of solidification microstructures with high accuracy, while others can simulate dendritic growth in large-scale domains with high computational efficiency.

Zinovieva et al[56] present an extension of CA approach in the specific contest of L-PBF. Some general definitions concerning the CA method are briefly resumed here: Cellular automata are defined on a regular mesh and characterized by state variables and neighborhood structure. In the framework of the CA theory, two types of neighborhoods are usually considered, namely Moore and Von Neumann neighborhoods. With the change of time variable, the cells can change their states depending on the states of neighboring cells. Certain transition rules define the state change. When one describes the formation of grain structure during solidification, the state indicates what phase of the matter the cell belongs to. In the study of Zinovieva et al for instance is exploited a regular mesh of cubic cells of the equal size and use the Moore first-order neighborhood, this way every cell takes into account the states of 26 neighboring cells, furtherly each cell can be in one of the four possible states: it can be liquid, solid, growing (mushy), or powder cell, and every cell is characterized by a crystallographic orientation, temperature, and the index defining that the cell belongs to a particular grain.

In the introduction Zinovieva et al also give an overview of the already presented possibilities in literature. Phase field models are, in fact, not the only option, recent progress has also been reported for the 3D simulations of grain structure evolution during metal AM with the use of Monte Carlo (MC) technique. The benefits of MC simulations are sufficiently low computational costs and thus ability to predict 3D microstructures with hundreds of heat source passes. Although the kinetic MC model allows grain morphology to be described, yet it does not incorporate a crystallographic texture of additive manufactured material[56]. For the interested reader deeper insight of this approach is addressed in Rodgers et al work[57].

The level set method is conceptually similar to a phase-field model in that the solid–liquid interface is represented as the zero contour of a level set function, f(**r**,*t*), which has its own equation of motion. The movement of the interface is taken care of implicitly through an advection equation for f(**r**,*t*). Thus, topology changes and the extension of the method to higher dimensions can be handled easily. Unlike the phase-field model, there is no arbitrary interface width introduced in the level set method; the interface equations can be solved directly and, as a result, no asymptotes are required. Discontinuous material properties can also be dealt with in a simple manner. In literature other models are to be found but, completed the discussion about phase field approaches which effectiveness results experimentally demonstrated, further discussion of this topic is beyond the scope of this thesis.

4.1.6 Meso scale models

The mesoscopic models focus on the length scale of individual powder particles, explicitly resolving these scales in order to study melt pool dynamics, melt pool heat transport as well as the wetting of melt on substrate and powder particles. These models are oriented to the prediction of part properties such as layer-to-layer adhesion, surface quality and defects on the mesoscale (pores, inclusions etc.). In these models, the initial powder grain distribution is either determined on the basis of contact mechanics simulations, for instance by employing the discrete element method (DEM)[58], or by means of more generic packing algorithms such as random placement algorithms and rain models[59]. Subsequently, thermo-mechanical simulations are performed considering the heat transfer within the powder bed, the melting process as well as the heat transfer and the hydrodynamics in the melt pool. Often, the not-melted powder grains are assumed to be spatially fixed and the powder phase is only solved for the pure thermal problem based on a proper laser beam model. In the following two sections the powder, heat source and melt pool models are briefly discussed, addressing references for a deeper discussion.

4.1.6a Heat source models

A holistic outlook on the phenomena due to heat transfer in the powder bed needs to integrate an appropriate heat model for the laser beam, because of its influence on the geometries of melt pools but also probable impact on the mechanical performance of final products. The simplest laser beam has been assumed to be a point source which is a very strong simplifying assumption reality. It has been found that the laser beam can be characterized using three parameters namely diameter, power, and intensity distribution. In the majority of the models to be found in literature the heat source models tend to be represented with a Gaussian bidimensional approach. The beam irradiance at any point (x, y) at time t for the fundamental transverse electromagnetic mode can be expressed as:

$$I(x,y,t) = \frac{2\beta P}{\pi r_l^2} exp\left(-2\frac{(x-vt)^2+y^2}{r_l^2}\right)$$

where P is the power of the stationary laser source, r_l is the radius of the laser beam, (x, y) are the coordinates of the heat source, v is the scanning velocity and β is the laser-beam absorptivity. Since the laser beam can penetrate into the powder-bed, in other words, laser energy is deposited not only on the top surface of a powder-bed but inside the powder-bed, it may be not accurate employ the two-dimensional heat source to simulate L-PBF. Thus, volumetric heat sources should be considered in order to describe the laser penetration into powders. As reported by Zhang et al [60], eight are the major volumetric models which can be considered for L-PBF simulation (figure 43):

a. Optical Penetration Depth (OPD) method,
b. three-dimensional Gaussian distribution,
c. ellipsoidal distribution,
d. conical heat source,
e. radiation transfer method,
f. absorptivity function method,
g. linearly decaying heat source,
h. exponentially decaying heat source.

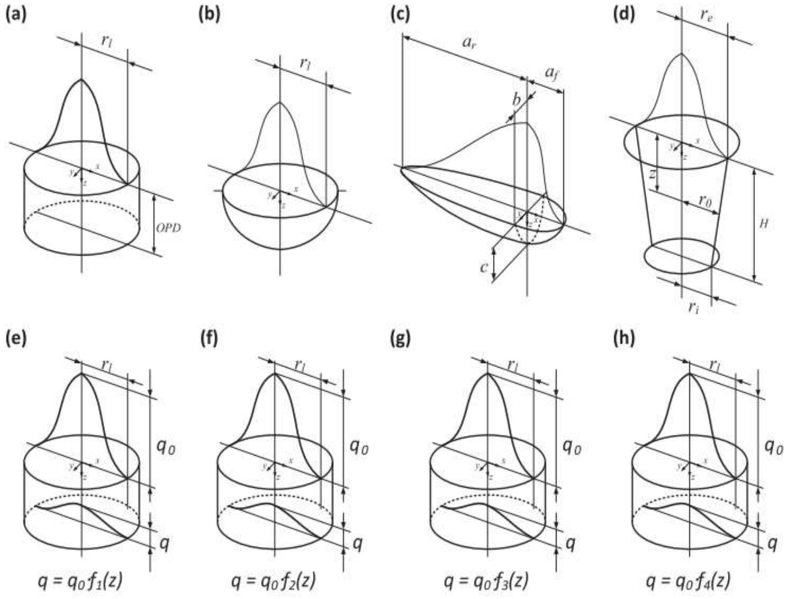

Figure 43

In the figure 43 equations q_0 represents the total energy input.

The aforementioned eight models can be associated in two main different families: the Genetically Modified group (GM group) including the models a, b, c and d; and the Absorptivity Profile group (AP group) including the models e, f, g and h.

The GM group is an evolution of the Gaussian distribution, changing the shape of the heat source from two-dimensional surfaces to three-dimensional geometries, which can be cylindrical, semi-spherical, semi-ellipsoidal, and conical shapes.

On the other hand, AP group models, the powder-bed can be viewed as an optical medium, whose optical absorptivity would be described by absorptivity profiles.

The heat source models in this group are not constrained in specific geometries as those in GMG, as it appears clear in figure 43. Their general form is that the two-dimensional Gaussian distribution is on the top surface while the laser beam is absorbed along the depth of the powder layer. The general formulation for the AP group is presented right below:

$I(x, y, t) = \frac{2P}{\pi r_l^2} exp\left(-2\frac{x^2+y^2}{r_l^2}\right) f(x)$ where $f(z) = \frac{d\beta(z)}{dz}$ is the absorptivity profile function and $\beta(z)$ is the absorptivity coefficient function.

The formulations of each model are below resumed in table 2, for a deeper insight please refer to Zhang et al work[60].

Table 2

heat source model	description	heat source intensity	parameters
Cylindrical Shape	the shape of the laser beam can be assumed as circular so that it is relatively straightforward to employ a 3D cylindrical heat source. Employing a uniform energy distribution for the heat source in the cylinder volume influenced by the Optical Penetration Depth (OPD). The OPD is defined as the depth where the laser intensity drops to ≈36.8% of the laser beam intensity absorbed on the top surface of the powder bed	$I(x,y,z) = \frac{\beta P}{V}$	where $V = S\alpha_{OPD}OPD$ β=absorptivity V=exposed volume S=area of laser spot α_{OPD}=correction coefficient of the OPD chosen
Semi-spherical shape	In the case that a three-dimensional heat source is considered, the evolution of two-dimensional Gaussian distribution may be a semi-spherical Gaussian distribution of energy density	$I(x,y,z) = q_0 exp\left[-2\frac{x^2+y^2+z^2}{r_l^2}\right]$	$q_0 = \frac{2^{5/2}\beta P}{\pi^{3/2}\eta^3}$ which is a coefficient based on energ balance
Semi-ellipsoidal shape	Since the melt pool in LPBF is often far from a spherical shape. In order to more accurately simulate the melt pool dimensions, the semi-ellipsoidal power distribution proposed (Goldak[61]). This distribution is a Gaussian distribution in an ellipsoid with semi-axes a, b, and c and center at (0, 0, 0), the semiaxe a is considered to differ among front and rear parts, to be have a better representation of reality.	$I(x,y,z) =$ $f_f q_0 exp\left[-2\frac{x^2}{a_f^2}+\frac{y^2}{b^2}+\frac{z^2}{c^2}\right]$ $I(x,y,z) =$ $f_r q_0 exp\left[-2\frac{x^2}{a_r^2}+\frac{y^2}{b^2}+\frac{z^2}{c^2}\right]$	$q_0 = \frac{2^{5/2}\beta P}{\pi^{3/2}abc}$ and $f_f+f_r=2$
Conical shape	In the welding area it has been employed conical shape heat source to simulate the welding process. Based on the inherent similarity between welding and LPBF, this model can be applied for simulating the L-PBF process.	$I(x,y,z) = q_0 exp\left[-2\frac{x^2+y^2}{r_0^2}\right]$	$r_0(z) = r_e + \frac{z}{H}(r_e - r_i)$ r_e=top radius r_i= bottom radius $q_0 = \frac{6\beta P}{\pi H(r_e^2 + r_e r_i + r_i^2)}$
Radiation Transfer Equation	This analytical approach will be discussed properly in the thermal-optical models of the powder bed, however the intensity distribution, considering z_{bed} the bed thickness, and an extinction coefficient of η, is here reported	$I(x,y,z) = \frac{2P}{\pi r_l^2} exp\left[-2\frac{x^2+y^2}{r_l^2}\right] f_1(z)$	$f_1(z) = \left(-\eta\frac{dq}{d\xi}\right)$ where ξ=ηz =dimensionless local depth coordinat q=dimensionless net radiative energy flux density
Ray tracing model	The absorptivity profile function can also be acquired by numerical methods, through simulation the laser beam can be divided in n singular rays, of each path, absorption, reflection can be studied, some more information of this model are to be found in the thermal-optical models paragraph.	$I(x,y,t) = \frac{2P}{\pi r_l^2} exp\left(-2\frac{x^2+y^2}{r_l^2}\right) f_2(x)$	$f_2(z) = \frac{d\beta(z)}{dz}$
Linearly Decaying Equation	In this model, the laser was modelled as a moving source heat generation with a Gaussian distributed, radially decaying, intensity in the build plane and linearly decaying intensity along the depth of the part. An example of this model implementation is to be found in [62]	$I(x,y,z) = \frac{2P}{\pi\eta^2}\left[-2\frac{x^2+y^2}{\eta^2}\right] f_3(z)$	$f_3(z) = \frac{2\beta}{\delta}\left(1-\frac{z}{\delta}\right)$
Exponentially Decaying equation	Yin et al[63] presented a model in which intensity decays exponentially deepening the powder bed.	$I(x,y,z) = \frac{2P}{\pi\eta^2}\left[-2\frac{x^2+y^2}{\eta^2}\right] f_4(z)$	$f_4(z) = \frac{2\beta}{\delta}\left(1-\frac{z}{\delta}\right)$

4.1.6b Powder Bed

Powder on a mesoscopic and microscopic level cannot be seen as a continuum, and it should not be, this mainly because powder metals have many differences if compared to the as-built corresponding same materials. In fact, powders for AM physical behavior can be described through Granular Physics, since Granular media are neither completely solid-like nor completely liquid-like in their behaviour, they pack like solids, but flow like liquids[64]. Powders for AM can be in this optic associated with non-Newtonian fluids. Most of the literature presents models for power absorption among the powder grains. The optical and thermal properties of the powder bed, in combination with the laser characteristics, crucially determine the heat distribution in the powder bed and the subsequent melt pool dynamics[3], in fact. But, it is necessary to have detailed analytical and experimental information on many other characteristics, since the absorptivity depends not only on the powder material and the laser beam profile, but also on the powder layer thickness and the distributions in size and space of the powder particles. In practice, these distributions are often not well characterized. Furthermore, the size distribution can vary with location within a powder layer, as size segregation can occur during spreading of the powder. As currently the powder recoating phase in order to prepare the material for a new layers is carried out with different techniques in different L-PBF machines present on the market, powder delivery takes place on the build plates with raking, rolling/raking, or gravitational feeding which are the most common delivery approaches. How these different approaches affect the uniformity of the powder bed is currently not examined very well. In general, during flow of granular materials, the size distributions might not remain uniform and size-demixing might occur [65]. In addition, freely poured powder, not compressed, has a high porosity in a range going mainly between 40 and 60%, this percentage is obtained through the ratio between the volume occupied by air on the total volume occupied by the powder, as it is reported in different studies, as Ali et al publication [66]. Therefore, in the author's opinion, an interesting plus to have a deeper understanding of the process, since the strong interrelation linked to heat transfer models the heat source models presented by Zhang et al in their study[60].

There are, however, many other parameters to take in account which influence metal powder energy absorption, as oxidation, hydroxidation and humidity content, resulting in high variability of the manufactured parts even among the use of the same alloy. Further insights on how powder handling and other process feature can affect L-PBF produced parts and process can be found in Herbert study[65].

i. Recoating/deposition models

The powder deposition or recoating process phase can be considered as a bi-phase problem and part of the mesoscopic modelling of the L-PBF, where the two phases involved are air and metal. There are mainly two modelling alternatives considering the powder bed: one considers the interaction between powder particles and with ambient gas during powder deposition or transport though a fully-coupled Finite Volume Method -Discrete Element Method (FVM-DEM) approach, in which the movement of the particles is simulated using the DEM while the surrounding gas is simulated using the FVM. The linear and angular momentum for powder particles can be represented as:

$$m_p \frac{dV_p}{dt} = -\breve{V}_p \nabla p + F_{drag} + m_p g + \sum F_{p-p} + \sum F_{p-w}$$

$$I_p \frac{d\omega}{dt} = \sum M_t + M_r$$

Where m_p, V_p, $\breve{V}_p$, and I_p are respectively the mass, velocity, volume and rational inertia of particle, t is time, p is ambient pressure and g the gravitational acceleration. F_{drag} is the drag force exerted on the particles by air, which can be calculated with the Hill Koch model (about which a discussion, for the interested reader, can be found in the work of Benyaha et al[67]). F_{p-p} is the interaction force among particles, while F_{p-w} is the interaction force among particles and wall. The angular velocity is ω, M_t is the momentum generated by tangential forces applied by other particles and M_r is the rolling frictional torque.

The continuity and momentum equations for the air result:

$$\frac{\partial \alpha_2}{\partial t} + \nabla(\alpha_2 \mathcal{V}) = 0$$

$$\frac{\partial}{\partial t}\left(\alpha_2 \rho_2 \mathcal{V}\right) + \nabla\left(\alpha_2 \rho_2 \mathcal{V} \otimes \mathcal{V}\right) = -\alpha_2 \nabla p - \nabla\left(\alpha_2 \mu_2 (\nabla \mathcal{V})\right) - S_p + \alpha_2 \rho_2 g$$

Where *V,* α_2, ρ_2 and μ_2 are respectively the velocity, volume fraction, density and dynamic viscosity of the second phase, air. The following equation represents, S_p, is the source term governing the momentum exchanges among particles and air:

$$S_p = \frac{1}{V_{cellI}} \sum_{\forall j \in cellI} \frac{V_p \beta \left(V - V_p\right)}{1 - \alpha_2} D(r_I - r)$$

Where V_{cellI} is the volume of the air cell, β is the empirical coefficient related to the particle void ratio 1-α_2 of the FVM Reynolds number, r is the position vector of the particles and r_I is the vector for the air cell I, D is a distribution function, which distributes the reaction forces on the fluid phase at the velocity nodes in staggered Eulerian grids. Through the drag force and the source term the interactions between particles and air are fully coupled, this model demands for the resolution of the Navier-Stokes equations.

The second modelling possibility is an approach based on a packing algorithm, there are different algorithms that can be exploited, the main types were presented in the study by Jia et al [59], some examples are:

-Ballistic algorithms, Particles follow well-defined or definable trajectories to find a resting place in the packing.

-Random placement algorithms, Particles from a given size distribution is placed one by one in randomly selected positions in the packing space. If a newly introduced particle does not overlap with others, it is allowed to stay; otherwise, another position is tried. If, after a predefined number of trials, the particle still has not found a place to stay, it is discarded, and another is selected and tried in the same manner.

-Growth algorithms, A particle packing can also be generated by 'growing' points, placed randomly or with some constraints with regard to inter-point distances, into the required shapes. One example is to let the points grow into spheres until they touch each other. These algorithms are characterized by different implementation and computational pros and cons, please refer to [59] for a complete insight.

ii. Thermo-optical models

A thermal and optical approach coupled with a powder distribution model is necessary to estimate the energy absorbed by the powder bed and melt pool dynamics. The thermal properties of the powder bed as well as the radiation-dominated energy transfer from the laser beam source into the powder bed and the conduction-dominated heat transfer within the powder bed. The considered approaches are typically employed as powder bed submodels within the three main categories of macroscopic, mesoscopic and microscopic models[3]. Radiation and conductivity will be hence, discussed in the current and subsequent paragraph.

The multiple reflection/absorption processes of the light in the powder bed is additionally influenced by powder characteristics formerly presented but also by the laser beam spot size. Also, the polarization of the laser beam relative to the powder particle surfaces, the weak thermal conduction in the powder bed linked to the prevalent porosity and melting time scales are typically smaller than heat conduction time scales for individual grains, non-uniform energy absorptions across the powder bed but also across individual powder particles will in general have considerable influence on the melt pool shape and the properties of the solidified track. In figure 44 a schematized representation of the thermo-optical phenomena is presented.

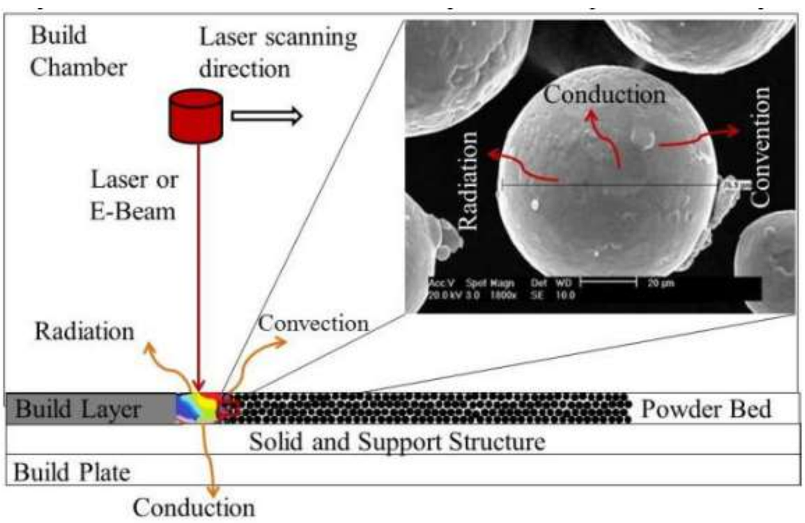

Figure 44

Two main families of approaches commonly used for modelling radiative transfer in dispersed media are discussed in this paragraph. One of these approaches is based on a continuous formulation of the radiative transfer equation (RTE). The medium is treated as a pseudo-continuous medium and the RTE is written in its classical continuous formulation. The other approach is based on discrete formulations of the RTE. This approach generally leads to ray tracing. Both approaches are based on assumptions of geometrical optics which considers light rays that: propagate in rectilinear paths as they travel in a homogeneous medium, bend, and can split in two at the interface between two medias with different characteristic, follow curved paths in a medium in which the refractive index changes and may be absorbed or reflected. The volumetric spectral radiative properties (required for integration of the RTE) may be determined in two principal ways:

- from theoretical models that describe the interaction of radiant energy with particulate media; Maxwell's equations solutions and geometric optics combined with diffraction theory are some theoretical ways for the prediction of the radiative properties of dispersed media;
- from identification methods, by using spectral and directional measurements of radiation transmitted through, reflected by, or emitted from samples of material, combined with RTE solutions;

The complete discussion of radiation in porous media, to which AM metal powders can be associated, is presented by Baillis and Sacadura[68]. However, for the scope of this thesis, the focus of this paragraph will remain in the discussion of the two RTE model families.

In the continuous approach, the governing equations are derived by using the principle of energy conservation. This approach is acceptable if the size of the system is much larger than the wavelength of the radiation, referring to L-PBF process the particle size is typically much greater than the wavelength, thereby justifying the applicability of the geometrical optics theory. The general radiation transfer equation (RTE) known for homogeneous media and underlying the homogenized, continuum models (Homogeneity is essential for the medium to be treated as a continuum, the powder needs here to be considered homogeneous if particle diameters are small compared with the medium thickness) can be formulated in a vectorial form as below:

$$\Omega\nabla I(x,\Omega) = -(\sigma+\kappa)I(x,\Omega) + \kappa I_{eb} + \frac{\sigma}{4\pi}\int_0^{4\pi} I(x,\Omega')S_c(\Omega'\rightarrow\Omega)d\Omega'$$

The RTE describes the rate of the direction- and position-dependent radiation energy flux density $I(x,\Omega)$ based on an energy balance considering radiation absorption, radiation and scattering. Ω represents a directional unit vector, dΩ is an infinitesimal solid-angle, and the product ΩI(x, Ω)d Ω represents the vector of energy flux density transferred by photons in direction of the unit vector Ω within a solid angle increment d at position x. The constants σ and κ are the scattering and absorption coefficients, which are, phase function of the medium may be calculated either by assuming independent scattering or by modelling the dependent scattering effects. Independent radiative properties can be scaled to represent the dependent properties of the particulate media. In fact, scattering and absorption coefficients are often replaced by the alternative constants: extinction coefficient (β=σ+κ) and albedo(ω=σ/β). The mapping S_c is the (normalized) scattering phase function stating the probability that radiation in Ω‘direction is scattered to the Ω direction and I_{eb} is Planck’s blackbody function representing radiation emission at a certain position and it is given by:

$$I_{eb} = k_{SB}\left(T^4 - T_{ref}^4\right)$$

Where k_{sb} is the Stefan-Boltzmann constant (it is usually named σ, but since in the previous equation σ is associated with the scattering coefficient it has been named differently), T is the powder temperature and T_{ref} is the environment gas temperature.

The model has been proved also on heterogeneous systems, where the continuous quantities and parameters introduced so far have to be replaced by their effective counterparts, determined via spatial averaging over a reference volume that has to be much greater than the length scales of prevalent heterogeneities (for instance individual particles in powder beds). When considering radiation heat transfer in powder beds, the extinction coefficient β is typically determined by the size and shape of particles and by their arrangement but, is independent of optical properties of the material of particles like reflectance. On the contrary, the scattering characteristics such as the albedo ω and phase function P(Ω'-> Ω) commonly depend on reflective properties of the material of particles.

The net radiation heat flux density q_r, results from the energy flux density per unit angle increment I(x, Ω) via integration over all directions of incident radiation. Expressed by means of solid-angle increments dΩ this is equivalent to an integration over the surface 4π of a unit sphere, assuming as coordinate system with the positive z-axis points into powder layer thickness direction with z = 0 representing the upper surface of the powder bed and z = L the boundary between powder bed (with thickness L) and the underlying solidified phase (substrate), and considering negligible the heat flux contributes along axis x and y, it is also possible the formulation of the power density per unite volume u_s as follows:

$$q_r = \int_0^{4\pi} I\Omega d\Omega \approx q_{rz} e_z \rightarrow u_s = \frac{\partial q_{rz}}{\partial z}$$

Gusarov et al. [49] propose a statistical model based on the powder porosity and specific powder surface areas in order to determine the model parameters required in the RTE equation above.

For a powder presenting mixed different powders it has been proposed the Vector Radiation Transfer Equation (VRTE). In this model, the partial values are obtained by averaging over each individual phase, phases are described by fraction of volume and surface boundaries. It consists of two transport equations for the partial homogenized radiation intensities. RTE and VRTE equations result similar but contain additional terms that take into account the exchange of radiation between the individual phases are to be found in the VRTE formulation. Thus, resulting in a more complex model, demanding for more computational time. It has been verified that the VRTE model reduces to the conventional RTE model in case one of the two phases is opaque or one phase prevails in volume[3].

As aforementioned, the RTE model, leads to the evolution of the ray tracing model (RT model).

RT model it's used in case the media cannot be considered continuous, it has been in fact proved, that RTE continuum model is questionable for very thin, low-porosity metal powder layers with a layer thickness in the range of a few powder particles and/or a laser spot size comparable to the size of the powder particles. These conditions lead to a strongly non-uniform energy absorption in comparison with the spatial position of the laser beam. Ray tracing modelling is one possible approach to resolve such heterogeneities. However, in absence of a strict accuracy demand from the model, RTE model results reliable and requests a lower computational effort. In ray tracing simulations, the total energy emitted by the laser beam in a certain time interval is represented by a discrete ensemble of rays with defined spatial position, orientation and energy. The position and energy associated with the individual rays is typically chosen such that the overall energy emission but also the spatial energy distribution resulting from the entire ensemble equals the corresponding characteristics of the laser beam (for instance a Gaussian energy distribution in a heat source model, however this aspect has been discussed in the former paragraph). For facilitating the partition of the total input energy among them, the emitted rays are assumed to be regularly located and equally spaced. The energy of each emitted ray is calculated from the energy distribution, which depends on the total laser power, the power density distribution and the scan speed. It varies only in the direction, perpendicular to the laser beam scanning direction. After defining the individual rays, the path of each ray is traced until striking an obstacle (powder particle). Based on the optical properties of the obstacle surface, part of the ray energy is absorbed whereas the remaining part of the ray energy is represented by a reflected ray with defined energy and orientation, which will further be traced trough the powder bed, several reflections are considered for each ray until the remaining energy drops below some predefined threshold. The individual ray energy contributions absorbed by each particle are accumulated during the simulation. The requirements mentioned above, since RT model is an applied Optics model too, have to be fulfilled, especially the particle radius R has to be considerably larger than the laser wavelength.

Wang et al[69] exploited the RT model to evaluate energy absorption in a bi-powder bed, taking in consideration only the radiation heat transfer mechanism. Boley et al[70] embedded also the angle and the polarization of the rays to RT model. These are, in the author’s opinion two of the mainly interesting implementation of the model, however many other similar and different examples are to be found in literature.

4.1.6c Melt pool models

Modelling the melt pool has to deal not only with heat transfer on a static level but also with fluid flow, induced by the laser beam velocity and the convection caused by the heat flux. This is results extremely useful for a prediction of the possible defects formation. In fact how reported by Khairalla et al[50] a three-dimensional high-fidelity powder-scale model reveals how the strong dynamical melt flow generates pore defects, material spattering (sparking, which happens when melt drops are ejected from the melt pool), and denudation zones(which is the zone in the nearby of the melt pool, where the powder is either attracted into the melt or can be made "jump" far from the laser track). An anticipation was given in the paragraph summarizing the physical phenomena taking place in the melt pool and track, to recall, the melt track is divided into three sections: a topological depression, a transition and a tail region, each being the location of specific physical effects and possible defects of the above mentioned. Different pore formation mechanisms are observed at the edge of a scan track, at the melt pool bottom (during collapse of the pool depression), and at the end of the melt track (during laser power ramp down).

Obviously, the melt pool shape and dynamics are not the only features to be blamed for all the defects that L-PBF process can produce along with the part building. But a not well calibrated set of process parameters can easily lead to melt pool characteristics suitable for the formation of the majority of the part low quality features. Therefore, it appears necessary, to have a model to investigate melt pool shape and dynamics, in order to prevent possible defects, and avoid the trial and error procedure, which is actually the aim behind the build of simulation tools in the whole manufacturing industry. Especially with the raising strictness on part quality demand. In the figure 45 below the main phenomena, formerly mentioned, linked to defect formation in the melt pool, such as surface tension, Marangoni effect and recoil pressure, are represented:

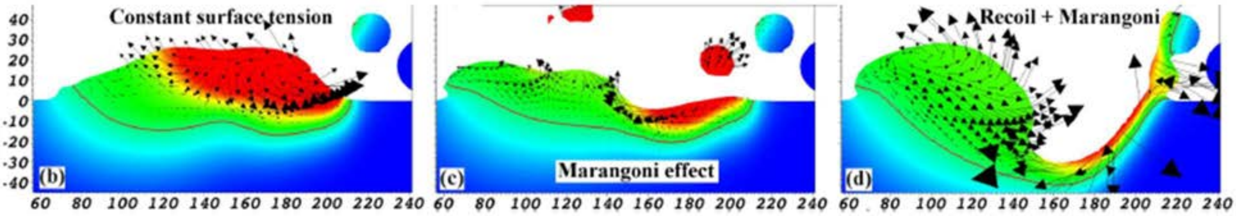

Figure 45

In the literature many different approaches have been chosen for representing melt pool models. In fact, representing the melt pool is a heat transfer and fluid flow coupled problem. Debroy et al.[5] identified several modelling methods: Analytical approach(Rosenthal), Finite Element Method (FEM), Finite Difference Method (FDM), Level Set Method (LSM), Volume of Fluid (VOF) or Finite Volume Method (FVM)or Computational Fluid Dynamics (CFD) using Difference Element Method (DEM), Lattice Boltzman method (LBM) and Arbitrary Lagrangian–Eulerian (ALE). Another alternative method to simulate melt pool evolution is represented by the smoothed particle method (SPH).

VOF/FVM/FDM combinations, FEM and CFD approaches result the most common, but their resolution require a big computational effort, temporal discretization of the fluid dynamics problem is predominantly based on explicit time integration schemes, spatial discretization and the small time step sizes admissible for explicit time stepping schemes lead typically to high computational costs.

Khairallah et al. [50] integrated the RT model to evaluate also the melt pool dynamics. Cattenone et al discussed LB method addressing some specification in case of AM process[71].

While on a macroscopic level the up-cited equations, describing the thermal problem, are to be coupled with a set of equation describing the solid mechanics problem underlying the prosess, for a mesoscopic model, to the aforementioned equations it's necessary to combine the latent heat of fusion and a set of balance equations, which are the following:

$$\nabla v = 0 \qquad \forall (x,t) \in \Omega \times]0, t_{end}[$$

The first equation just presented above is a formulation of the required conservation of energy. The above equation should recall the discussion of the governing equations of HPDC process, since it's a formulation of the N-S momentum equation:

$$\frac{\partial(\rho v)}{\partial t} + \nabla(\rho v \otimes v) = \nabla p + \nabla(2\mu\tilde{\epsilon}) + \rho b \qquad \forall (x,t) \in \Omega \times]0, t_{end}[$$

The term b takes in account the effect of gravity and it may contain additional contributes, for instance related to phase change change phenomenon or temperature induced buoyancy forces. Following the bounadaries conditions are presented, respectively for the velocity field, initial velocity and and traction tensor tensor values at a certain boundary:

$$v = \bar{v} \qquad \forall (x,t) \in \Gamma_v \times]0, t_{end}[$$

$$v = v_0 \qquad \forall (x,t) \in \Omega \times 0$$

$$\sigma n = \bar{t} \qquad \forall (x,t) \in \Gamma_t \times]0, t_{end}[$$

The flow is typically considered of a Newtonian fluid characterized by the following stress tensor $\sigma(v,p) = -pI + 2\mu\tilde{\epsilon}(v)$ where $\tilde{\epsilon}(v)$ stands for the rate of deformation, p is the pressure and μ is the kinematic viscosity.

The equation above represents a formulation of the energy equation generally employed for AM process models, where Ω it's the domain, $(0,t_{end})$ is the time step considered, ρ the density, c_p the specific heat at constant pressure, T the temperature, v stands for the velocity field, k is the tensor representing thermal conductivity and u_s it's the heat source term. On the left side of the equation the two terms represent the materiale time derivative of the thermal energy density constituted of the local convective time derivative. A more accurate thermodynamical model would consider the material *compressible*, demanding for additional terms, but most of the models are built on the approximation of considering the material *incompressible*, and in this case the equation above is accountable as complete. The conductivity is usually considered isotropic and can be derivated from the effective conductivity models above mentioned. The heat source term is often based on the RTE model, but can be derivated also from the RT model, and the other approaches presented.

$$T = \bar{T} \qquad\qquad \forall(x,t) \in \Gamma_T \times]0, t_{end}[$$

$$q = \bar{q} \qquad\qquad \forall(x,t) \in \Gamma_q \times]0, t_{end}[$$

The right above two equations are boundaries formulations of the Dirichlet boundary condition respectively of the temperature and heat flux differentials each of the along its own boundary of the domain. Relatively to the natural boundary condition of heat flux $\bar{q}$, which usually takes in account radiation emission $\bar{q}_r$ and thermal convection$\bar{q}_{conv}$ along powder surface normal (n_p), with T_{ref} as the temperature of the gas atmosphere, c the convection coefficient and ε the emissivity:

$$\bar{q}_{conv} = c\left(T - T_{ref}\right)n_p \qquad \bar{q}_r = \varepsilon k_{SB}\left(T^4 - T_{ref}^4\right)n_p$$

The Stefan-Neumann equation, presented right below, describes the phase change at the interface powder-melt, where the indices $_s$ and $_l$ refers to temperature gradients and termahl conductivites gradients respectively in the solid and liquid phase; T_m is the melting temperature, H_m is the latent heat of melting and n_{sl} is the normal vector of the solid-liquid interface.

$$T = T_m \ \ and \ \ n_{sl}\left(k_s\frac{\partial T_s}{\partial x} - k_l\frac{\partial T_l}{\partial x}\right) = H_m \rho n_{sl}\dot{x} \qquad\qquad \forall(x,t) \in \Gamma_m \times \left]0, t_q\right[$$

Least the above equation prescribes the initial temperature T_0:

$$T = T_0 \qquad\qquad \forall(x,t) \in \Omega \times 0$$

While on a macroscopic level the up-cited equations, describing the thermal problem, are to be coupled with a set of equation describing the solid mechanics problem underlying the prosess, for a mesoscopic model, to the aforementioned equations it's necessary to combine the latent heat of fusion and a set of balance equations, which are the following:

$$\nabla v = 0 \qquad \forall (x,t) \in \Omega \times]0, t_{end}[$$

The first equation just presented above is a formulation of the required conservation of energy. The above equation should recall the discussion of the governing equations of HPDC process, since it's a formulation of the N-S momentum equation:

$$\frac{\partial(\rho v)}{\partial t} + \nabla(\rho v \otimes v) = \nabla p + \nabla(2\mu\tilde{\epsilon}) + \rho b \qquad \forall (x,t) \in \Omega \times]0, t_{end}[$$

The term b takes in account the effect of gravity and it may contain additional contributes, for instance related to phase change change phenomenon or temperature induced buoyancy forces.

Following the bounadaries conditions are presented, respectively for the velocity field, initial velocity and and traction tensor tensor values at a certain boundary:

$$v = \bar{v} \qquad \forall (x,t) \in \Gamma_v \times]0, t_{end}[$$

$$v = v_0 \qquad \forall (x,t) \in \Omega \times 0$$

$$\sigma n = \bar{t} \qquad \forall (x,t) \in \Gamma_t \times]0, t_{end}[$$

The flow is typically considered of a Newtonian fluid characterized by the following stress tensor $\sigma(v,p) = -pI + 2\mu\tilde{\epsilon}(v)$ where $\tilde{\epsilon}(v)$ stands for the rate of deformation, p is the pressure and μ is the kinematic viscosity.

$$\left(v_l^{]} - v_l^{-}\right) = 0 \;\; and \quad (\sigma^{+} - \sigma^{-})n_l = \left[\gamma\kappa_l n_l + \frac{d\gamma}{dT}(I - n \otimes n)\nabla T\right] \quad \forall (x,t) \in \Gamma_l \times]0, t_{end}[$$

This last equation aims to take in accountthe surface tension effects on the free surface Γ_l between melt pool and ambient gas. While the velocity field is assumed to be continuous while the surface stress shows a discontinuity at the interface. The jump in interface-normal direction (first term in square brackets) is already present for the case of spatially constant surface tension leading to fluid surfaces with curvature κ_I and capillary effects already for hydrostatic problems. The jump in the interface-tangential direction (second term in square brackets) only occurs for spatially varying surface tension values, here solely considered due to spatial temperature gradients, and will for Newtonian fluids (with shear stresses being proportional to velocity gradients) always induce flow[3]. The Marangoni effect resulting from such surface tension variations crucially influences the convective heat transfer within the melt pool. All in all, surface tension significantly determines the melt pool shape and the resulting solidified surface. Since the mesoscopic scale of the problem, and the experimental results of the most recent studies, in the paragraph below a formulation of LB model will be discussed.

5.1.6d Effective conductivity

The effective conductivity is a metric to model conduction, convection, and radiation between particles in the powder bed[72]. Given as follows:

$$k_{eff} = k_r + k_{conv} + k_{cond}$$

If the powder bed is included in the computational domain, the thermophysical properties of the powder are established in terms of the properties of the solid material and the porosity of the granular bed, ξ. Therefore, the powder density and specific heat are represented respectively as follows:

$$\rho_p = \rho_{solid}(1-\xi)$$

$$c_p = c_{solid}$$

but the value of the thermal conductivity, k_p, of metal powders is frequently estimated with empirical expressions, that also depend on the conductivity of the surrounding air or gas, k_{gas}. Many formulations derived experimentally are present in literature for example Romano et al[72] reported:

where $k_r = \frac{16}{3} I\sigma T^3$ and $k_{cond} = \Lambda k_{bulk} x$

The convective term, k_{conv} is assumed to be negligible, since the use of the inert gas flow above the powder bed. The radiation term derived from the scattering model for isotropic material, l represents the mean free path of photons emitted from the powder particles, σ is the Stefan-Boltzmann constant, and T is the temperature measured in Kelvin. In the formulation for the conduction term, Λ is the normalized contact conductivity, which is a function of packing structure, k_{bulk} is the conductivity of the as-built material, and x is the ratio of particle contact radius to particle radius.

Another equation that enables the derivation of the effective conductivity, again neglecting the convection term, is derived by Sih et al[73]:

$$\frac{k}{k_g} = \left(1 - \sqrt{1-\varphi}\right) + \sqrt{1-\varphi}\left\{(1-\phi)\left[\frac{2}{1-\frac{Bk_g}{k_s}}\left(\frac{B}{\left(1-\frac{Bk_g}{k_s}\right)^2}\left(1-\frac{k_g}{k_s}\right) ln\frac{k_s}{Bk_g} - \frac{B+1}{2} - \frac{B-1}{1-\frac{Bk_g}{k_s}}\right) + \frac{k_R}{k_g}\right] + \phi\frac{k_{contact}}{k_g}\right\}$$

In the above equation, k corresponds to the effective thermal conductivity of the powder bed, k_g the thermal conductivity of the continuous gas phase, k_s thermal conductivity of the solid phase, j the porosity of the powder bed k_R thermal conductivity part of the powder bed due to radiation, denoted by Damköhler's equation: $k_R = 4F\sigma T^3 x_R$ where σ is the Stefan-Boltzmann constant, F a view factor according to Damköhler equal to 1/3, T the mean absolute temperature of the powder bed and x_R is the effective length of radiation between particles and can be approximated by the particles diameter; furtherly in the formulation of the effective conductivity ϕ represents the flattened surface fraction of particle in contact with another particle, ranging from 0 in absence of contact, to 1 for complete contact (it is the flattened surface area divided by the cross-sectional area of the particle), B represents a deformation parameter of the particle, estimated for the powder bed being equal to $B \approx 1.25\left(\frac{1-\varphi}{\varphi}\right)^{\frac{10}{9}}$ calculated from the porosity(voids among the particles), $k_{contact}$ is equal to 18ϕk_s, for $\phi<3\text{x}10^{-4}$; $k_{contact}$ is near to k_s in value only when ϕ is greater than 0.01.

Alternatively, if the powder bed is not included in the domain, the heat loss by conduction through the powder q_p can be expressed using an equivalent boundary condition, as follows[74]:

$q_p(T) = h_p(T - T_p)$ on $\partial\Omega_p$

T_p represents the temperature of the powder fairly enough distant from the HAZ, h_p denotes the heat transfer coefficient (HTC) by conduction between powder and component. T_p has to be estimated in time, during the complete process, a constant value can work it out, if the interference among different parts being printed on the platform is negligible, otherwise the temperature dependant formulation of this HTC comes as follows:

$$h_p(T) = \frac{k_p(T)}{s_p}$$

Where s_p accounts for the average size of the region around the printed part thermally influenced by the AM process. Introducing an equivalent boundary condition for heat transfer through the powder-bed simplifies the physics of the problem but, has obvious consequences in the error of the predictions[74]. Therefore, is not the preferable model in case of strict accuracy demand.

5.1.6e Lattice Boltzmann method

The Lattice Boltzmann method, which is a model derived from Boltzmann equation and is well suited to describe particles interactions and also thermal flows, that does not require the solving of N-S equations hence, it appears then suitable for the description of the heat transfer and changing phase phenomena.

The statistical behaviour of a thermodynamic system in a non-equilibrium state is governed by the Boltzmann Equation (BE):

$$\frac{\partial f}{\partial t} + \xi \nabla f = Q(f,f)$$

Where $f=f(x,\xi,t)$ is a particle distribution function describing the probability to find each particle at a position x with velocity ξ at time t, while Q(f,f) is the collision term describing the interaction among particles. It is possible to linearize Q(f,f) through the so called Bhatnagar-Gross-Krook (BGK) approximation as follows:

$$Q(f,f) = \frac{f - f^{eq}}{\lambda}$$

Where λ is the relaxation time of the collision operator and f^{eq} is the equilibrium distribution function, with the shape of a Maxwellian distribution function, reported below:

$$f^{eq} = \frac{\rho}{(2\pi RT)^{d/2}} exp\left(-\frac{(\xi - v)^2}{2RT}\right)$$

With d the space dimension, ρ the macroscopic density, v the macroscopic velocity, R the gas constant and T the temperature. The quantities of ρ, v and ε can be recovered from f, integrating along the velocity space $\boldsymbol{\xi}$.

To derivate LB model three are the necessary components: an evolution equation discretized in time, a quadrature formula to approximate the integration in velocity space and and a discrete equilibrium distribution function that alloys a loyal reproduction of macroscopic quantities. Introducing the total derivative operator in Q(f,f) and then substituting it in BE the result is a differential first order equation with a constant coefficient 1/λ:

$$\frac{df}{dt}+\frac{1}{\lambda}f=\frac{1}{\lambda}f^{eq}$$

Hence, integrating this formulation over a time interval Δt, and some regularity assumptions and linearizations (to a more detailed derivation please refer to [71] and [75]), it is obtainable:

$$f(x+\xi\Delta t,\xi,t+\Delta t)=f(x,\xi,t)-\frac{1}{\tau}[f(x,\xi,t)-f^{eq}(x,\xi,t)]$$

Where τ is a dimensionless relaxation time defined as $\tau = {}^{\lambda}/_{\Delta t}$

Using the equilibrium function proposed in [71], a generic quadrature formula, which leads to a discretization of velocities, which is coupled with a spatial discretization through a grid of physical points, with resolution Δx, commonly known as lattice grid. In literature the combination of the grid and discrete velocities is called lattice discretization. A characteristic lattice velocity is also introduced as c=Δx/Δt.

The discretization must be applied to the distribution and equilibrium function, that will now depend on ξ (more specifically f_i, f_i^{eq} terms result evaluated along the corresponding i-esim discrete velocity e_i). Following He and Lou formulation[71] for a discrete equilibrium distribution:

$$f_i^{eq}=w_i\rho\left[1+\frac{e_iv}{c_s^2}-\frac{v^2}{2c_s^2}+\frac{(e_iv)^2}{2c_s^4}\right] \qquad (1)$$

Where w_i are the weights relate to the lattice scheme and $c_s = \sqrt{RT} = c/\sqrt{3}$ the so called, lattice speed. The macroscopic quantities can consequently be derived as:

$$\rho=\rho(x,t)=\sum_{i=0}^{n}f_i$$

$$\nu=v(x,t)=\frac{1}{\rho}\sum_{i=0}^{n}e_if_i \qquad (2)$$

$$\varepsilon=\varepsilon(x,t)=\frac{1}{2\rho}\sum_{i=0}^{n}(e_i-v)^2f_i$$

The discrete distribution function can be split in two subprocess: *streaming* step (describing the advection of particle distributions) and *collision* step (describing the collision among particles). The streaming step and the streaming step are respectively defined as follows:

$$f_i^s(x + e_i\Delta t, t + \Delta t) = f_i^s(x, t) \qquad (3)$$

$$f_i^c(x + e_i\Delta t, t + \Delta t) = f_i^s(x + e_i\Delta t, t + \Delta t) - \tfrac{1}{\tau}\left[f_i^s(x + e_i\Delta t, t + \Delta t) - f_i^{eq}(x + e_i\Delta t, t + \Delta t)\right] \qquad (4)$$

Equations (1), (2),(3) and (4) represent the fundamentals of the LBGK method which is the simplest of LBM formulations, suitable for laminar flow(low Reynolds numbers), in case of high Reynolds numbers it is to prefer, Multiple Relaxation Time (LB-MRT), where τ is substituted with a relaxation matrix, composed of various relaxation times τ_i, this last formulation results a stable method to simulate the turbulent phenomena along the melt pool.

It is important to note that the up/derived model describes only a fluid dynamic problem, therefore it's not sufficient to fully describe the melt pool phenomena. But, the LB method is well suited also to describe the thermal flows. In literature, the mostly adopted thermal Lattice Boltzmann (TLB) methods are the multi-distribution methods[3]. Practically besides f, another distribution function is placed into the whole picture, while f deals with the fluid dynamic problem, g is added to consider the thermodynamic part, thus meaning some additional equations are to be presented and coupled with the aforementioned ones. Below naming τ_F is the relaxation time for the thermal problem, g is defined as follows:

$$g(x + \xi\Delta t, \xi, t + \Delta t) = g(x, \xi, t) - \frac{1}{\tau_F}[g(x, \xi, t) - g^{eq}(x, \xi, t)]$$

Also g is considered in the two steps of streaming and collision as follows:

$$g_i^s(x + e_i\Delta t, t + \Delta t) = g_i^s(x, t) \qquad (5)$$

$$g_i^c(x + e_i\Delta t, t + \Delta t) = g_i^s(x + e_i\Delta t, t + \Delta t) - \tfrac{1}{\tau_F}\left[g_i^s(x + e_i\Delta t, t + \Delta t) - g_i^{eq}(x + e_i\Delta t, t + \Delta t)\right] \qquad (6)$$

Where the equilibrium function for g is formulated as:

$$g_i^{eq} = w_i T\left[1 + \tfrac{e_i v}{c_s^2}\right] \qquad (7)$$

The thermal relevant macroscopic quantities are obtained as reported:

$$\begin{aligned}
&\rho = \rho(x,t) = \sum_{i=0}^{n} f_i \\
&v = v(x,t) = \frac{1}{\rho}\sum_{i=0}^{n} e_i f_i \qquad\qquad (8) \\
&\varepsilon = \varepsilon(x,t) = \frac{1}{2\rho}\sum_{i=0}^{n}(e_i - v)^2 f_i \\
&T = T(x,t) = \sum_{i=0}^{n} g_i^s
\end{aligned}$$

Also g is considered in the two steps of streaming and collision as follows:

$$g_i^s(x + e_i\Delta t, t + \Delta t) = g_i^s(x,t)$$

$$g_i^c(x + e_i\Delta t, t + \Delta t) = g_i^s(x + e_i\Delta t, t + \Delta t) - \frac{1}{\tau_F}\left[g_i^s(x + e_i\Delta t, t + \Delta t) - g_i^{eq}(x + e_i\Delta t, t + \Delta t)\right]$$

To introduce the coupling between mass-momentum conservation and advection–diffusion, when considering buoyancy driven flows, can be performed by introducing the so-called *Boussinesq* approximation. This approximation states that density variations, caused by temperature gradients, are taken into account only when they are multiplied by the gravity. For more information about Boussinesq approximation please refer to[71].

The coupling occurs introducing the term F, which is derived from the extension of the body force, the up-cited approximation and a discretization respectively in the following way:

$$F = \rho g$$

$$F = \rho g + \rho \alpha g (T - T_0)$$

Where T_0 is the average temperature of the fluid and α is the coefficient of thermal expansion. F is then included as a coupling term into the distribution function f:

$$f(x + \xi\Delta t, \xi, t + \Delta t) = f(x, \xi, t) - \frac{1}{\tau}[f(x,\xi,t) - f^{eq}(x,\xi,t)] + F$$

After the discretization F can be rewritten as follows:

$$F_i = \rho\alpha\omega_i\left[\frac{e_i g}{c_s^2}\right](T - T_0)$$

The collision step formulation of f is now reformulated as follows:

$$f_i^c(x + e_i\Delta t, t + \Delta t) = f_i^s(x + e_i\Delta t, t + \Delta t) - \frac{1}{\tau}\left[f_i^s(x + e_i\Delta t, t + \Delta t) - f_i^{eq}(x + e_i\Delta t, t + \Delta t)\right] + F_i \quad (9)$$

The derived TLB method is represented by the formulations (1), (3), (5), (6), (8) and (9). The presented model it is based on two non-dimensional numbers describing a convective flow:

Prandtl (*Pr*) number and Rayleigh (*Ra*) number. Prandtl number describes the ratio between kinematic viscosity and thermal diffusivity and Rayleigh number states if the heat is primarily transferred by conduction or convection, below their formulation:

$$Pr = \frac{\nu'}{\kappa'}$$

$$Ra = \frac{g'\alpha\Delta T'L'^3}{\nu'\kappa'}$$

These two numbers are, for the TLB method combined in a product and a ratio (PrRa and Ra/Pr), which are reformulated to maintain the same value along the change from physical to lattice quantities, through two conversion factors, ν and κ, that are also implied for the derivation of the relaxation times as follows:

$$\tau = \frac{\nu}{c_s^2} + \frac{1}{2}$$

$$\tau_F = \frac{\kappa}{c_s^2} + \frac{1}{2}$$

Furtherly, LB method can be adjusted for multi-phase flows, which are strongly present in PBF processes, since the compresence of liquid, vapour and solid pahases. The innovation introduced by this method is the possibility to simulate phase segregation without the necessity of any method to track the surface between different phases. The base of the multi-phase model is again LBGK method, with the inclusion of a pseudo-potential function, Ψ(x,t) which is introduced to simulate the interaction among neighbouring particle distributions. For the interested reader, the approach is presented precisely by Schan and Chen[76] and a brief overview is present in Cattenone's et al already cited study[71].

4.1.5 Macro scale models

Macroscopic simulation models in the context of SLM processes typically treat the powder phase as a homogenized continuum described by means of effective, spatially averaged, thermal and mechanical properties, without resolving individual powder grains. This homogenization procedure yields efficient numerical tools capable of simulating

entire SLM builds of practically relevant size across practically relevant time scales[3]. On a macro scale models are generally built on the coupling of a thermal and a solid mechanics problem, to take in account also the evolution of strain and stress due to the main thermal nature of the AM process. The spatial discretization of the heat equation and the momentum equation is typically based on the Finite Element Method (FEM), which requires transfer of these equations into the (equivalent) weak form. The weak form reduces the continuity requirements on the basis functions used for approximation which gives way to using lesser degree polynomials. This is done by converting the differential equation into an integral form which is usually easier to solve comparatively. The weak formulation is one of the reasons behind the widely known technique of increasing the number of elements for higher simulation accuracy. Using higher order shape functions is one more method to improve the accuracy in addition to using efficient stabilization techniques. Once you have the weaker integral formulation, this can be converted into a matrix formulation (algebraic) which becomes easier to solve as there are a lot of proven and tested algorithms in place. For time integration, explicit as well as implicit approaches can be found.

4.1.5a Coupled Thermo-Mechanical Analysis

The coupling between the thermal and the solid-mechanical problem is often realized in a staggered partitioned manner. Hence meaning, the heat model is resolved first and its output is consequentially input of the mechanical model. In the figure 42 a general scheme of what a macroscopic model elaborated with FEM aims to achieve is presented. In literature many different approaches are to be found.

Hodge et al.[77] proposed to consider the heat losses, due to for instance to emissivity, through a reduction of the laser nominal power to 2/3 of the real value and integrated a phase field function. Importantly, the consolidated phase considered in this model is assumed to have a vanishing porosity and captures both, the melting as well as the solidified phase. In other words, only the phase transition from powder to liquid during melting is explicitly considered by means of a phase function, while the phase boundary between melt pool and solidified material is accounted for by means of high gradients in the material properties at these spatial locations. All of the relevant thermal material parameters (like conductivity, heat capacity etc.) are considered to be a function of both temperature and phase (thus, of porosity).

In the spatial discretization process based on the FEM approach and the subsequent numerical implementation, the phase boundary between powder and melt pool is not resolved in a sharp manner. Instead, there is typically a small band of finite elements where both phases are prevalent. Correspondingly, the Stefan-Neumann equation is not evaluated in its original form (as presented at page 46) at a 2D interface, but rather in an equivalent form within 3D volume elements.

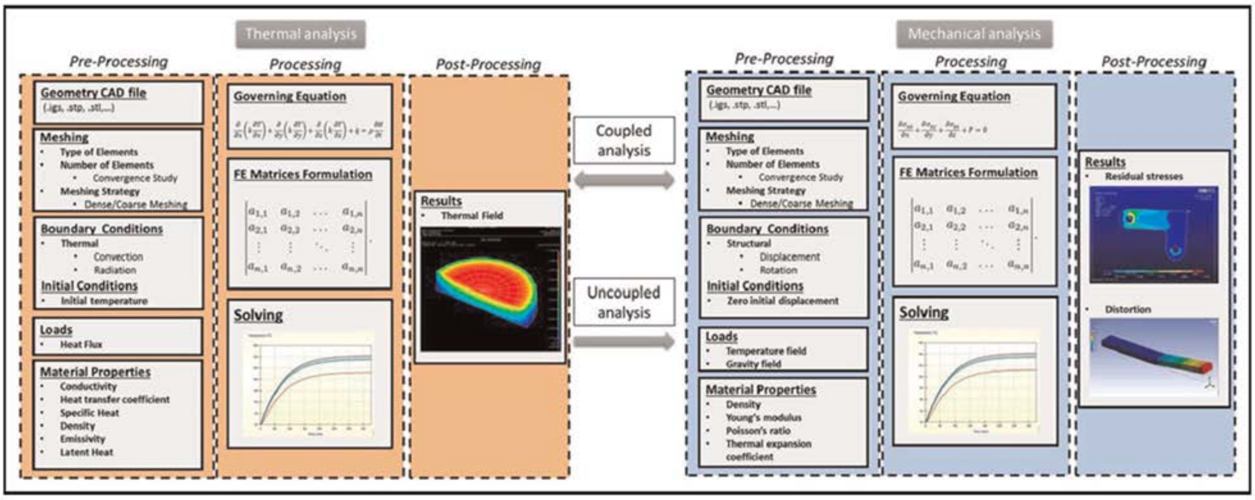

Figure 46

In addition to the set of thermal and mechanical equation presented an elasto-plastic formulation is taken into account, in Hodge et al. model, accounting for thermal expansion and consolidation shrinkage, has been employed while the boundaries between powder, melt and solidified phase have been considered implicitly via strong gradients of the associated mechanical material parameters with respect to temperature and porosity. This means, the interfaces are not tracked explicitly, and the elasto-plastic behaviour has been applied to all the three phases (powder, liquid and solidified phase), hence the melt pool dynamics are not carried out in this model. Actually however, it's a characteristic common to many of the macroscopic models present in literature.

4.1.5b Inherent Strain (IS) model

Another interesting modelling approach, in the author's opinion, is the Inherent Strain (IS) method. This method has been formulated for welding mechanics and, since the similarities with L-PBF process, it has been proved to give good results for a fast prediction of the residual stresses and distortions. Briefly, it consists of an elastic FE quasi-static analysis where the deformation is induced by user-defined inherent strains. This approach is very compelling from a computational point of view since time-consuming thermo-mechanical simulations are avoided[78]. The total strain, ε^{tot}, can be represented with the following equation, where ε^{e} is the elastic strain, ε^{in} is the inelastic strain, ε^{T} is the thermal component and ε^{ph} is a strain related to the phase change:

$$\varepsilon^{tot} = \varepsilon^{e} + \varepsilon^{in} + \varepsilon^{T} + \varepsilon^{ph}$$

The inelastic strain can be considered as composed by the creep and plastic strain, respectively ε^{cr} and ε^{pl}; the inherent strain is defined as the total strain minus the elastic component:

$$\varepsilon^{inh} = \varepsilon^{tot} - \varepsilon^{e} = \varepsilon^{pl} + \varepsilon^{cr} + \varepsilon^{T} + \varepsilon^{ph}$$

Respectively below the balance of momentum in a quasi-static problem, with σ as the stress tensor b as the body force, and the stress tensor are defined, with E as the elastic tensor:

$$\nabla \cdot \sigma + b = 0$$
$$\sigma = E\varepsilon^{e} = E(\varepsilon^{tot} - \varepsilon^{inh})$$

The inherent strain method has been successfully adapted to PBF processes in a multi-scale simulation framework. Typically, the building strategy is approximated by layer-by-layer sequence. Hence, at each time-step a new layer is added to the computational domain. In fact, it is a common practice to discretise a part into layers with a thickness which is multiple of the real layer thickness referred to as lumping strategy. Hence, according to the definition of the inherent strain tensor components, it is possible to take into account the "effects" of the actual scanning strategy. From the numerical point of view, this implies the use of a FE activation strategy. At each time step a new layer must be activated and the AM building process is simulated as a sequence of mechanical calculations, one for each manufacturing layer.

The layer activation strategy is based on the so called "born and death elements" technique[78]. According to this activation strategy, elements are not part of the model until they are activated according to the nominal height due to the powder feeding in PBF processes, this approach is not only implemented in the inherent strain model, since it suits well the characteristics of AM processes, also considering a staggered or uncoupled thermal and mechanical model.

The inherent strain method is a simplified model which consists of a mechanical linear elastic problem complemented with the activation strategy and user defined inherent strains. The key to this simplified approach is how the inherent strains are determined also considering the lumping of layers. To characterise the prescribed deformations responsible for the formation of both residual stresses and the distortions (after the stress release by cutting operation), a fine calibration of the inherent strains it’s necessary.

Two families of methods can be distinguished for this purpose: reduced order methods and empirical methods. The reduced order methods deal with the building of a higher fidelity model (a coupled or staggered thermomechanical analysis) to simulate on a local level different scan patterns and create a database of inherent strains, their weakness reside in the mapping the local strains from a high fidelity FEM to a complete part global analysis accurately, further investigation are needed and the calibration of the process parameters in both local and global level. Empirical methods on the other hand consist in characterize the inherent strains belonging to each layer though an iterative experimental and fitting strategy, the procedure must follow general established rules to produce comparable results (fixed values have to be decided at the start, like manufacturing layer height, number of physical layers contained in a super-layer, every layers has its own local coordinate system, while the global is fixed in one and unique position,etc). the methods result very similar to the ones established for Classical Laminate Theory (CLT), this because PBF processes have many similarities to the production of laminate composites, since they are both layer-wise processes and linked to this along the produced parts anisotropy is identified. For a deeper insight in the inherent strain method and its consequent numerical models please refer to Setien et al study[78].

Scanning strategy

One further added feature of the FEM activation technique is the possibility of specifying the scanning path using the same input data as for the process machine, for instance, with a Common Layer Interface (CLI) file format. A CLI file describes the movement of the laser in the plane of each layer with a complex sequence of polylines, to define the (smooth) boundary of the component, and hatch patterns, to fill the inner section[4]. And is first of all of a great user, for end-users having direct use of AM machines. The scanning path, by the way, only defines the sequence of points along which the power input moves, as well as the reference plane where the laser beam is focused. The scanning path does not contain any information regarding the velocities of the laser, the size of the melt pool, the spot-size of the laser or the thickness of the deposited layer, which have to be evaluated on smaller scale models. During a time increment the laser movement can be represented as follows:

$$\Delta x = (x^{n+1} - x^{n}) = v_s \Delta t$$

Where v_s is the scanning speed, and Δt the time increment, it is easier to prescribe Δx, and derive then the time increment from the knowledge of scan speed and related Δx. In this way different scanning path approximations, the so-called scanning strategies, can be defined. For instance, taking $\Delta x \approx s_{el}$, where s_{el} is the element size, leads to a high-fidelity representation of the scanning path, an element-by-element activation at the cost of a high number of time steps. Alternatively, the simulation can be accelerated by defining Δx as the length of one hatch, several hatches or even a whole layer. As a counterpart, this strategy only recovers average temperature fields, being not able to capture the local thermal history. High fidelity representation of the scan pattern results though, not well suited for PBF process simulation since the common layers dimensions, which would cause the computational time to be unreasonable.

4.2 Material modelling

Since in this thesis, the simulation is carried out on a macrospic scale, in this section the relevant material properties for the simulation are discussed. Furtherly, consideration about the materials implementation are presented in the second paragraph.

4.2.1 Relevant material properties for the simulation of the process

Thermo-mechanical numerical simulation requires an extensive list of temperature dependent thermo-physical properties for a given material[79]. During the process the metal is present in three different phases: powder, liquid and solidified phase. Also, metal vapour may be present, in addition to the inert gas flow protecting the layers from oxidation. Considering just the metal there are many thermo-mechanical properties. Powder properties result in literature to display different properties from as-built same material, function of temperature, to take in account. For instance, mechanical properties difference between as-built and L-PBF processed probes is evaluated on stainless steel (304L and 316L) in DebRoy et al. work as figure 47 displays, elongation especially is affected by the manufacturing process.

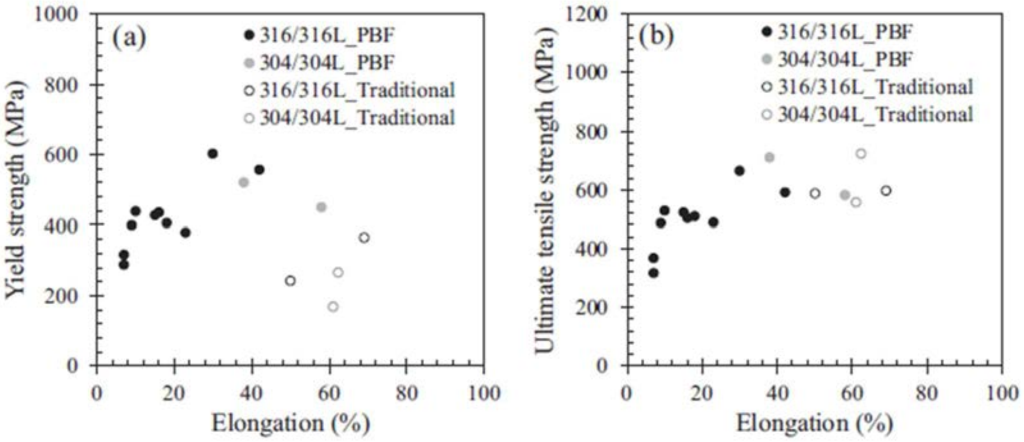

Figure 47

Within the relevant properties one of relevant interest is conductivity. And the values reported from experimental evaluation did not appear to agree with analytical models of powder thermal conductivity presented in literature. Therefore a characterization of each metal powder properties is necessary, this can be achieved with a laser flash analysis (FLA) method, as carried out by Nottingham et al. [79] for Ti6Al4v. A general approach should firstly take in account the alloy composition of the metal, in this thesis H13 steel will be mainly considered, below in table 3 [16], its composition is reported, as Mazur et al. evaluated two batches of H13 powder in comparison to the ASTM specification composition of H13 steel alloy:

Table 3

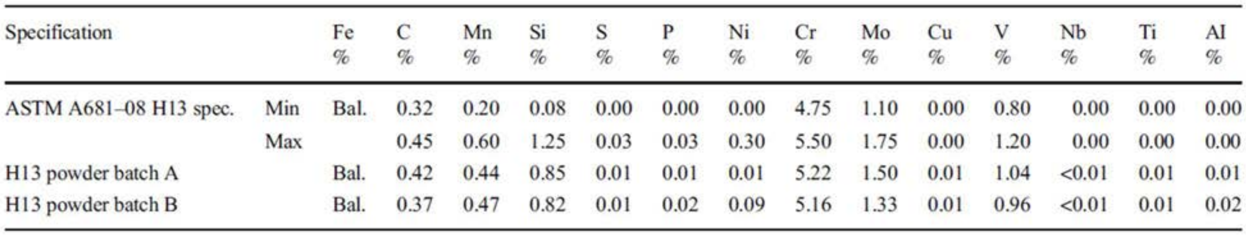

Specification		Fe %	C %	Mn %	Si %	S %	P %	Ni %	Cr %	Mo %	Cu %	V %	Nb %	Ti %	Al %
ASTM A681–08 H13 spec.	Min	Bal.	0.32	0.20	0.08	0.00	0.00	0.00	4.75	1.10	0.00	0.80	0.00	0.00	0.00
	Max		0.45	0.60	1.25	0.03	0.03	0.30	5.50	1.75	0.00	1.20	0.00	0.00	0.00
H13 powder batch A		Bal.	0.42	0.44	0.85	0.01	0.01	0.01	5.22	1.50	0.01	1.04	<0.01	0.01	0.01
H13 powder batch B		Bal.	0.37	0.47	0.82	0.01	0.02	0.09	5.16	1.33	0.01	0.96	<0.01	0.01	0.02

The powder batches analysed present a composition in the range of the ASTM specifications. The main intrinsic powder parameters affecting powder thermo-mechanical properties include chemical composition, as up cited, but also particle morphology and particle size distribution need to be characterized for more complete evaluation since they significantly affect a range of secondary powder bed characteristics relevant to L-PBF such as density and rheology, laser energy absorption, and thermal conductivity[16]. In figure 44[79] a schematic representation of flash laser process and machine involved are shown;

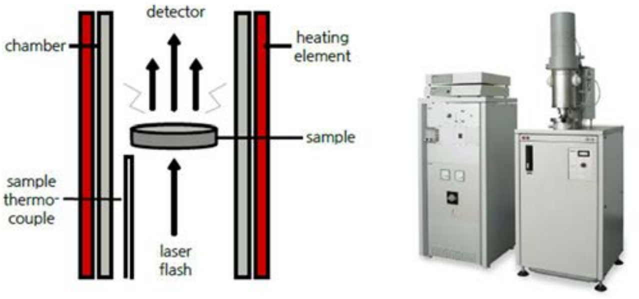

Figure 48

The FLA technique measures the thermal diffusivity of a sample with uniform thickness inside a controlled heated chamber under a protective atmosphere, a half-time signal is then captured showing the temperature difference against time.

Diffusity is part of the thermal properties which enter the conductivity evaluation as follows:

$$k(T) = \alpha(T)\rho(T)c_p(T)$$

Density, which can be referred to pressed or unpressed powder, also depends on temperature change, as specific heat, which can be evaluated solely for the powder and one modified to take in account the change of phase, as reported by Hodge et al. [77] Additionally, the process of sintering occurring among grains, with the formation of tracks and and joining of layers, increases the network of path connections between adjacent particles, and therefore improves thermal conduction throughout the medium. Heat specific assessment can be made through differential scanning calorimetry (DSC).

To carry out thermal stresses and strains analysis, also mechanical properties are needed in function of temperature in literature and databases are available simple approximations (as bilinear,…) or finer approximation, like multilinear, which takes in account multiple punctual values, of Linear Young's modulus, Yield stress, Plastic tangent modulus. In the following diagram (figure 49 [61]) thermal conductivity depending on temperature for stainless Steel is presented)

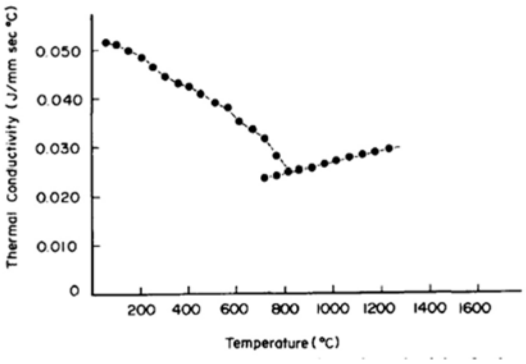

Figure 49

The difference among powder, solid and liquid phase are well represented in figure 50, as was presented by Nottingham et al.[79] for Ti6Al4V.

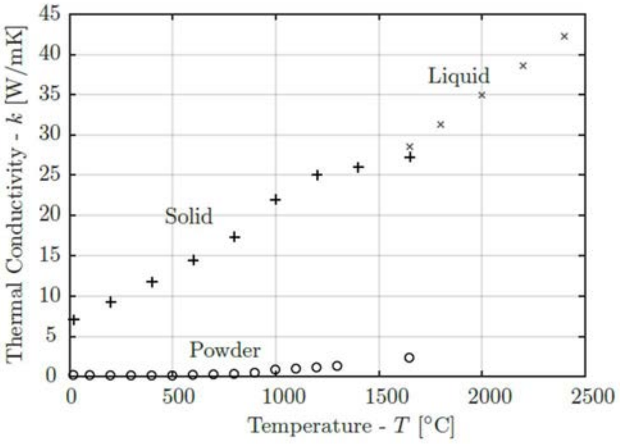

Figure 50

4.2.2 Material implementation in simulation

Another issue concerning PBF processes is linked to the metal powders available on the market, that are not that numerous, and among the same powder alloy different batches of powder feedstock, even when considering one and only manufacturing process([16]), present a high variability in properties and characteristics due to strong influence of storing and handling, thus meaning the experimental evaluation of their properties is still far from complete. This reflects even more negatively on a simulation tool level, since the database for powder metals in simulation tools are very limited, and in many of the licensed software tools new alloys cannot be added or customized in the database, leading to many limits on the value of the results of the analysis one can carry out. Also, when it is possible, it is not easy to define material thermo-physical characteristics. Since the complexity of the process, material properties must be considered temperature dependent without forgetting the changing of phase intercurring from powder to liquid and to liquid to a continuous solidified phase. But simulation tools may not be able to process correctly the temperature dependent functions chosen to represent the properties, since every function (constant, bilinear, multilinear,…) is an approximation of the real properties values, different functions can be found in different databases, some multilinear functions do not take in account maximum peak values to not rise the computational effort. And these functions may collide with the models implemented in the simulation tools, meaning an analysis fail. More research is definitely needed, on this issue, but a simple way to deal with this problem adopted in many models in literature, is a quite strong approximation, deals with characterizing metal powders of known alloys (metallic compounds in use both in the conventional as-built form and powder form) by scaling the functions of properties of interest by certain factors, the table below (reported in figure 51) by Hodges et al. [77] summarizes the most relevant scale factor quantities:

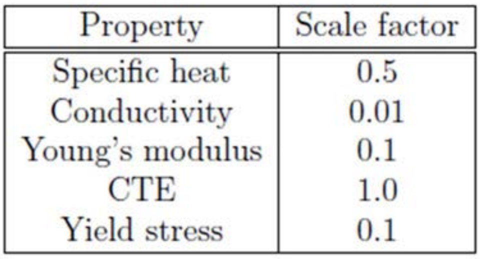

Property	Scale factor
Specific heat	0.5
Conductivity	0.01
Young's modulus	0.1
CTE	1.0
Yield stress	0.1

Figure 51

The scale factor of conductivity may be justified thinking that the inter-particle heat transfer takes place mainly through the convection mechanism, in fact, is typically governed by the gas in the powder bed pores, with commonly negligible overall conductivity contributions from particle-to-particle contact points, as long as powder layers are considered loose and not mechanically compressed. Heat transfer within the powder bed is linked to the powder bed morphology, particle shape, size distribution and packing density, are also central to radiative transfer. Consequently, the thermal conductivity of loose powder is comparable to the conductivity of gas and by orders of magnitude smaller than the conductivity in the solidified phase[3].

4.3 L-PBF models and simulation

In the last years simulation tools for AM processes are continuously evolving towards the support of the establishment of an optimum design, taking in account the compound of different thermophysical phenomena, the materials, etc.

The goals at which this technological development is aiming are many, but probably they could be summarized in one fundamental point: the drop-out of physical trial and error procedures that have been adopted at the early stages of AM processes development to achieve a simulation capability and models that can predict part performance, support development of processing and materials strategies, and enable materials design in an integrated fashion. Abandoning trial and error part manufacturing means less quality variability, avoidance of part failure during the process, less costs for experimental physical manufacturing evaluation and on many different levels. Hence, many different simulation tools can be already found from open-source codes to licensed software packages.

The computational challenges of macro or part scale thermo-mechanical simulations are driven by the disparate spatial scales of the laser energy source and the overall part geometry compounded by the disparate time scales of local heating versus overall heat transfer during the entire fabrication, which can be hours and is often days. Melting can be represented thermally through a latent heat and mechanically as a near-total loss of strength. This is achieved with elements birth-death method. This means that they are visually present in the model, but they are not all active in the computational domain. The elements are divided into active, activated, and inactive elements:

- Active elements are those elements representing the base plate, as well as the ones already activated.
- Activated elements are the ones present in the current time step and inactive previously to this moment.
- Inactive elements have not yet been included into the computational domain.

On a mechanical level the inactive, or dead, elements don’t participate to the overall stiffness of the matrix, through the multiplying of the stiffness with severe reduction factor. As it can be found, for instance in Ansys®, the elements are activated a whole computational layer at a time step, many studies in literature present an additional step, adding a control loop to activate elements which are affected by the heat source passes, an example can be found in Chiumenti et al. [80].

Many studies in literature point out the efficiency of an adaptive mesh refinement and coarsening. A common technique among AM simulation studies is using mesh density which varies across different regions of the model. Certain regions, especially close to the heat source present high and steep temperature gradients, to achieve an accurate level of analysis, require denser mesh elements than regions far away from the heat source. For that reason, a local refinement technique is employed in order to update the mesh density in each load step, according to the needs presented above. Furtherly a mesh that coarsens with increasing distance from the heat source can be beneficial on a level of computational efficiency. This enables a multiscale analysis of the problem, including in a FEM approach also mesoscopic and microscopic levels. Patil et al.[80]

[81]proposed a model which comprises a feed-forward adaptive refinement and definement mesh (FFA-RDF mesh).

By the way, despite the many algorithms and improved method proposed in literature, market simulation tools are arguably, still far from reaching their full potential, but steps forward a holistic approach to analyze and simulate AM process are made continuously. While the first dedicated software package where derived directly by AM machines manufactures, to enable the elaboration of CAD models to be printed (slicing, etc.), the advancements made in the last years, gave birth to software able to: automatically generate supports of different types for over-hanging regions, to evaluate the best alternative for print direction (more specifically how the part is oriented on the build plate), to carry put topological optimisation, to compensate automatically the design taking in account the distortion and to insert different pre-modelled lattice structures. The tools for support of the design parts for AM processes are evolving along with the simulation dedicated ones. In literature the many models and approaches presented, some of which are referenced in this thesis, use different software packages and codes, the most common choice results in multiphysics software, which either with AM dedicated modules or not, enable the analysis of the many physical phenomena behind the PBF processes. In this study, the AM part will be simulated through Ansys®. More specifically Ansys® presents a suite dedicated to AM from part design to process simulation and evaluation, it can be considered divided in three modules concerning AM processes Ansys PRINT, Ansys SCIENCE, and the Ansys Workbench module through which it's possible to carry out a coupled staggered thermo-mechanical analysis in the mechanical ambient of Ansys®, where is possible to simulate also the part removal from the base plate and possible post-process heat treatment such as annealing. Meanwhile Ansys PRINT is a stand-alone module, which is a rapid stress-strain evaluation tool, more prone to the part optimal setup for manufacturing (part orientation, etc.). And last, Ansys SCIENCE aims to determine optimum machine/material parameters, control microstructure and material properties [82].

The choice for this thesis, since the macroscopic approach, will be simulating the process through Ansys Mechanical ambient.

Sames et al. [4] have highlighted some of the computational challenges for the future of AM simulation tool development, which can be summarized as follows:

- The large amount of powder particles and melt passes in comparison with a typical machine processing volume (for instance for 1 m^3 processing volume can contain 10^{12} particles and 10^9 m of welding lines);
- A huge computational time is needed to simulate the process on a micro-scale level;

- Rapid heating and cooling results in very large temperature gradients as a function of space and time leading to very fine mesh to capture the physical phenomena even if the major part of the build volume is not in the region of interest (this point addresses the interest in the FFA-RDF method and other adaptive mesh methods);
- the region of interest is confined to a very small region and the process is very heterogeneous and multi-scale at any point in time;
- Hours of build with very small time steps is not tractable, as one cannot parallelize in time for these complex simulations;
- Accurate computational tools to predict the residual stress, geometry and quality of the build do not exist;
- Integrated and validated multi-physics and multi-scale capability that includes phase change dynamics including surface tension, residual stress, microstructure, etc. do not exist;
- Path optimization in terms of beam path sequencing, beam speed, heat source focus and applied power, as a function of space and time, leads to an infinite dimensional parameter space that is difficult to manage computationally as well as experimentally;
- Large number of thermo-physical and other parameters such the ones characterizing the beam interaction with the substrate, microstructural changes as a function of phase change dynamics, etc.;
- Validation results complex since non-intrusive characterization in current machine configurations is mostly limited to surface and boundary measurements through viewing windows or post-build characterization of microstructures.

These challenges are common to the welding process, even though, PBF processes result having a different order of magnitude of complexity. The possibilities nowadays, are different micro, meso and macro models, which consecutive resolution provides input parameters for the higher scale consecutive simulation, to couple across the various scales and physics, this can be reached through offline tabulation of data and correlations as Sames et al. [4] suggest.

4.4 Post processing of L-PBF manufactures

After the deposition of the last layer, there are many steps that are typically taken, to prepare an as-fabricated part into an end-use part. Excess of powder has to be removed, as well as support structure if present and the part must be removed from the base plate. Furtherly, heat treatment process is proved to improve mechanical properties are usually and surface treatment as polishing are carried out to achieve the desired levels of strength and finishing.

4.4.1 Powder, supports and base plate removal

The excess powder after part manufacturing must be vacuumed or blasted off with a similar powder in case (of sintered powder, common in EB-PBF). Supports are removed mechanically by cutting or application of force. The base plate results joined to the part

4.4.2 Thermal Post processing- Heat treatment

Thermal post processing is used to improve as-fabricated part mechanical properties and relief the residual stresses and/or close pores. The various treatment options can effect changes in grain size, grain orientation, precipitate phases, porosity and mechanical properties. And, it is actually the goal to affects grains structure obtaining recovery, recrystallization and growth. On a microstructural level dissolution, precipitation and growth.

a. Stress relief

Stress relief involves recovery; atomic diffusion increases at high temperatures, and atoms in regions of high stress can move to regions of lower stress, which results in the relief of internal strain energy. It’s common, for L-PBF as-fabricated parts, to undergo annealing before support and base plate removal. Stress relief treatments must be performed at a high enough temperature to allow atomic mobility but remain short enough in time to suppress grain recrystallisation (unless desired) and growth (which is usually associated with a loss of strength). Recrystallisation may be desirable in metal AM to promote the formation of
equiaxed microstructure from columnar microstructure[4].

b. Recrystallization

Research has shown how a prolonged heat treatment can provide recrystallization, for instance Song et al. [83] reported an experimental evaluation of vacuum heat treatment of L-PBF manufactured iron parts evolve their grain structure, in figure 52 [83] the evolution of the grains subjected to heat treatment is schematized:

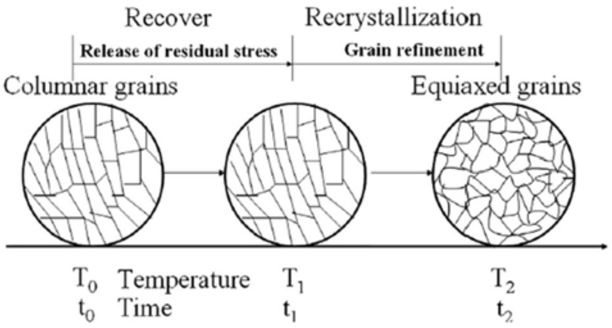

Figure 52

c. Hot Isostatic Press (HIP)

HIP can be used to close internal pores and cracks in metal AM parts. Internal pores, or "closed" pores, are surrounded by material in the centre of the sample. When pores form at the surface, they are considered "open" pores. Open pores caused by surface defects are a problem for post-processing, as allowing deeper air infiltration at high temperature during heat treatment. HIP on the other hand significantly affect grain structure, towards coarsening. But in case or little sparse hard phase as carbides or oxides grain may remain of a small size as experimentally proved Blackwell[84] investigating IN718 microstructure after HIP treatment.

d. Solution treatment (ST) and aging

A ST can be useful to dissolve undesired phases, while aging may enable the growth of precipitate phase of interest. These two processes may be applied subsequentially, the names are then generally agglomerated in STA. After a material is solutionised to form a solid solution, the matrix of the material is essentially "reset". Aging can be carried out on
the reset material, without the need to consider prior phase structure. The aim of aging is to harden a material through precipitation formation.

4.5.3 Surface finishing

AM as-fabricated parts are characterized by high roughness surfaces, machining is then often applied to obtain a smooth finished surface. CNC machining, for instance via milling, is the main choice. Actually, hybrid processes implying L-PBF and CNC machining of each layer have been developed for specific tooling processes.

5 PRESENTATION of the CASE STUDY

5.1 Introduction

All the theoretical and analytical background presented in the first 4 chapters of this thesis paved a scientific understanding of the phenomena behind HPDC and AM processes, both from a general point of view and to the possible inefficiencies, for instance in terms of defects. Conformal Cooling has still to be evaluated in detail, especially applied to HPDC dies. This unexplored branch has its appeal for more research and evaluation, thus the decision to investigate a real case of HPDC problematic production to evaluate conformal cooling possible cost-effectiveness. This has been achieved exploiting the consolidated and novel simulation tools, respectively for HPDC process and L-PBF process, a CAD software and economical characteristics of each process.

As mentioned in the chapter 2 paragraph 3, conformal cooling has been investigated more furtherly for Plastic Injection Moulding (PIM) than for HPDC, and, despite the common aspects of these two processes there are also many relevant differences, both in process characteristics and in the results that conformal cooling can achieve applied either in PIM or in HPDC process. PIM process temperatures and pressures are less severe than in HPDC process, hence the die is subjected to higher stress. Furtherly many conformal cooling formulations for IM dies are structured on the minimization of the cycle time, since it easier analytically formulated than cycle time in HPDC. Despite the existence of the Chvorinov rule for estimating casting solidification time, it cannot be used in its general formulation in case of HPDC process, since the complex geometry and the varying thickness of the part, and even if some adapted formulation has been proposed in literature[85][86], not calibrated on every single case analytical formulation do not give results well comparable with experimental solidification times. HPDC cycle time is usually firstly evaluated from the solidification of the part to be produced through simulation. It must be also noted the solidification time is much more prevalent over other times composing the cycle time in PIM than in HPDC process, the PIM cycle time is 70% to 80% determined by cooling time[87]. On the other hand, considering PIM fabricated parts, they suffer much more of warpage then HPDC produced parts, this because of the differences between respectively polymer parts and light weight alloys ones, so many approaches of conformal cooling in IM dies are linked to the minimizing of warpage.

Consequently, the aims of conformal cooling application to HPDC dies slightly differ from the aims in the sector of plastic injection. The goals of this study, that can be considered general goals for conformal cooling L-PBF produced inserts for HPDC process, can be summarized under the main goal of the manufacturing industry, reaching the optimum of cost-effectiveness.

This can be exploded on different levels for this thesis as follows:

- Improved die life →
  - Improved thermoregulation of the dies
    - Smaller temperature gradients along the inserts and dies surface
    - Longer thermal fatigue life
    - Absence of die soldering effects
- Improved part quality →
  - Improved quality parameters
    - Minimized porosity
    - Minimized Hot spots possibility
- Decrease of cycle time
- Die inserts L-PBF assessed manufacturability →
  - Successful simulation of L-PBF process
    - Material implementation
    - Mesh sensitivity analysis
    - Inherent Strain (IS) simulation
- Cost competitivity of the L-PBF conformally cooled solution →
  - Smaller manufacturing time
  - Smaller cost of tooling equipment

The first three points are to be investigated through the HPDC process simulation, criteria for their investigation will be furtherly explained in paragraph 5.4 where the conventional design will be evaluated. The fourth point will be investigated through AM simulation results evaluation, more detailed discussion of this point will be presented in paragraph 5.7. The last point will be dealt with in paragraph 5.8, where the comparison of conventional tooling and L-PBF process will be carried out in terms of time and costs in the light of the simulations results.

The workflow of the approach followed along this study is represented in figure 53 below.

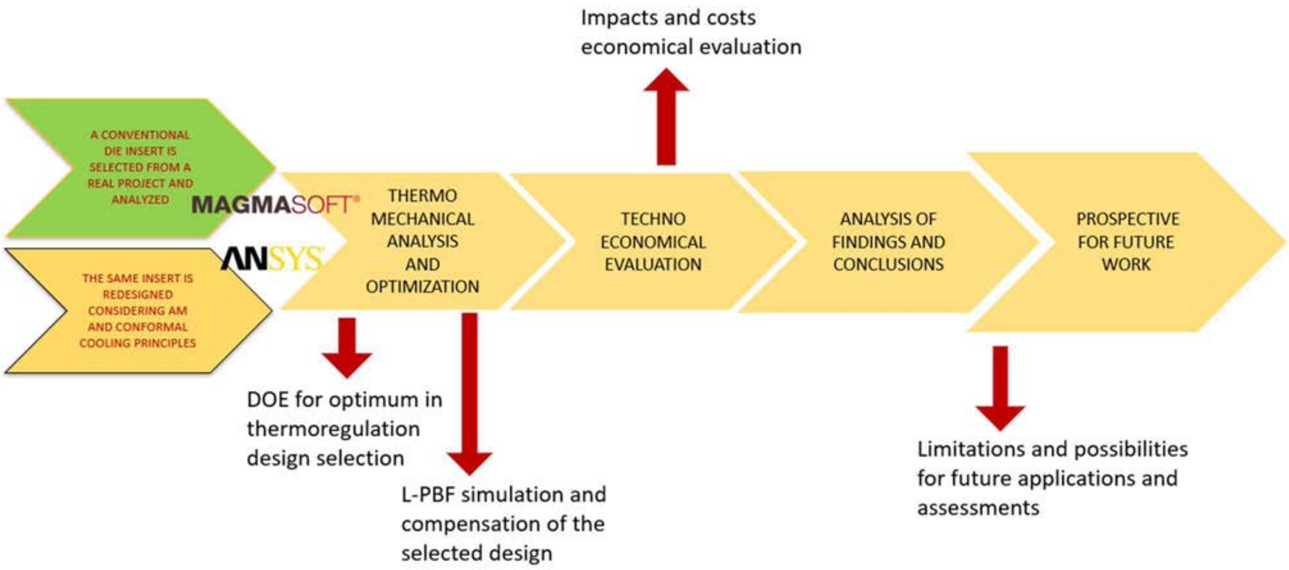

Figure 53 – Approach workflof

5.2 Outline

The research method and the workflow of this thesis was split into two main steps, after the selection of a case study and it's analysis, first step faced the establishment of a methodology for the design of conformal cooling alternatives, while the second step dealt with the analysis of these new designs, to solve conventional designs issues but also to achieve a manufacturable design that can economically compete with the conventional one. Also, other two main steps in this thesis work may be identified by the manufacturing processes and its simulations this work dealt with, HPDC and AM. Nevertheless, besides these macro-steps dividing this work in smaller steps could be more useful:

- Analysis of a conventional design;
- Design of innovative circuits for 4 inserts;
- Evaluation and selection of the best alternatives;
- Comparison between the conventional and the new design selected in terms of costs and impacts;
- Conclusions;

In figure 54 the logical procedure to manufacture a conformal cooling die insert for HPDC is presented, as well besides the conventional procedure. It's clear that only a small part of the die is to be produced through AM process. This is a limit imposed by economical, time and feasibility needs. Therefore, the focus of this thesis will be on four die inserts, with possible different design combination of geometries, utilizing them all or partly, inside of a real case project.

Based on the result analysis of the conventional design, some hypothetical very basic conformal cooling designs were carried out, to carry out new simulations and see if it would have really been beneficial on the defects. The results showed improvement, so it had been decided to proceed with a more accurate designing of the conformal cooling channels and subsequent analysis and simulations.

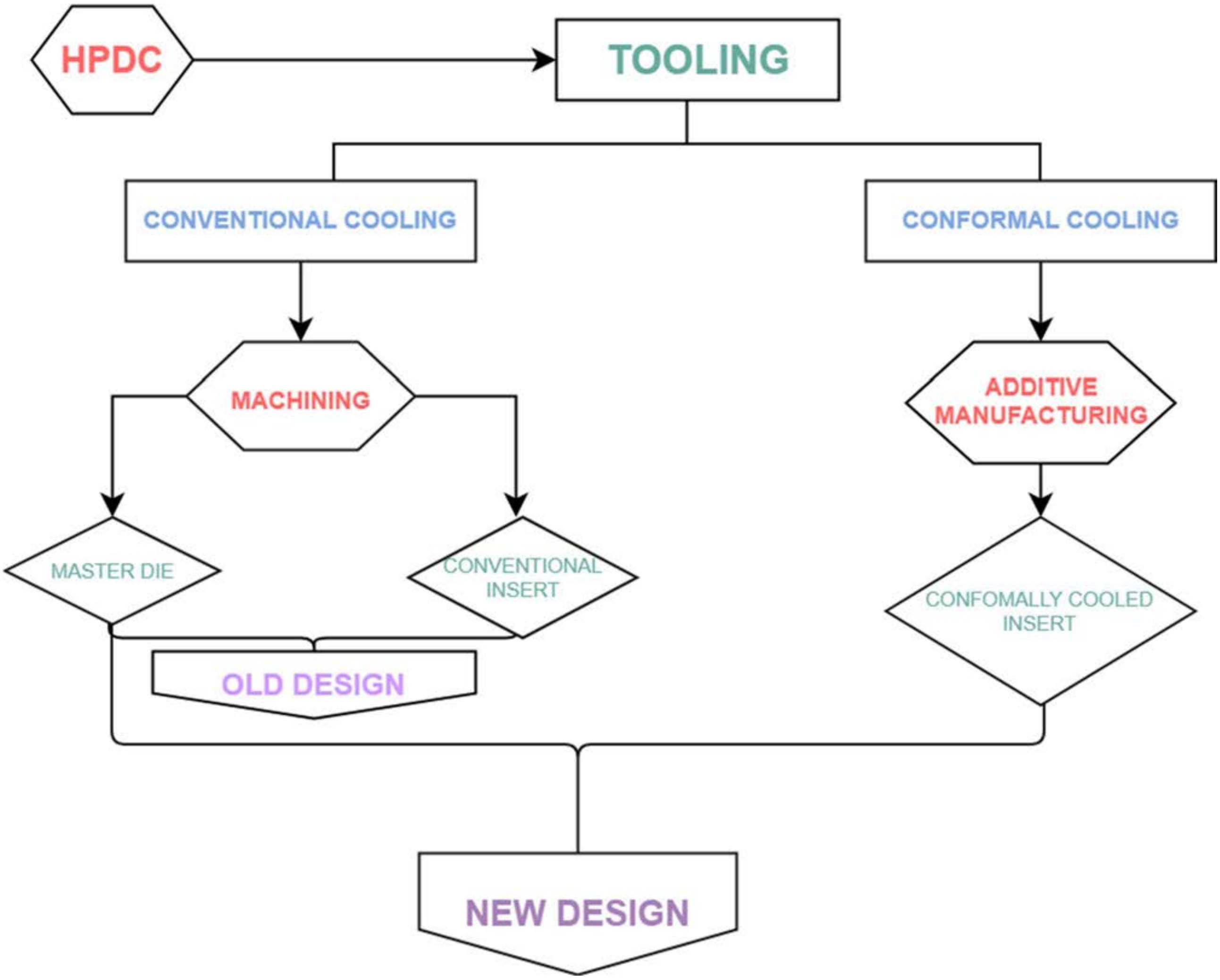

Figure 54 – Tooling possibilities for HPDC dies

5.3 Delimitations on the thermal effectivity of the conformal cooling solutions

There some delimitations to discuss before entering in the merit of the analysis carried out for this case study. Delimitations that draw a boundary to the depth of the study, but also which may pave the way to deeper analysis of conformal cooling application to HPDC die inserts.

On the HPDC process side, simulations were chosen to analyze only the thermal effectivity of the conformal cooling solutions, not taking in account fluid dynamic simulations. Hence, different cross-sections from the conventional circular have not been investigated in this thesis in their dynamic mode. The cooling medium has been chosen as pressurized water, so oil medium has not been investigated, the input temperature of the cooling medium has been fixed at 20°C to achieve the maximum cooling effect, as it is the lowest temperature in use for cooling circuits in HPDC. The cooling flow rate is assumed to be of 15 l/min (0.9 m^3/h) to maintain a turbulent flow since the length of all the circuits considered remains in a range of 0,5 to 1 m. Furtherly, casting filling was not performed, considering it in first approximation instantaneous to lessen the computational time.

On the AM process side, since the lack of material models and experimental data the material has been implemented with the respective solid properties, also dealing with the IS method, the scaling factors of strains of the material should undergo calibration, a procedure for accomplish this will be presented, but not implemented. Since the lack of strains calibration and material characterization, the results presented for AM simulations convey a qualitative idea of the most critical zones in the build part for stress and deformation fields, but the quantitative output values have not precise reliability.

In addition, for confidentiality reasons, the images regarding the case study are sections of the CAD and simulation models to show only relevant zones and not the whole design.

5.4 Conventional Design and analysis

The choice of the case of study has been taken through the evaluation of a number of projects which reported in the simulation results relevantly negative values in parameters measuring the quality of the casting or the die life. The final choice was a project with a high porosity value, implying a not acceptable quality level of most of the parts produced (a waste of nearly 50% of the produced parts). The project chosen refers to the HPDC of an AlSi9Cu3 alloy part. In figure 55 some general information of the cycle are reported, from the top to the bottom the information represent the type of casting process, the main alloy component, alloy name, machine, weight of the casting, weight of the casting plus casting system, yield is a percentage referred to the ratio of casting weight on the total weight, the last information refers to the number of cycles simulated, 8 was set as the number of cycles, saving only the results for the last cycle when is considered the process have reached the steady state.

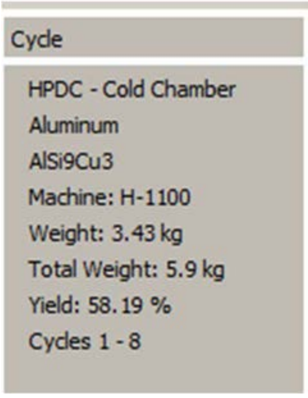
Cycle
HPDC - Cold Chamber
Aluminum
AlSi9Cu3
Machine: H-1100
Weight: 3.43 kg
Total Weight: 5.9 kg
Yield: 58.19 %
Cycles 1 - 8

Figure 55- cycle information

The cycle time is set to 85 s, divided in 40 s for the preparation phase (including lubricant spraying, blowing, placing of the inserts and a delay of 10 s), 40 s for filling, solidification and die open and 5 s for the ejection of the casting.

The calculation of the locking force required based on the total volume of molten metal required (2227.25 cm^3 considering casting and casting system) is of 8095.09 kN which increased of a 30% safety factor draws a new required locking force of 10523.61 kN, hence the machine selected for this casting is characterized by a locking force maximum of 12500 kN. The molten alloy oven temperature is set to 710.75 °C estimating a temperature of 640°C in the shot chamber, the plunger stroke is of 519 mm. Since the simulations run did not comprise the filling phase, by first approximation considerable as instantaneous, to evaluate only the thermal balance. Hence information about plunger velocity of first, second phase can be neglected.

So, simulation results already existed for the conventional design, but a new simulation was set, in order to set the same mesh parameters as it would have been set for the conformal cooling designs. The same mesh parameters in every version of the project enables more solidly comparable results. After the simulation had run results were analysed, the most relevant to this study are reported in this paragraph as follows.

The criteria selected for the comparison of the different designs are the following:

- Porosity→ the result of this criterion is a qualitative indicator linked to the porosity volume, no information is given on how this volume is distributed, as it may be divided in little cavities or clustered in a big one, therefore the comparison of different designs appears to be necessary, the more the porosity value decreases, the better the new design works;
- Hot spot→ The coloured volumes indicate the zones which may be interested by hotspots, leading to possibility of shrinkage porosities, on a scale of colours linked to the solidification time. More specifically it is linked to the solidification time in the sense that, the highlighted volumes are coloured relatively to the

time scale, which is linked to the colour palette on the right of the pictures, from blue to white going up the scale the time increases, this means that the higher is the time linked to the hot spot volume detected the major is the risk of having problems linked to hot spot formation.

- Solidification time→ different colours map different solidification times depending on the casting area and volume;
- Die soldering on die→ linked to the material (melt or die alloy) critical temperature for interactions among casting and die a colour map points at which cycle time the ejection of the casting would probably cause soldering, bounding issues;
- Temperature→ temperature fields are plotted at the surface with time steps that can be set by the user in the results definition section of the software, in this case the temperature field has been saved with a time step of 1 s;

As aforementioned the case was selected due to its high porosity values, the images 55 and 56, report the porosity affected areas and the picked value, to be compared with the subsequent designs, also a multi coloured can be noted in the bottom area of figure 56, it highlights the squeeze, an additional little shot of molten metal introduced generally to reduce porosity problems, the value of porosity reported remains by the way significant:

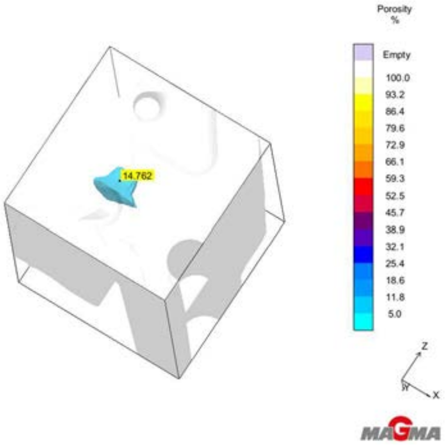

Figure 56- Porosity 1

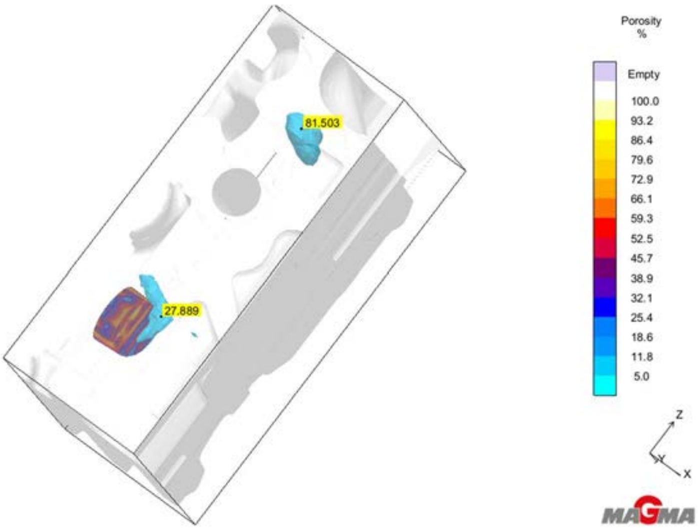

Figure 57- Porosity in the proximity of the squeeze and Porosity 2

Porosities may be linked to hot spots formation in the casting volume, as these hot zones can remain isolated and form cavities due to solidification shrinkage without the possibility of additional material to compensate the problem. In the casting, two hotspot volumes are actually detected by the simulation in the same zones porosities are found, as it can be seen in figure 58 and 59:

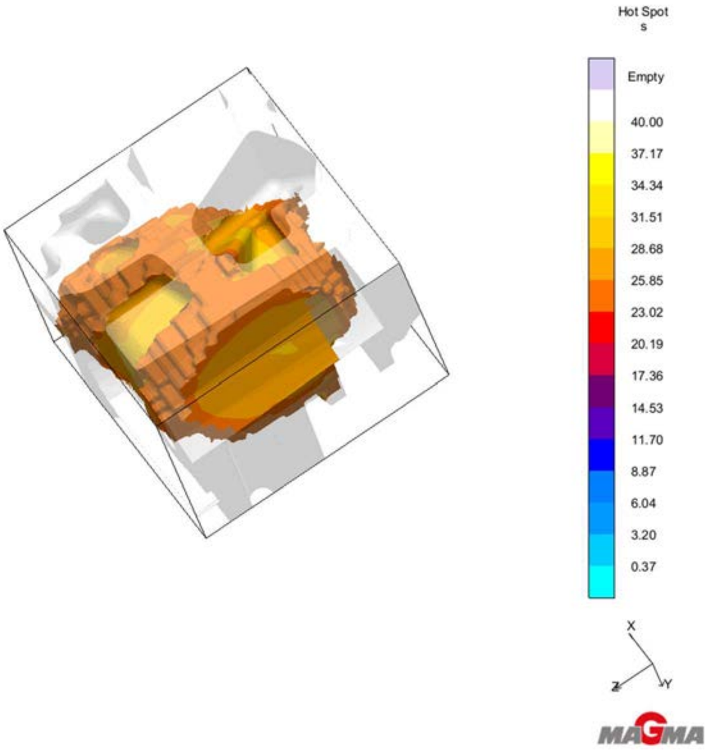

Figure 58- Hot spot in the same area where Porosity 1 was detected

Figure 59 presents a bright yellow colouring, thus meaning the risk is there high. Furtherly, attention must be payed in case of colours at the top of the scale, this may mean the casting is ejected before complete solidification, in this case examining the solid fraction result at the opening of the dies revealed that the open dies time is sufficient.

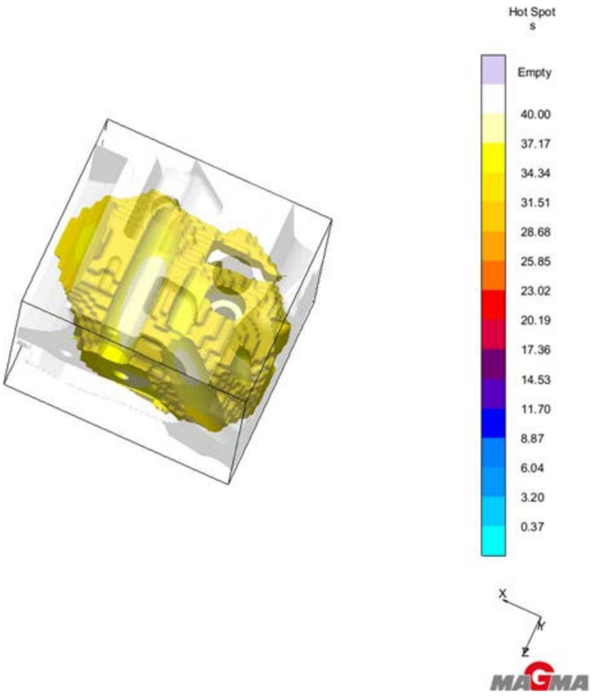

Figure 59- Hot spot in the same area where Porosity 2 and near squeeze Porosity are detected

Hot spots are located, as it could be reasonably expected in the thickest part of the casting, this case presents a big variability of thickness of the casted part and this may be an influent reason of the defects formation, a re-designing of the part with a more little range of thickness could be resolutive, but this is not what this thesis is about, therefore the casting will be considered to remain as it is.

In figure 60 the part of the casting showing the most critical solidification time is reported:

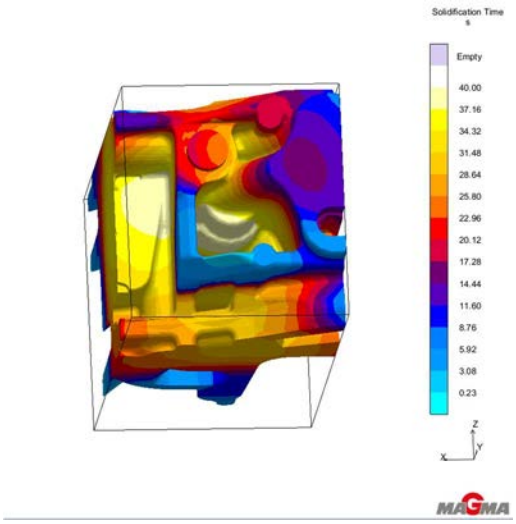

Figure 60- color map of solidification time, critical casting part

The most critical area is highlighted in light yellow, in the upper image (figure 60) it's linked values is of 40s.

Since the die opening is planned after 40 s since the filling started, the closest is the solidification time the highest is the probability of difficult ejection, with all the linked problematics. One issue strongly affecting the die life is the die soldering possibility, this risk is evaluated in the simulation through the die soldering on die criterion, since it represents the die surface/casting interactions it exists also its corresponding criterion for the casting part (named simply die soldering) in case the users would like to evaluate two different critical temperatures, respectively the die alloy one and the casting one. In this case the set temperature is 471.58°C for both criteria, that is the critical temperature for the alloy casted, precisely ALSi9Cu3, since it is assumable that reached that value, the casting may start to interact with the die surface, in image 61 a part of the side core is reported showing the die soldering on die result, the problem in this zones appears to be limited, the slide die is subjected to the critical temperature for consistent time only on a small area:

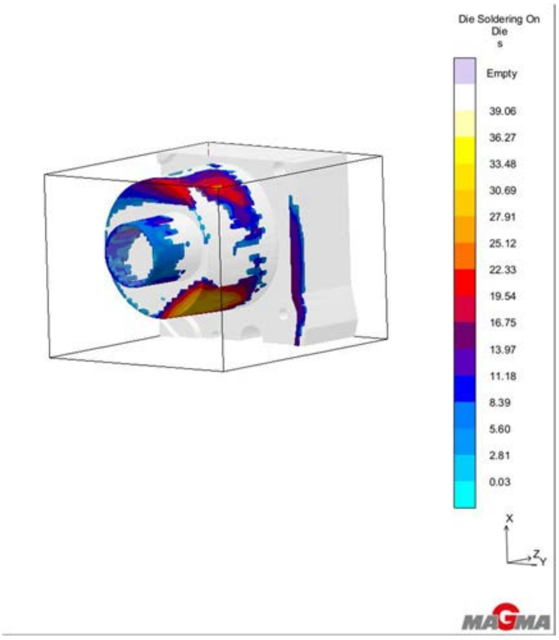

Figure 61- die soldering on the side core

A similar situation is also is show in figure 62, a part of the cover die it's been selected as the situation is similar along all the surface with peak values, as it could be expected, on thin spires surrounded by the casting:

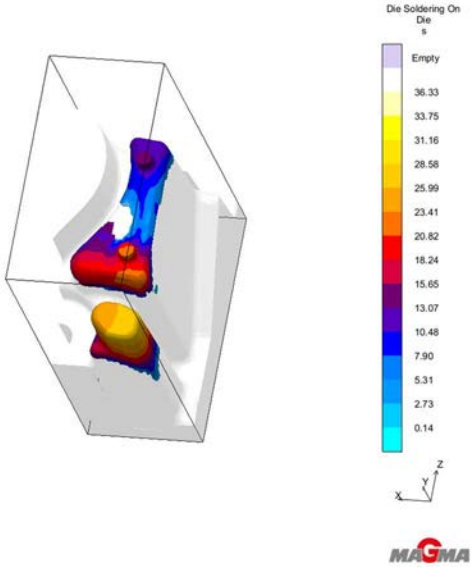

Figure 62- die soldering on the cover die

Analogue situation can be spotted on most of the surface of the ejector die, except for an area that results more critical therefore the representation of the high risk of casting/die interaction is below reported, figure 63:

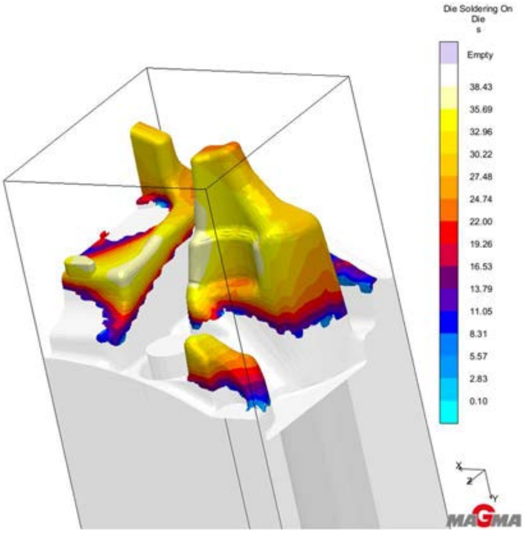

Figure 63- die soldering on the ejector die

The cooling channels present in the conventional design are all straight-line drilled channels of 8 cm of diameter, for this kind of channels is impossible to convey uniform cooling along the many spires and depressions of the dies. Furtherly absence in the insert of the side core of any cooling circuit and its proximity to the problematic zones suggest that a conformal cooling circuit there could be beneficial. In figure 64 and 65, the temperature fields on the side core insert are showed on three selected points, the two different moments to evaluate maximum and minimum temperature are respectively at the die opening and right after the spraying phase. It can be clearly noted how the maximum temperature exceeds the 300 °C suggesting possible problematics with the insert die life.

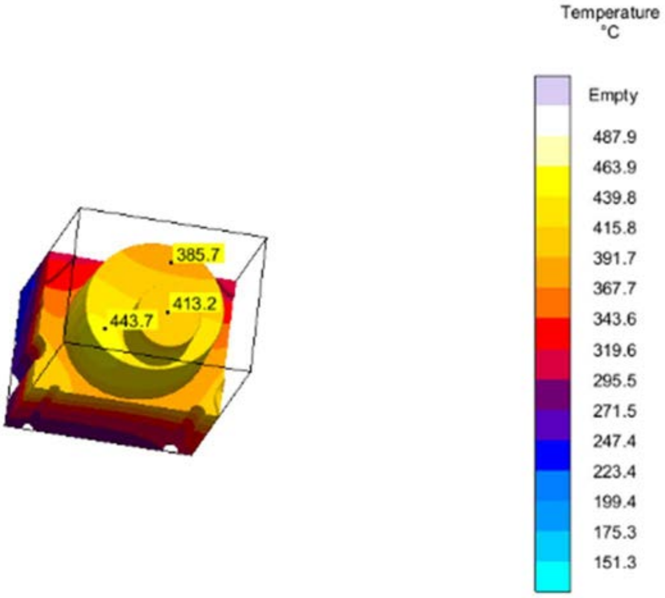

Figure 64- temperature field on the side core insert at die opening conventional design

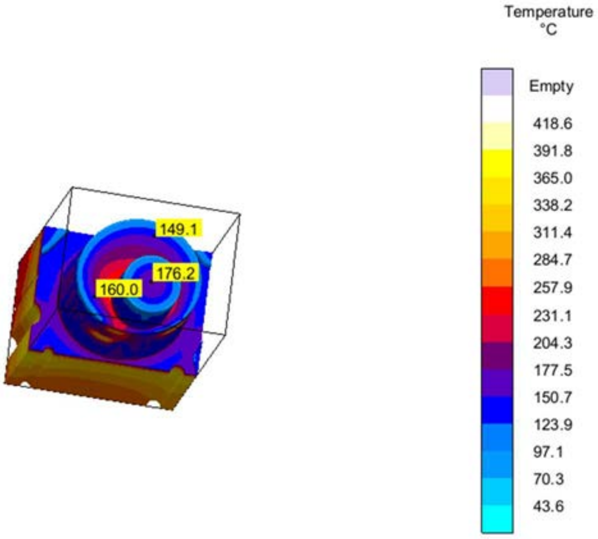

Figure 65- temperature field on the side core at the end of spraying conventional die

5.5 Conformal Cooling Design

After the analysis of the conventional design it appeared that the main issue of the HPDC castings was to be found in localized porosity, to resolve this issue four inserts where selected to be candidates, on their own or in different combinations, for conformal cooling circuits. The first of this insert is an actual separated insert already existing on the slide, the other three inserts where derivated respectively one from the fixed and two form the ejector die. To assess if a conformal cooling design could be beneficial and where to obtain the additional inserts a preliminary analysis where carried by adding in the spires of the cover and ejector die in the nearby the detected porosities some basic conformal cooling channels. This first assessment tried to activate one by one the circuits, in addition to different combination of them, in a project built in the MAGMASOFT®, using the optimization module to create a test full factorial design of experiments (full factorial DOE). In a full factorial DOE the response of the system is evaluated on two or more factors and linked levels. In this project zero, as it may be called, 5 where the factors varying along the sample, as 5 basic circuits where set to be either active or not. Four of the five circuits were just very simple U-shaped channels with circular cross-section of diameter 2 mm, as can be seen in figure 66, just to assess which zones of cover and ejector die where mostly influential. The fifth circuit, which were placed in the side core insert had more freedom of design since the bigger volume available in comparison to the spires of the fixed and mobile dies, thus a simple circular cross-section, helical circuit was designed, as figure 67 shows. The objectives delimitating the analysis where set to minimize the sum of active circuits, minimize porosity and FS time (which is the time at which the fraction of solid upon liquid makes the feeding problematic).

Figure 66- simple conformal channel design for evaluation of the most influential zones on ejector and cover die

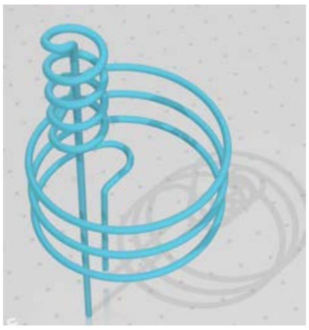

Figure 67- first conformal cooling circuit for assessment of the possibility of effectiveness of conformal cooling applied to the side core

Once the more influent spires of the cover and ejector die were detected the three additional zones were cut off to create three inserts. In the set of images below (figure 68) respectively from the left the slide insert (A), the cover die insert (B) and the ejector die insert 1 (C) and the ejector die insert 2 (D).

A B C D

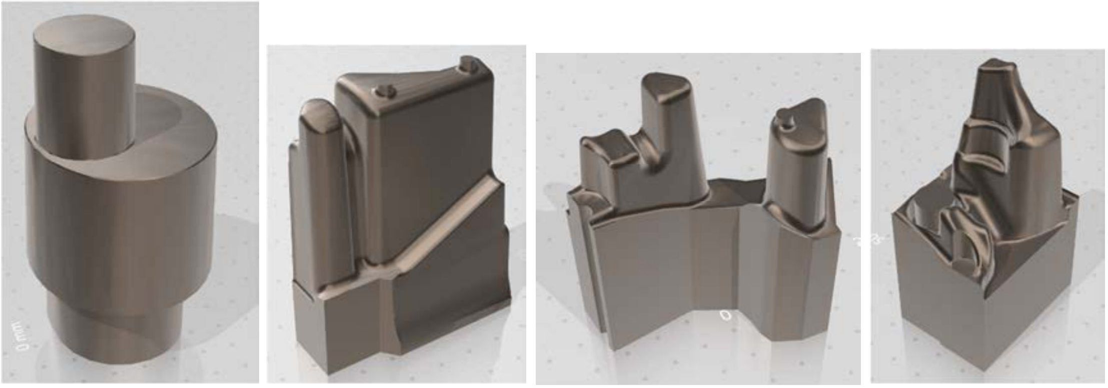

Figure 68- side core insert and the three inserts taken respectively one from the cover die, two from ejector die

For the three inserts created from cover and ejector die since the small thickness (from 5 to 9 mm on the top of spires) only a conformal cooling circuit was designed for each. Keeping a circular cross-section, with a diameter of 2 mm, which results experimentally as the smallest diameter enabling the excess powder removal after the printing of H13 steel, as reported by Mazur et al. [15]. From this study also emerged the absence of need to adapt a circular channel with diameter in a range from 2 to 8 mm to be self-supportive, because channels of this kind are already stable enough. The design strategy followed to design this first three circuits since the little volume available there was not much space for design creativity.

Cooling channels can be considered as geometrical discontinuities among the die, therefore many evaluate the stress factor to assess if a die with circuits can withstand the process or not. Mazur et al., for instance, investigated on two dimensions the stress concentration factor for channels with circular cross-section, the variables considered where diameter, pitch (distance between two channels or two passes of the same channels) and depth (distance between the cavity surface and the channel surface), the obtained results show, as it could be imagined, that magnitude of the stress concentration increases with an increase in channel diameter and with a decrease in channel depth and pitch. The results show low ($k \leq 4$) for channels of 2 mm diameter even with little depth and pitch (smallest value 1.5 mm). Considering that the up cited study is carried out in the sector of PIM process, so the stresses may be lower than in HPDC cases, it is assumed though that a 2 mm diameter value and 4 mm for the other variables, depth and pitch, could be applicable in this case. A further analysis, on the range of HPDC thermo- mechanical stresses, could be in the future a very useful assessment for the designers, at least to assess some good designing rules in the conformal cooling applied to HPDC. After making this assumption, a circuit for every one of the three inserts has been designed, trying to follow at best the shape of the inserts. The inserts with the casting in their proximity (A) and their respective cooling circuit (B) are shown in figure 69, 70 and 71:

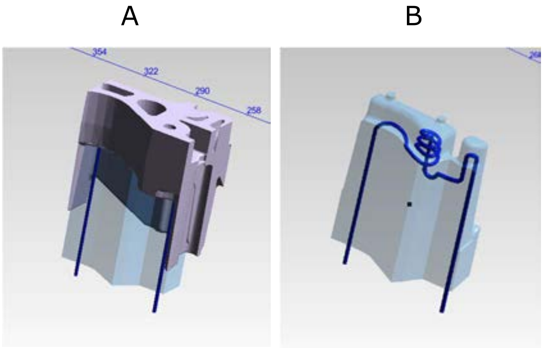

Figure 69- casting surrounding the cover die insert and its conformal cooling circuit design

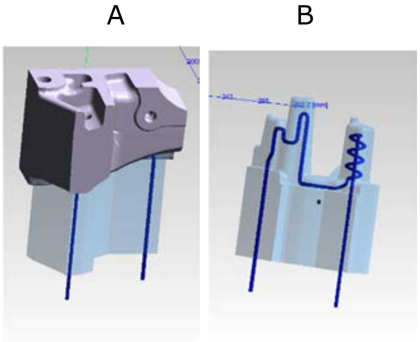

Figure 70- casting surrounding the ejector die insert (1) and its conformal cooling circuit design

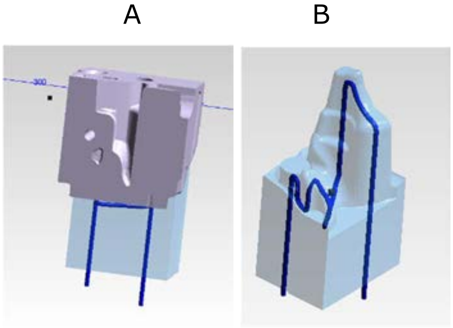

Figure 71- casting surrounding the ejector die insert (2) and its conformal cooling circuit design

For the side core insert on the other hand more than one circuit has been designed, since the available volume gave more freedom of shape. Four circuits have circular cross-section, but the diameter this time has been chosen of 4 mm, a larger diameter prevents problems linked to water impurities as incrustations, which would compromise the heat exchange and furtherly even the functioning of the circuit. The four circular circuits where designed with a double helical path to get closer to the surface of the insert which can be approximated considering the part surrounded by the casting to a sum of two cylinders, the upper of diameter 29 mm and of height 31 mm, below a second cylinder of diameter 55 mm and height 45 mm. Since the dimeter of the cooling circuits it's doubled the minimum distance from the surface is enhanced. Two circuits present two helixes, the upper of diameter 16, the downer with diameter 40 mm, ensuring a distance from the surface ≥ 6 mm; the two designs characterized by the up cited helixes, differ in the number of passes, the upper has respectively 3 and 4 passes, the downer 3 and 5. The same number of passes was applied to other two alternatives, getting closer to the surface, with the upper helix of diameter 19, the downer of diameter 42.5, ensuring a distance ≥5 mm from the surface. The insert with the casting in its proximity and the four resulting designs are reported in the picture below (respectively 72 and 73 A, B, C and D):

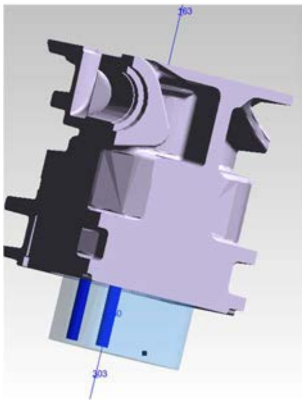

Figure 72- casting surrounding the side core insert

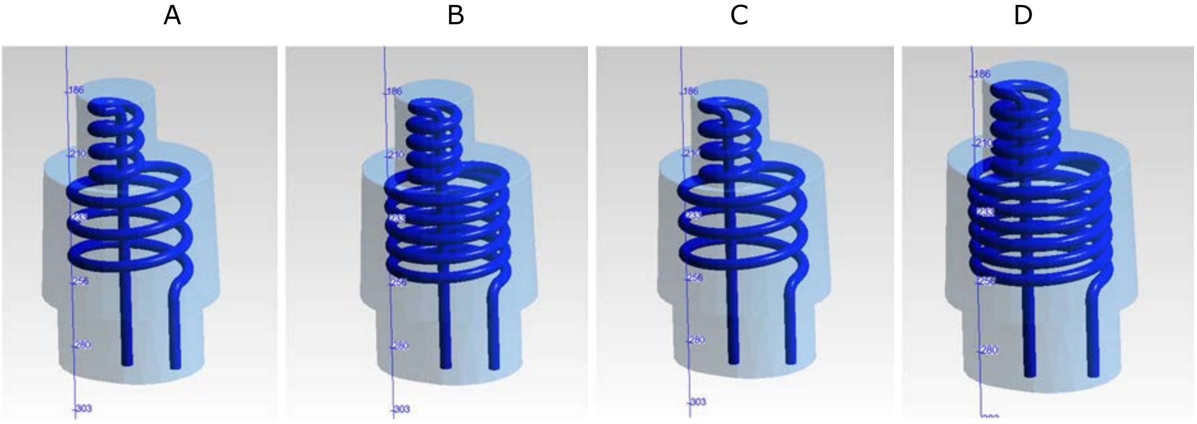

Figure 73- circular cross-section circuits for the side core insert

Additional four designs were built for the side core insert to exploit the power of the freedom of shape resulting from L-PBF manufacturing process. All the four designs present four passes on the minor helix, and 5 on the bottom one. One design has a drop cross-section and is actually the adapted design to be self-supporting in case of holes-channels that may appear in designs with circular cross-section not always perpendicular to the building direction (especially when it comes to be parallel). Even though in literature, as already mentioned, channels in H13 tool steel were built without part fail up to 10 mm, the drop-shaped cross-section may give to the channel surface less roughness. Other two designs were built with respectively with a square and a rhombus cross-section, meant to be filled with an automatic lattice structure, to enhance

the turbulence of the cooling medium. The last design was thought to maximize the surface of heat exchange with a rotating ellipsoidal cross-section.
In the following set of images (A: drop-shaped cross-section, B: square cross-section, C: rhombus cross-section and D: rotating ellipsoidal cross-section) of figure 74 the designs above mentioned are shown:

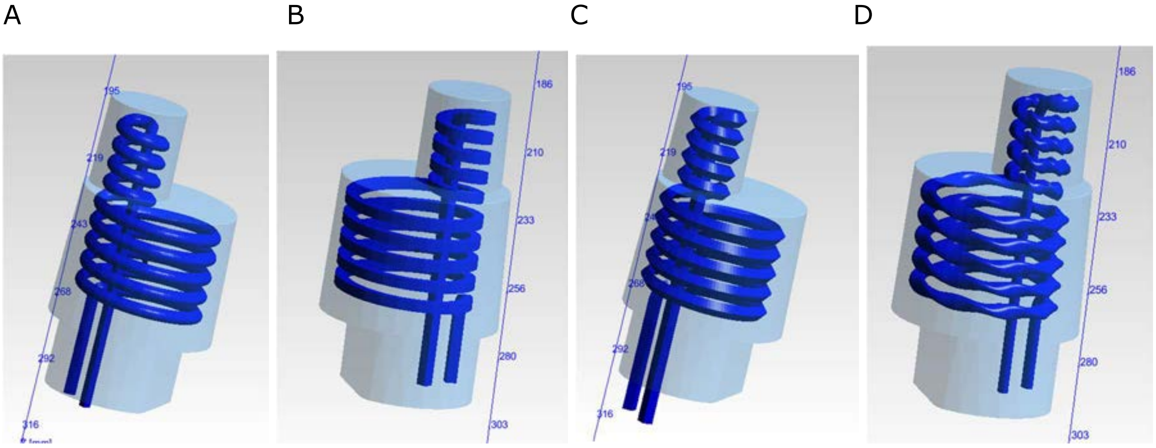

Figure 74- from the left: drop shaped, square, rhombus and rotating ellipsoid cross-section circuits for the side co

It’s important to remember that the following analysis were set static, only thermal, hence the fluid dynamics effectivity of the designed circuits is still to be validated, even though, some are studies on circuits of different shapes and/or with inner lattice structure are carried out, as in the Italian national institution of nuclear physics (INFN) for welding electrodes[88].

5.6 HPDC: Simulation and Selection of best alternatives

To evaluate the best alternatives another full factorial DOE was set up based on the created designs. This time four factors were defined, three factors were set as the three circuits designed for ejector and cover die were set to be either active or not, the fourth factor took in account the side core insert, in its eight circuit designs plus the possibility of absence of any cooling circuit there. This series of alternative different geometries was achieved setting a “geometry exchange”, a tool in MAGMAsoft® enabling the generation, in one single project, of a multitude of designs activating a selected set of geometries one at a time. Four objectives have been set to minimize: porosity, porosity on an evaluation area, FS time the sum of the active circuits. Since the parameter evaluating porosity is a dimensionless number, as it is a weighted value (volume of porosity/volume of the casting), to ensure the minimization would act on the most critic zones detected in the early analysis an evaluation area was obtained from the casting including the most critical zones to carry out a porosity evaluation specially there. As a result, not considering the design in which none of the conformal cooling circuits is active, the possible designs are 80. FS time criteria is the criterion evaluating the time at which the filling/feeding of the cavity becomes difficult because of the melted metal solidifying and becoming mushy, as the fraction of already solidified material makes difficult the flow of the still liquid part, it gives an insight on how quickly the injected metal cools down, it's linled to the solidification time. After the simulation have run it showed interesting results, the general situation is represented in the scatter chart in figure 75. On the vertical axis of the chart "cool number" represents the sum of active circuits, which varies from 1 to 4, while on the horizontal axis the values for weighted porosity in the evaluation area are reported. The symbols ◇ indicate actually often more than a design, as the results appeared to be nearly equal for many designs, the majority of the designs reports to having a value of weighted porosity in the range of 0.07-0.08.

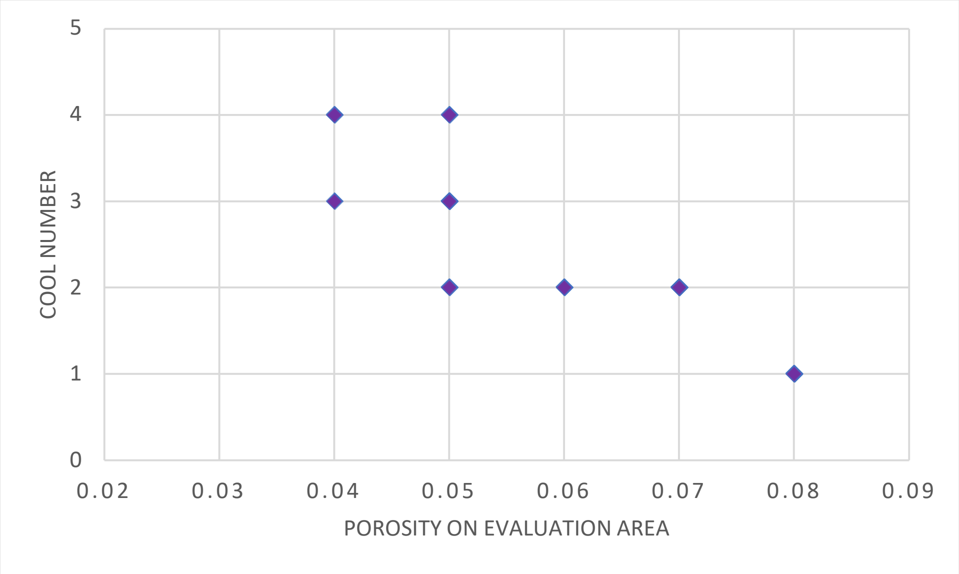

Figure 75- scatter chart: porosity/number of active circuits

Another interesting insight is given by the scatter chart evaluating FS time and Porosity reduction, respectively on y-axis and x-axis, the range of variation for porosity reduction is not wide, but the difference is sensible in terms of FS time especially passing from a weighted value of porosity of 0.06 to 0.07, as reported in figure 76:

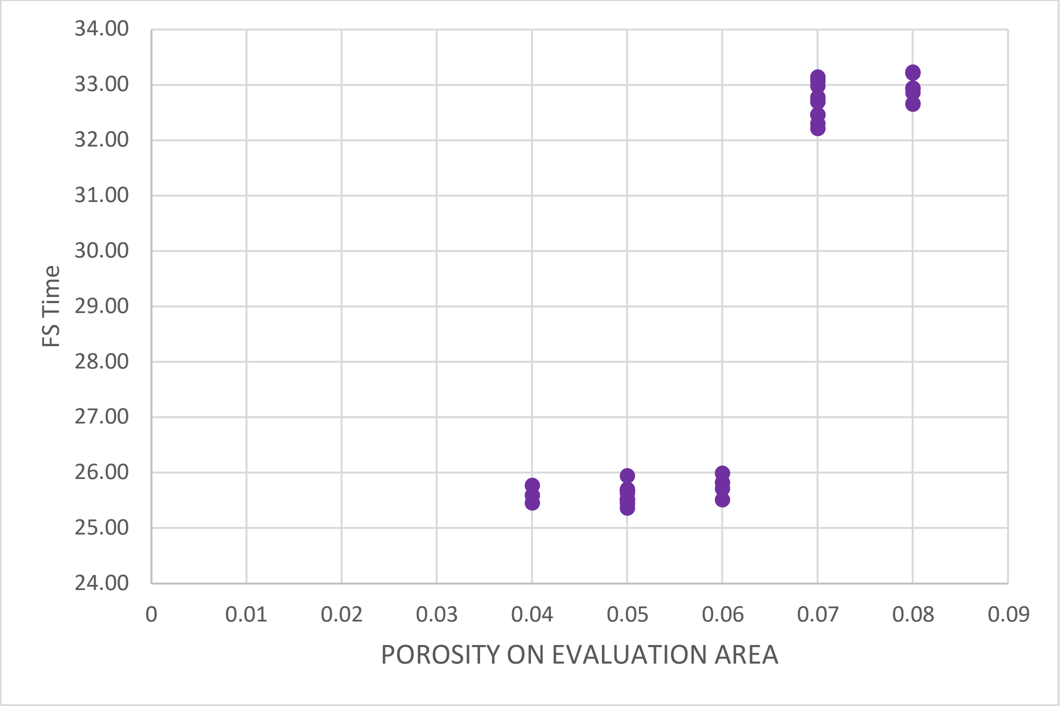

Figure 76- scatter chart: Porosity/FS Time

An interesting thing to note is that porosity values between the choice of four and three active circuits are almost the same and since the aim is to maximize the cost effectiveness, producing four inserts when nearly the same result can be achieved with three inserts, is not justified. Therefore, the designs implying four conformal cooling circuits were less considered in the analysis. On the other hand, while one circuit designs present the minor influence on reducing porosity, interesting alternatives may be found among the designs with two and three conformal cooling circuits.

MAGMAsoft® assessment ambient offers, in addition to the ranking of the designs involved in projects such as DOE and/optimizations, a variety of charts and diagrams for the evaluation of the output data. For instance, a three-dimensional scatter chart considering FS time vs porosity and plus the cool number represents by the size of the area of the indicators the sum of active circuits, as can be noted in figure 77 below:

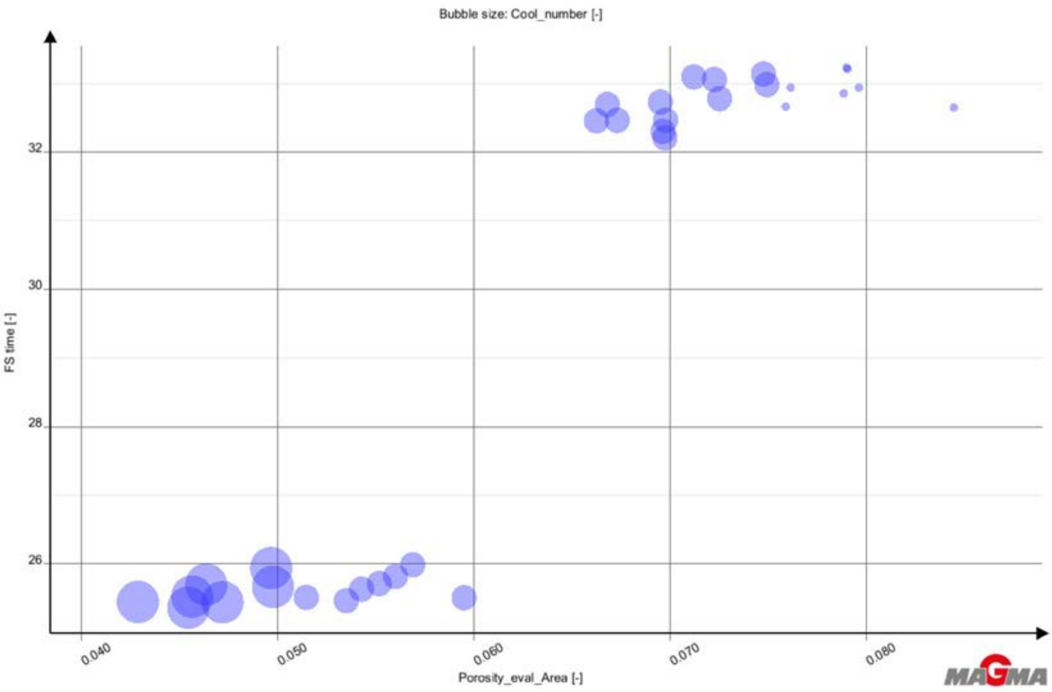

Figure 77- scatter chart: Porosity/FS Time/number of active circuits

The indicators are circles, the smallest represent the one active circuit and consequently growing with size they represent an increasing number of active circuits. As the biggest indicators can be found in the left bottom corner, it’s visually clear how three and four circuits are the best solution in term of part quality, while all the smallest indicators on the right up corner show how the beneficial impact of one circuit is much lesser.

To investigate the correlation between circuit activations and different geometries in the side core insert, a correlation matrix was generated, as to be seen in figure 78:

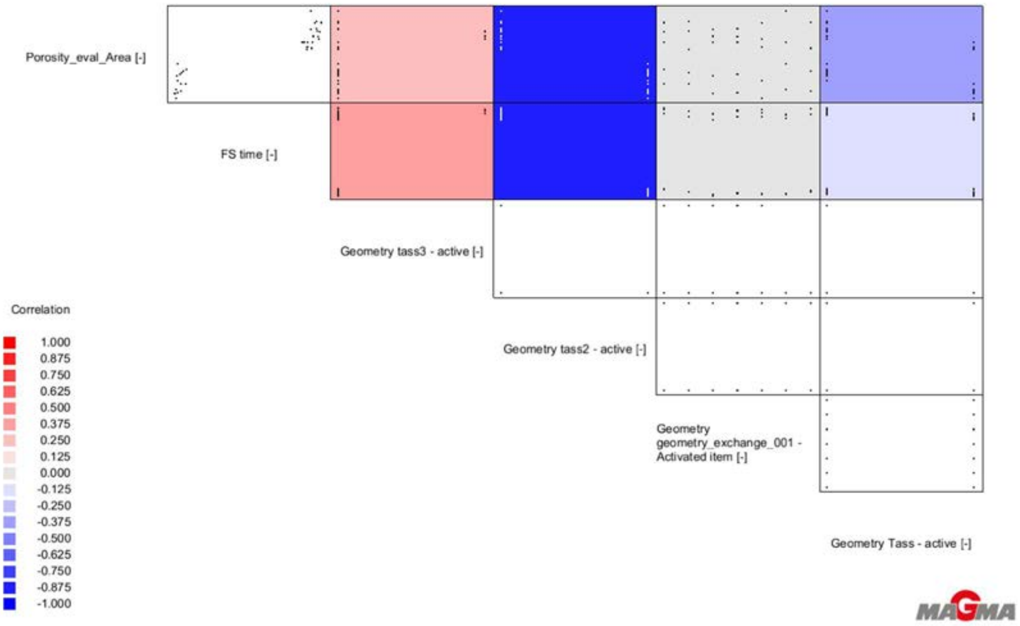

Figure 78- correlation map

Respectively the blue and the red areas indicate negative and positive correlation, in this case a negative correlation is to be considered beneficial since the objectives are to be minimized.

The matrix must be read selecting a variable from the bottom, crossing the row of an objective, the cell color gives the type of correlation, and the intensity of the color may give an idea of the strength of the relationship. It's interesting to note how the geometry exchange, does not show a correlation with the objectives, while different correlations appear for the activation of different circuits. The activation of "tass2" as one of the ejector die circuits (the one shown in figure 70) was called in the geometry ID definition of the project, results to have the most positive influence on both the objectives of minimizing porosity and FS time. "tass 3", which is the other ejector die conformal cooling circuit, activation shows also a positive effect, even though milder. "Tass", which is the circuit on the cover die insert, activation on the other hand demonstrates a negative effect, therefore it may be generally beneficial choosing an alternative without that circuit and insert, focusing on the other inserts. On the other hand looking at the values of the correlation, the positive correlation is ≈0.2, this means it's a weak correlation, and is not that influential on the results, as it will be noted in the following considerations about specific designs.

A useful tool to visualize and select alternatives is the parallel coordinates diagram, inside the assessment ambient of MAGMAsoft®, moving up and down the red triangular indicators to respectively include or exclude values assigned to the vertical axis, which in this case, figure 79, are three: cool number, FS time and porosity.

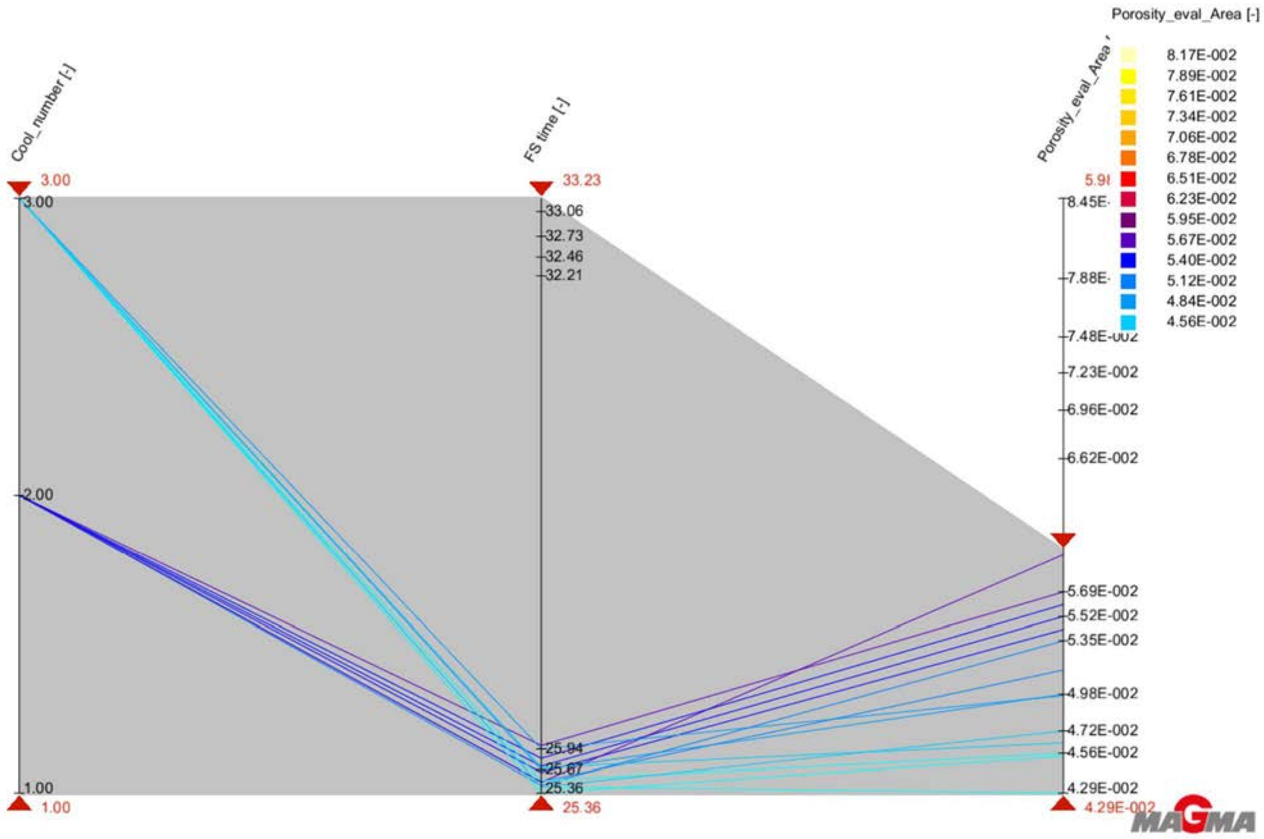

Figure 79- parallel coordinates diagram

In this parallel diagram reported (figure 79) the values for the weighted porosity greater than 0.057 have been excluded, this has excluded all the designs exceeding this value, as a matter of fact all the deigns characterized by one active circuit.

To have a deeper insight of the results, some single relevant designs were chosen to be analyzed through a separate simulation. This choice was necessary, since for the DOE the choice of results investigated and saved was limited to maintain a medium computational effort and time. From the DOE ranking, the first design chosen to be furtherly investigated, was the first place taking design, as we may call it by the DOE numbering of the alternatives, design 21. The results of the simulation show considerable improvement in comparison with the conventional design. Design 21 is characterized by the presence of two functioning conformal cooling circuits, the rotating ellipsoidal one in the side core insert and the cover die insert one. It is important to note that design 21 is not the absolute optimum, meaning that is not the best alternative for every objective, because the research was set to find the optimum compromise, unifying the best part quality and die life criteria detected with also the minimization of the number of L-PBF produce inserts, in order to minimize the costs, which are for AM tooling generally higher that for conventional tooling. Other two designs were selected to carry out a whole simulation, one chosen from the best values for the objectives, the minimum porosity is to be found in the designs with four circuits, therefore the best of the four circuits, named design 40 in the DOE was chosen along with one of the worst resulting alternatives, with only one circuit active named as design 33 in the DOE design generations. In the following figures the criteria for evaluation and comparison of the results are presented in a view split in four, containing all the up cited designs for a higher visual impression of the differences in the results along the DOE sample.

In the left upper corner, it is to be found the conventional design, on its right side there is design 21, while on the bottom on the left there is design 40 and on the right design 33. This disposition has been maintained for all the figures for a higher ease of comparison (from figure 80 to figure 83).

Evaluating the porosity criteria shows that the better results are obtained by the four active circuit option, which makes disappear one of the detected porosities (the so-called porosity 1) as it can be seen in left bottom corner of figure 80. Design 21 (which is also highlighted with a red boarder) by the way shows a reduction for porosity 1 around 50%, the “worst” design simulation, design 33, shows improvement in comparison with the conventional design, but obvious lesser significant output than the design 21 and 40.

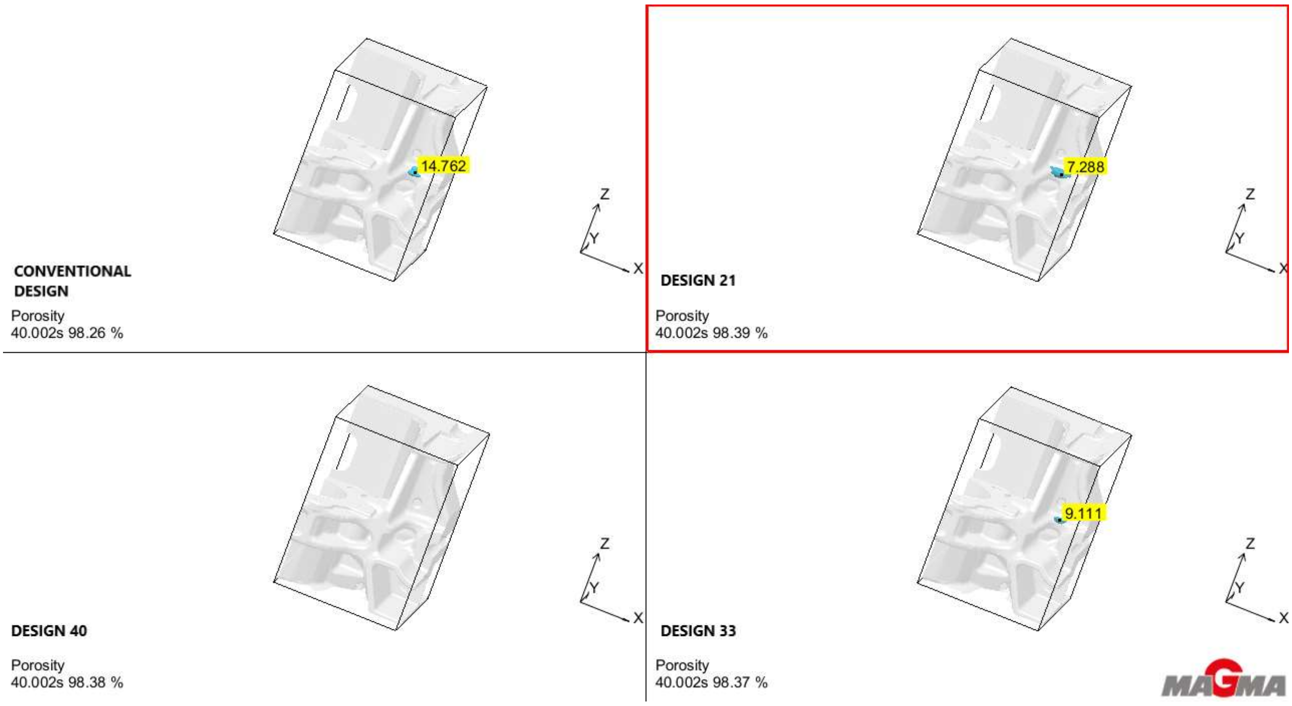

Figure 80- Porosity 1

In figure 81 the comparison for the porosity in proximity of the squeeze and porosity 2 is reported, in this case the improvement of the best DOE design(21) and the four circuit alternative are closer to each other, while for the squeeze porosity in the result of design 33 the value is even worsened, underlying the little appeal of that alternative.

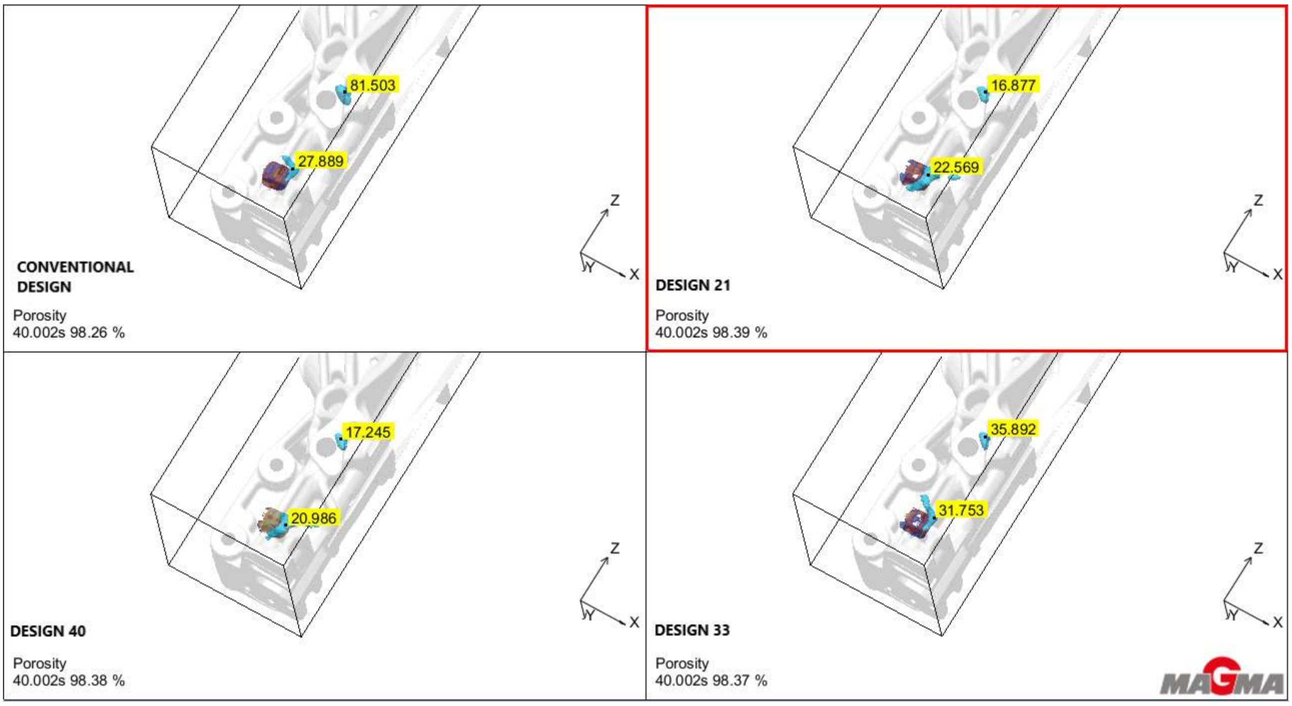

Figure 81- Squeeze porosity and porosity 2

The hot spot risk was reduced as can be seen in the figure 82 the colour of the critical volumes are darker for design 21, 40 and 33 in comparison with the conventional design, that means they are solidifying faster than in the conventional design, so there is less risk of hot isolated zones which may be responsible in defect formation, on the evaluated time scale equal to ejection time, this is also linked to faster solidification time;

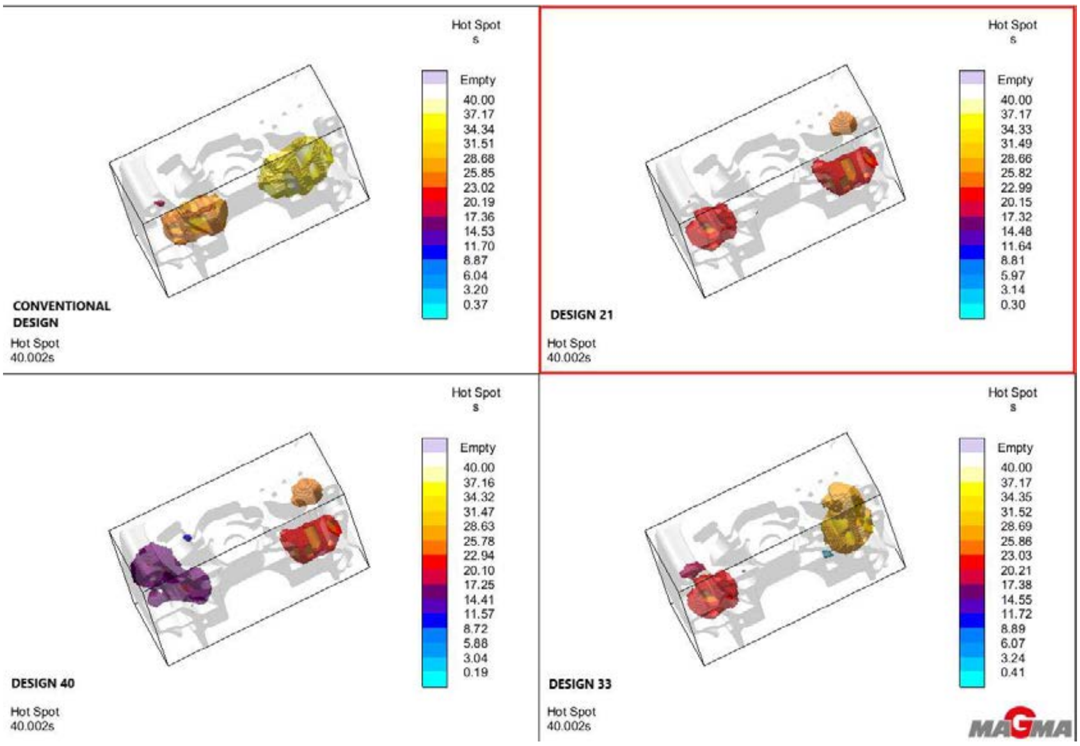

Figure 82-hotspot

The most graphically appreciable result of the simulation is by the way, to be seen in the die soldering on die result, in the following images the same samples of cover die, side core and ejector die are respectively reported (images 83, 84 and 85).

The direct comparison with the conventional design shows the benefits of conformal cooling application, the samples of the dies where cut in correspondence with the inserts but it is to be also noted that the conformal cooling presence beneficially affects also the rest of the surfaces in contact with the melt.

Specifically considerating figure 83, the cover die sample, results almost freed from die soldering risk in design 40, as in that alternative the cover die conformal cooling circuit is active, but also in design 21 and 33 active not in this location conformal cooling circuits, still convey beneficial effects on the criterion:

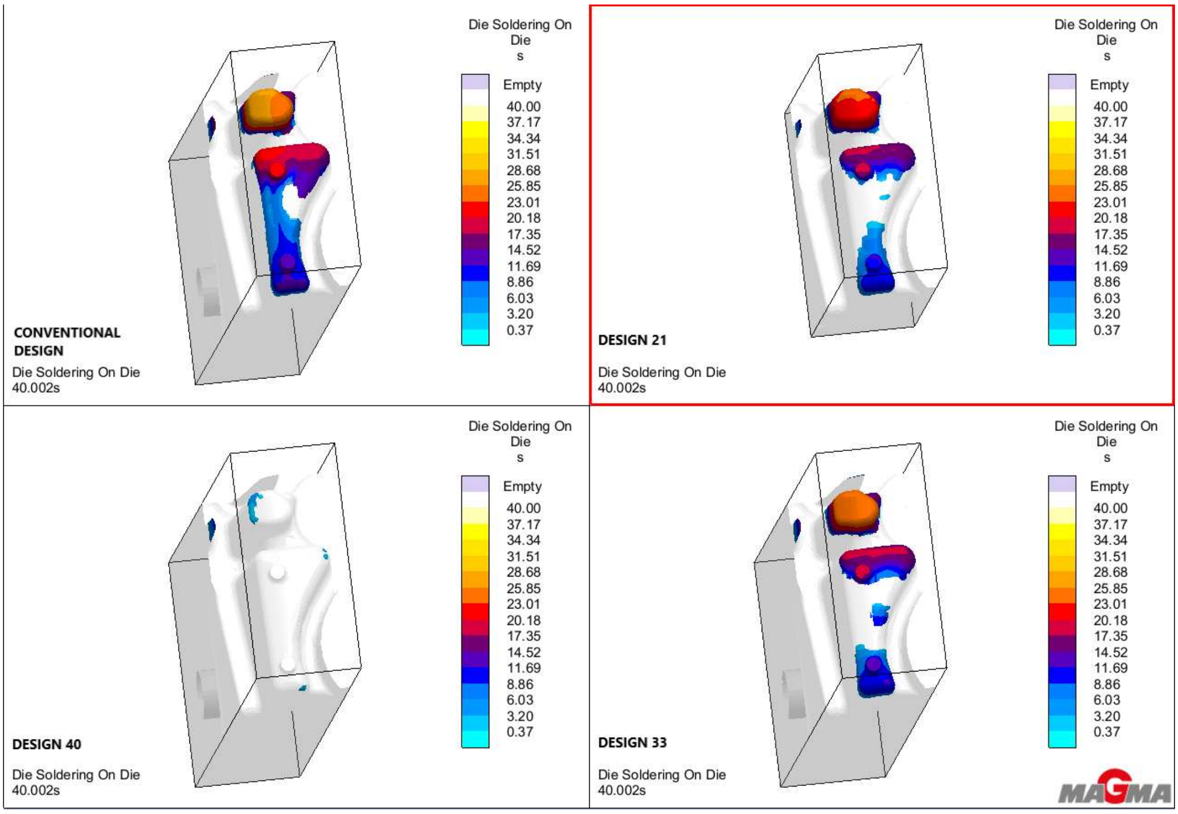

Figure 83- die soldering on cover die

Considering figure 84, all the design evaluated had an active conformal cooling circuit in the side core, and it brings to absence of die soldering risk:

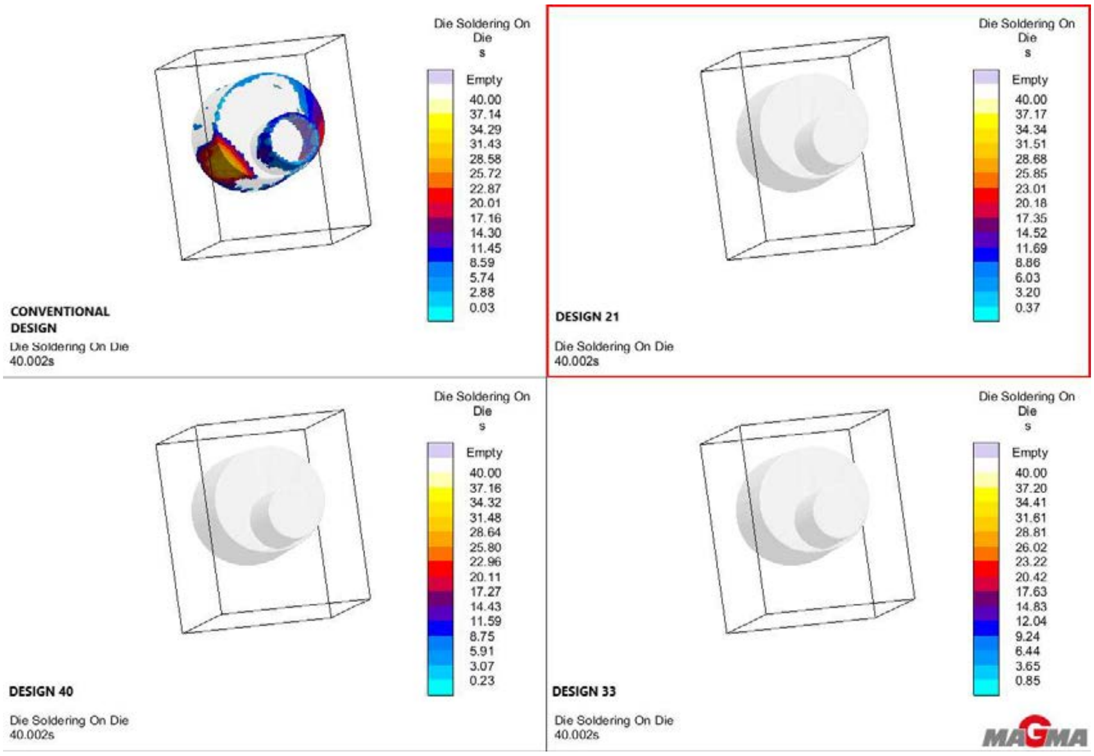

Figure 84- die soldering on side core

While in figure 85, in the nearby of one of the two inserts obtained by the ejector die, was actually the most critical area detected in the conventional design, design 21 and 33, as they have activated the corresponding conformal cooling circuit show that its presence is resolutive. On the right bottom corner, design 33 shows little improvement, but still a betterment in comparison with the conventional design:

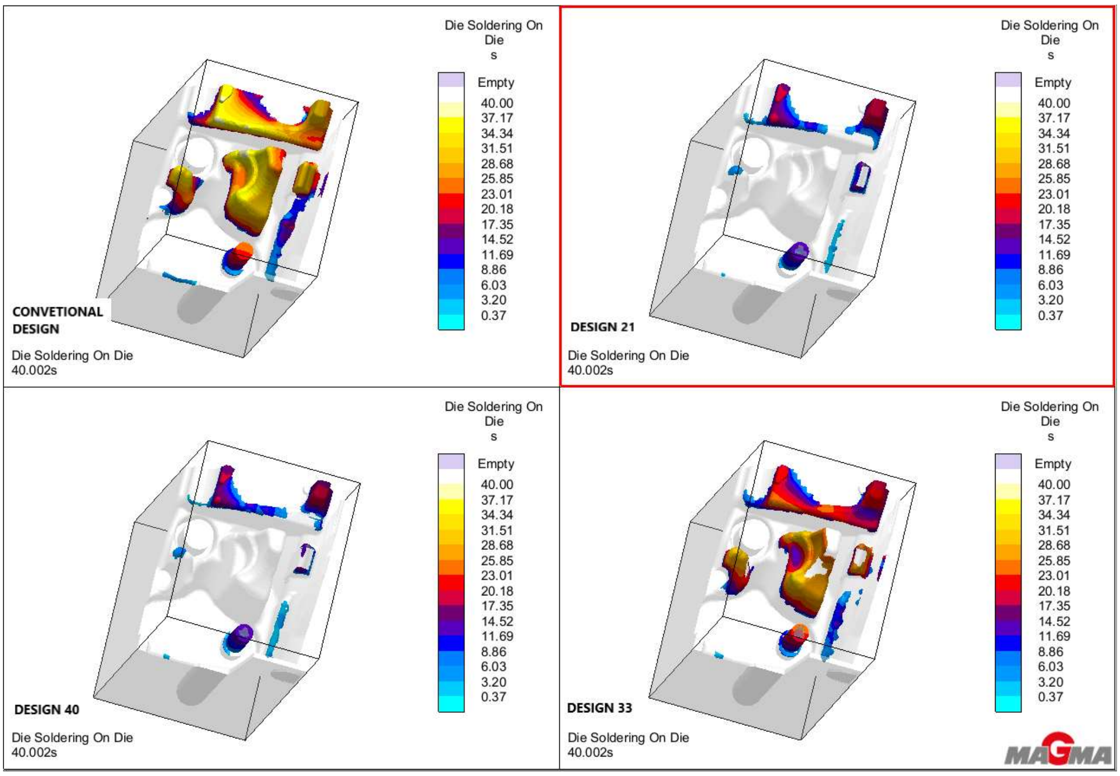

Figure 85- die soldering on ejector die

The temperature fields of the two moments chosen as representative, die opening and end of spraying phase, are reported for the four alternatives in figure 86 and 87.

It appears immediately clear the difference with different designs, at the die opening figure 86, all the free innovative designs show that the three samples points report a temperature knocked down of much more than 50% in comparison to the conventional designs.

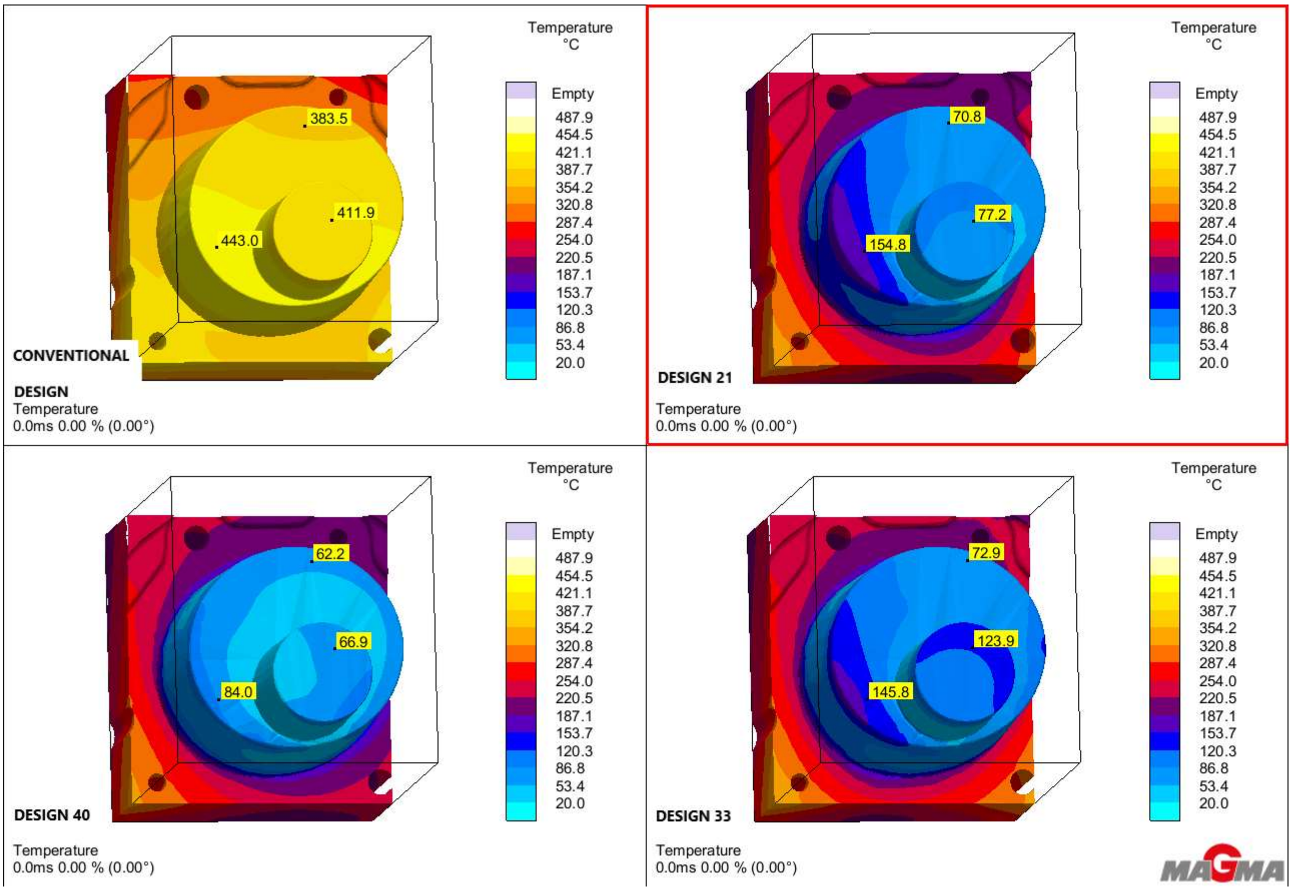

Figure 86- Temperature field on side core insert at die opening phase

The temperature at the end of spraying phase, figure 87, also shows a huge knocking down comparing the conformal cooling designs, to the conventional one, but another improvement can be seen in the color changing along the side insert in the conventional design, pointing out a non-homogenous temperature along the insert, while the three new designs, thanks to the conformal cooling circuit inside of the side core present basically one color on the surface on the insert, meaning the temperature variation along the surface presents much less variance. Homogenous surface temperature can only improve the insert life, this because, the most a body absorbs heat measuring a rising homogenous temperature, the most the body dilatates or contracts itself in an isotropic way, preventing material stress, strains and ultimately damage, if the thermal loads are cycles.

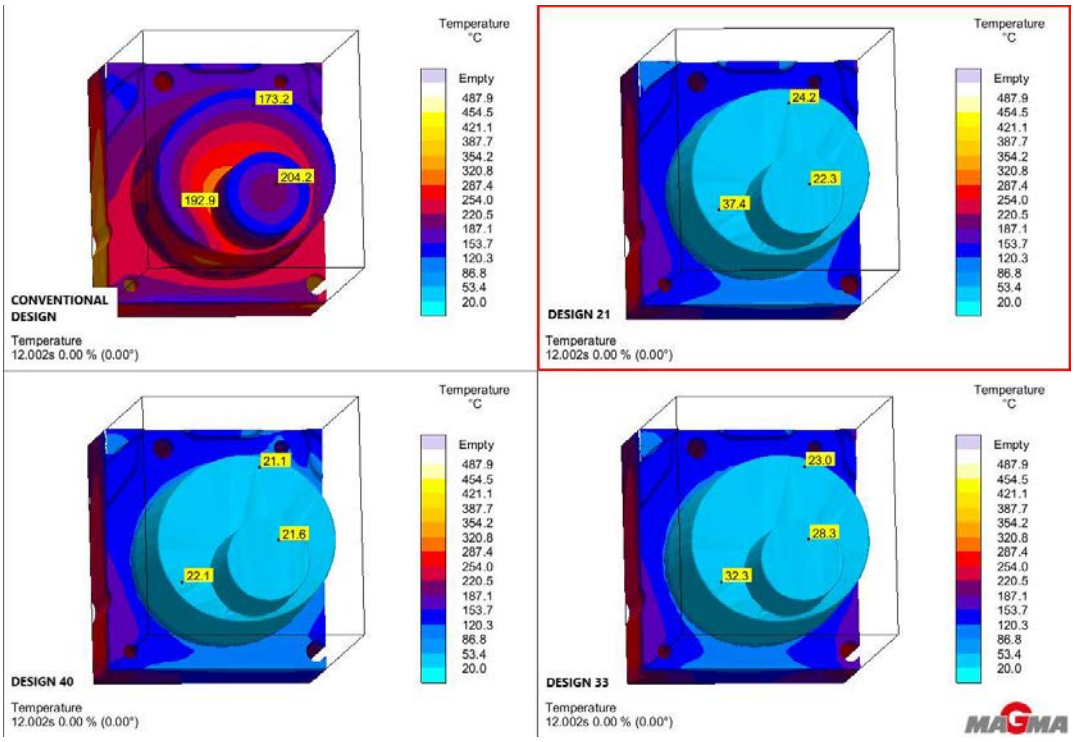

Figure 87- Temperature field on side core insert at the end of sprayting phase

The side core insert life was furtherly investigated with two supplementary simulations, which have been set to evaluate specifically the insert life in terms of productive cycles assessing thermal fatigue linked to the thermal loads extracted from the previous simulations. The first of these last two simulations has been set on the conventional design, the second on design 21, the results are reported in figure 88 respectively A and B. The conventional side core die insert shows a sensibly lower life duration the light blue areas report in fact a die life estimation of 200 cycles, while looking at the side core insert of design 21 the areas with shortest life predict a duration of 8 million of cycles and the main areas go up to 16 million of cycles, suggesting a high cost saving on the side of die maintenance and replacement. It is important to be noted that

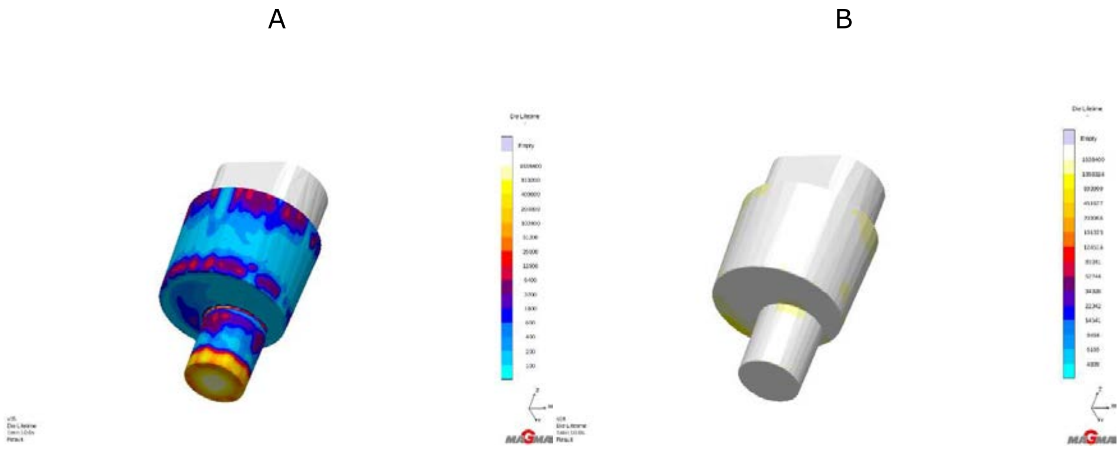

Figure 88- A: conventional insert die life *B:design 21 insert die life*

Least, but not last, solidification time has been investigated to access the possibility of a cycle time reduction. A sample of the casting is presented in figure 89 for the four designs analysis, the range of the criterion was set show the minimum and maximum solidification time resulting from the simulation. The scales show that a decrease of cycle time would be definitely possible, rising the production rate. The conventional design shows that the last part to reach solidification of the casting starts the solidification at 40 seconds, and for this reason the die opening happens to be scheduled right around that time. Conformal cooling designs show a sensible diminution of the maximum solidification time, design 21 and 40 show close values, a decrement around 35% from the stating solidification time of 40 s. Design 33 shows a minor improvement, a decrease around 15% in comparison to the conventional design, still representing a littler progress.

The visual difference has been presented with three significant designs, the extreme of the created sample and the winning of a multi-objectives analysis, hand-in-hand with the figures some tables created with the data extracted during the result screening above is necessary to have a more quantifiable understanding on the differences among the simulated designs.

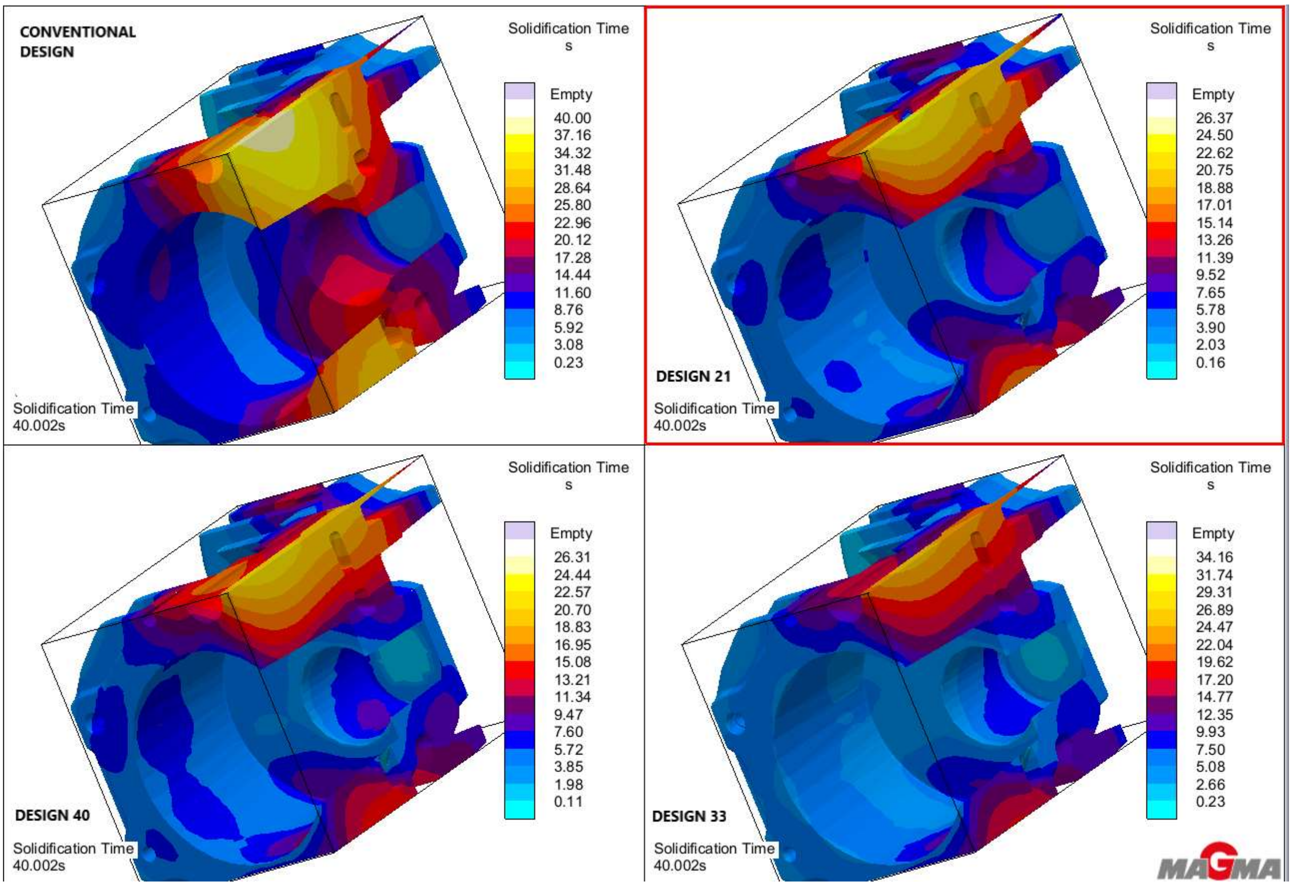

Figure 89- solidification time

The percentage variations of the results for porosity detection of the four designs (conventional, 21,40 and 33) are reported in the table 4, where porosity 1, is the volume detected on the opposite side of the location of the squeeze, while the squeeze porosity refers to the volume detected in the proximity of the squeeze and porosity 2 is the volume detected on the same side of the squeeze.

Table 4- porosity comparison between conventional and innovative designs

design	porosity 1	porosity 2	squeeze porosity	Δporosity1%	Δporosity2%	Δporositysqueeze%
conventional design	14,762.00	81,503.00	27,899.00	0.00	0.00	0.00
design 21	7,288.00	16,877.00	22,569.00	50.63%	79.29%	19.10%
design 40	0.00	17,245.00	20,986.00	100.00%	78.84%	24.78%
design 33	9,514.00	36,658.00	37,261.00	35.55%	55.02%	-33.56%

The range of reduction is reported in percentage in comparison to the conventional design, the highest levels of reduction are highlighted in green, while in design 33 can be noted, despite the reduction of the first two values of porosity, the squeeze porosity is worsened by 33.56%.

Another important achievement refers to the ΔT during the production cycles, which decreases of much more than 50% considering the surface on the side core insert, the temperature values were measured on three sample points (pick 1, pick 2, pick 3) at two moments of the cycle which can be considered representative of the maximum and minimum temperature. Respectively for the maximum temperature the reference moment can be the opening of the dies, and for the minimum the end of the spraying phase.

Table 5 summarizes the resulting temperature and ΔT, for the conventional design on the first row and under it design 21,33 and 40. On the left side the values detected are reported for the three points at the two chosen moment, on the right in the upper part of the table for each point the temperature variance among the two different in time measurements of the same picked point, while on the right bottom of the table, the difference of ΔT between conventional and new designs is reported in percentage, all these values are close to a difference of 80%, exception design 33, which on two points present a variance close to 50%.

Table 5- ΔT during at stable regime

	T at die opening °C			T at end of spraying °C			ΔT pick 1	ΔT pick 2	ΔT pick 3
design	pick 1	pick 2	pick 3	pick 1	pick 2	pick 3			
conventional	383.5	443	412	173	192.9	204.2	210.3	250.1	207.7
design 21	70.8	54.8	77.2	24	37.4	22.3	46.6	17.4	54.9
design 40	62.2	84	66.9	21	22.1	21.6	41.1	61.9	45.3
design 33	72.9	146	124	23	32.3	28.3	49.9	113.5	95.6
comparison % 1							77.84%	93.04%	73.57%
comparison % 2							80.46%	75.25%	78.19%
comparison % 3							76.27%	54.62%	53.97%

Solidification times are reported in table 6, also in this case the reduction, and therefore the improvement towards a more productive process, is represented by percentage difference with the conventional design, on the left part of the table, while on the right the cycle time is reported adjusted to the new solidification time measured, also equipped with percentage quantification in comparison to the conventional cycle time. Solidification time reduction give much more sensible results in PIM where it is the main part (ca 60/80%) of the cycle time, considering HPDC process the influence on the cycle time of the solidification time is smaller, but still reducing it means rise the process productiveness, in this case considering the conventional design the solidification time is around 52 % of the cycle time, the new designs enable a reduction of the cycle time from 5% to 16% how is presented in the fifth column of table 6:

Table 6- Solidification time and cycle time reduction

design	Solidification time (s)	$\Delta t_{solidification}$ %	cycle time (s)	Δ cycle time %	Q (parts/h)	Productivity rise %
conventional	40	0	85	0	42	0.00%
design 21	26.37	34.08%	71	16.47%	51	19.72%
design 40	26.31	34.23%	71	16.47%	51	19.72%
design 33	34.16	14.60%	80	5.88%	45	6.25%

On the right side of the table (three columns on the right) consideration on productivity per hour (parts/h) of the HPDC process is carried out considering the different possibilities for cycle time reduction, it was simply considered the smallest integer near to one hour of work (3600 s) divided by the cycle time. This productivity estimation, as it was called in table 6, Q shows an increment of nearly 20% for design 21 and 40, while design 33 shows less than a half of this improvement (near 6%).

It’s obvious, eventually, that a higher number of conformal cooling circuits enables to get the best part quality and surely extends the life of the die, because an optimized thermoregulation would give the best results. On the other hand the costs linked to have multiple L-PBF produced inserts, which are specific for the production of that exact casting they are designed for, not only could, but would, probably, rise the tooling costs to a level that would end up making the application of L-PBF manufactured inserts in HPDC process not cost-effective.

5.7 AM: Inserts manufacturability and compensation assessment

For evaluation of manufacturability through L-PBF process of the inserts designed as the designs proposed are in total a number of 11 different geometries one relevant alternative was selected to be simulated. As already mentioned, the simulation of AM process will remain on a macroscopic scale. Therefore the choice was between a thermo-mechanical coupled analysis and an Inherent Strain (IS) analysis, the first one results of a higher computational effort since it requires two analysis, thermal and mechanical, which can be coupled in the resolution of each layer or staggered in a subsequent way, as firstly the thermal analysis is carried out for the printing of the whole part, and then, the results, as thermal loads, are input for the mechanical analysis. The second option, IS analysis, is a leaner alternative as it does not comprise a thermal analysis but is based on the strains evaluation, leading to assessment mainly of deformations and in second place residual stresses and strains the reliability of these results is strongly affected by the choice of the elements type for the analysis. In fact, using for instance cartesian elements, which will be furtherly described in the following paragraphs, leads to a stair effect of the model surface leading to less reliable for instance stress results on the edges of the elements. Deformations are by the way an important factor to assess if a compensation is needed in order to achieve the geometry required. For having the possibility of running a bigger number of simulations the IS analysis was preferred for this case study. Considering the three insert to be placed in the cover and ejector, despite the different geometries both in the path and in the insert shape, these conformal cooling circuits have all the same cross-section (circular with 2 mm diameter) and have some similarities, all the inserts are characterized by an irregular shape, with spines of small thickness at the top, length of the channels are also similar. Since the AM manufacturability with H13 tool steel for circular cross-section channels from 1.5 mm up to 8 mm diameter has been proved experimentally by Mazur et al. [15] none of these three inserts has been selected for simulation. Obviously in a real case application the simulations of the all the exploited inserts should be carried out. Considering on the other hand the 8 different geometries proposed for the side core insert, it has been chosen to simulate one alternative, the rotating ellipsoidal circuit, which was one of the circuits in the optimum alternative from the DOE results. The AM as fabricated inserts results joined to the base plate and have to be removed therefore a machining allowance has to be considered for the cutting operation, 0.5 mm in case the part is cut off through electrical discharge wire machining while 1 mm in case of a rotary saw choice. Machining allowance is to be considered also in case of specific requirements on the surface finishing to be obtained through for instance a milling or other process. In this study the machining allowance will be considered only for the cutting step, which is common to all metal 3D printed parts.

The simulations have been carried out through Ansys® Workbench, setting a mechanical analysis for the Inherent strain analysis.

For reliable IS analysis results a calibration is necessary as it was already mentioned in the theoretical presentation of the IS method in paragraph 5.1.5b. The calibration may be developed in two ways:

- Reduced Order Methods
- Empirical Methods

[78]

To follow a completely computational approach, fully predictive method, the choice is the first methodology, but it implies a complete knowledge of the material properties, which is not always possible considering powder alloys. Furtherly, the methodology to map strains from a local (microscopic) level to the global part (macroscopic) level is still not clearly established. An empirical method is easier to implement in case of not well characterized material, but it requires many experimental trials to populate a database of strains. Therefore, a mixed approach is presented in the following paragraph (6.7.2).

5.7.1 Material implementation and process parameters

The material to be used in HPDC application are hot-work steels, in this case H13 or 1.2344, X40CrMoV5-1, as it is named respectively in America and Europe, has been considered. Since this chromium stainless steel is fabricated for being exploited in high temperature, its processing through PBF processes has been assessed in some studies such as [89], [16], [15] and [90]. The material database still does not comprehend a big variety of metallic powders for AM process simulation. But there is the possibility to copy and customize the present materials, therefore temperature dependent mechanical properties were entered into the database, even though carrying out an IS analysis do not take in account temperature variance, these properties result necessary in case of a coupled thermo-mechanical approach. Since the macroscopic nature of the analysis carried out, the properties have been considered the same of the as-built material. An important consideration has been considering isotropic hardening as a bilinear stress/strain function, because the first choice, which was a multilinear function, lead to simulation instability and fail. The implemented material holistic view in the engineering data ambient is reported below in figure 90:

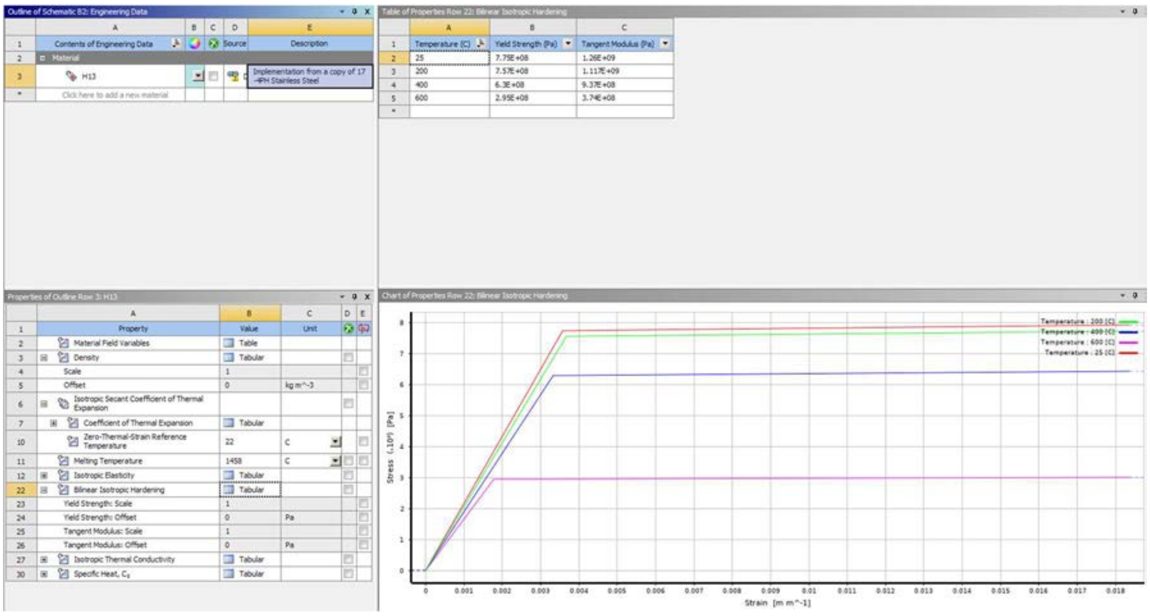

Outline of Schematic B2: Engineering Data

	A	B	C	D	E
1	Contents of Engineering Data			Source	Description
2	Material				
3	H13		☐		Implementation from a copy of 17 -4PH Stainless Steel
*	Click here to add a new material				

Table of Properties Row 22: Bilinear Isotropic Hardening

	A	B	C
1	Temperature (C)	Yield Strength (Pa)	Tangent Modulus (Pa)
2	25	7.75E+08	1.26E+09
3	200	7.57E+08	1.117E+09
4	400	6.3E+08	9.37E+08
5	600	2.95E+08	3.74E+08
*			

Properties of Outline Row 3: H13

	A	B	C	D	E
1	Property	Value	Unit		
2	Material Field Variables	Table			
3	Density	Tabular		☐	
4	Scale	1			☐
5	Offset	0	kg m^-3		☐
6	Isotropic Secant Coefficient of Thermal Expansion			☐	
7	Coefficient of Thermal Expansion	Tabular			
10	Zero-Thermal-Strain Reference Temperature	22	C		☐
11	Melting Temperature	1458	C	☐	☐
12	Isotropic Elasticity	Tabular		☐	
22	Bilinear Isotropic Hardening	Tabular		☐	
23	Yield Strength: Scale	1			☐
24	Yield Strength: Offset	0	Pa		☐
25	Tangent Modulus: Scale	1			☐
26	Tangent Modulus: Offset	0	Pa		☐
27	Isotropic Thermal Conductivity	Tabular		☐	
30	Specific Heat, C_p	Tabular		☐	

Chart of Properties Row 22: Bilinear Isotropic Hardening

Figure 90 – material properties as shown in the engineering data section in Ansys Workbench

The list of material properties for the H13 tool steel are diagrammed in the left corner of the image 89, the most relevant properties in this case will be elasticity and plasticity, since the choice of exploiting IS analysis.

For this study the process parameters selected are the optimum parameters assessed in Mazur et. Al. work [15] for H13 tool steel, more precisely the laser energy density selected is of 80 J/mm^3, the laser power is of 175 W, the scan speed 607.64 mm/s. These parameters lead to a part density of 99.87% achieving the best compromise between porosity minimization and maximum respect of dimensionality.

5.7.2 Calibration for IS analysis

Calibration procedure was not carried out in this study, but in this paragraph the general methodology is presented.

Calibration goal is to determine Strain Scaling Factor (SSF) and the Anisotropic Strain Coefficients (ASCs), which are necessary to rise the reliability of the results, as they are linked to specific material considered, to the chosen printing machine, to the process parameters and stress mode considered (linear elastic or J_2 plasticity). SSF is a scaling multiplier for the yield strain its default value is 1, the ASCs on the other hand consider the high anisotropy affecting AM produced parts, it's a total of three coefficients taking in account respectively the anisotropy along parallel direction, orthogonal direction and at a 45° angle to the longitudinal scan direction. ASCs default values are in order 1.5, 0.5 and 1.

Since the strong link to the type of material, machine and machine parameters, changing or altering one of these parameters lead to the necessity of a re-calibration. Even changing a material supplier may imply the need of a new calibration.

The procedure presented consists of building parts, taking measurements, running simulations and calculating factors using a spreadsheet, as is represented in figure 91.

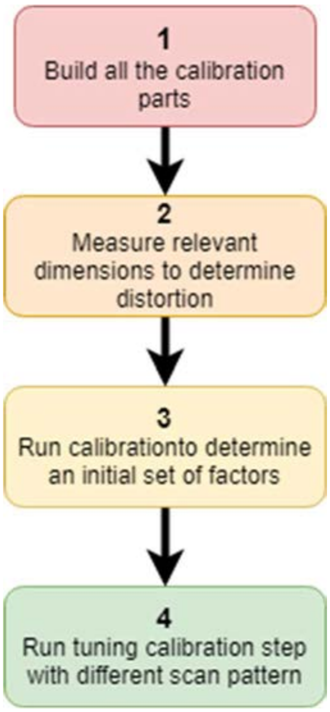

Figure 91- SSF and ASCs calibration procedure

The part commonly used for the calibration is the cantilever beam, an example suitable for the application is shown in figure 92.

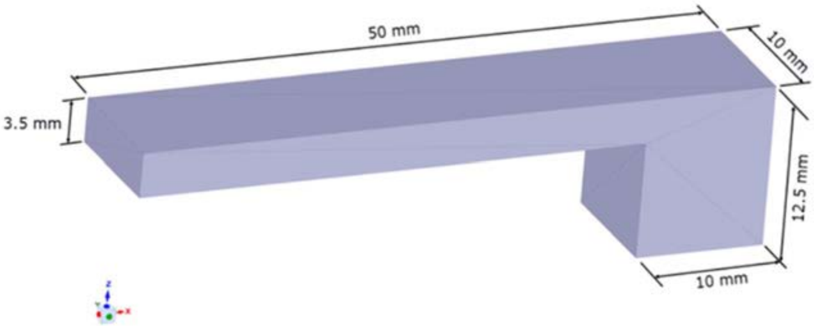

Figure 92-cantilever beam geometry

The cantilever beam needs also a series of supports to sustain the 90° overhanging angle. In figure 93 the geometry is added with supports and the outlined red line highlight the location the supports are cutoff.

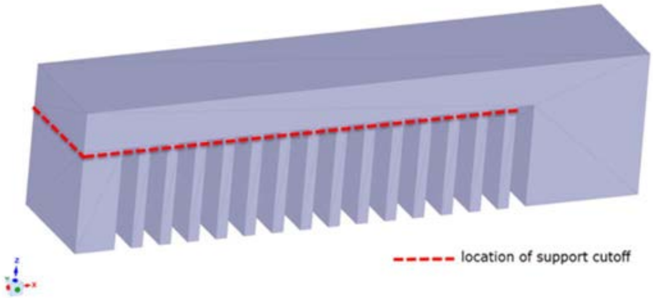

Figure 93- cantilever beam with supports

The process parameters to be used are the ones intended to be used for the building of the real components, with the exception of the scan patterns which are varied in order to obtain the SSF and the ASCs.
For the first step of calibration, building parts, three scan patterns are selected, two scan patterns selected may have orthogonal laser passes, one at 0° starting angle in respect to the longest dimension of the cantilever beam an and the second at 90° respectively, a third at a certain angle (60/70°) of rotation of the first alternative.
When the parts are built is time for the second step, the distortion is measured on the part either before support removal or after, an example of a measurement relevant for assessing the strain is to be found in figure 94.

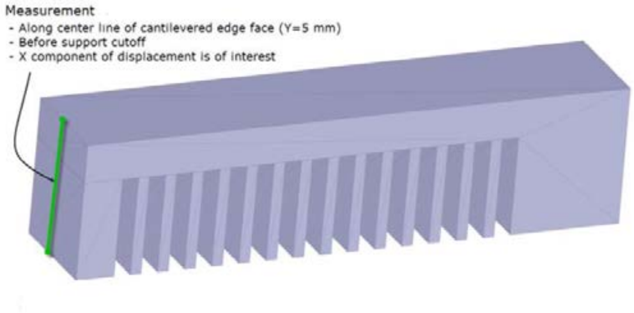

Figure 94- distorsion measurement

Retrieved the strain information, the third step is to run simulations of the three scan patterns starting from the default values of SSF and ASCs which are respectively set to 1, 1.5, 0.5 and 1 in Ansys® Print module for the first two scan patterns, keeping the third scan pattern to achieve a fine tuning of the calibrated results. After the first calibration through simulation the results must be compared to the experimental ones, repeating the simulations with adjustment of SSF and ASCs to achieve a convergence to an acceptable level of error between measured and simulated distortions. [91]

Due to lack of time and resources carrying out a calibration procedure for this study was not possible, hence the IS analysis were run with the default SSF, which is the only data needed for a macroscopic analysis, the ASCs are necessary on mesoscale analysis.

5.7.2 IS analysis

The first set of simulation where set up to assess results convergence with mesh of different sizes. The first group of evaluation was carried out choosing a cartesian mesh, which discretize the part with cubical elements (voxels) and requires a minor computational effort, since they are described by first order linear functions. For the side core insert supports are necessary to prevent a part fail, since the presence of 90° overhanging area, the supports have been created through Space Claim (CAD ambient in Ansys®) through an extrusion of the projection of the overhanging surface, as shown in figure 94.

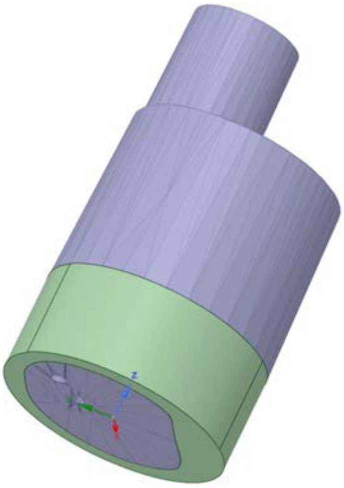

Figure 95 – built part in grey (die insert in grey and supports in green)

In the real AM process the supports would not be a full volume, therefore a penalty factor must be applicated to penalize the material properties which are implemented from the database for the solid material. Considering the base of the supports, the green area in figure 96, they may be realized as beams and thin wall supports, the ratio of the overall volume over the volume of the supports could result around a value of 0.7. The penalty factor is established to consider that the material properties are lessened in comparison to a full solid volume and also that the supports are usually build with less resolution than the part, for instance, as it will be considered in this study, the laser may be applied on the supports not every single layer but every two.

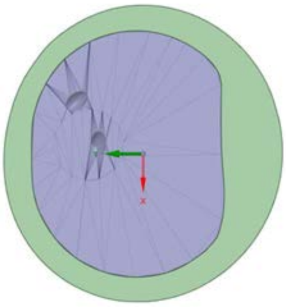

Figure 96 – part and supports surface attached to the base plate

The volume extruded to represent the supports was set to share topology with the insert, as they are in contrast with the base plate the parts to be built by the L-PBF process. To enable this both the insert and the supports have been placed in the same component set, named build. This can be noted in the structure of geometries reported in left upper corner of figure 97 below:

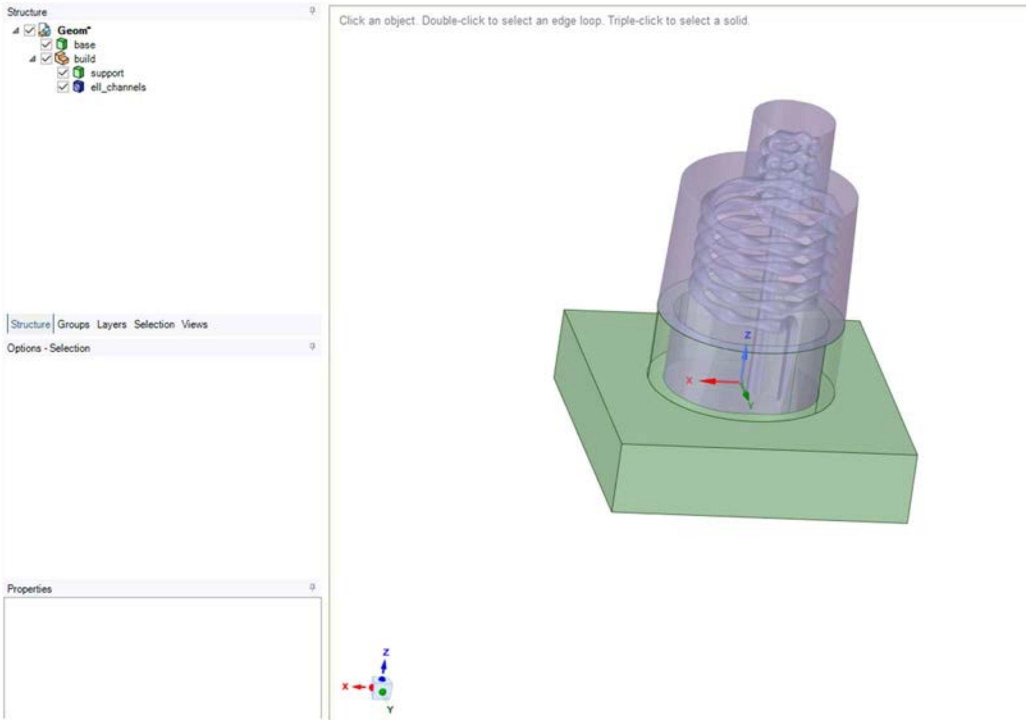

Click an object. Double-click to select an edge loop. Triple-click to select a solid.

Figure 97- geometry of side core insert with rotating ellipsoid circuit with addition of supports and base plate

The workflow for the L-PBF simulations can be resumed as follows in figure 98:

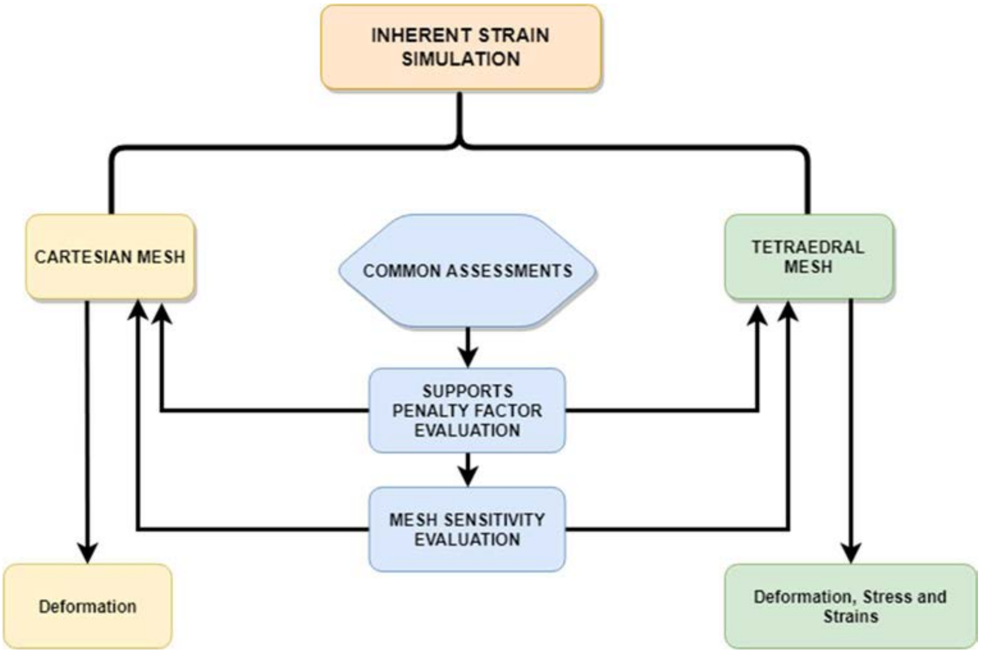

Figure 98- workflow

For this thesis the cartesian mesh has been more deeply explored, for future perspective it would be interesting to study on a same case in depth both of the meshing methods, to assess each strengths and weaknesses.

5.7.2a Mesh considerations

Of the retrievable results when the part is meshed with cartesian elements the total deformation can subsequently be plotted on a tetrahedral mesh of the simulated part, this leading to an evaluation of deformations, stresses and strains. Furtherly, while on the cartesian solved model the results are retrievable at any layer of desire, once the results field is plotted on the tetrahedral meshed build, the insight is confined to the totally built part, without the possibility of evaluation of the evolution of the maximum deformation, for instance, along the layers during the building process. Obviously, there are results such as total equivalent stress or equivalent strain with a smaller reliability in comparison to deformation especially if compared to the one associated with tetrahedral meshed models results, this because the tethraedral mesh is perfectly conformal to the part model surface. In figure 99 a first cartesian mesh with element size 2 mm for part and supports while for the base the mesh was guided by the setting of 5 divisions for the edges parallel to axis z, is presented. This mesh was used in the evaluation of the better value of penalty factor to be applied.

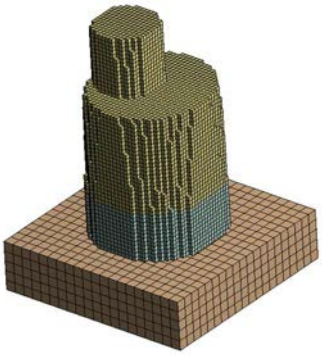

Figure 99- 2 mm cartesian mesh

i. Penalty factor sensitivity analysis

The penalty factor, as aforementioned, knocks down the material properties for taking in account the not completely filled volume and the poorer laser passes. It obviously varies according to the type of supports chosen for sustaining the part build. Supports may be characterized by their ratio volume surface dividing them into two main groups: thick wall and thin wall supports. Thick wall supports may be beams like, they are characterized by a higher ratio of volume/surface, the main purpose of these type of supports is to give structural stability to the build part, with the second effect of enhancing the part heat dissipation. Thin wall, or volume less supports as they commonly are called, have their primary scope in enhancing heat dissipation, which enables a reduction of the deformation, in second place they obviously provide some contribution to structural stability. Different kind of supports may also be copresent, therefore for the establishment of the penalty factor is necessary to investigate the ratio overall volume over the volume of material building the supports. in this case, for the side core insert, the supports main aim is to enable the build of an overhanging surface at an angle of 90°, therefore the supports considered are a mix of beams and volume less supports. In this case a volume ratio of 0.6 can be considered employable, chosen this value as reference, another penalty giving by the laser active passes along the supports cross-sections should be considered, since the less precision of soldering with laser activated every two layers, decreasing furtherly the thermo-mechanical properties of the material. This second penalizing factor can be considered in the nearby of 0.6/0.8. In table 7, the deformation results, on axis-y, for values of the penalty factor in a range of 0.1÷0.5 are reported for each layer, with a 2 mm cartesian mesh the total number of layers results to be 51.

Table 7- supports penalty factor sensitivity analysis

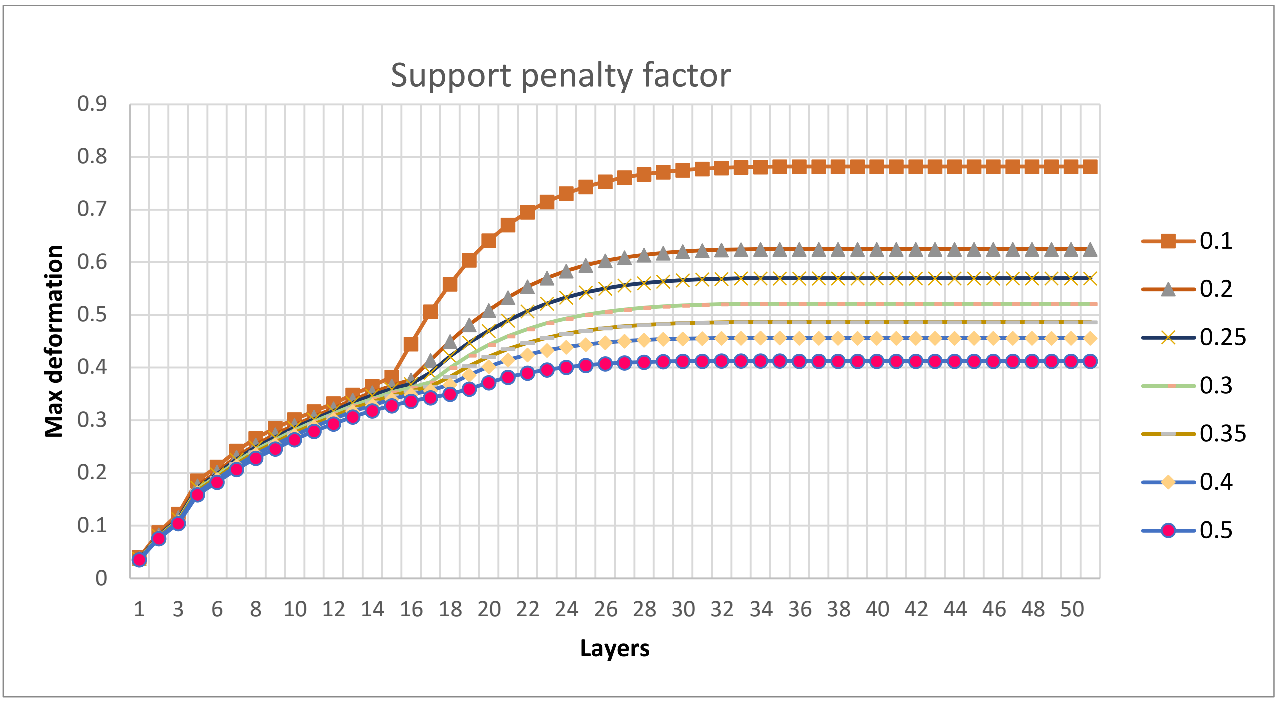

The harder is the penalization, the biggest are the deformation reported, as can be seen for the evolution reported for every penalty factor simulated, the curves from the top going to the bottom of the chart are increasing penalty factors, as the legend on the right of the diagram associates the factors to the different curves. This result is what should have been expected to be seen, the smallest the penalty factor is the more the material properties are knocked down, and it is to be linked with a smaller volume ratio, meaning thinner or less supports. Experimental data report measurements of penalty factors around 0.3÷0.4, with the hypothesis aforementioned, volume ratio of 0.6 and absorbed energy ratio of 0.6÷0.7, everything results aligned justifying the choice of a penalty factor of 0.4 for this case study simulations.

ii. Mesh sensitivity analysis

The IS analysis results were compared for a set of different mesh sizes, voxel sizes from 0.5 mm to 1.5 mm. In the range 0.5÷1 mm the step of 0.1 mm was adopted, then a 1.25 mm and a 1.5 mm models were added to have deeper understanding in the computational times demanded and, in the results variance, and possible convergence in function of the element size. The computational time is referred to the solution elapsed time which presents an evolution reducible with a power law. The sensitivity analysis was carried out on a 6 cores device. As represented in the graph reported in figure 99 in which the time on y-axis, are related to the different mesh sizes, x-axis. The difference in computational times becomes very palpable when the element size decreases under the value of 0.7 going from a simulation elapsed time of around 4 hours up to almost 25 hours with an element size of 0.5. At this stage removal of base and support where not considered, hence only the building phase was simulated.

For this sensitivity evaluation three have been the evaluation criteria:

- Deformation
- Stress
- Time

First of all, deformation and stress, as they are the outputs of the simulation are to be considered, secondly the third criterion is computational time required.

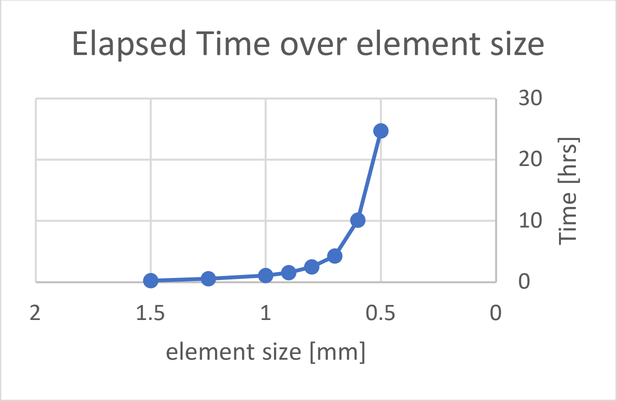

Figure 100 – Elapsed Time for decreasing element size

Carrying out multiple simulations becomes sensibly time consuming with a mesh finer than 0.7 mm. Comparing the results for deformation and stresses of the different mesh alternatives it's crucial to select the optimum compromise between results reliability and solution elapsed time. Diagrammed results on the y-axis with element size on x-axis, should show with increasing number of elements (smaller element size) a plateau, meaning there is a convergence of the measured values, therefore a greater reliability of the results. Deformation results have been the first to be evaluated, both the maximum and average deformation results show little differences along the range of elements sizes. Total deformation maximum varies along a range of 0.5242 mm, its evolution is presented in the graph of figure 101. Along the points representing an element size between 1 and 0.7 mm the results present a sort of plateau due to minor variance in comparison to the other results, this may suggest that along these sizes the results present a sort of stability. But a deeper discussion on the variation of the results and the choice of mesh will be developed in the following of this paragraph.

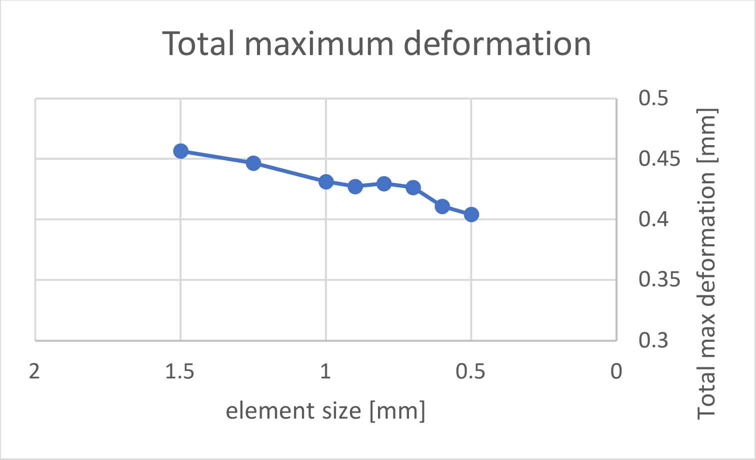

Figure 101 – Total maximum deformation for decreasing element size

Considering average deformation the situation to be found is not much different, as is shown in figure 102, again the results show a decrement with decreasing element size. The graph reports that the average deformation detected varies in a range of 0.3223 mm.

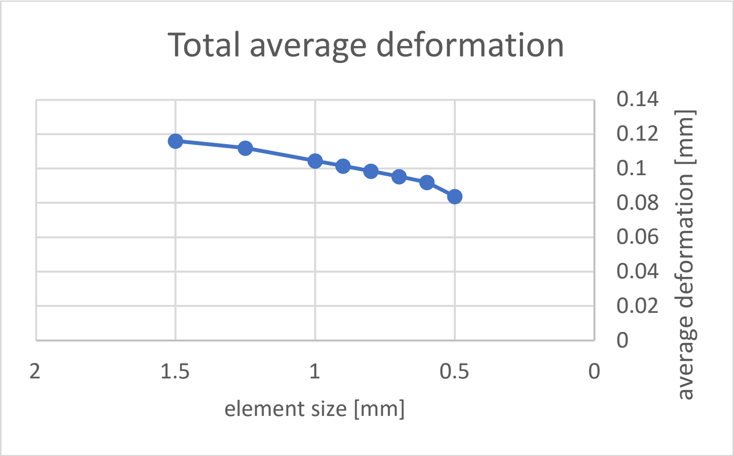

Figure 102 – Total average deformation for decreasing element size

The results collected for the maximum Equivalent stress, represented in figure 103, report an evolution with maximums and minimums, the results vary in a range of nearly 300 MPa, which is a consistent value, which may lead to a miscalculation about the part being successfully printed or fail. It's interesting to note that the maximum and the minimum values for the maximum equivalent stress are to be found in the greater element sizes, while the delta associated with element size decreasing under 1 mm is around 80 MPa, which is less than 1/3 of the range detected for all the sample.

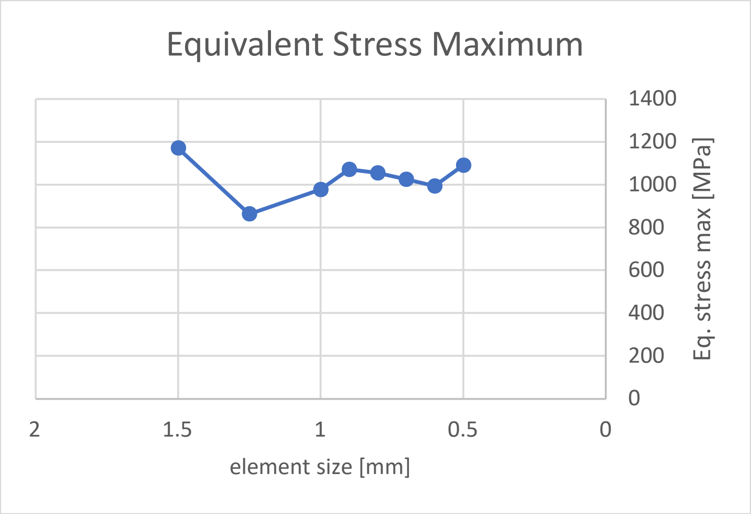

Figure 103 – Equivalent maximum stress for decreasing element size

The minimum and average of the equivalent stress evolutions are respectively reported in figure 104 and 105. The results for the minimum vary in a range of 0.1257 MPa, meaning the variance detected for the minimum is slightly influenced by the mesh size. Furtherly, considering the resulting minimum equivalent stresses a situation similar to plateau can be noted.

On the other hand, the results of the average equivalent stress are sparse in a range of nearly 21 MPa, showing a decreasing trend for stresses hand in hand with the elements size decrement.

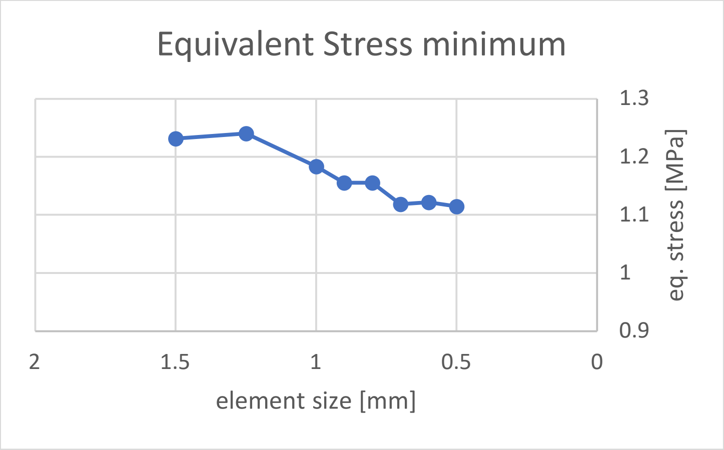

Figure 104 – equivalent stress minimum for decreasing element size

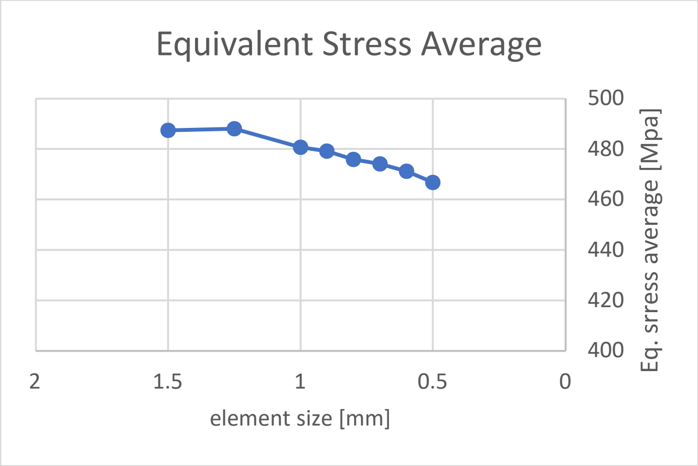

Figure 105 – Equivalent Stress Average for decreasing element size

The results analyzed do not show a clear convergence with the decrement of element size, but the values of the results seem to be plausible real values. Therefore, an analysis of percentage variations considering the mesh subsequent decrement starting from the bigger element size has been carried out too. The biggest element size investigated in this analysis is 1.5 mm, and the results of the simulation characterized by this mesh set the comparison for element size 1.25 mm. 1.25 mm element sized simulation itself is the comparison term for element sized 1 results, and so on, every decrement was compared to its nearer bigger element sized simulation. In table 8 all the percentage variations are reported.

Table 8- Percentage variations with mesh refinement

element size	Δ% size	Δ% max def	Δ% aver def	Δ% stress min	Δ% stress max	Δ% stress average
1.5						
1.25	16.67%	2.21%	3.62%	-0.72%	26.27%	-0.14%
1	20.00%	3.40%	6.66%	4.59%	-13.22%	1.52%
0.9	10.00%	0.93%	2.70%	2.38%	-9.63%	0.31%
0.8	11.11%	-0.56%	2.95%	0.01%	1.55%	0.68%
0.7	12.50%	0.76%	3.31%	3.15%	2.76%	0.39%
0.6	14.29%	3.64%	3.50%	-0.28%	3.13%	0.61%
0.5	16.67%	1.64%	8.87%	0.64%	-9.70%	0.94%

The smaller variations are to be found around the alternatives with mesh size of 0.9 ÷ 0.7 mm. To have a clearer vision of how results vary a bar chart was built from table 8, as reported in figure 106:

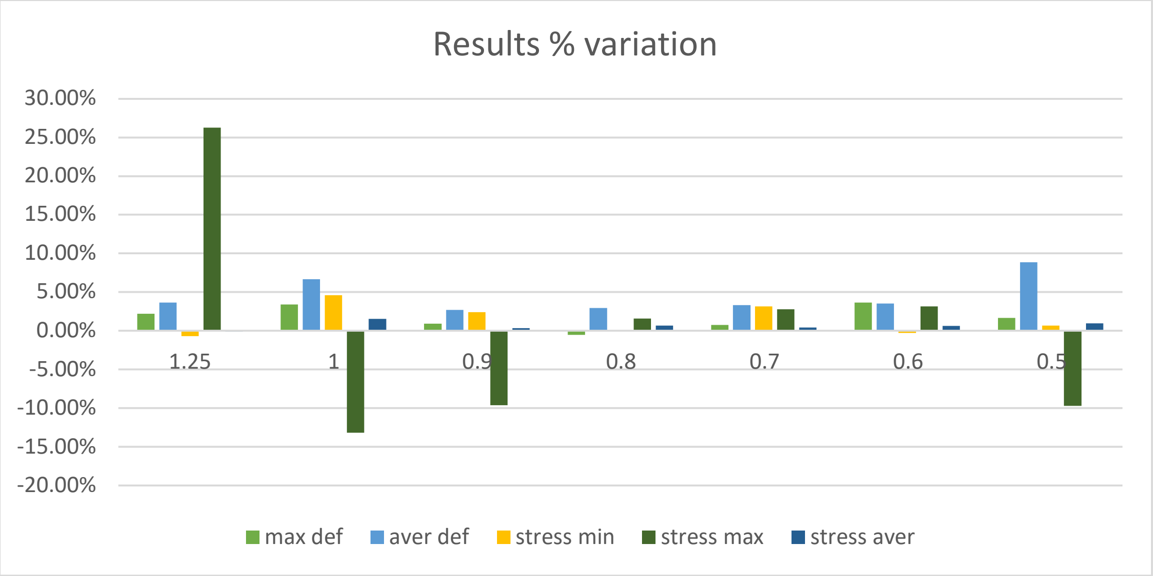

Figure 106- bar chart for variance of results with decreasing element size

In figure 106 in the range of 0.9÷0.6, how it was noted for the tabled results, the results present a smaller variance, which may probably imply a greater stability of the results. Therefore, the chosen element size for this study it has been 0.8 mm, the size showing the smallest variances, and an acceptable simulation time (2.47 hours) for the continuation of the analysis of this case.

5.7.3 AM simulations results and considerations

The selected geometry has been simulated with an element size of 0.8 mm, exploiting the IS analysis, in this paragraph the retrieved results are presented. The achievements of this analysis are to be considered a preliminary study, first of all because of the lack of a calibration. Furthermore, simulations on a macroscopic level are useful solely for determination of the deformations with a cartesian mesh, and to assess also stresses and strains exploiting a tetrahedral mesh. For a fully predictive simulation the analysis must be carried out on a multiscale level, defects, such as porosity, are predictable through a mesoscale level simulation since the melt pool and all the connected physical phenomena are represented, while processed material properties are assessable from a microscopic level simulation which considers the microstructure evolution.

The aims of the reported results were solely to assess: the manufacturability of the channels, the supports validation, the most critical zones for residual stresses and deformation.

5.7.3a Cartesian Mesh

The mesh of the side core insert is reported in figure 107, the mesh was set to have linear elements. For the base plate a sizing guided the mesh, with element size 5 mm, and a division in five of the edges parallel to z-axis. The supports which can be seen in grey are meshed as the build part with cartesian elements of 0.8 mm size.

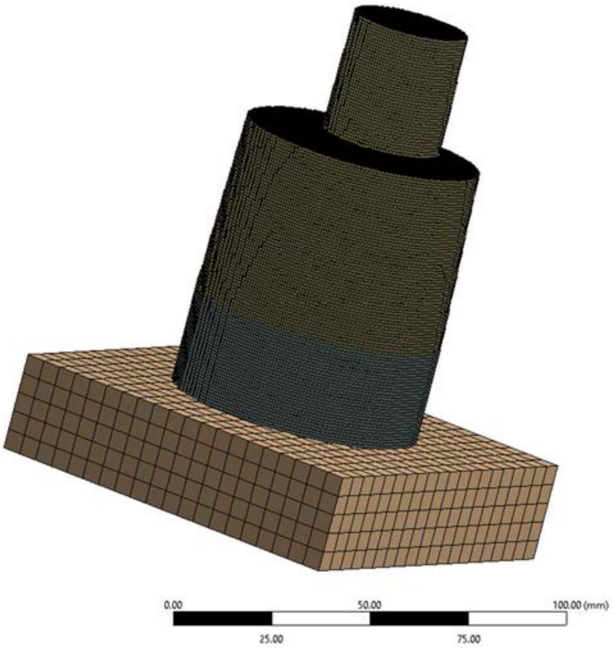

Figure 107- 0.8 mm element size mesh

This time the base and supports removal was considered, therefore two additional steps have been considered their elimination. In figure 108 the process workflow is presented with all the steps considered:

Figure 108- stages of the AM process simulation

Considering the total deformation results, the most affected zone is to be found at the edge where build part and supports are in contact, as presented by figure 109 below.

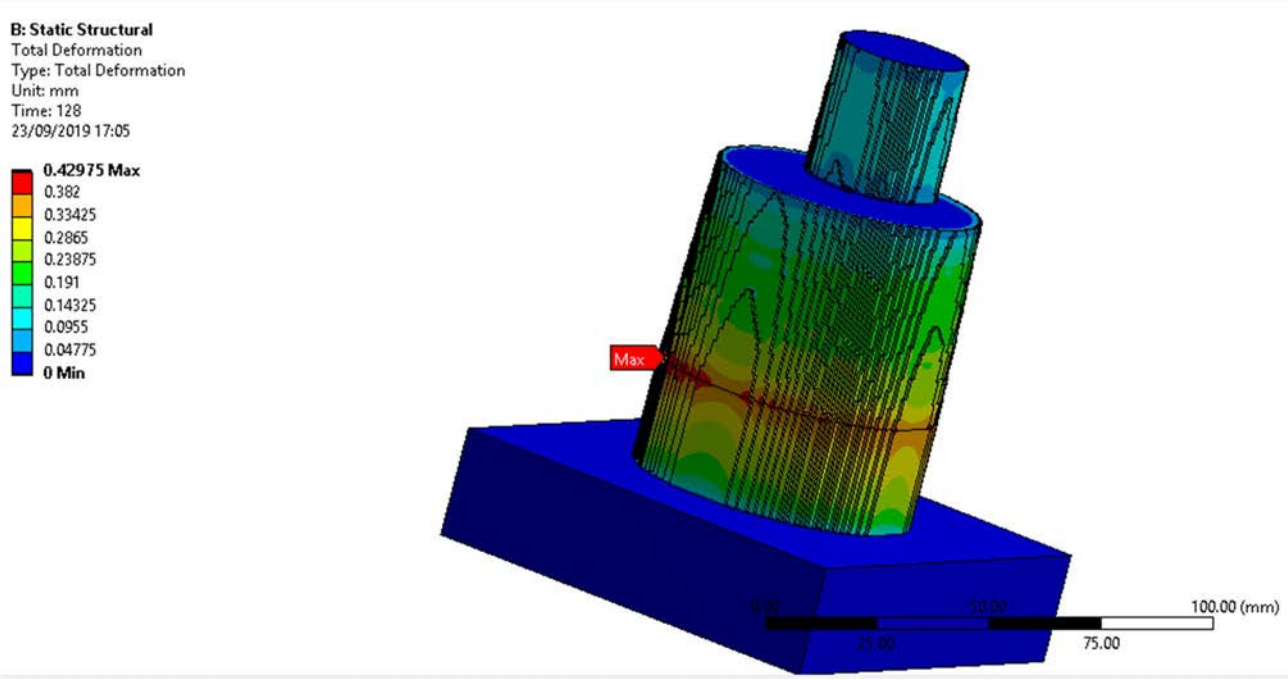

Figure 109-total deformation before support removal

This is to be found also after supports removal, after this step, the deformation actually increases from a value of 0.42975 mm, as can be noted in figure 108 to a value of 0.57259 mm as figure 110 shows.

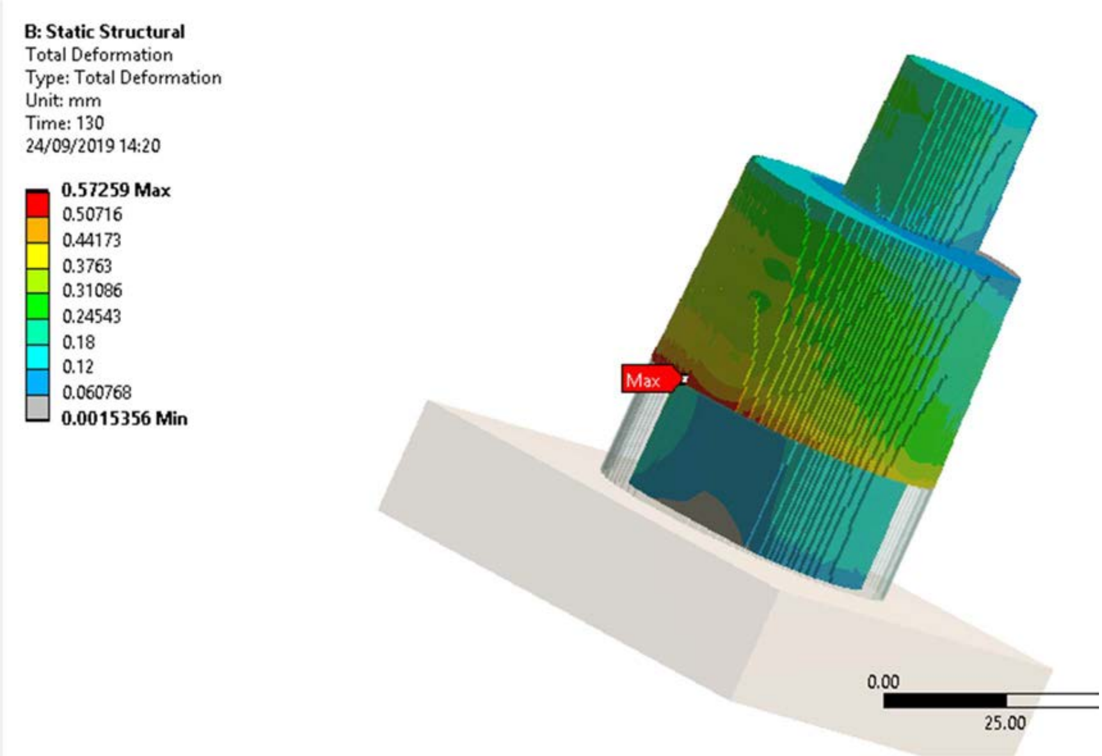

Figure 110- total deformation with supports removed

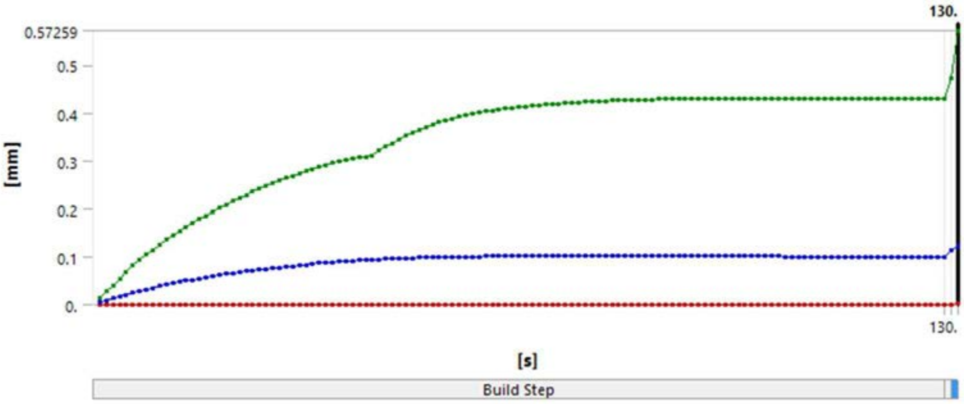

Figure 111 – Deformation evolution (maximum in green, average in blu and minimum in red)

Looking to the deformation evolution along the manufacturing process is to be noted an increment of the slope increasing in correspondence with the building of the overhanging layers, despite the presence of supports. On the last two steps the deformation increases much quicker and this is due to the part removal of base and supports, which make the part less constrained so free to furtherly deform.

Considering the stress results the maximum equivalent stress is greater than the yield stress of the material, but is localized on an edge on the skin of the part, which may be linked to cartesian elements approximating the model since there is no knockdown factor to approximate the geometry and every cartesian element is considered full also the ones along the surface, as appears in figure 112, on the rest of the parts the level of residual stresses is beneath the value of 775 MPa which is the yield strength considered for the H13 tool steel.

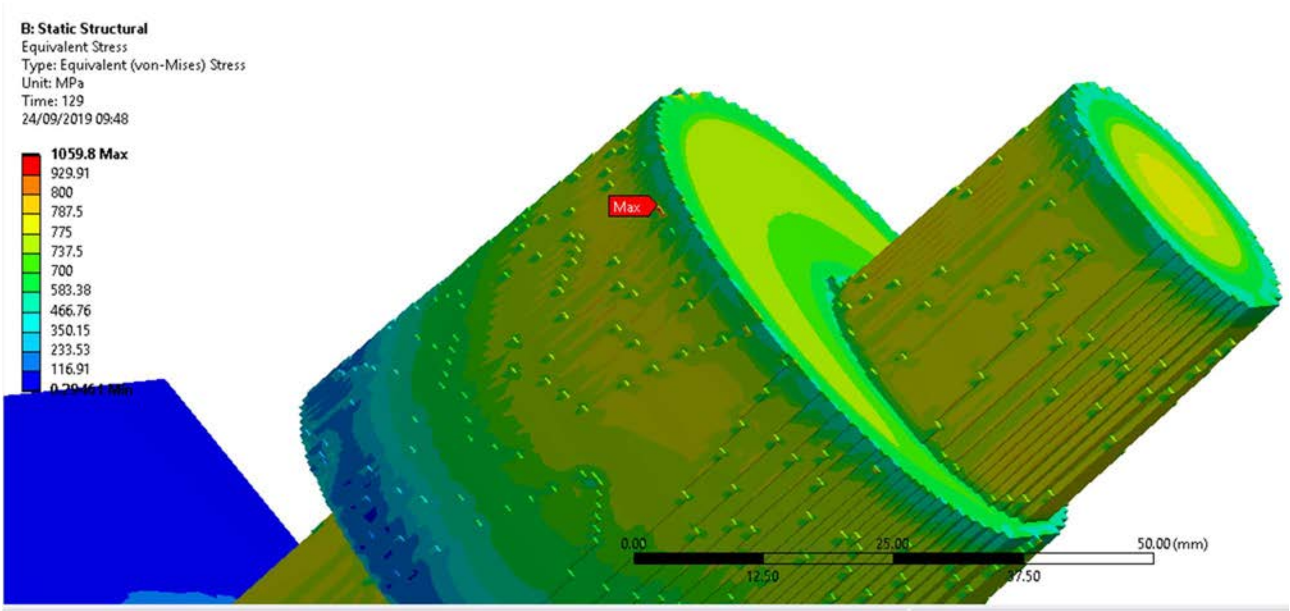

Figure 112- equivalent stress maximum on the edge of a cartesian element

After plotting the deformation and the stress on a conformal tetrahedral mesh the results can be better analyzed, as can be seen in figure 113, the result was also plotted by activating the deformed edges auto-scale to highlight how the part is going to deform; it is important to note that the results numerical value show a variation after being plotted on a conformal mesh, the absence of a knockdown is to be charged of this phenomenon.

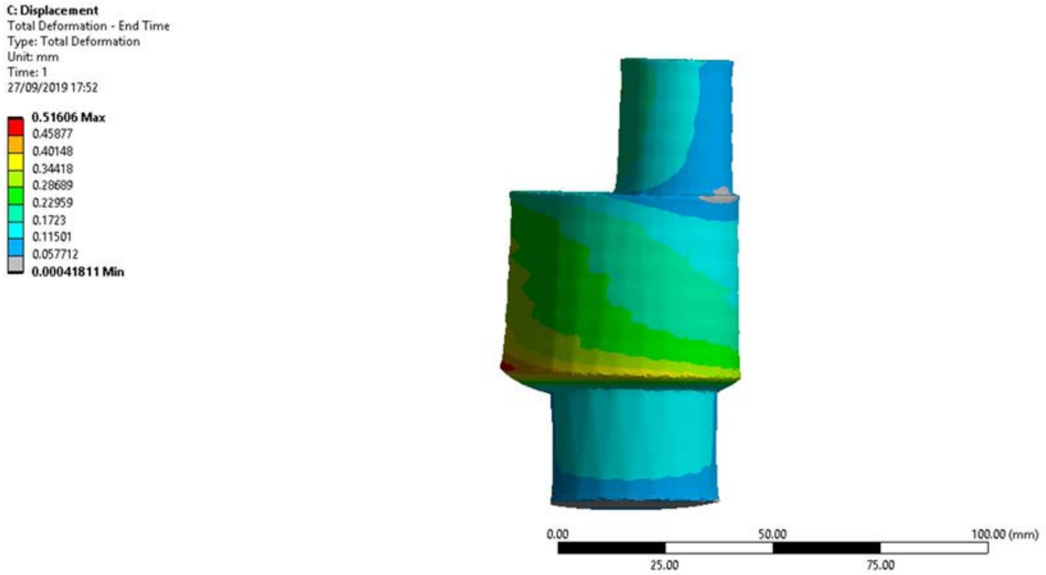

Figure 113- deformation plotted on conformal mesh

Analyzing the deformation along the three axis it is to be noted that the greater values are to be found along z-axis, to confirm that the build direction is the direction to show more shrinkage, as with solidification and cooling the residual traction stress comports the edges to rise. Directional deformation can be compared along the three axes, respectively x, y and z, in figures 114,115 and 116.

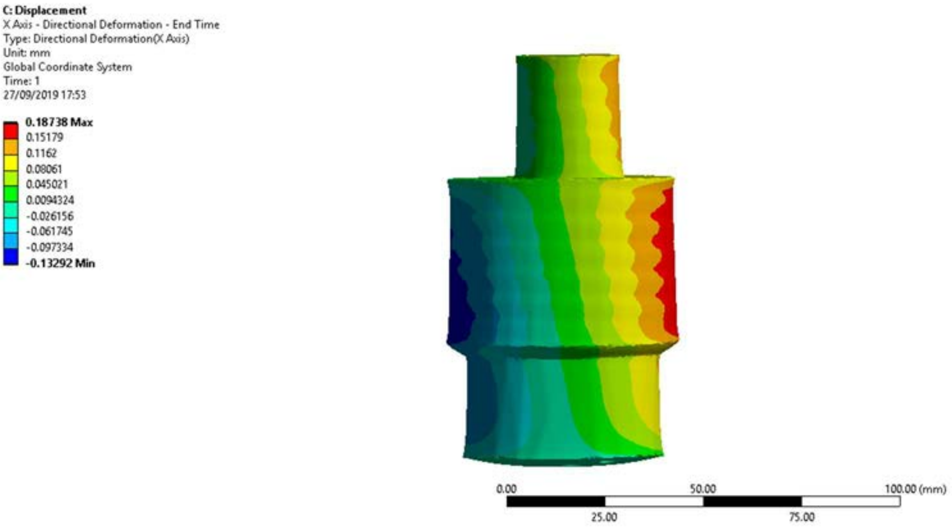

Figure 114- deformation along x-axis

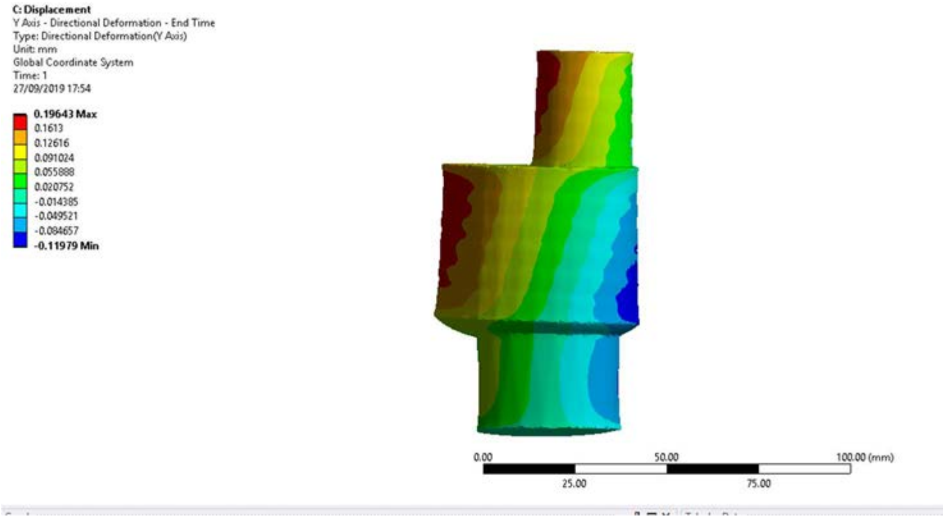

Figure 115- deformation along y-axis

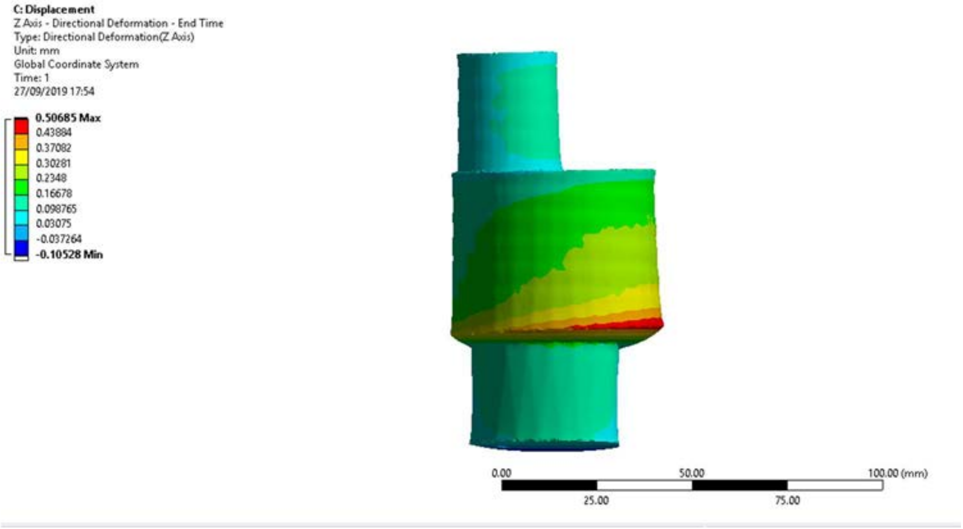

Figure 116- deformation along z-axis

The deformation and the stress analysis along part sections enables the evaluation of how the deformation and stress affects the conformal cooling channels, from the color field is clear that both deformation, in figure 117, and stress, in figure 118, influence only marginally the circuit, thus meaning its manufacturability.

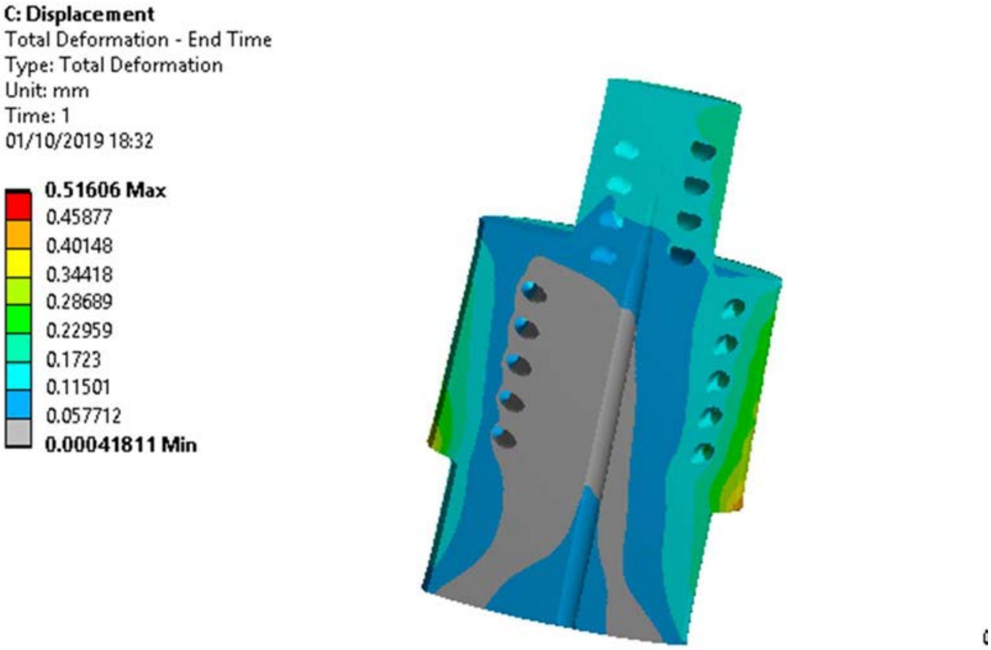

Figure 117- deformation along a part section from cartesian mesh plotted result

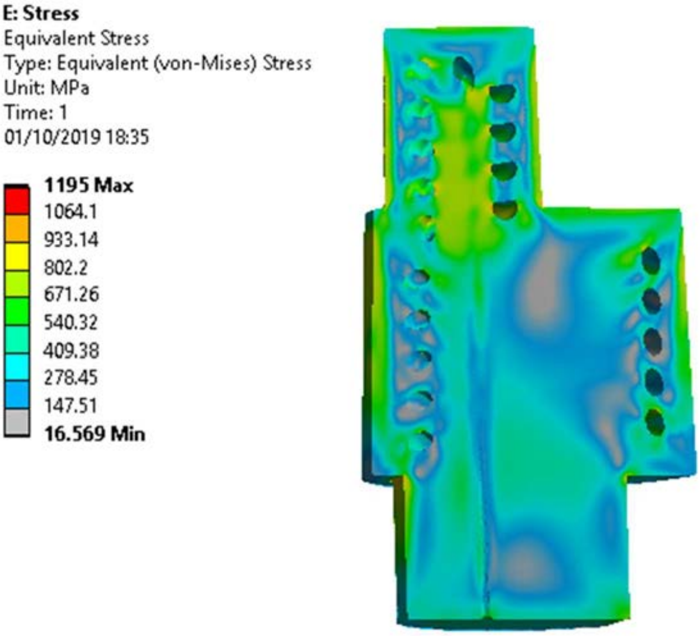

Figure 118- stress along a part section from cartesian mesh plotted result

6.7.3b Tetrahedral Mesh

An IS analysis has been carried out utilizing then a tetrahedral mesh, characterized by elements defined by quadratic functions. The results show some differences in the numerical values form the simulation carried out with cartesian elements, by the way without a calibration procedure completed or experimental trials the most predictive results can only be hyphotised on the base of finite element method principles and common sense. Therefore the reliability of the following results it’s to be considered higher, since quadratic elements follow easier the deformation, and the conformity of the mesh to the part not only makes possible the direct results evaluation without going through the plotting step, but also does not present full elements beyond the part surface. The mesh is presented in figure 119 below, characterized by a layer height of 1 mm and element size of 1.2 mm.

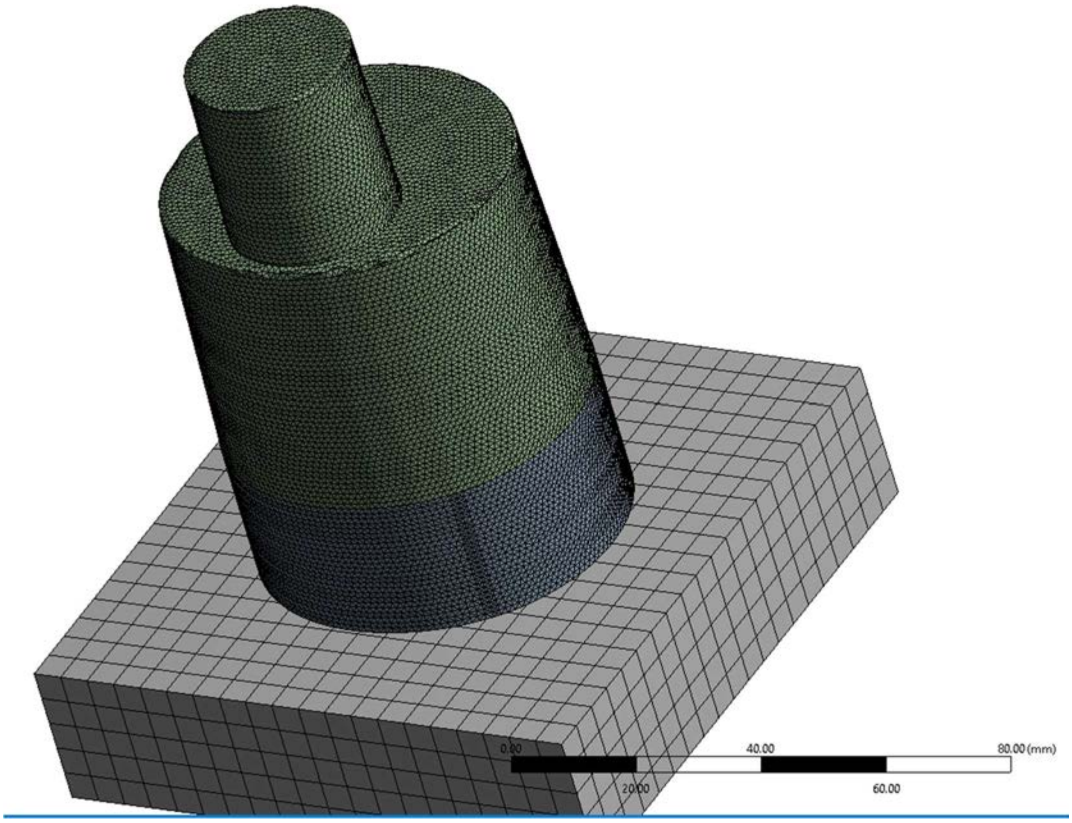

Figure 119- side core insert and supports tetrahedral mesh

The base plate was meshed as for the previous simulation. Deformation results are subsequently reported respectively as the build phase has been completed, after base plate removal and after supports removal in figures 120, 121 and 122. The most important conclusion observing these results is that, despite the numerical differences the color map evaluate the same critical zones as for the previous simulation.

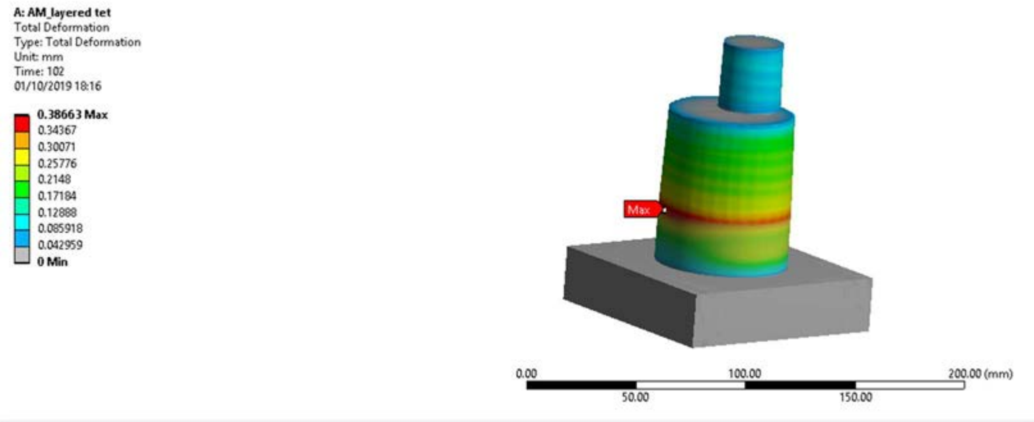

Figure 120- deformation results before base and supports removal

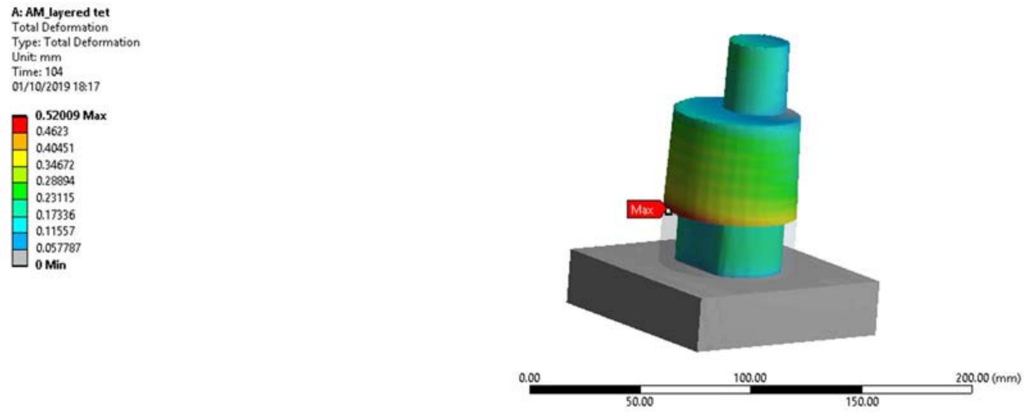

Figure 121- deformation after base removal

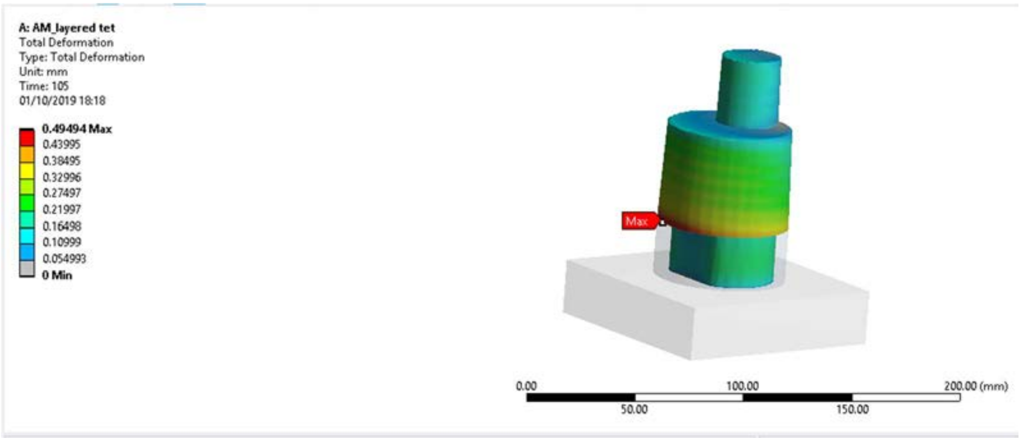

Figure 122- deformation after base and supports removal

Along the part sections and the channels surface the part show the smaller results of deformation as to be seen in figure 123.

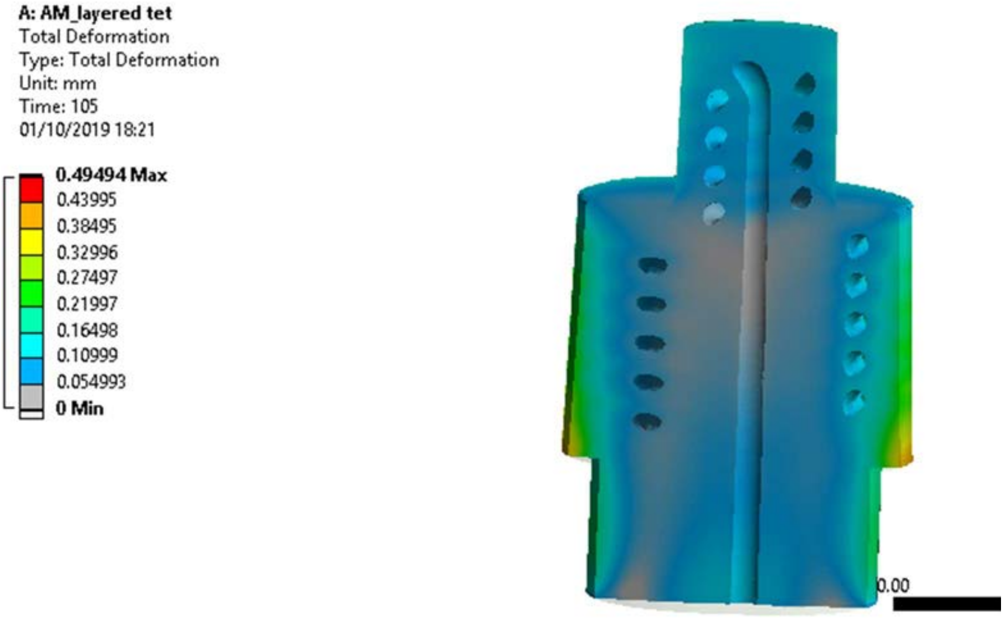

Figure 123- deformation along a part section

Considering the stress field the results are again in accordance with the previous results retrieved for the cartesian mesh simulation, with the higher values to be found on the external surface.

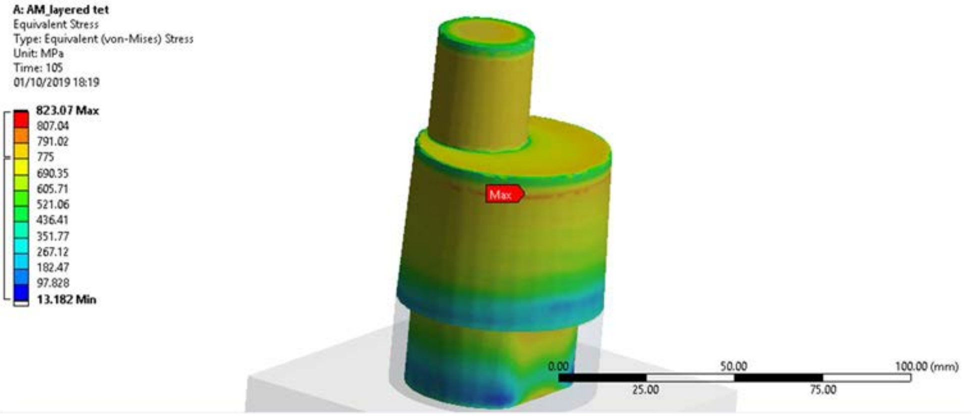

Figure 124 - equivalent (Von-Mises) stress

The channels result affected by the lower range present on the scale, confirming the manufacturability of the part, the values on the surface though suggest the need of a heat treatment to relax the residual stresses.

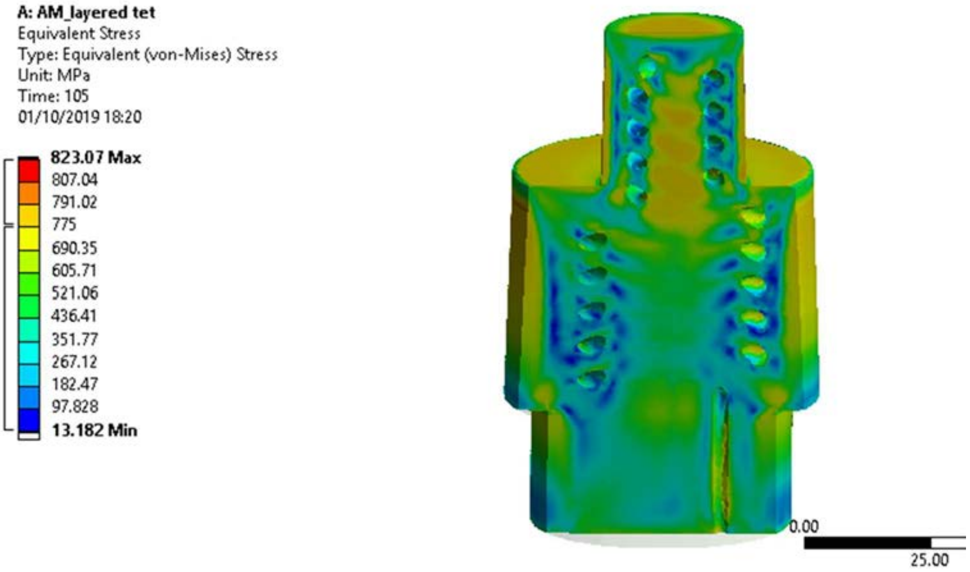

Figure 125- equivalent stress along the channels

5.7.3c Compensation and machining allowance

To complete the evaluations of the two simulations a compensated geometry for the manufacturing is presented. The deformation results have been scaled with a factor of 0.6 for x and y axes deformation vectors, while a factor of 0.8 has been selected for the displacement vectors along z-axis. This choice was drove by two factors, first compensated geometries are commonly never completely compensated at first step but it’s usually an iterative procedure to find the geometry which results optimally printable, the second factor took in account the greater deformation along z-axis by differencing the scale factors.

Scaled deformation vectors field have been then reversed to generate the compensated geometry of the side core insert. Which can be observed in figure 126 and 127.

In figure 126 can be noted how the edges result lowered to compensate the traction effect during solidification and cooling which is due to the shrinkage.

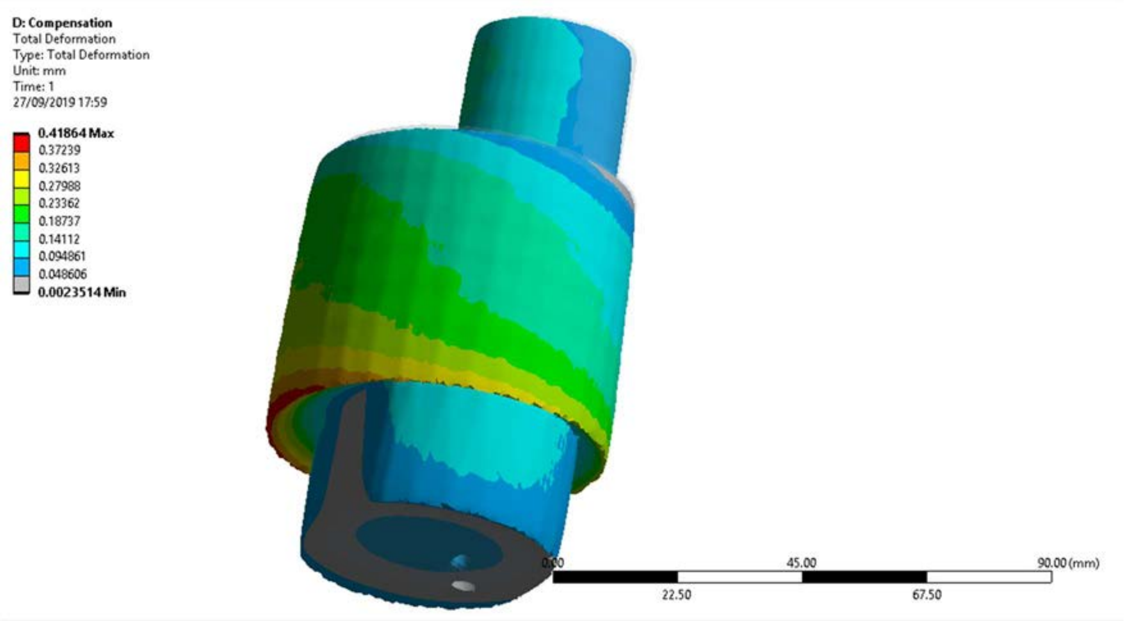

Figure 126- Compensation of the side core insert to optimize printing

In figure 127 the compensated geometry is presented together with the original side core insert to have a visual comparison of the lowering happened through the reversion of the scaled deformation.

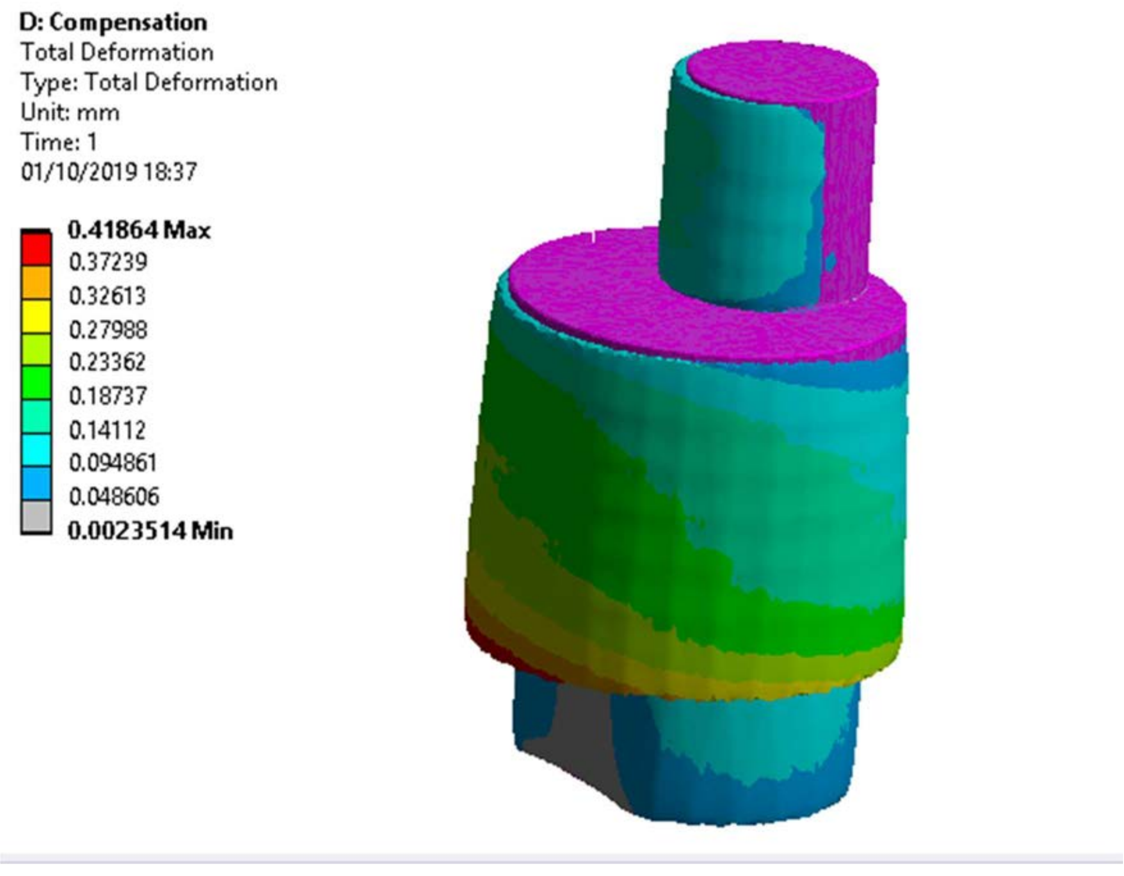

Figure 127- comparison of compensated side core insert and original cad in purple

A machining allowance of 0.5 mm was considered to carry out possible post processing finishing, through surface machining additionally the material most affected by build residual stress would be removed.

5.7.3d Limits of this case study and perspective for future work

The available time for this study didn't make possible a deeper analysis of the AM effectiveness for the production of HPDC die inserts, but in an ideal workflow for this thesis the analysis would have, as aforementioned, comprised a calibration procedure and would have been moved forward towards an evaluation of the defects and of the capability to withstand the conditions of the HPDC process.

After the calibration the IS simulations should be repeated, possibly with a tetrahedral mesh, to have more precise and reliable results. Then machining allowance or a compensation should be assessed through simulations to get the part as neare to the CAD model as possible required. An additional step which should be evaluated is a heat treatment, since it's common practice to apply heat treatment to relieve residual stress of AM manufactured parts. Therefore, the consideration of a heat treatment may lower the machining allowance demanded by the as-built part. The simulation results at this point would give not only a qualitative idea for deformations and stresses.

The following step towards a finer detailed assessment would be carrying out a thermo-mechanical analysis on a meso scale level, simulating the laser passes to predict part quality with a correlation to process parameters which could be verified and possibly finetuned to the case. Studying the possibility to integrate the different scales, facing the issues linked to the rise of computational effort, would enable a holistic evaluation of the part manufacturability and quality.

5.8 Impacts: TIME/COST

The ratio between conventional and additive manufacturing is approximately of 1/9. There are many reasons for this to sensible difference, the metal powders are more expensive than the corresponding alloy in solid blocks, furtherly heat treatment and surface polishing are usually exploited respectively to relieve residual stresses and to mitigate surface roughness. Also, L-PBF process is more energy consuming in comparison with CNC machining as can be seen in the bar chart of figure 109[92], which compares the energy consumption of different manufacturing processes comprising L-PBF and CNC machining processes per kg of material. Considering the red bar which refers to tool steel, which energy consumption is assimilable to the one needed for processing H13 since it's a stainless steel too, the difference between AM processing and CNC machining is of 31.7 kWh/kg, meaning that the energy consumption for AM process is around 180% higher in respect to CNC machining.

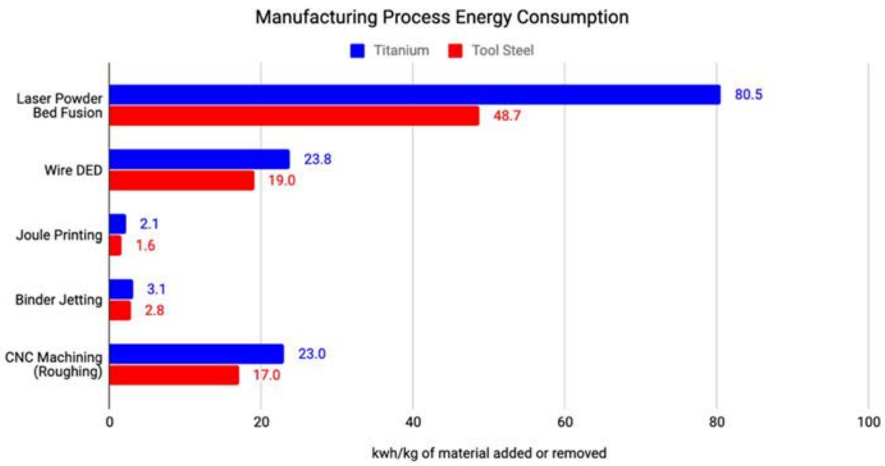

Figure 128

Furtherly, the manufacturing direct cost factors/items of an HPDC die insert can be classified identified as follows respectively for conventional machining and AM.

Conventional design costs:

- Material cost C_{mat} →necessary mass [kg] x cost [€/kg];
- Machine cost→function of processing time [hours] x (energy cost [€/hrs], work force [€/hrs], maintenance cost [€/hrs], additional material cost [€/kg], amortization cost [€/hrs]);
- Additional treatments for residual stress relief and surface requirements → heat treatment and surface finishing;

L-PBF design costs:

- Material cost→ necessary mass of powder alloy (Support structure x waste factor x number of parts x parts volume x mass density) [kg] x cost [€/kg];
- Machine cost→function of processing time [hours] x (energy cost [€/hrs], work force [€/hrs], maintenance cost [€/hrs], additional material cost [€/kg], amortization cost [€/hrs]);
- Additional treatments for residual stress relief and surface requirements → heat treatment and surface finishing;

Considering the material cost the price of metallic powders is way higher than as cast, the cost per kg results 100 times greater or more considering the powders, but it is also to be considered that the material quantity required is much lesser considering AM in comparison to traditional manufacturing. As reported by Bauer and Malone [93] for EB-

PBF the material consumption for the same part is ten times lower than in conventional manufacturing as reported in figure 129.

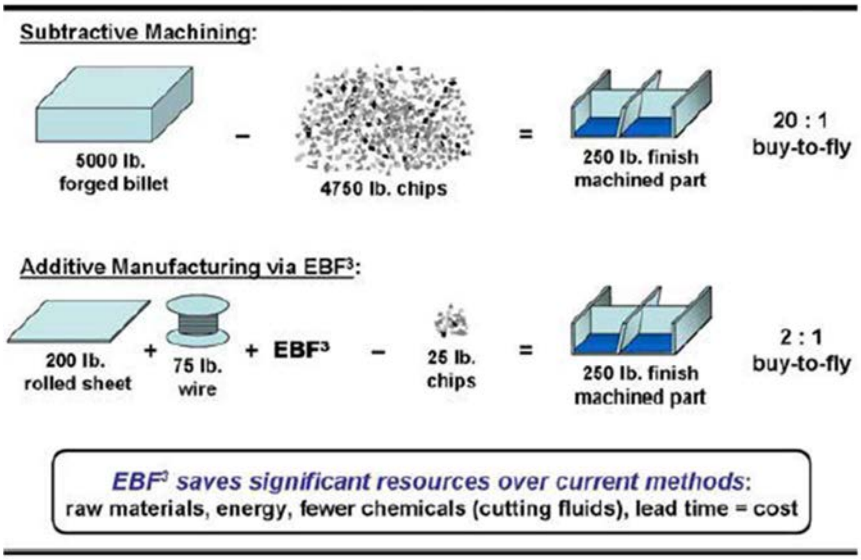

Figure 129- material consumption in conventional and AM (EB-PBF)

It is assumable that the same ratio can be encountered considering L-PBF manufacturing, therefore the material cost for the part is reduced by the smaller quantity required by a factor of 10, the ratio between the conventional material cost and AM one is then 1 to 10.

Considering the machine cost the biggest difference is probably to be found in energy consumption which results per hour 2.8 times higher for AM (from figure 122), amortization, maintenance and work force are strongly dependent on the type of machine for the specific part production, considering to reach a similar level of finishing of the part surface as-built and as machined the possible additional post processing heat treatment can be considered the same for both cases giving a ratio of costs 1 to 1. Also, Gobber et al. [94] reported a negative correlation of die soldering issue with die surface roughness, therefore the surface do not need excessive additional processing.

In general, speaking about tooling, it can be said that the AM process has 1.6 times the production cost of conventional manufacturing of the same part as in the cost model presented by Previtali et al. [95] figure 130:

Figure 130- L-PBF production cost compared to conventional manufacturing cost

Speaking of the case study addressed in this thesis some considerations can be drawn, note that these are purely linked to simulation results. The higher costs of L-PBF must be linked to the benefits the L-PBF die insert brings to the HPDC process:

- Casting waste reduction due to higher part quality: an improvement of the quality part considering the porosity at least lessened by 50%, the waste castings rate is expected to decrease from of a 40%;
- Thermal fatigue assessment drawn an interesting scenario where reduction of machine downtime for insert substitution due to longer die insert life: the simulation results shows that the down time for insert substitution considering an average life of 100’000/200’000 cycles can be sensibly decreased exploiting an AM produced die insert;
- Reduction of the HPDC cycle time: the reduction of the solidification time and therefore cycle time reduction enables a rise of 19% of the production rate, enabling a fix costs redistribution and therefore decrease of the same percentage;
- Reduction of insert supply costs: acquiring a L-PBF machine would reduce transport, storage and lead time costs for insert supply, the company would be then also able to produce different HPDC inserts with the same machine;

6 CONCLUSIONS

Recalling figure 53, at 5.1 paragraph the main steps which characterized this study can be summarized as follows:

- Selection and analysis of a case study;
- Design of conformal cooling alternatives to possibly replace conventional design inserts;
- Thermo-mechanical simulation and optimization of the HPDC process;
- AM manufacturability assessment of a conformal cooling die insert;
- Techno-economical comparison of conventional and AM tooling for die insert production;
- Reasoning about the findings resulting from this study and related limits, future perspective of the study;

Numerical evaluation of conformal cooling solutions for HPDC die inserts and L-PBF manufacturability of the have drawn an interesting scenario for the future application of these techniques and process in the industry. The most relevant achievements can be divided in two main categories:

1. HPDC process improved cost-effectiveness
2. AM manufacturability of HPDC die inserts

The first point may be considered achieved thanks to two aligned results. Firstly, the higher effectiveness of the HPDC manufacturing process is to be found in the improvement of the part quality, which has been assessed by the reduction of the values detected representing porosity, hot spot and die soldering effects. Secondly a goal going hand in hand with the effectiveness of the process is a cost reduction of the process itself and is to be found in the cycle time reduction, enabling a higher productivity and in the elongation of the die inserts through smaller thermal cycles and higher homogeneity of the temperature fields, lessening therefore the down time for insert substitution.

The second point more specifically deals with the L-PBF manufacturability, which has been tested in terms of part deformation and residual stress and strains. The results of the set of AM simulations gave the basis to part compensations and machining allowance proposals in order to obtain a printed part respecting the demanded specifications, also paved the way to a more structured methodology for the complete analysis of L-PBF manufacturability on a computational level.

7 AKNOWLEDGEMENTS

Many people have supported and helped along the way of this thesis project and in my opinion is important to give credit to these wonderful, competent people.

Considering university, thank you to professor Franco Bonollo, who accepted to be my relator and addressed me towards the company, Enginsoft SPA, with which I collaborated for the thesis development and internship.

A big thank you to Enginsoft SPA with special merits in the following lines.

Thank you to Nicola Gramegna, who gave me the possibility to collaborate with Enginsoft SPA being my internship tutor along all the project.

Thank you to Francesca Lago, who helped with the training with MAGMAsoft® and supported me, giving the example of a strong woman, taking her place in the engineering world.

Thank you to Diego Boscolo Bozza, who helped with the training with Ansys® and gave useful suggestions and supported me to structure the work.

Another big thank you to all the people working in Enginsoft SPA in Padova who made me feel at ease from the start of the internship and introduced me to the world of work.

Thank you to my family and friends who supported me all my life, especially during the period of the thesis writing, when I was speaking only of process simulation, HPDC and AM.

8 BIBLIOGRAPHY

[1] C. Favi, M. Germani, and M. Mandolini, "Analytical Cost Estimation Model in High Pressure Die Casting," *Procedia Manuf.*, vol. 11, no. June, pp. 526–535, 2017.

[2] ASTM and ISO, "Standard Terminology for Additive Manufacturing – General Principles – Terminology," *Iso/Astm*, vol. 52900, p. 9, 2015.

[3] C. Meier, R. W. Penny, Y. Zou, J. S. Gibbs, and A. J. Hart, "Thermophysical Phenomena in Metal Additive Manufacturing by Selective Laser Melting: Fundamentals, Modeling, Simulation and Experimentation," 2017.

[4] W. J. Sames, F. A. List, S. Pannala, R. R. Dehoff, and S. S. Babu, "The metallurgy and processing science of metal additive manufacturing," *Int. Mater. Rev.*, vol. 61, no. 5, pp. 315–360, 2016.

[5] T. DebRoy *et al.*, "Additive manufacturing of metallic components – Process, structure and properties," *Prog. Mater. Sci.*, vol. 92, no. 5, pp. 112–224, 2018.

[6] J. Meckley and R. Edwards, "A Study on the Design and Effectiveness of Conformal Cooling Channels in Rapid Tooling Inserts," *Technol. Interface J.*, vol. 10, no. 1, pp. 1523–9926, 2009.

[7] H. S. Park and N. H. Pham, "DESIGN OF CONFORMAL COOLING CHANNELS FOR AN AUTOMOTIVE PART," *Int. J. Automot. Technol.*, vol. 10, no. 1, pp. 87–93, 2009.

[8] Y. Wang, K. M. Yu, C. C. L. Wang, and Y. Zhang, "Automatic design of conformal cooling circuits for rapid tooling," *CAD Comput. Aided Des.*, vol. 43, no. 8, pp. 1001–1010, 2011.

[9] K. M. Au, K. M. Yu, and W. K. Chiu, "Visibility-based conformal cooling channel generation for rapid tooling," *CAD Comput. Aided Des.*, vol. 43, no. 4, pp. 356–373, 2011.

[10] J. H. Choi, J. S. Kim, E. S. Han, H. P. Park, and B. O. Rhee, "STUDY ON AN OPTIMIZED CONFIGURATION OF CONFORMAL COOLING CHANNEL BY BRANCHING LAW," 2014, pp. 25–26.

[11] S. A. Jahan, T. Wu, Y. Zhang, J. Zhang, A. Tovar, and H. Elmounayri, "Thermo-mechanical Design Optimization of Conformal Cooling Channels using Design of Experiments Approach," *Procedia Manuf.*, vol. 10, 2017.

[12] S. A. Jahan *et al.*, "Implementation of Conformal Cooling & Topology Optimization in 3D Printed Stainless Steel Porous Structure Injection Molds," *Procedia Manuf.*, vol. 5, pp. 901–915, 2016.

[13] S. Jahan and H. El-Mounayri, "A Thermomechanical Analysis of Conformal Cooling Channels in 3D Printed Plastic Injection Molds," *Appl. Sci.*, vol. 8, no.

12, p. 2567, 2018.

[14] A. Agazzi, V. Sobotka, R. Legoff, and Y. Jarny, “Optimal cooling design in injection moulding process-A new approach based on morphological surfaces,” *Appl. Therm. Eng.*, vol. 52, no. 1, pp. 170–178, 2013.

[15] Maciej Mazur Martin Leary Matthew McMillan Joe Elambasseril Milan Brandt, “SLM Additive Manufacture of H13 Steel with Conformal Cooling and Lattice structures Nomenclature,” *Rapid Prototyp. J.*, vol. 22, no. 3, 2016.

[16] M. Mazur, P. Brincat, M. Leary, and M. Brandt, “Numerical and experimental evaluation of a conformally cooled H13 steel injection mould manufactured with selective laser melting,” *Int. J. Adv. Manuf. Technol.*, vol. 93, no. 1–4, pp. 881–900, 2017.

[17] M. F. V. T. PEREIRA, “Additive Manufacturing of Components for in-Die Cavity Use , Suitable To Withstand Aluminium High Pressure Die Casting (Hpdc) Process Conditions Magister Technologiae : Engineering : Mechanical Declaration With Regard To,” *Giesserei*, vol. 92, no. 02, p. 144, 2005.

[18] A. T. Pradeep, “HPDC Die design for Additive Manufacturing,” 2018.

[19] B. Andresen, *Die Casting Engineering - A Hydraulic, Thermal and Mechanical Process*. 2004.

[20] P. Kotas and J. H. Hattel, *Integrated Modeling of Process , Structures and performance in Cast Parts by*. 2011.

[21] F. M. White, *Fluid Mechanics*, Seventh. Mc Graw Hill, 2011.

[22] R. E. Smallman and A. H. W. Ngan, “Modern Physical Metallurgy,” 2014, pp. 93–119.

[23] W. M. Rohsenow, J. R. Hartnett, and Young I. Cho, *Handbook of Heat Transfers*. 1998.

[24] J. Campbell, *Castings*. 2003.

[25] L. Andreoni, M. Casè, and G. Pomesano, *Il lavoro termico dello stampo*. .

[26] N. Gramegna and S. Enginsoft, “Analysis of the factors contributing to the heat balance of an high pressure die-casting mould .,” pp. 1–7.

[27] Tchoudenou, “http://pcfarina.eng.unipr.it/Public/Termofluidodinamica/Dispense-2013/,” *University of Parma*. .

[28] E. Gariboldi, F. Bonollo, and M. Rosso, “Proposal of a classification of defects of high-pressure diecast products,” *Metall. Ital.*, vol. 99, no. 6, pp. 39–46, 2007.

[29] CEN, “BSI Standards Publication Aluminium and aluminium alloys — Classification of Defects and Imperfections in High Pressure , Low Pressure and Gravity Die Cast Products,” *B S I Stand.*, p. 44, 2014.

[30] D. M. Stefanescu, “Computer simulation of shrinkage related defects in metal castings – a review,” vol. 18, no. 3, pp. 129–143, 2005.

[31] M. C. Flemings, “Flemings_Solidification Processing.”

[32] T. Fujii, D. R. Poirier, and M. C. Flemings, “Macrosegregation in a multicomponent low alloy steel,” *Metall. Trans. B*, vol. 10, no. 3, pp. 331–339, 1979.

[33] M. J. Aziz, “Model for solute redistribution during rapid solidification,” *J. Appl. Phys.*, vol. 53, no. 2, pp. 1158–1168, 1982.

[34] J. Wanqi, “Further discussions on the solute redistribution during dendritic solidification of binary alloys,” *Metall. Mater. Trans. B*, vol. 25, no. 5, pp. 731–739, 1994.

[35] W. Zhuang and N. Swansson, “Thermo-mechanical fatigue life prediction: A critical review,” *DSTO Aeronaut. Marit. Res. Lab.*, p. 34, 1998.

[36] S. Oller, O. Salomón, and E. Oñate, “A continuum mechanics model for mechanical fatigue analysis,” *Comput. Mater. Sci.*, vol. 32, no. 2, pp. 175–195, 2005.

[37] J. Mao, C. C. Engler-Pinto, T. Li, J. Hsieh, and X. Su, “Effect of Constitutive Model on Thermomechanical Fatigue Life Prediction,” *Procedia Eng.*, vol. 133, no. 313, pp. 655–668, 2015.

[38] E. Flender and J. Sturm, “Technical development report thirty years of Casting Process simulation,” *Foundry*, pp. 7–24, 2010.

[39] E. Anglada, A. Meléndez, I. Vicario, E. Arratibel, and G. Cangas, “Simplified Models for High Pressure Die Casting Simulation,” *Procedia Eng.*, vol. 132, pp. 974–981, 2015.

[40] “MAGMA committed to Casting Excelence,” *Aachen, Germany*. [Online]. Available: https://www.magmasoft.de/en/solutions/magmasoft/.

[41] C. Kleeberg, “Latest Advancements in Modelling and Simulation for High Pressure Die Castings,” *ALUCAST India 2010*, pp. 1–18, 2010.

[42] J. HA, P. W. CLEARY, M. PRAKASH, V. ALGUINE, T. NGUYEN, and C. SCOTT, “SPH, MAGMAsoft and water analogue modellings of die filling of a servo piston,” *Proc. 3rd Int. Conf. CFD Miner. Process Ind.*, no. December, pp. 587–592, 2003.

[43] R. Scardovelli and S. Zaleski, “Direct Numerical Simulation of Free-Surface and Interfacial Flow,” *Annu. Rev. Fluid Mech.*, vol. 31, no. 1, pp. 567–603, 1999.

[44] F. Bonollo and S. Odorizzi, *Numerical Simulation of Foundry Processes*. 2001.

[45] A. Cattenone, “Analysis and Simulation of Additive Manufacturing Processes,” 2019.

[46] P. A. Joly and R. Mehrabian, “Complex alloy powders produced by different atomization techniques: relationship between heat flow and structure,” *J. Mater. Sci.*, vol. 9, no. 9, pp. 1446–1455, 1974.

[47] C. D. Boley, S. C. Mitchell, A. M. Rubenchik, and S. S. Q. Wu, "Metal powder absorptivity: modeling and experiment," *Appl. Opt.*, vol. 55, no. 23, p. 6496, 2016.

[48] I. Gibson, D. Rosen, and S. Brent, *Additive Manufacturing technologies*. 2015.

[49] A. V. Gusarov, I. Yadroitsev, P. Bertrand, and I. Smurov, "Heat transfer modelling and stability analysis of selective laser melting," *Appl. Surf. Sci.*, vol. 254, no. 4, pp. 975–979, 2007.

[50] S. A. Khairallah, A. T. Anderson, A. Rubenchik, and W. E. King, "Laser powder-bed fusion additive manufacturing: physics of complex melt flow and formation mechanisms of pores, spatter, and denudation zones," *J. Chem. Inf. Model.*, vol. 53, no. 9, pp. 1689–1699, 2016.

[51] E. Malekipour and H. El-Mounayri, "Common defects and contributing parameters in powder bed fusion AM process and their classification for online monitoring and control: a review," *Int. J. Adv. Manuf. Technol.*, vol. 95, no. 1–4, pp. 527–550, 2018.

[52] C. Teng *et al.*, "A review of defect modeling in laser material processing," *Addit. Manuf.*, vol. 14, pp. 137–147, 2017.

[53] "Grain Refinement of Freeform Fabricated Ti-6Al-4V Alloy Using Beam/Arc Modulation Scott Mitzner," pp. 536–555.

[54] I. Steinbach *et al.*, "A phase field concept for multiphase systems," *Phys. D Nonlinear Phenom.*, vol. 94, no. 3, pp. 135–147, 1996.

[55] M. Berghoff, M. Selzer, and B. Nestler, "Phase-field simulations at the atomic scale in comparison to molecular dynamics," *Sci. World J.*, vol. 2013, 2013.

[56] O. Zinovieva, A. Zinoviev, and V. Ploshikhin, "Three-dimensional modeling of the microstructure evolution during metal additive manufacturing," *Comput. Mater. Sci.*, vol. 141, pp. 207–220, 2018.

[57] T. M. Rodgers, J. D. Madison, and V. Tikare, "Simulation of metal additive manufacturing microstructures using kinetic Monte Carlo," *Comput. Mater. Sci.*, vol. 135, pp. 78–89, 2017.

[58] Z. Wang, W. Yan, W. K. Liu, and M. Liu, "Powder-scale multi-physics modeling of multi-layer multi-track selective laser melting with sharp interface capturing method," *Comput. Mech.*, vol. 63, no. 4, pp. 649–661, 2019.

[59] X. Jia and R. A. Williams, "A packing algorithm for particles of arbitrary shapes," *Powder Technol.*, vol. 120, no. 3, pp. 175–186, 2001.

[60] Z. Zhang *et al.*, "3-Dimensional heat transfer modeling for laser powder-bed fusion additive manufacturing with volumetric heat sources based on varied thermal conductivity and absorptivity," *Opt. Laser Technol.*, vol. 109, no. July 2018, pp. 297–312, 2019.

[61] J. Goldak, A. Chakravarti, and M. Bibby, "A New Finite Element Model for Welding Heat Sources JOHN," vol. 52, no. 1, pp. 1–7, 1983.

[62] W. Zhou, X. Wang, J. Hu, and X. Zhu, "Melting process and mechanics on laser sintering of single layer polyamide 6 powder," *Int. J. Adv. Manuf. Technol.*, vol. 69, no. 1–4, pp. 901–908, 2013.

[63] J. Yin *et al.*, "A finite element model of thermal evolution in laser micro sintering," *Int. J. Adv. Manuf. Technol.*, vol. 83, no. 9–12, pp. 1847–1859, 2016.

[64] A. Mehta, *Granular Physics*. 2007.

[65] R. J. Hebert, "Viewpoint: metallurgical aspects of powder bed metal additive manufacturing," *J. Mater. Sci.*, vol. 51, no. 3, pp. 1165–1175, 2016.

[66] U. Ali *et al.*, "On the measurement of relative powder-bed compaction density in powder-bed additive manufacturing processes," *Mater. Des.*, vol. 155, pp. 495–501, 2018.

[67] S. Benyahia, M. Syamlal, and T. J. O'Brien, "Extension of Hill-Koch-Ladd drag correlation over all ranges of Reynolds number and solids volume fraction," *Powder Technol.*, vol. 162, no. 2, pp. 166–174, 2006.

[68] D. Baillis and J. F. Sacadura, "Thermal radiation properties of dispersed media: Theoretical prediction and experimental characterization," *J. Quant. Spectrosc. Radiat. Transf.*, vol. 67, no. 5, pp. 327–363, 2000.

[69] X. C. Wang, T. Laoui, J. Bonse, J. P. Kruth, B. Lauwers, and L. Froyen, "Direct selective laser sintering of hard metal powders: Experimental study and simulation," *Int. J. Adv. Manuf. Technol.*, vol. 19, no. 5, pp. 351–357, 2002.

[70] C. D. Boley, S. A. Khairallah, and A. M. Rubenchik, "Calculation of laser absorption by metal powders in additive manufacturing," *Addit. Manuf. Handb. Prod. Dev. Def. Ind.*, vol. 54, no. 9, pp. 507–517, 2017.

[71] A. Cattenone, S. Morganti, and F. Auricchio, "Basis of the Lattice Boltzmann Method for Additive Manufacturing," *Arch. Comput. Methods Eng.*, no. 0123456789, 2019.

[72] J. Romano, L. Ladani, and M. Sadowski, "Thermal Modeling of Laser Based Additive Manufacturing Processes within Common Materials," *Procedia Manuf.*, vol. 1, pp. 238–250, 2015.

[73] S. S. Sih and J. W. Barlow, "The prediction of the emissivity and thermal conductivity of powder beds," *Part. Sci. Technol.*, vol. 22, no. 4, pp. 427–440, 2004.

[74] M. Chiumenti *et al.*, "Numerical modelling and experimental validation in Selective Laser Melting," *Addit. Manuf.*, vol. 18, pp. 171–185, 2017.

[75] X. He and L. Luo, "Theory of the lattice Boltzmann method: From the Boltzmann

equation to the lattice Boltzmann equation," vol. 56, no. 6, pp. 6811–6817, 1997.

[76] X. Shan and H. Chen, "Lattice Boltzmann model for simulating flows with multiple phases and components," *Phys. Rev. E*, vol. 47, no. 3, pp. 1815–1819, 1993.

[77] N. E. Hodge, R. M. Ferencz, and J. M. Solberg, "Implementation of a thermomechanical model for the simulation of selective laser melting," *Comput. Mech.*, vol. 54, no. 1, pp. 33–51, 2014.

[78] I. Setien, M. Chiumenti, S. van der Veen, M. San Sebastian, F. Garciandía, and A. Echeverría, "Empirical methodology to determine inherent strains in additive manufacturing," *Comput. Math. with Appl.*, 2018.

[79] T. Nottingham and N. E. User, "Investigation of Residual Stress in Selective Laser Melting," 2018.

[80] B. Schoinochoritis, D. Chantzis, and K. Salonitis, "Simulation of metallic powder bed additive manufacturing processes with the finite element method: A critical review," *Proc. Inst. Mech. Eng. Part B J. Eng. Manuf.*, vol. 231, no. 1, pp. 96–117, 2017.

[81] D. Pal *et al.*, "A generalized feed-forward dynamic adaptive mesh refinement and derefinement finite-element framework for metal laser sintering-part II: Nonlinear thermal simulations and validations," *J. Manuf. Sci. Eng. Trans. ASME*, vol. 138, no. 6, pp. 1–10, 2016.

[82] Pittsburgh, Pennsylvania, and USA, "https://www.ansys.com/products/structures/ansys-additive-suite." .

[83] B. Song and C. Coddet, "Vacuum heat treatment of iron parts produced by selective laser melting : Microstructure , residual stress and tensile behavior," no. February 2016, 2014.

[84] P. L. Blackwell, "The mechanical and microstructural characteristics of laser deposited IN718," vol. 170, pp. 240–246, 2005.

[85] G. Leranth, "Solidification Time Estimation and Simulation - In Case of HPDC," *Mater. Sci. Forum*, vol. 649, pp. 467–472, 2010.

[86] M. Tiryakioğlu, E. Tiryakioğlu, and D. R. Askeland, "The effect of casting shape and size on solidification time: A new approach," *Int. J. Cast Met. Res.*, vol. 9, no. 5, pp. 259–267, 1997.

[87] Z. Shayfull, S. Sharif, M. F. Ghazali, and R. M. Saad, "Cycle Molding : A Review," vol. 33, no. 1, 2013.

[88] INFN, "http://diam.pd.infn.it/index.php/blog/177-ricerca-diam-sistemi-di-raffreddamento-per-elettrodi-di-saldatura." .

[89] A. Dwarkanath, *Laser powder fusion of H13 tool steel using pulsed Nd:YAG*

laser. 2002.

[90] D. Cormier, O. Harrysson, H. West, D. Cormier, and O. Harrysson, "Characterization of H13 steel produced via electron beam melting," 2009.

[91] Ansys, "Additive User's Guide (Print and Science)," .

[92] "https://www.digitalalloys.com/blog/energy-consumption-metal-additive-manufacturing/." .

[93] J. Bauer, P. Systems, and P. Malone, "Cost Estimating Challenges in Additive Manufacturing," pp. 1–8, 2015.

[94] F. Gobber, A. Pisa, D. Ugues, S. Lombardo, E. Fracchia, and M. Rosso, "Study of the Effect of Surface—Roughness of Dies and Tooling for HPDC on Soldering," *Miner. Met. Mater. Ser.*, vol. Part F4, pp. 977–981, 2018.

[95] B. Previtali, A. G. Demir, M. Bucconi, A. Crosato, and M. Penasa, "Comparative costs of additive manufacturing vs. machining: the case study of the production of forming dies for tube bending," *Solid Free. Fabr. Symp.*, pp. 2816–2834, 2017.